Terahertz Device Characterization Based on Electro-optic Near-field Measurement

HAI HUY NGUYEN PHAM

March 2018

Terahertz Device Characterization Based on Electro-optic Near-field Measurement

A dissertation submitted to
THE GRADUATE SCHOOL OF ENGINEERING SCIENCE
OSAKA UNIVERSITY

in partial fulfillment of the requirements for the degree of
DOCTOR OF PHILOSOPHY IN ENGINEERING

BY

HAI HUY NGUYEN PHAM

March 2018

ABSTRACT

Whereas a variety of electromagnetic waves from microwaves to light waves have been widely used in industrial applications such as the communications, energy, and medical fields, terahertz (THz) waves, which are located between them at frequencies from 100 GHz to 10 THz, have just started to be deployed in the 21st century toward practical applications.

THz waves have been attracting much interest owing to both their unique and inherited properties from neighboring frequency regions. These include the capability to penetrate dielectric materials (paper, ceramic, plastic, etc.) like microwaves, the high-directivity propagation like light waves, millimeter to sub-millimeter focused beam sizes, the existence of the fingerprint signatures of numerous materials, which enables nondestructive spectroscopy and imaging applications of THz waves for security inspection and material identification. An ultrahigh-speed wireless communication with data rates over 100 Gbit/s, which will become necessary within a decade for the age of the Internet of Everything, advanced high-definition video signal transmission, etc., is also expected by the use of THz waves owing to their broad bandwidth.

For these applications, devices to manipulate THz waves such as antennas, lens, mirrors, and their integrated structures are important in addition to signal sources and detectors. The characterization of such THz-wave manipulating devices is in urgent need of research and development. In particular, the near-field visualization of radiation and/or propagation of THz waves is greatly effective for the characterization.

Among various types of near-field measurement techniques, a photonics-based technique to measure electric fields (E-fields) with the use of an electro-optic (EO) material is considered to be the most promising because of the low invasiveness and wide bandwidth from microwave to THz frequencies. The EO material is formed to the optical fiber-mounted probe, referred to as an EO probe, to enable easy scanning of the probe over devices under test to visualize a dynamic three-dimensional E-field distribution.

In general, however, one of the problems of the near-field measurement using the fiber-mounted EO probe is measurement instability due to fluctuation in the sensitivity. This is caused by a change in the polarization state of the optical beam due to mechanical stress and ambient temperature. Several techniques to solve this problem have been proposed, such as active control of the polarization state, passive polarization compensation, and nonpolarimetric detection. Throughout this study, the nonpolarimetric detection scheme is adopted together with a self-heterodyne technique, because of its simplicity and simultaneous acquisition of both amplitude and phase information of the E-field.

Another practical issue in the EO measurement is its poor sensitivity, which limits the applicability of the EO probe below the frequency of 100 GHz, where the generated E-field is not strong enough for the currently available sensitivity of the EO measurement. Because the output power of semiconductor devices generally decreases in reciprocal proportion to the fourth power of the frequency, highly sensitive EO measurements are required for characterizing THz devices.

The objective of this study is to expand the use of the EO probes in the characterization of THz-wave manipulating devices at frequencies from 100 GHz to 500 GHz based on EO near-field measurements, and to show the "value" of the EO measurement by demonstrating essential results of THz device characterization.

Novel approaches are proposed for enhancing the sensitivity and reducing the invasiveness in the nonpolarimetric self-heterodyne EO detection system. The originality of this study includes the exploitation of an organic material, which exhibits a large EO coefficient, to enhance the sensitivity; introducing a holder, which has a refractive index closed to air, to reduce the invasiveness; finding the origin of the interference issue and proposing solutions; and finally employing a research object to improve the research means, i.e., enhancing the sensitivity of the EO probe by the near-field localizing device.

In Chapter 1, a background of this study is presented by introducing THz waves, near-field measurements, and the EO measurement.

In Chapter 2, the principles and experimental setups of the EO detection system are described.

In Chapter 3, an evaluation of polarimetric and nonpolarimetric techniques is presented, and the superiority of nonpolarimetric technique is experimentally verified with respect to measurement stability.

In Chapter 4, performance improvement techniques are discussed, including the sensitivity enhancement technique and the invasiveness reduction technique. An organic material, which exhibits a large EO coefficient, 4-dimethylamino-N-metyl-4-stilbazolium tosylate—DAST, was employed. The minimum detectable E-field is improved by 6 dB to 0.28 V/m at both the 100-GHz and 300-GHz bands. A new scheme employing differential detection to reduce the common laser noise is also introduced with a reduction of noise power by about 4 dB. For the reduction of the invasiveness, a styrofoam holder, which has the refractive index close to air, is introduced to reduce the invasiveness by approximately 8 dB. The origin and solutions of the issue of unwanted phase front appearing in the amplitude images are investigated and proposed.

In Chapter 5, the real impact of the EO probe is demonstrated by characterizing several THz devices, including an antenna, metal hole array (MHA), spherical-wave generation device, and near-field localizing device, referred to as "Terajet." In particular, the results of characterizing an antenna confirm the effectiveness of the near-to-far-field transformation technique employing the EO probe. The first experimental verification of the beam collimating phenomenon in the MHA and an explanation of the physical mechanism are obtained. The characterization of a spherical-wave generation device is the first THz device characterization up to 500 GHz. The obtained results also confirm that the EO probe can diagnose a malfunction of this device at high frequency. The Terajet generation is successfully observed.

In Chapter 6, two practical applications of the Terajet are proposed and experimentally demonstrated; one is to enhance the sensitivity of the EO probe —the research means. The other is to enhance the resolution of THz imaging.

In Chapter 7, the conclusion and future perspective of this study are presented.

TABLE OF CONTENTS

Chapter 1

Introduction

1.1 Background

1.1.1 Terahertz waves and their applications

Terahertz waves

The existence of electromagnetic (EM) waves, which are oscillations of electric fields (E-fields) and magnetic fields, and which transmit energy through space at the speed of light (3×10^8 m/s), were predicted theoretically by James Clerk Maxwell [1.1]. In 1888, Heinrich Hertz validated this theory experimentally [1.2, 1.3]. Since then, EM waves have become irreplaceable resources for various practical uses all over the world. Figure 1.1.1 illustrates the EM spectrum, showing the specific names for each region from microwaves to light waves, depending on their frequencies or wavelengths. Each EM region is exploited for different applications, e.g., 4G mobile phones uses the microwave region (approximately 2 GHz), radar in vehicles exploits the millimeter wave region (24 GHz to 77 GHz), cameras work in the visible light region, and the X-ray region is used in medical applications.

Terahertz (THz) waves are EM waves that are located between millimeter waves and infrared waves (Fig.1.1.1). THz frequencies range from 0.1 THz to 10 THz, corresponding to the wavelength range from 3 mm to 30 µm, and photon energy from 0.41 meV to 41.36 meV. In contrast to the microwave and light wave regions, which were studied centuries ago, the THz region had rarely been studied until

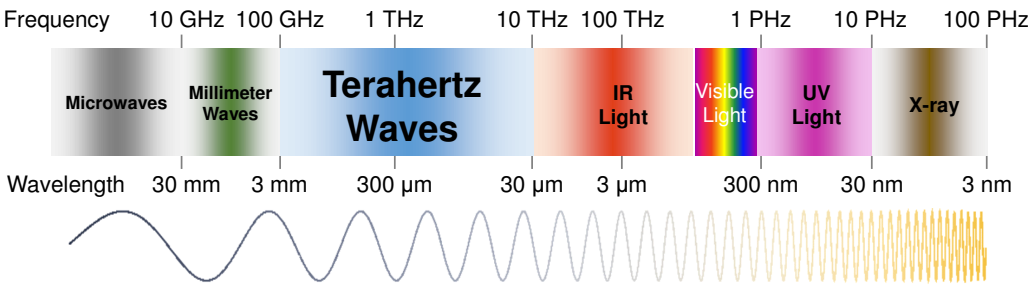

Figure 1.1.1: Location of terahertz waves in the electromagnetic spectrum.

recently, apart from in astronomy, owing to technical difficulties involved in making efficient and compact generators and detectors in this frequency band. This lack of suitable technologies led to the THz band being called the "THz gap" [1.4–1.7]. For instance, conventional electronics sources such as transistors or solid-state devices based on semiconductors were not yet ready to operate at high frequencies of several hundred gigahertz with a sufficient output power, because the motion of the carrier cannot follow the speed of THz oscillation [1.4,1.5], the output frequency and power of semiconductor devices have a physical trade-off [1.8], and the thermal-damage threat can be critical when making a short gate lengths for high-frequency operation [1.9]. The low photon energy of THz waves can make it difficult for solid-sate lasers, in which light is emitted from the transition between different energy states, to operate at this frequency because the THz-photon energy levels are comparable to the thermal relaxation energy, which can obscure the distinction between two energy states [1.5, 1.10].

Recently, the development of photonics-based sources [1.11], e.g., quantum cascade lasers [1.12–1.14], uni-traveling-carrier photodiodes (UTC-PD) [1.15–1.17], photoconductive devices [1.18, 1.19], and so on are driving forces to explore the THz region. The contributions of electronics-based THz sources such as resonant tunneling diodes and multiplexers are also important [1.6]. The THz region has been attracting tremendous research interest from different fields. As shown in Fig. 1.1.2, the number of publications related to "terahertz" is increasing exponentially [1.20] owing to its unique and inherited properties from the neighboring frequency regions, and its potential for various practical applications.

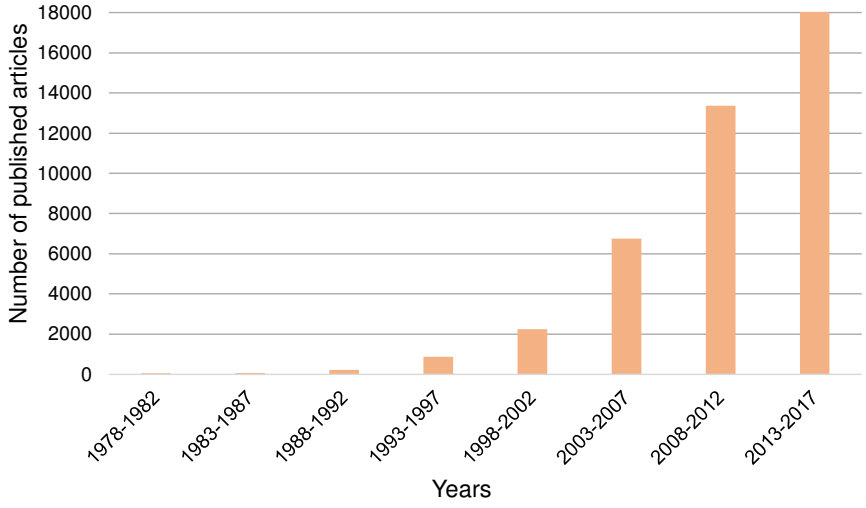

Figure 1.1.2: Number of publications in the THz field.

Promising applications

THz waves can penetrate many substances such as plastics, papers, and ceramics like microwaves; they have a high-directivity propagation and can be easily manipulated by optical devices such as mirrors, lenses, and polarizers like light waves. The spatial resolution, which is determined by the wavelength of EM waves, at THz frequencies is in the millimeter-to-submillimeter range. These THz properties are advantages in many applications of nondestructive imaging of packaged products for security and industrial inspection [1.21–1.23]. For example, nondestructive imaging for the inspection of a semiconductor integrated circuit inside a package was demonstrated in the 1–3 THz range with the spatial resolution of 0.25 mm [1.24]. A knife inside a briefcase was identified by nondestructive THz imaging at 0.2 THz [1.25]. In those inspections, the THz imaging is quite similar to X-ray inspection. Moreover, the THz imaging is safer, noninvasive, and has few hazardous effects on biological tissue, owing to the low photon energy (4 meV at 1 THz, whereas that of X-rays is above 100 eV) [1.10].

The THz band also contains unique absorption spectra or fingerprint signatures of many materials such as water, explosive molecules, and cancer cells that are beneficial for biomedical spectroscopy and material identification applications [1.26–1.29]. A reflection THz spectroscopy system based on pulsed generation was

introduced to detect explosives [1.30]. Another demonstration of security applications was reported in [1.31,1.32], in which the illicit drugs inside mail envelops were identified nondestructively. As for the biomedical applications, demonstrations of THz spectroscopy to inspect the thickness of coatings as well as the homogeneity of pharmaceutical tablets were reported [1.29, 1.33]. Several studies involving human tissues and cancer diagnosis based on THz spectroscopy and imaging were also reported [1.34–1.36], taking advantage of the non-ionizing property of THz radiation.

Another potential application of the THz band is ultra-broadband wireless communication [1.37]. It is known that there has been explosive growth in wireless data traffic, which may exceed 2 ZB (zettabyte, 10^{21} bytes) per year globally by 2021 owing to the increasing use of online services by mobile users, advanced video communications in the enterprise segment, and the growth of machine-to-machine (M2M) connections resulting from the Internet of Everything (IoE) phenomenon [1.38]. Wireless data rates of 100 Gbps are expected by approximately the year 2020 [1.39]. The carrier frequency has been increasing from the microwave region (2.4–5 GHz) to the millimeter wave region (60 GHz and 70–95 GHz) to meet the bandwidth requirements for the high-rate data transmission. However, the bandwidth of 7–9 GHz in the millimeter wave band is still insufficient to satisfy the demand of 100 Gbps data rate [1.40]. The THz band, therefore, is attracting significant research interests, owing to its naturally available broad bandwidth, e.g., 18 GHz bandwidth of 120-GHz band and over 50 GHz bandwidth for 300-GHz band [1.41]. Although the optical band using infrared light waves, named free-space optics (FSO) communication, can even offer larger bandwidth that can compete with THz communication [1.42], FSO faces lower tolerance for alignment, and suffers more than two orders of magnitude higher losses due to weather conditions such as fog and scintillation effects [1.40, 1.43, 1.44]. Which technologies will be adopted in the marketplace in the future is still under consideration [1.41]. Several attractive high data rate THz transmissions have been demonstrated, such as 10 Gbps in the 120-GHz band over a distance of 5.8 km for outdoor communication [1.45], single-channel 50 Gbps at 300-GHz band for indoor communication [1.46]

at a distance of 100 m [1.47, 1.48], and multichannel 160 Gbps in the 300-GHz to 500-GHz band with forward error correction (FEC) rate [1.49]. These results indicate the potential prospects of the THz region for practical applications in the near future.

1.1.2 THz devices

Recently, a significant number of devices in the THz region have been designed and studied for the exploitation of the THz band in practical applications. In those applications, devices to manipulate THz beams, which can collimate the beams in wireless communication system (Fig. 1.1.3(a)) or focus the beams in imaging or spectroscopy systems (Fig. 1.1.3(b)), are important in addition to signal sources and detectors. Figure 1.1.3(c) shows some examples of these devices such as antennas, lenses, mirrors, and their integrated structures. The characterization of such THz devices is becoming a critical requirement [1.50]. In particular, the near-field visualization of radiation and/or propagation of THz waves is effective for the device characterization. The near-field region is commonly defined at a distance below $\frac{2D^2}{\lambda}$ from the device under test (DUT) [1.51], where D and λ are the largest dimensions of the DUT aperture and the wavelength of THz waves, respectively. We now briefly introduce several THz-wave manipulating devices.

Antenna

The antenna, one of the fundamental components in any THz system, is a device that converts freely propagating EM radiation into localized energy and vice versa. The number of studies of THz antennas has been increasing rapidly. For example, several antennas have been designed for practical THz wireless communication such as the Cassegrain antenna for long-distance transmission of over 800 m [1.52] and the plate-laminated waveguide slot array antenna for a short distance transmission of 2.5 m at 120 GHz [1.53]. The characterization of directivity, gain, field distribution, and radiation patterns of designed and fabricated THz antennas is becoming necessary.

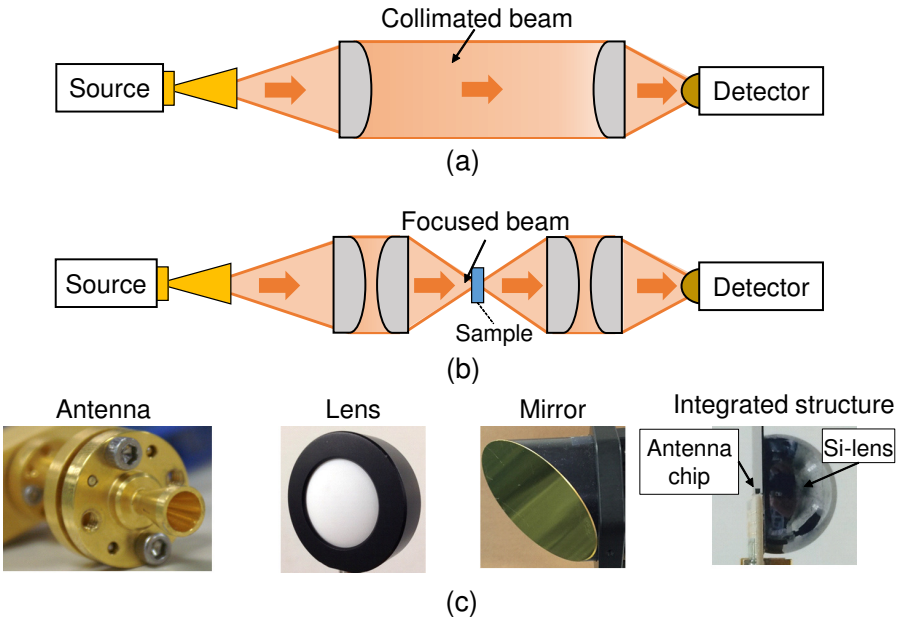

Figure 1.1.3: Simple schematics of (a) THz communication system, (b) imaging and spectroscopy systems, and (c) examples of THz-wave manipulating devices.

Wavefront manipulating device

Lenses and mirrors are examples of wavefront manipulating devices [1.54–1.57]. These devices are used to enhance the directivity of the antenna for wireless communication applications [1.54–1.56], or produce a hotspot for high-resolution imaging applications [1.57–1.59]. Commonly, the radiation patterns are measured directly in the far-field to characterize these devices. However, the direct observation and characterization of the phase front distribution of these devices are also important to verify their accurate operation. This leads to the necessity of effective THz near-field measurement technology.

Near-field localization device

Near-field localization devices, which manipulate THz waves in the near-field region based on interesting phenomena such as concentrating E-field on tips [1.60, 1.61], surface plasmons [1.62, 1.63], and photonic nanojets [1.64], have been attracting increasing interest. The main attraction of these phenomena is that a spatial imaging resolution below the diffraction limit (one wavelength) can be expected.

This can be a benefit of THz imaging and spectroscopy applications.

A photonic nanojet is the generation of localized EM fields in the shadow side of a low-dielectric particle, which has dimension of approximately the incident free-space wavelength. This phenomenon is based on Mie scattering theory and was initially studied in the photonic region [1.65, 1.66]. Photonic nanojets were predicted to occur in other regions of EM spectrum if the materials and the dimensions of the devices satisfy certain criteria. Some studies were reported in the microwave region (8–35 GHz) [1.67, 1.68]. In the THz region, this phenomenon is also named a "Terajet" [1.69], and it was studied by simulation [1.70]. Experimental studies based on visualizing near E-field distribution are necessary for the practical exploitation of this phenomenon in THz applications. In order to characterize these devices as well as the interesting near-field phenomena in the THz region, minimally invasive near-field measurement technology is required.

Integrated structure of antenna and lens

Integrated structures of an antenna and lens are widely studied in the THz region, because the wavelength of THz waves is sufficient for compact integrated devices such as an integrated structure of silicon-lens (Si-lens) and antenna [1.71–1.73] for spectroscopy and imaging applications. The broadband Si-lens mounted UTC-PD [1.15] is an example of commercially available integrated devices used in THz spectroscopy systems. The radiation direction of THz beam from these integrated devices is significantly influenced by the alignment between the antenna and the lens [1.74], material and thickness of substrates [1.75], and the impedance matching [1.76]. The experimental near-field characterization of THz radiation from these devices in a broad bandwidth is important for the diagnosis [1.77].

1.1.3 Near-field measurements

Near-field measurements can be roughly divided into two categories: electronics-based and photonics-based technologies.

Electronics-based techniques

Figure 1.1.4 shows a simple scheme of a measurement system based on electronic technology. Generally, a vector network analyzer, multipliers, mixers, antenna probe, and coaxial cables are used. The E-field perturbation or invasiveness is one of critical concerns in near-field measurements because it directly affects the accuracy of the measurement. Therefore, the E-field invasiveness has been decreasing in near-field measurement techniques.

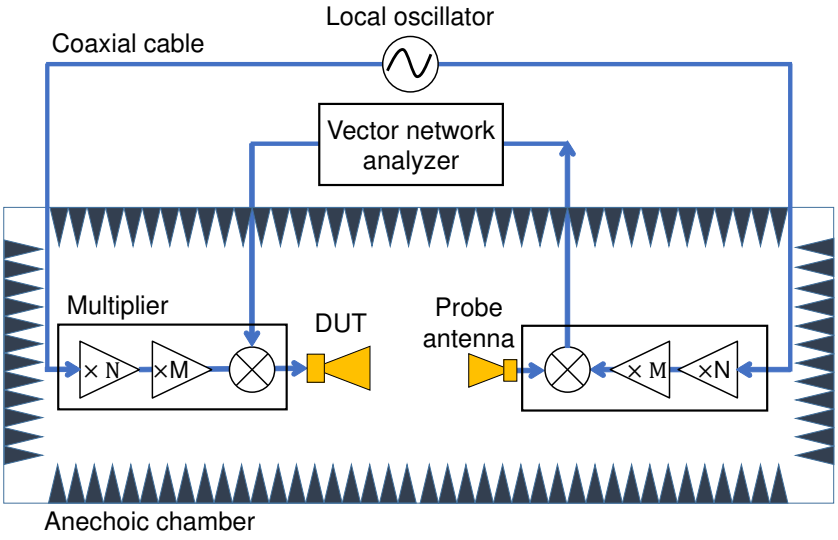

Figure 1.1.4: Schematic of electronics-based system for near-field measurement.

Figure 1.1.5(a) depicts the initial electronics-based near-field measurement technique using a small antenna probe such as a horn antenna, dipole antenna, or open-ended waveguide [1.78, 1.79]. A complex probe compensation is usually required in this technique, owing to the multiple reflection between the antenna probe and the DUT [1.80].

In Fig. 1.1.5(b), a small metallic tip was used in the near-field microscopy technique [1.81] to reduce the multiple reflection that can be caused by the small antenna. A two-dimensional (2D) mapping of amplitude and phase distributions from a monolithic microwave integrated circuit (MMIC) was demonstrated by this technique [1.81]. The limitation of this technique is that the radiation of the E-field cannot be measured because of the significant dependence of the sensitivity

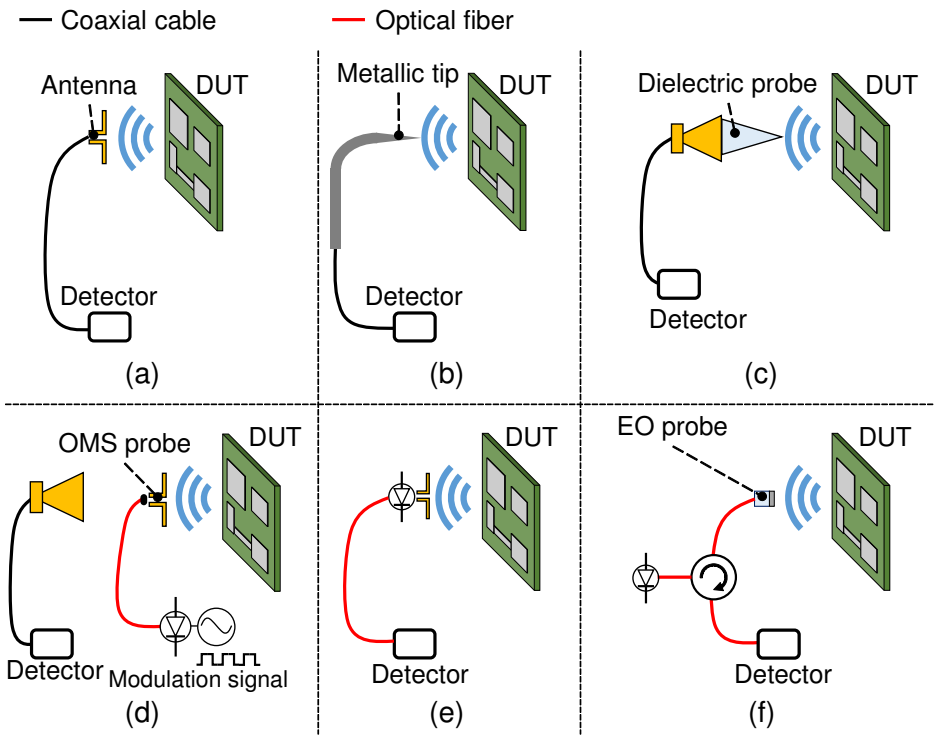

Figure 1.1.5: Near-field measurement techniques including electronics-based techniques: (a) small antenna probe [1.78,1.79], (b) metallic tip probe [1.81], (c) dielectric probe [1.82], (d) optically modulated scattering probe [1.83–1.85]; photonics-based techniques: (e) active modulating laser diode technique [1.92, 1.93] and (f) electro-optic probe.

on the distance between the tip and the DUT.

A dielectric probe was proposed, as shown in Fig. 1.1.5(c), to further reduce the invasiveness caused by the metallic probe [1.82]. The radiating EM wave can also be measured by this technique.

In order to avoid the invasiveness of the probe in the direct measurement, an indirect measurement based on an optically modulated scattering (OMS) technique was proposed [1.83–1.85], as shown in Fig. 1.1.5(d). An OMS probe was used as a scatterer, in which the impedance of the dipole antenna of the probe can be intentionally modulated by a laser diode (LD) through an optical fiber. Another antenna and detector are placed in the far-field to detect the scattering E-field from the probe. The OMS probe is scanned freely in space and the E-field distribution can be mapped. The disadvantage of this technique is that separate antenna and sensitive detector are required in the system, and the optimization of the spatial

resolution, sensitivity, and detectable bandwidth is complicated and shows a trade-off among these factors [1.86, 1.87].

Photonics-based techniques

Generally, coaxial cables, made from metallic materials, used in the electronics-based near-field measurement system (Fig. 1.1.4) can disturb the E-field to be measured [1.88–1.91]. However, in photonics-based systems, the coaxial cables are replaced with optical fibers that can significantly reduce the E-field perturbation.

Figures 1.1.5(e) depicts a photonics-based technique employing a direct radio frequency (RF) modulation of LD [1.92, 1.93]. This technique has been commercialized to measure the near-field distribution for device characterization at microwaves frequencies [1.94]. However, the limitation of the detectable bandwidth of components such as the antenna, amplifier, and detecting photodiode (PD) in this technique makes it difficult to extend to the THz frequencies.

Figure 1.1.5(f) shows a near-field measurement based on an electro-optic (EO) probe, which is made from a small cubic dielectric material exhibiting an EO effect. This technique is the best candidate for near-field measurements for the THz device characterization, owing to the significantly low invasiveness and broad detectable bandwidth up to THz frequencies [1.95, 1.96]. In this study, the near-field measurement technique based on EO measurement was chosen. The specific technologies of the EO measurement are introduced in the next section.

1.1.4 EO measurement

The EO effect consists of variations in the birefringence properties or dielectric tensor inside the EO crystal of the EO probe when the E-field is applied to the crystal. Therefore, the refractive index of the crystal changes with the applied E-field. In the Pockels effect [1.97], the change in refractive index is linearly proportional to the E-field, whereas it is proportional to the square of the E-field in Kerr effect. The Pockels effect is often preferred for EO measurement applications, owing to the higher coefficient.

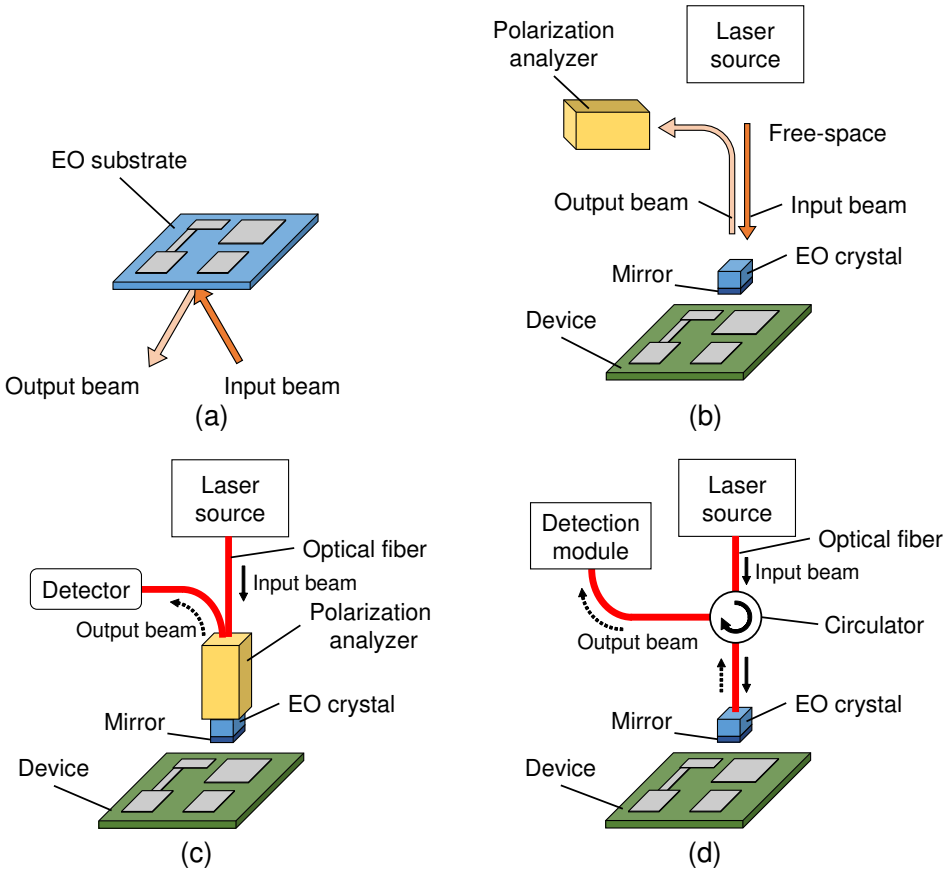

Figure 1.1.6: Four types of EO measurement configurations: (a) substrate EO measurement, (b) free-space EO measurement, (c) packaged polarization analyzer module and EO crystal, and (d) optical-fiber-mounted EO measurement.

The change or modulation of the refractive index of the EO crystal leads to the polarization modulation of the input optical probe beam or phase modulation to generate sidebands of input optical carrier frequency. Commonly, the EO measurement was based on the polarization modulation technique [1.98]. The circular polarization state of the optical probe beam changes to elliptical polarization when the EO crystal interacts with the E-field to be measured. Then, this polarization change is detected by the polarization analyzers and PD. Figure 1.1.6 depicts four configurations of EO measurement systems to visualize the E-field distribution for device characterization.

Substrate EO measurement

The first configuration is a substrate EO measurement, as illustrated in Fig. 1.1.6(a). The substrate of a DUT is made from an EO material such as GaAs

or InP [1.99, 1.100]. Demonstrations of 2D potential mapping of a microstrip line [1.101] and MMICs [1.102] indicated the potential of this configuration for internal device characterization. Because no external sophisticated EO probe is required, the E-field inside the substrate can be measured by illuminating the input optical beam to the DUT and detecting the reflected or transmitted output beam. However, this configuration has a drawback of limited DUTs that can be measured, because many devices are not fabricated on an EO-material substrate. Moreover, the radiated E-field cannot be measured with this EO configuration [1.103].

Free-space EO measurement

The second configuration employs a distinct small EO crystal for the measurement, as shown in Fig. 1.1.6(b). The optical probe beam is illuminated to the EO crystal through free space. The reflected output optical beam from a mounted mirror on the EO head can be detected by a polarization analyzer and PD. The E-field distribution from the DUT can be mapped flexibly in different positions by scanning the DUT or the EO crystal. However, the alignment procedure is sophisticated because a free-space optical beam is needed to focus on a small EO crystal [1.103]. Consequently, the DUT is scanned for mapping the E-field [1.104], or else this configuration is primarily utilized for time-resolved measurements at a specific position rather than spatially-resolved measurements [1.105]. The measurement of the near-field patterns of both amplitude and phase distributions of a microstrip patch antenna at 4 GHz [1.104], a planar resonator at 7 GHz [1.106], and a coplanar waveguide at 1 GHz [1.107] based on this configuration were demonstrated by scanning DUTs.

Packaged polarization analyzer module and EO crystal

The third configuration employs optical fiber technology (Fig. 1.1.6(c)). The polarization analyzer module is packaged and integrated with the EO crystal to form a convenient probe [1.108–1.110]. The input and output optical beam are transmitted through optical fibers. Owing to the flexibility and compactness of optical fibers, this configuration offers good measurement versatility without sophisticated

free-space optic alignment. Moreover, the optical fibers and small EO crystal show minimal E-field disturbance. Several demonstrations of near-field mapping using this configuration were reported, such as a monopole antenna at 0.9 GHz [1.109], a test board and cellular phone at 0.93 GHz [1.110], and a horn antenna at 60 GHz [1.111]. However, the polarization analyzer module with dimension of approximately several tens of centimeters may disturb the E-field in the near-field region at a high frequency, such as THz frequency, where the wavelength is several millimeters to submillimeters.

Optical fiber-mounted EO measurement

The fourth configuration of EO measurement can solve the above disturbance issue by utilizing only a small EO crystal mounted to the optical fiber without the polarization modulation package, as shown in Fig. 1.1.6(d). In 1998–2000, different research groups reported this EO measurement system using pulse laser sources [1.112, 1.113] and continuous-wave (CW) laser sources [1.114, 1.115]. The invasiveness, compactness, and flexibility of the EO measurement can be improved significantly by this configuration. Several E-field distribution mappings were demonstrated, such as from a microstrip line at 1 GHz [1.116–1.118], from a horn antenna, and from a slot antenna at 11 GHz [1.113].

The pulse laser sources were initially used for EO measurement, also named EO sampling technique, owing to the emergence of femtosecond and picosecond pulse lasers [1.119]. However, EO sampling using pulse lasers is bulky, costly, and requires long acquisition times [1.117,1.119]. Moreover, characterizing devices at a single frequency in the frequency domain are rather common [1.117, 1.118]. Thus CW sources, which are more compact and cost-effective, are indispensable for these types of device-characterization applications, owing to their frequency tunability, high frequency resolution, and stability [1.15, 1.103].

1.2 Motivation

1.2.1 Issue of stability

Generally, one of the problems of the fiber-mounted EO measurement is a measurement instability due to the sensitivity fluctuation. The polarization modulation technique is used in this fiber-mounted EO measurement [1.50] similar to other EO measurement configurations. However, the intrinsic problem of this technique is that the polarization state of the optical probe beam is strongly influenced by the deviations of the birefringence or the refractive index of the optical fibers due to the ambient temperature fluctuation and/or mechanical stress when bending or touching the optical fibers [1.117, 1.120, 1.121]. Several techniques to solve this problem have been proposed.

Wakana et al. [1.117] suggested that it is necessary to control the polarization state of the optical probe beam fixed to the optimum in the EO crystal. Bernier et al. and Garzarella et al. [1.121, 1.122] introduced an automated controller to actively control the polarization state of the probe beam through wave plates. Others [1.120, 1.123] introduced a passive sensitivity-stabilization technique using a Faraday rotator to compensate the polarization-mode-dispersion and cancel out the phase difference between the lights transmitted on the fast and slow axes of the optical fiber (polarization-maintaining fiber, PMF).

From an idea employing a resonator mode, which exhibits whispering gallery modes, to the EO materials [1.124], an EO measurement system, using a Fabry–Perot resonance-based EO probe and reducing the polarization analyzer module, was proposed [1.125]. With a sophisticated design of an EO probe sandwiched between Fabry–Perot materials [1.125,1.126], the resonant frequency in the optical probe beam can be formed. When the E-field is applied to this EO probe, the resonant frequency is shifted owing to the variation in the refractive index of the EO crystal by the Pockels effect [1.125–1.127]. Therefore, the optical heterodyne detection can be realized with the reduction in the polarization analyzer module. Measurements of the near-field patterns of a patch antenna at 18.5 GHz and 35 GHz were demonstrated by this technique [1.128, 1.129]. However, the drawback

of the narrow detectable bandwidth due to exploiting resonance-based EO probe structure cannot be avoided [1.126, 1.129].

Recently, a nonpolarimetric EO detection technique [1.130], based on the coherent detection of the generated sideband due to the phase modulation of the optical probe beam inside the EO crystal when interacting with the EM waves, was proposed. A self-heterodyne system, which is based on the photonics generation and detection, was also proposed to realize a broad-bandwidth measurement [1.131–1.133].

In this study, the nonpolarimetric EO detection scheme is adopted together with a self-heterodyne technique because of its simplicity and simultaneous acquisition of both amplitude and phase information of the THz E-field [1.133, 1.134].

1.2.2 Issue of sensitivity

Another practical issue in the EO measurement is the poor sensitivity or minimum detectable E-field. To date, the minimum detectable E-field of EO probe has been above 1 V/m, which limits the applicability of the EO probe below the frequency of 100 GHz, because the generated E-field is not strong enough for the currently available sensitivity, as depicted by the blue dashed-box in Fig. 1.2.1. Because the output power of semiconductor devices generally decreases in reciprocal proportion to the fourth power of the frequency [1.135, 1.136], highly sensitive EO measurement systems are required for characterizing THz devices.

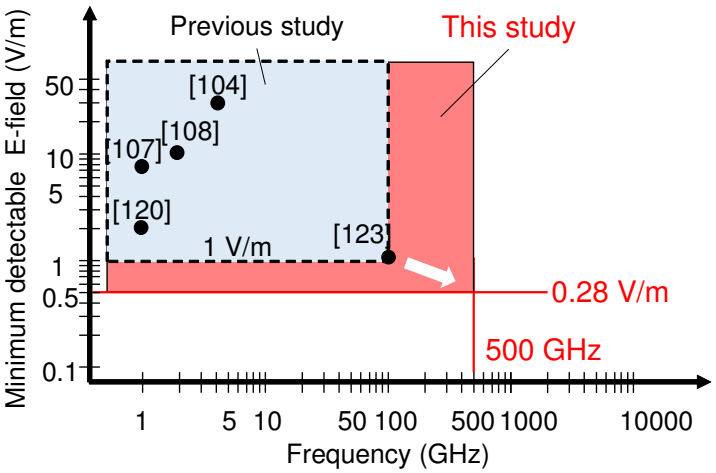

Figure 1.2.1: Sate-of-the-art device characterization based on EO measurement.

The motivation of this dissertation is to expand the use of the EO probe in the characterization of THz-wave manipulating devices beyond 100 GHz, based on EO near-field measurement, as depicted in the red area in Fig. 1.2.1, and to show the "value" of the EO measurement by demonstrating important results of THz device characterization. Novel approaches are proposed for enhancing the sensitivity and reducing the invasiveness in the nonpolarimetric self-heterodyne EO detection system [1.133, 1.134].

1.3 Objective

The objective of this dissertation is to enable the characterization of THz devices from 100 GHz to 500 GHz by improving the sensitivity and invasiveness of EO detection systems. Practical characterization of THz devices is demonstrated to prove the impact of EO measurement. These devices are (1) an antenna, (2) a wavefront manipulating device, (3) a spherical-wave generation device, and (4) a near-field localization device. Key approaches include exploiting an organic EO material, which exhibits a large EO coefficient, to enhance the sensitivity; employing a holder, which has refractive index closed to air, to reduce the invasiveness; finding the origin and proposing solutions to the interference issue; and employing one of researched devices to improve the sensitivity of the EO probe.

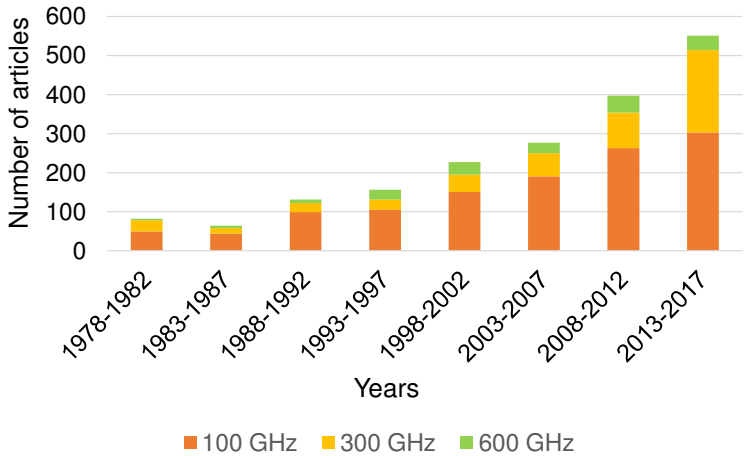

Figure 1.3.1: Articles related to 100 GHz, 300 GHz, and 600 GHz.

Figure 1.3.1 shows the number of published articles related to 100 GHz, 300 GHz, and 600 GHz [1.20]. The number of articles is increasing dramatically. This

indicates that the trend of exploiting high frequencies is also increasing. The study reported in this dissertation aims to adapt the EO near-field measurement technology to this developing trend.

1.4 Outline of this dissertation

This dissertation covers four main topics: an experimental evaluation of the non-polarimetric self-heterodyne EO detection system (Chapter 3); performance improvement techniques (Chapter 4); practical THz device characterization based on an EO detection system (Chapter 5), including (5.1) an antenna, (5.2) wavefront manipulating devices, (5.3) a spherical-wave generation device, and (5.4) a near-field localization device, which is referred to as "Terajet"; and applications of the characterized Terajet device (Chapter 6). The contents and organization of this dissertation are summarized as follows and the outline is depicted in Fig. 1.4.1.

Chapter 1 introduces the background of this study, including THz waves, on-going developments of various THz devices, near-field measurement techniques, and the EO measurement. The motivation, objective, and structure of this dissertation are also described.

Chapter 2 describes the principles and experimental setups of fiber-mounted EO detection systems based on the photonic generation and detection including homodyne, self-heterodyne, polarimetric, and nonpolarimetric techniques.

Chapter 3 describes the experimental evaluation of polarimetric and nonpolarimetric techniques. The superiority of the nonpolarimetric technique is experimentally verified with respect to measurement stability and near-field visualization.

Chapter 4 describes the performance improvement techniques, including the sensitivity enhancement technique and the invasiveness reduction technique. In particular, an organic EO material, which exhibits a large EO coefficient, 4-dimethylamino-N-metyl-4-stilbazolium tosylate (DAST), is exploited as an EO probe. The evaluations of the sensitivity, stability, and repeatability of the DAST probe and the ZnTe probe, which is known as one of the best inorganic materials for EO detection, are discussed. A signal-to-noise ratio (SNR) improvement of over 10 dB was obtained. The minimum detectable E-field is improved to 0.28 V/m

at both the 100-GHz and 300-GHz bands. A new scheme employing differential detection to reduce the common laser noise is also introduced with a reduction of noise power by approximately 4 dB. In addition, the optimization of the optical components in the EO detection system is discussed. For the reduction in the invasiveness, both a theoretical study by simulation and experimental evaluation of the invasiveness of the EO probe are described. A styrofoam holder, which has a refractive index close to that of air, is introduced to reduce the invasiveness by approximately 8 dB. The origin of the issue of an unwanted phase front appearing in the amplitude images is investigated. Solutions by signal processing methods and hardware improvements are described.

Chapter 5 describes the real impact of the EO measurement by demonstrating the practical characterization of several THz devices. In particular, the results of characterizing an antenna confirmed the effectiveness of near-to-far-field transformation technique employing the EO probe. The obtained far-field patterns of a standard F-band (90–140 GHz) horn antenna show good agreement with the simulated results. For the wavefront manipulating devices, the first experimental verification of the beam collimating phenomenon in the MHA and the explanation of physical mechanism are obtained through the comparison with the collimating phenomenon of commercially available lens. The characterization of spherical-wave generation device, a broadband Si-lens-integrated UTC-PD, is the first THz device characterization up to 500 GHz, where the output power of THz radiation is 1.2 μW. The obtained results also confirm that the EO probe can diagnose malfunctions of this device at high frequency. The Terajet-generation from a dielectric cube is successfully observed.

Chapter 6 describes two proposed and demonstrated practical applications of one of characterized THz devices, the Terajet. One is to enhance the sensitivity of the EO probe, and the other is to enhance the resolution of THz imaging. An enhancement in the detected THz intensity of the EO probe of approximately 6 dB, and an improvement in the resolution of the THz imaging system equivalent to the diffraction-limited resolution at 2.2 times higher THz frequency are achieved.

Chapter 7 concludes this dissertation and discusses the future perspective.

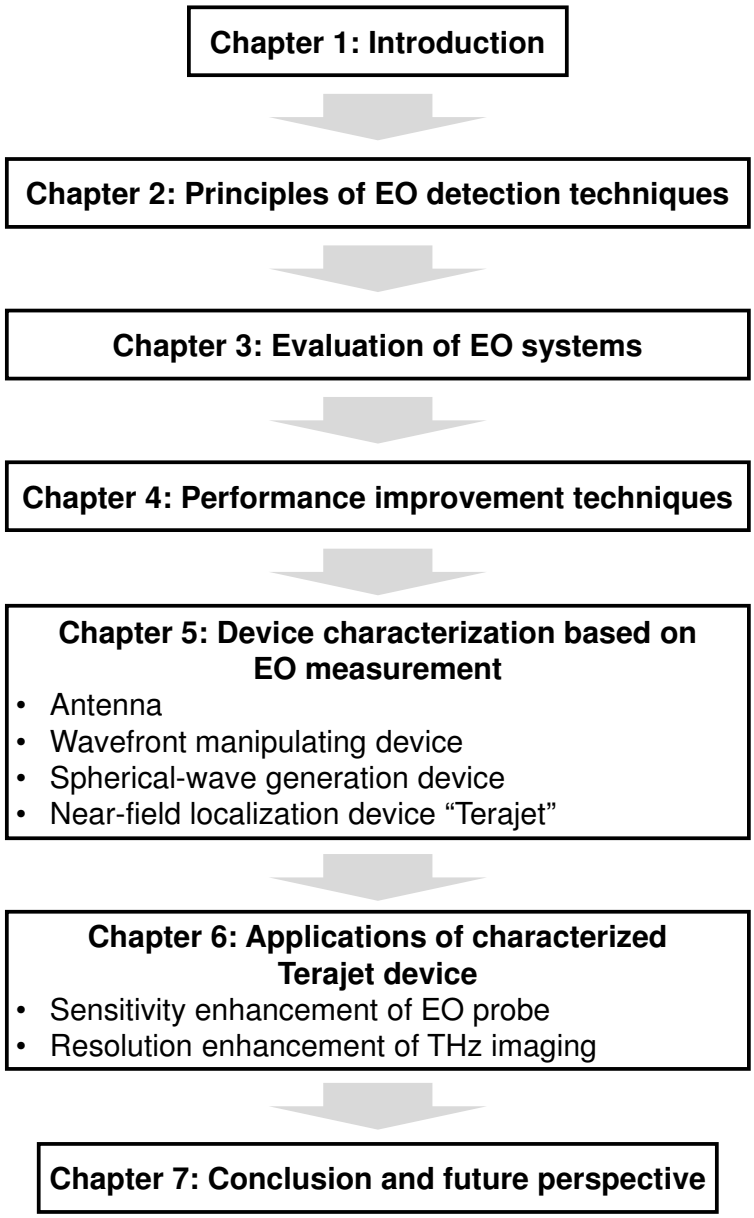

Figure 1.4.1: Organization of this dissertation.

References

[1.1] J. C. Maxwell, *"A dynamical theory of electromagnetic field,"* Phil. Trans., **166**, pp. 459-512, 1865.

[1.2] H. Hertz, *"On the finite velocity of propagation of electromagnetic action,"* Sitzungsber. D. Berl. Akad. D. Wiss., **34**, p. 551, 1888, in H. Hertz (translated by D. E. Jones), Electric Waves, **110**, 1962.

[1.3] D. L. Sengupta and T. K. Sarkar, *"Maxwell, Hertz, the Maxwellians, and the early history of electromagnetic waves,"* IEEE Antennas Propag. Mag., **45**, pp. 13-19, 2003.

[1.4] G. P. Williams, *"Filling the THz gap high power sources and applications,"* Rep. Prog. Phys., **69**, pp.301-326, 2006.

[1.5] P. H. Siegel, *"Terahertz technology,"* IEEE Trans. Microw. Theory Techn., **50**, pp. 910-928, 2002.

[1.6] M. Tonouchi, *"Cutting-edge terahertz technology,"* Nat. Photonics, **1**, pp.97-105, 2007.

[1.7] T. Nagatsuma, H. Ito, and T. Ishibashi, *"High-power RF photodiodes and their applications,"* Laser & Photon. Rev., **3**, pp. 123-137, 2009.

[1.8] E. O. Johnson, *"Physical limitations of frequency and power parameters of transistors,"* RCA Review, **26**, pp. 163-177, 1965.

[1.9] R. J. Trew, *"High−frequency solid−state electronic devices,"* IEEE Trans. Electron Devices, **52**, pp. 638-649, 2005.

[1.10] X. C. Zhang and J. Xu, *"Introduction to THz wave photonics,"* Springer, pp. 3-15, 2010.

[1.11] S.S. Dhillon et al., *"The 2017 terahertz science and technology roadmap,"* J. Phys. D: Appl. Phys., **50**, p. 043001, 2017.

[1.12] R. Kohler, A. Tredicucci, F. Beltram, H. E. Beere, E. H. Linfield, A. G. Davies, D. A. Ritchie, R. C. Iotti, and F. Rossi, *"Terahertz semiconductor-heterostructure laser,"* Nature, **417**, pp. 156-159, 2002.

[1.13] B. S. Williams, *"Terahertz quantum cascade lasers,"* Nat. Photon., **1**, pp. 517-525, 2007.

[1.14] M. A Belkin and F. Capasso, *"New frontiers in quantum cascade lasers: high performance room temperature terahertz sources,"* Phys. Scr., **90**, p. 118002, 2015.

[1.15] T. Ishibashi, Y. Muramoto, T. Yoshimatsu, and H. Ito, *"Unitraveling-carrier photodiodes for terahertz applications,"* IEEE J. Sel. Topics Quantum Electron., **20**, 3804210, 2014.

[1.16] H. Ito, H. Yamamoto, T. Yoshimatsu, and T. Ishibashi, *"Enhanced-output-power broadband terahertz-wave emitter based on slot-antenna-integrated uni-travelling-carrier photodiode,"* Electron. Lett., **51**, pp. 1670-1671, 2015.

[1.17] S. Hisatake, J. Y. Kim, K. Ajito, and T. Nagatsuma, *"Self-heterodyne spectrometer using uni-traveling-carrier photodiodes for terahertz-wave generators and optoelectronic mixers,"* J. Lightw. Technol., **32**, pp. 3683-3689, 2014.

[1.18] D. H. Auston and M. C. Nuss, *"Electrooptical generation and detection of femtosecond electrical transients,"* IEEE J. Quantum Electron., **24**, pp. 184-197, 1988.

[1.19] K. Peng, P. Parkinson, L. Fu, Q. Gao, N. Jiang, Y. N. Guo, F. Wang, H. J. Joyce, J. L. Boland, H. H. Tan, C. Jagadish, and M. B. Johnston, *"Single Nanowire Photoconductive Terahertz Detectors,"* Nano Lett., **15**, pp. 206-210, 2015.

[1.20] *https://academic.microsoft.com,* 2017.

[1.21] W. L. Chan, J. Deibel, and D. M. Mittleman, *"Imaging with terahertz radiation,"* Rep. Prog. Phys., **70**, pp. 1325-1379, 2007.

[1.22] D. M. Mittleman, M. Gupta, R. Neelamani, R. G. Baraniuk, J. V. Rudd, and M. Koch, *"Recent advances in terahertz imaging,"* Appl. Phys. B, **68**, pp. 1085-1094, 1999.

[1.23] C. Jansen, S. Wietzke, O. Peters, M. Scheller, N. Vieweg, M. Salhi, N. Krumbholz, C. Jordens, T. Hochrein, and M. Koch, *"Terahertz imaging applications and perspectives,"* Appl. Opt., **49**, pp. E48-E57, 2010.

[1.24] B. B. Hu and M. C. Nuss, *"Imaging with terahertz waves,"* Opt. Lett., **20**, pp. 1716-1718, 1995.

[1.25] N. Karpowicz, H. Zhong, C. Zhang, K. I. Lin, J. S. Hwang, J. Xu, and X. C. Zhang, *"Compact continuous-wave subterahertz system for inspection applications,"* Appl. Phys. Lett., **86**, p. 054105, 2005.

[1.26] Y. C. Shen, *"Terahertz pulsed spectroscopy and imaging for pharmaceutical applications: a review,"* Int. J. Pharm., **417**, pp. 48-60, 2011.

[1.27] E. Pickwell and V. P. Wallance, *"Biomedical applications of terahertz technology,"* J. Phys. D: Apply. Phys., **39**, pp. R301-R310, 2006.

[1.28] P. H. Seigel, *"Terahertz technology in biology and medicine,"* IEEE Trans. Microw. Theory Techn., **52**, pp. 2438-2447, 2004.

[1.29] K. Ajito and Y. Ueno, *"THz chemical imaging for biological applications,"* IEEE Trans. THz Sci. Technol., **1**, pp. 293-300, 2011.

[1.30] Y. C. Shen, T. Lo, P. F. Taday, B. E. Cole, W. R. Tribe, and M. C. Kemp, *"Detection and identification of explosives using terahertz pulsed spectroscopic imaging,"* Appl. Phys. Lett., **86**, p. 241116, 2005.

[1.31] K. Kawase, Y. Ogawa, and Y. Watanabe, *"Non-destructive terahertz imaging of illicit drugs using spectral fingerprints,"* Opt. Express, **11**, pp. 2549-2554, 2003.

[1.32] M. Kato, S. R. Tripathi, K. Murate, K. Imayama, and K. Kawase, *"Non-destructive drug inspection in covering materials using a terahertz spectral imaging system with injection-seeded terahertz parametric generation and detection,"* Opt. Express, **24**, pp. 6425-6432, 2016.

[1.33] A. J. Fitzgerald, B. E. Cole, and P. F. Taday, *"Nondestructive analysis of tablet coating thickness using terahertz pulsed imaging,"* J. Pharm. Sci., **94**, pp. 177-183, 2005.

[1.34] N Chopra, K. Yang, Q. H. Abbasi, K. A. Qaraqe, M. Philpott, and A. Alomainy, *"THz time-domain spectroscopy of human skin tissue for in-body nanonetworks,"* IEEE Trans. THz Sci. Technol., **6**, pp. 803-809, 2016.

[1.35] S. J. Oh, J. Kang, I. Maeng, J. S. Suh, Y. M. Huh, S. Haam, and J. Son, *"Nanoparticle-enabled terahertz imaging for cancer diagnosis,"* Opt. Express, **17**, pp. 3469-3475, 2009.

[1.36] P. C. Ashworth, E. P. MacPherson, E. Provenzano, S. E. Pinder, A. D. Purushotham, M. Pepper, and V. P. Wallance, *"Terahertz pulsed spectroscopy of freshly excised human breast cancer,"* Opt. Express, **17**, pp. 12444-12454, 2009.

[1.37] T. Nagatsuma, *"Terahertz technologies: present and future,"* IEICE Electron. Express, **8**, pp. 1127-1142, 2011.

[1.38] Cisco *"The zettabyte era: trends and analysis,"* (Cisco and/or its affiliates, 2017).

[1.39] T. Kurner and S. Priebe, *"Towards THz communications-status in research, standardization and regulation,"* J. Infrared Millim. Terahertz Waves, **35**, pp. 53-62, 2014.

[1.40] A. J. Seeds, H. Shams, M. J. Fice, and C. C. Renaud, *"Terahertz photonics for wireless communications,"* J. Lightwave Technol., **33**, pp. 579-587, 2015.

[1.41] T. Nagatsuma, G. Ducourmau, and C. C. Renaud, *"Advances in terahertz communications accelerated by photonics,"* Nat. Photon., **10**, pp. 371-379, 2016.

[1.42] J. Wang, J. Y. Yang, I. M. Fazal, N. Ahmed, Y. Yan, H. Huang, Y. Ren, Y. Yue, S. Dolinar, M. Tur, and A. E. Willner, *"Terabit free-space data transmission employing orbital angular momentum multiplexing,"* Nat. Photon., **6**, pp. 488-496, 2012.

[1.43] *"International Telecommunication Union ITU-R P.840-3: Attenuation due to Clouds and Fog,"* ITU, 1999.

[1.44] J. Federici and L. Moeller, *"Review of terahertz and subterahertz wireless communications,"* J. Appl. Phys., **107**, p. 111101, 2010.

[1.45] A. Hirata, T. Kosugi, H. Takahashi, J. Takeuchi, H. Togo, M. Yaita, N. Kukutsu, K. Aihara, K. Murata, Y. Sato, T. Nagatsuma, and Y. Kado, *"120-GHz-band wireless link technologies for outdoor 10-Gbit/s data transmission,"* IEEE Trans. Microw. Theory Techn., **60**, pp. 881-895, 2012.

[1.46] T. Nagatsuma and G. Carpintero, *"Recent progress and future prospect of photonics-enabled terahertz communications research,"* IEICE Trans. Electron., **E98-C**, pp. 1060-1070, 2015.

[1.47] T. Nagatsuma, K. Oogimoto, Y. Yasuda, Y. Fujita, Y. Inubushi, S. Hisatake, A. M. Agoues, and G. C. Lopez, *"300-GHz-band wireless transmission at 50 Gbit/s over 100 meters,"* 41st International Conference on Infrared, Millimeter, and Terahertz waves (IRMMW-THz), 2016.

[1.48] T. Kurokawa, Y. Fujita, Y. Inubushi, S. Hisatake, M. Fujiwara, R. Koma, and T. Nagatsuma, *"100 meter wireless transmission at 50 Gbit/s in 300-GHz-band,"* 24th Congress of International Commission for Optics (ICO-24), Tu1G-03, 2017.

[1.49] X. Yu, S. Jia, H. Hu, M. Galili, T. Morioka, P. U. Jepsen, and L. K. Oxenlowe, *"160 Gbit/s photonics wireless transmission in the 300–500 GHz band,"* APL Photonics, **1**, pp. 081301-1 - 081301-6, 2016.

[1.50] H. Togo, N. Shimizu, and T. Nagatsuma, *"Tip-on-fiber electro-optic probe for near field measurement,"* NTT Technical Review, **4**, pp. 12-20, 2006.

[1.51] R. C. Johnson, H. A. Ecker, and J. S. Hollis, *"Determination of far-field antenna patterns from near-field measurements,"* Proc. IEEE., **61**, pp. 1668-1694, 1973.

[1.52] A. Hirata, R. Yamaguchi, T. Kosugi, H. Takahashi, K. Murata, T. Nagatsuma, N. Kukutsu, Y. Kado, N. Iai, S. Okabe, S. Kimura, H. Ikegawa, H. Nishikawa, T. Nakayama, and T. Inada, *"10-Gbit/s wireless link using InP HEMT MMICs for generating 120-GHz-band millimeter-wave signal,"* IEEE Trans. Microw. Theory Techn., **57**, pp. 1102-1109, 2009.

[1.53] D. Kim, J. Hirokawa, K. Sakurai, M. Ando, T. Takada, T. Nagatsuma, J. Takeuchi and A. Hirata, *"Design and measurement of the plate laminated waveguide slot array antenna and its feasibility for wireless link system in the 120 GHz band,"* IEICE Trans. Commun., **E96-B**, pp. 2102-2111, 2013.

[1.54] Z. C. Hao, J. Wang, Q. Yuan, and W. Hong, *"Development of a low-cost THz metallic lens antenna,"* IEEE Antennas Wireless Propag. Lett., **16**, pp. 1751-1754, 2017.

[1.55] H. Yi, S. W. Qu, K. B. Ng, C. H. Chan, and X. Bai, *"3-D Printed Millimeter-Wave and Terahertz Lenses with Fixed and Frequency Scanned Beam,"* IEEE Trans. Antennas Propag., **64**, pp. 442-449, 2016.

[1.56] K. Konstantinidis, A. P. Feresidis, C. C. Constantinou, E. Hoare, M. Gashinova, M. J. Lancaster, and P. Gardner, *"Low-THz dielectric lens antenna with integrated waveguide feed,"* IEEE Trans. THz Sci. Technol., **7**, pp. 572-581, 2017.

[1.57] A. D. Squires, E. Constable, and R. A. Lewis, *"3D printed terahertz diffraction gratings and lenses,"* J. Infrared Millim. Terahertz Waves, **36**, pp. 72-80, 2015.

[1.58] Y. H. Lo and R. Leohardt, *"Aspheric lenses for terahertz imaging,"* Opt. Express, **16**, pp. 15991-15998, 2008.

[1.59] N. V. Chernomyrdin, M. E. Frolov, S. P. Lebedev, I. V. Reshetov, I. E. Spektor, V. L. Tolstoguzov, V. E. Karasik, A. M. Khorokhorov, K. I. Koshelev, A. O. Schadko, S. O. Yurchenko, and K. I. Zaytsev, *"Wide-aperture aspherical lens for high-resolution terahertz imaging,"* Rev. Sci. Instrum., **88**, p. 014703, 2017.

[1.60] N. Klein, P. Lahl, U. Poppe, F. Kadlec, and P. Kuzel, *"A metal-dielectric antenna for terahertz near-field imaging,"* J. Appl. Phys., **98**, p. 014910, 2005.

[1.61] H. Gao, Q. Cao, M. Zhu, D. Teng, and S. Shen, *"Nanofocusing of terahertz wave in a tapered hyperbolic metal waveguide,"* Opt. Express, **22**, pp. 32071-32081, 2014.

[1.62] H. Zhan, R. Mendis, and D. M. Mittleman, *"Superfocusing terahertz waves below $\lambda/250$ using plasmonic parallel-plate waveguides,"* Opt. Express, **18**, pp. 9643-9650, 2010.

[1.63] C. R. Williams, S. R. Andrews, S. A. Maier, A. I. F.-Dominguez, L. M.-Moreno, and F. J. G.-Vidal, *"Highly confined guiding of terahertz surface plasmon polaritons on structured metal surface,"* Nat. Photonics., **2**, pp. 175-179, 2008.

[1.64] A. Heifetz, S. C. Kong, A. V. Sahakian, A. Taflove, and V. Backman, *"Photonic nanojets,"* J. Comput. Theor. Nanosci., **6**, pp. 1979-1992, 2009.

[1.65] Z. Chen, A. Taflove, and V. Backman, *"Photonic nanojet enhancement of backscattering of light by nanoparticles: A potential novel visible light ultramicroscopy technique,"* Opt. Express, **12**, pp. 1214-1220, 2004.

[1.66] P. Ferrand, J. Wenger, A. Devilez, M. Pianta, B. Stout, N. Bonod, E. Popov, and H. Rigneault, *"Direct imaging of photonic nanojets,"* Opt. Express, **16**, pp. 6930-6940, 2008.

[1.67] L. Zhao and C. K. Ong, *"Direct observation of photonic jets and corresponding backscattering enhancement at microwave frequencies,"* J. Appl. Phys., **105**, p. 123512, 2009.

[1.68] A. Heifetz, K. Huang, A. V. Sahakian, X. Li, A. Taflove, and V. Backman, *"Experimental coniňĄrmation of backscattering enhancement induced by a photonic jet,"* Appl. Phys. Lett., **89**, p. 221118, 2006.

[1.69] V. P. Pena, M. Beruete, I. V. Minin, and O. V. Minin, *"Terajets produced by dielectric cuboids,"* Appl. Phys. Lett., **105**, p. 084102, 2014.

[1.70] I. V. Minin and O. V. Minin, *"Diffractive optics and nanophotonics: resolution below the diffraction limit,"* Springer, 2016.

[1.71] N. Llombart, G. Chattopadhyay, A. Skalare, and I. Mehdi, *"Novel terahertz antenna based on a silicon lens fed by a leaky wave enhanced waveguide,"* IEEE Trans. Antennas Propag., **59**, pp. 2160-2168, 2011.

[1.72] N. Llombart, C. Lee, M. A. DelPino, G. Chattopadhyay, C. Jung-Kubiak, L. Jofre, and I. Mehdi, *"Silicon micromachined lens antenna for THz integrated heterodyne arrays,"* IEEE Trans. THz Sci. Technol., **3**, pp. 515-523, 2013.

[1.73] M. A. DelPino, N. Llombart, G. Chattopadhyay, C. Lee, C. J. Kubiak, L. Jofre, and I. Mehdi, *"Design guidelines for a terahertz silicon micro lens antenna,"* IEEE Antennas Wireless Propag. Lett., **12**, pp. 84-87, 2013.

[1.74] Y. S. Chung, C. Cheon, J. H. Son, and S. Y. Hahn, *"FDTD analysis of propagation characteristics of Tera-hertz electromagnetic pulses,"* IEEE Trans. Magn., **36**, pp. 951-955, 2000.

[1.75] A. J. Seeds, M. J. Fice, K. Balakier, M. Natrella, O. Mitrofanov, M. Lamponi, M. Chtioui, F. V. Dijk, M. Pepper, G. Aeppli, A. G. Davies, P. Dean, E. Linfield, and C. C. Renaud, *"Coherent terahertz photonics,"* Opt. Express, **21**, pp. 22988-23000, 2013.

[1.76] C. C. Renaud, M. Natrella, C. Graham, J. Seddon, F. V. Dijk, and A. J. Seeds, *"Antenna integrated THz uni-traveling carrier photodiodes,"* IEEE J. Sel. Topics Quantum Electron., **24**, p. 8500111, 2018.

[1.77] M. T. Reiten, S. A. Harmon, and R. A. Cheville, *"Terahertz beam propagation measured through three-dimensional amplitude profile determination,"* J. Opt. Soc. Am. B, **20**, pp. 2215-2225, 2003.

[1.78] K. Pokovic, *"Advanced electromagnetic probes for near-field evaluations,"* Dissertation of Swiss Federal Institute of Tech., Zurich, Switzerland, 1999.

[1.79] H. I. Bassen and G. S. Smith, *"Electric field probes—a review,"* IEEE Trans. Antennas and Propag., **31**, pp. 710-718, 1983.

[1.80] D. T. Paris, W. M. Leach, Jr., and E. B. Joy, *"Basic theory of probe-compensated near-field measurements,"* IEEE Trans. Antennas Propag., **AP-26**, pp. 373-379, 1978.

[1.81] J. D. Chisum and Z. Popovic, *"Performance limitations and measurement analysis of a near-field microwave microscope for nondestructive and subsurface detection,"* IEEE Trans. Microw. Theory Techn., **60**, pp. 2605-2615, 2012.

[1.82] E. Kume and S. Sakai, *"Millimeter-wave radiation from a Teflon dielectric probe and its imaging application,"* Meas. Sci. Technol., **19**, p. 115501, 2008.

[1.83] W. Liang, G. Hygate, J. F. Nye, D. G. Gentle, and R. J. Cook, *"A probe for making near-field measurements with minimal disturbance: the optically modulated scatterer,"* IEEE Trans. Antennas Propag., **45**, pp. 772-780, 1997.

[1.84] R. R. Lao, W. L. Liang, W. T. Shay, R. P. Thompson, R. A. Dudley, O. Merckel, N. R. Tharaud, J. C. Bolomey, and J. H. Tarng, *"High-sensitivity optically modulated scatterer for electromagnetic-field measurement,"* IEEE Trans. Instrum. Meas., **56**, pp. 486-490, 2007.

[1.85] J. H. Choi, J. I. Moon, and S. O. Park, *"Measurement of the modulated scattering microwave fields using dual-phase lock-in amplifier,"* IEEE Antennas Wireless Propag. Lett., **3**, pp. 340-343, 2004.

[1.86] J. C. Bolomey, H. M. Tehran, and J. J. Laurin, *"Optimization of optically and electrically modulated scattering probes for field measurements,"* IEEE Trans. Instrum. Meas., **63**, pp. 154-165, 2014.

[1.87] H. M. Tehran, J. J. Laurin, and R. Kashyap, *"Optically modulated probe for precision near-field measurements,"* IEEE Trans. Instrum. Meas., **59**, pp. 2755-2762, 2010.

[1.88] M. Tokuda and N. Kuwabara, *"Recent progress in fiber optic antennas for EMC measurement,"* IEICE Trans. Commun., **E75-B**, pp. 107-114, 1992.

[1.89] S. Ishihara and T. Onishi, *"Measurement of electric field distributions in the MHz band around an electromagnetic source employing the electro-optic conversion,"* IEICE Trans. Commun., **J97-B**, pp. 286-293, 2014.

[1.90] D. Baudry, A. Louis, and B. Mazari, *"Characterization of the open-ended coaxial probe used for near-field measurements in EMC applications,"* Progress In Electromagnetics Research, PIER, **60**, pp. 311-333, 2006.

[1.91] K. Tajima, N. Kuwabara, and R. Kobayashi, *"Evaluation of an electric field sensor with very small elements using a Mach-Zehnder interferometer,"* Electron. Commun. Jpn., **80**, pp. 69-78, 1997.

[1.92] S. Kuehn, S. Pfeifer, E. Grobbelaar, B. Kochali, P. Sepan, and N. Kuster, *"A validated reactive near-field phasor measurement system for antenna pattern measurements,"* 10th European Conference on Antennas and Propagation (EuCAP), 2016.

[1.93] A. Kramer, P. Muller, U. Lott, and N. Kuster, *"Electro-optic fiber sensor for amplitude and phase detection of radio frequency electromagnetic fields,"* Opt. Lett., **31**, pp. 2402-2404, 2006.

[1.94] *"https://www.speag.com/products/icey/."*

[1.95] D. J. Lee and J. F. Whitaker, *"An optical-fiber-scale electro-optic probe for minimally invasive high-frequency field sensing,"* Opt. Express, **16**, pp. 21587-21597, 2008.

[1.96] P. Y. Han and M. Tani, *"Use of the organic crystal DAST for terahertz beam applications,"* Opt. Lett., **25**, pp. 675-677, 2000.

[1.97] F. Pockels, *"Lehrbuch der kristalloptik,"* Leipzig: Teubner, 1906.

[1.98] F. Cecelja, W. Balachandran, M. Berwick, M. Soghomonian, and S. Cvetkovic, *"Optical sensors for the validation of electromagnetic field distributions in biological phantoms,"* Proc. Euro. Symp. Opticas for Environmental and Public Safety Fiber Optic and Laser Sensors XIII, SPIE, **2510**, pp. 244-254, 1995.

[1.99] K. J. Weingarten, M. J.W. Rodwell, and D. M. Bloom, *"Picosecond optical sampling of GaAs integrated circuits,"* IEEE J. Quantum Electron., **QE-24**, pp. 198-220, 1988.

[1.100] J. M. Wiesenfeld, R. S. Tucker, A. Antreasyan, C. A. Burrus, A. J. Taylor, V. D. Mattera, and P. A. Garbinski, *"Electro-optic sampling measurements of high-speed InP integrated circuits,"* Appl. Phys. Lett., **50**, p. 1310, 1987.

[1.101] D. R. Hjelme, M. J. Yadlowsky, A. R. Mickelson, *"Two-dimensional mapping of the microwave potential on MMICs using electrooptic sampling,"* IEEE Trans. Microw. Theory Techn., **41**, pp. 1149-1158, 1993.

[1.102] G. David, D. Jager, R. Tempel, and I. Wolff, *"Analysis of microwave propagation effects using two-dimensional electrooptic field mapping techniques,"* Opt. Quant. Electron., **28**, pp. 919-932, 1996.

[1.103] J. F. Whitaker, K. Yang, R. Reano, and L. P. B. Katehi, *"Electro-optic probing for microwave diagnostics,"* IEICE Trans. Electron., **E86-C**, pp. 1328-1337, 2003.

[1.104] K. Yang, G. David, J.-G. Yook, I. Papapolymerou, L. P. B. Katehi, and J. F. Whitaker, *"Electrooptic mapping and finite-element modeling of the near-field pattern of a microstrip patch antenna,"* IEEE Trans. Microw. Theory Techn., **48**, pp. 288-294, 2000.

[1.105] M. Shinagawa and T. Nagatsuma, *"An automated electro-optic probing system for ultrahigh-speed IC' s,"* IEEE Trans. Instrum. Meas., **43**, pp. 843-847, 1994.

[1.106] T. Pfeifer, T. LoïňĎer, H.G. Roskos, H. Kurz, M. Singer, and E.M. Biebl, *"Electro-optic near-field mapping of planar resonators,"* IEEE Trans. Antennas Propag., **46**, pp. 284-291, 1998.

[1.107] W. K. Kuo, C. H. Pai, S. L. Huang, H. Y. Chou, and H. S. Huang, *"Electro-optic mapping systems of electric-field using CW laser diodes,"* Opt. Laser Technol., **38**, pp. 111-116, 2006.

[1.108] F. Cecelja and W. Balachandran, *"Electrooptic sensor for near-field measurement,"* IEEE Trans. Instrum. Meas., **48**, pp. 650-653, 1999.

[1.109] F. Cecelja and W. Balachandran, *"Optimized CdTe sensors for measurement of electric and magnetic fields in the near-field region,"* IEEE Trans. Instrum. Meas., **49**, pp. 483-487, 2000.

[1.110] M. Shinagawa, T. Nagatsuma, K. Ohno, and Y. Jin, *"A real-time electro-optic handy probe using a continuous-wave laser,"* IEEE Trans. Instrum. Meas., **50**, pp. 1076-1080, 2001.

[1.111] H. Togo, A. Sasaki, A. Hirata, and T. Nagatsuma, *"Characterization of millimeter-wave antenna using photonic measurement techniques,"* Int. J. RF Microwave Comput. Aided Eng., **14**, pp. 290-297, 2004.

[1.112] T. Nagatsuma, N. Sahri, M. Yaita, T. Ishibashi, N. Shimizu, and K. Sato, *"All optoelectronic generation and detection of millimeter-wave signals,"* Tech. Dig. Int. Top. Meeting Microwave Photonics, pp. 5-8, 1998.

[1.113] K. Yang, L. P. B. Katehi, and J. Whitaker, *"MicrowavE-field imaging with a fiber-based electro-optic probe,"* Tech. Dig. Conf. Lasers Electro-Optics, pp. 388-389, 2000.

[1.114] S. Wakana, T. Ohara, M. Abe, E. Yamazaki, M. Kishi, and M. Tsuchiya, *"Novel electromagnetic field probe using electro/magneto-optical crystals mounted on optical fiber facets for microwave circuit diagnosis,"* 2000 IEEE MTT-S Int. Microwave Symp. Dig., **3**, pp. 1615-1618, 2000.

[1.115] T. Ohara, R. Namiki, K. Igarashi, S. Wakana, and M. Tsuchiya, *"Proposal of electro-optic sensor head attached to optical fiber edge,"* Technical report of IEICE, **MW99-38**, pp. 55-60, 1999.

[1.116] K. Yang, L. P. B. Katehi, and J. Whitaker, *"Electric-field mapping system using an optical-fiber-based electro-optic probe,"* IEEE Microwave Wireless Comp. Lett., **11**, pp. 164-166, 2001.

[1.117] S. Wakana, T. Ohara, M. Abe, E. Yamazaki, M. Kishi, and M. Tsuchiya, *"Fiber-edge electrooptic/magnetooptic probe for spectral-domain analysis of electromagnetic field,"* IEEE Trans. Microw. Theory Techn., **48**, pp. 2611-2616, 2000.

[1.118] T. Ohara, M. Abe, S. Wakana, M. Kishi, M. Tsuchiya, and S. Kawasaki, *"Two-dimensional field mapping of microstrip lines with a band pass filter or a photonic bandgap structure by fiber-optic EO spectrum analysis system,"* Proc. IEEE Topical Meeting Microw. Photonics, pp. 210-213, 2000.

[1.119] T. Nagatsuma, M. Shinagawa, N. Sabri, A. Sasaki, Y. Royter, and A. Hirata, *"1.55-μm photonic systems for microwave and millimeter-wave measurement,"* IEEE Trans. Microw. Theory Technol., **49**, pp. 1831-1839, 2001.

[1.120] H. Togo, N. Kukutsu, N. Shimizu, and T. Nagatsuma, *"Sensitivity-stabilized fiber-mounted electrooptic probe for electric field mapping,"* J. Lightw. Technol., **26**, pp. 2700-2705, 2008.

[1.121] M. Bernier, L. Duvillaret, G. Gaborit, A. Pauper, and J. -L. Lasserre, *"Fully automated E-field measurement system using pigtailed electro-optic sensors for temperature-dependent-free measurements of microwave signals in outdoors conditions,"* IEEE Sensors J., **9**, pp. 61-68, 2009.

[1.122] A. Garzarella, S. B. Qadri, D. H. Wu, and R. J. Hinton, *"Responsivity optimization and stabilization in electro-optic field sensors,"* Appl. Opt., **46**, pp. 6636-6640, 2007.

[1.123] H. Togo, D. Moreno-Dominguez, and N. Kukutsu, *"Frequency response and applications of optical electric-field sensor at frequencies from 20 kHz to 180 GHz,"* IEICE Trans. Electron., **E96-C**, pp. 227-234, 2013.

[1.124] K. Sasagawa and M. Tsuchiya, *"An electrooptic sensor with sub-millivolt sensitivity using a nonlinear optical disk resonator,"* Microw. Photon., **12**, pp. 355-358, 2005.

[1.125] D. J. Lee, M. H. Crites, and J. F. Whitaker, *"A simplified Fabry Perot electrooptic-modulation sensor,"* IEEE Phot. Tech. Lett., **20**, pp. 866-868, 2008.

[1.126] D. J. Lee, N. W. Kang, J. H. Choi, J. Kim, and J. F. Whitaker, *"Recent advances in the design of electro-optic sensors for minimally destructive microwave field probing,"* Sensors, **11**, pp. 806-824, 2011.

[1.127] D. J. Lee and J. F. Whitaker, *"Optimization of sideband modulation in optical-heterodyne-downmixed electro-optic sensing,"* Appl. Opt., **48**, pp. 1583-1590, 2009.

[1.128] D. J. Lee and J. F. Whitaker, *"Bandwidth enhancement of electro-optic sensing using high-even-order harmonic sidebands,"* Opt. Express, **17**, pp. 14909-14917, 2009.

[1.129] D. J. Lee, M. H. Crites, and J. F. Whitaker, *"Electro-optic probing of microwave fields using a wavelength-tunable modulation depth,"* Meas. Sci. Technol., **19**, p. 115301, 2008.

[1.130] S. Hisatake and T. Nagatsuma, *"Nonpolarimetric technique for homodyne-type electrooptic field detection,"* Appl. Phys. Express, **5**, p. 012701, 2012.

[1.131] S. Hisatake, G. Kitahara, K. Ajito, and Y. Fukada, *"Phase-sensitive terahertz self-heterodyne system based on photodiode and low-temperature-grown GaAs photoconductor at 1.55 μm,"* IEEE Sensor J., **13**, pp. 31-36, 2013.

[1.132] S. Hisatake and T. Nagatsuma, *"Continuous-wave terahertz field imaging based on photonics-based self-heterodyne electro-optic detection,"* Opt. Lett., **38**, pp. 2307-2310, 2013.

[1.133] S. Hisatake, H. H. Nguyen Pham, and T. Nagatsuma, *"Visualization of the spatial-temporal evolution of continuous electromagnetic waves in the terahertz range based on photonics technology,"* Optica, **1**, pp. 365-371, 2014.

[1.134] H. H. Nguyen Pham, *"Visualization of terahertz waves based on electro-optic measurement,"* Master thesis of Graduate School of Engineering Science, Osaka University, Japan, 2015.

[1.135] H. Ito, S. Kodama, Y. Muramoto, T. Furuta, T. Nagatsuma, and T. Ishibashi, *"High-speed and high-output InP-InGaAs unitraveling-carrier photodiodes,"* IEEE J. Sel. Topics Quantum Electron., **10**, pp. 709-727, 2004.

[1.136] H. Ito, S. Kodama, Y. Muramoto, T. Furuta, T. Nagatsuma, and T. Ishibashi, *"Photonic generation of continuous THz wave using uni-traveling-carrier photodiode,"* J. Lightwave Technol., **23**, pp. 4016-4021, 2005.

Chapter 2

Principles of electro-optic detection techniques

In this chapter, principles of fiber-mounted EO detection systems using continuous-wave (CW) lasers are described. First, CW coherent detection configurations including homodyne [2.1] and self-heterodyne schemes [2.2,2.3] are explained. Then, two principles of EO detection techniques based on a polarization modulation technique [2.4,2.5] and nonpolarimetric technique [2.6] are compared. Finally, the experimental setup of nonpolarimetric self-heterodyne EO detection system [2.7], which is employed in this study, is introduced.

2.1 Continuous-wave coherent detection configurations

2.1.1 Homodyne detection

Figure 2.1.1 illustrates a schematic of homodyne CW-THz wave detection configuration [2.1]. Two tunable laser diodes (LDs) with frequencies f_1 and f_2 ($f_1 < f_2$) are combined for generation and detection of THz waves. An optical-to-electrical (O/E) converter is used to generate THz waves or the RF signal at the frequency of the beat note of the two lasers $f_{THz} = f_2 - f_1$. The local oscillator (LO) path also contains the same optical frequencies f_1 and f_2. THz waves are detected based on the photomixing process using a mixer pumped by the LO signal. The detected

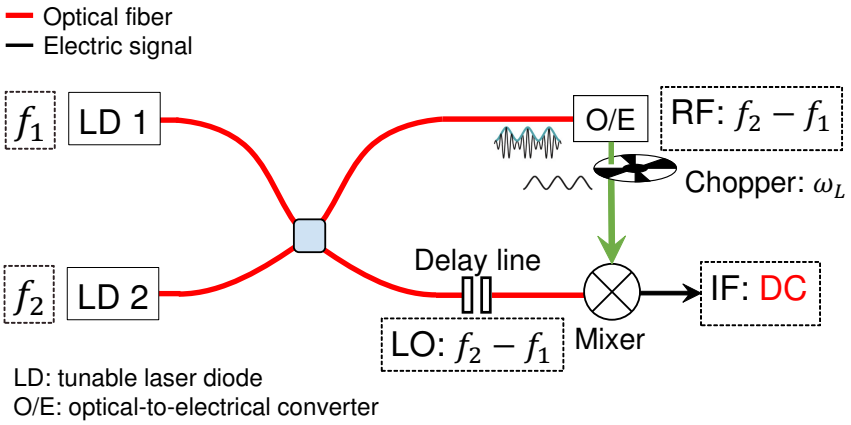

Figure 2.1.1: Schematic of homodyne detection.

intermediate frequency (IF) signal, $i(t)$, is expressed as:

$$i(t) \propto A(\omega)\cos[\phi(\omega) + \omega\tau]\cos(\omega_L t) \tag{2.1.1}$$

where $\omega = 2\pi(f_2 - f_1)$, $A(\omega)$, and $\phi(\omega)$ are the THz angular frequency, amplitude, and phase distributions of the THz wave, respectively. τ and ω_L are the path delay difference between the RF and LO paths, and the lock-in angular frequency for the lock-in detection. Generally, an intensity modulation by a mechanical chopper or electro-optic modulator (EOM) in the optical or THz path, or DC bias modulation of the THz emitter is installed to the system to realize the lock-in detection for the homodyne detection configuration. The drawbacks of the additional installations are that the system becomes bulky and there is an increase in excess noise in the detection due to parasitic signals appearing in the DC modulation process [2.8].

According to equation (2.1.1), after the lock-in detection, the obtained signal $A(\omega)\cos(\phi(\omega) + \omega\tau)$ exhibits mutual coupling of the amplitude $A(\omega)$ and phase $\phi(\omega)$ information. To separate $A(\omega)$ and $\phi(\omega)$, the IF signal should be measured at two different values of $\omega\tau$, such as $\omega\tau = h\pi$ and $\omega\tau = (2h+1)\frac{\pi}{2}$, where h is an integer. A variable optical delay line (Fig. 2.1.1) was generally used to change the path delay difference between the RF and LO arms. This process increases the measurement time and measurement errors caused by the distortions of the THz

beam and variation in THz path due to the variable delay line stage [2.8].

When τ is nonzero, the frequency fluctuations of the THz wave are converted to phase fluctuations of the detected signal, $\Delta\phi_n = 2\pi\,\Delta f\,\tau$, where Δf is the deviation of the THz frequency. Therefore, in order to increase the accuracy of the phase measurement, the frequency of the LDs should be stabilized in the homodyne detection schematic [2.2].

Several groups tried to avoid the drawback of the homodyne detection configuration, such as by replacing the mechanical optical delay line with an electrical modulation of the THz phase [2.8] to improve the scanning speed or by a fast phase modulator using a fiber stretcher [2.9].

2.1.2 Self-heterodyne detection

Figure 2.1.2 shows the schematic of self-heterodyne detection [2.2, 2.3]. Two free-running LDs, LD1 and LD2, are used to generate the CW single-mode optical signal at frequencies f_1 and f_2 ($f_1 < f_2$), respectively. Fiber couplers (50/50) are used to divide and combine the optical signal f_1 and f_2 for the RF and LO paths. The difference between the RF and LO paths is that one of the optical frequencies is slightly shifted by f_s (several kHz to MHz) by a frequency shifter (FS). Optical isolators are used to prevent the modulated optical frequency from leaking to the LO path. In Fig. 2.1.2, the frequency of LD1 is shifted from f_1 to $f_1 + f_s$. Therefore, in the RF path, there are two optical frequency components f_2 and $f_1 + f_s$. The CW-THz waves are generated by photomixing using an O/E converter. The THz frequency or RF frequency is $f_{THz} = f_2 - f_1 - f_s$. In the LO path, there are two optical frequency components f_2 and f_1. The RF signal is then mixed with the LO signal to produce the IF signal, where the frequency is equal to the frequency difference between the RF and LO signals, f_s. Both photodiodes (PDs) and photoconductors can be used as O/E converters and mixers.

The RF signal, $E_{\mathrm{RF}}(t)$, at the mixer can be expressed as:

$$E_{\mathrm{RF}}(t) \propto A(\omega)\cos[\omega t + \phi(\omega) + \phi_{\mathrm{nRF}}(t)] \tag{2.1.2}$$

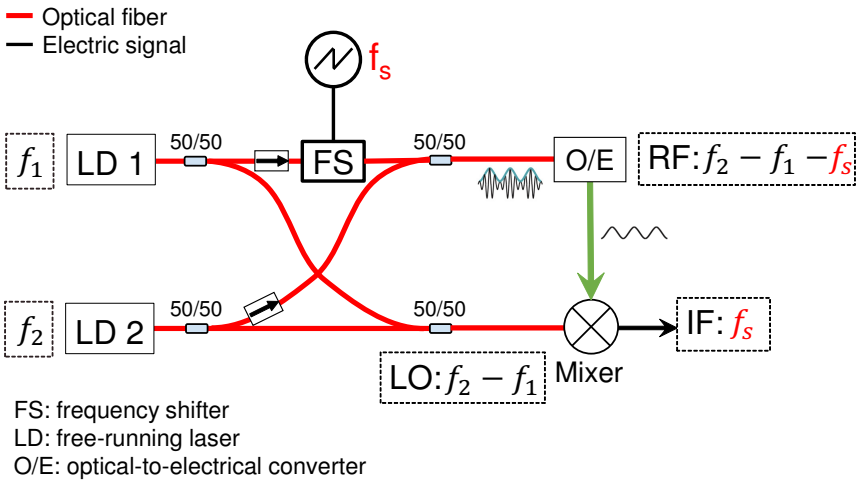

Figure 2.1.2: Schematic of self-heterodyne detection.

where $\omega = 2\pi(f_2 - f_1 - f_s)$, $A(\omega)$, and $\phi(\omega)$ are the THz angular frequency, amplitude, and phase of the THz E-field, respectively. The phase noise of the RF signal $\phi_{\mathrm{nRF}}(t) = \phi_{n1}(t) + \phi_{n2}(t) + \phi_{\mathrm{exRF}}$ includes the phase noises of LD1 (ϕ_{n1}(t)) and LD2 (ϕ_{n2}(t)), and the excess phase noise induced by optical pass fluctuations in the optical fiber of RF path (ϕ_{exRF}).

The LO signal, $E_{\mathrm{LO}}(t)$, at the mixer can be expressed as:

$$E_{\mathrm{LO}}(t) \propto \cos[\omega_{\mathrm{LO}}(t+\tau) + \phi_{\mathrm{nLO}}(t+\tau)] \tag{2.1.3}$$

where $\omega_{\mathrm{LO}} = 2\pi(f_2 - f_1)$, $\phi_{\mathrm{nLO}}(t+\tau) = \phi_{n1}(t+\tau) + \phi_{n2}(t+\tau) + \phi_{\mathrm{exLO}}$ is the phase noise of the LO signal including the phase noises of LDs ($\phi_{n1}(t+\tau)$, $\phi_{n2}(t+\tau)$), and the excess phase noise induced by optical pass fluctuations in the fiber of the LO path (ϕ_{exLO}). τ is the path delay difference between the RF and LO arms.

The detected photocurrent of the IF signal, $i_{\mathrm{IF}}(t)$, obtained after the mixing process by a slow PD, is expressed as:

$$
\begin{aligned}
i_{\mathrm{IF}}(t) &\propto [E_{\mathrm{RF}}(t) + E_{\mathrm{LO}}(t)]^2 \\
&\propto \frac{1}{2} A^2(\omega) \left[1 + \cos[2(\omega t + \phi(\omega) + \phi_{\mathrm{nRF}}(t))]\right] \\
&\quad + \frac{1}{2} \left[1 + \cos[2(\omega_{\mathrm{LO}}(t+\tau) + \phi_{\mathrm{nLO}}(t+\tau))]\right] \\
&\quad + 2\, A(\omega) \cos[\omega t + \phi(\omega) + \phi_{\mathrm{nRF}}(t)] \cos[\omega_{\mathrm{LO}}(t+\tau) + \phi_{\mathrm{nLO}}(t+\tau)] \\
&\propto \mathrm{A}(\omega) \cos(\omega_{\mathrm{s}}\mathrm{t} + \omega_{\mathrm{LO}}\tau - \phi(\omega) + \phi_{\mathrm{nLO}}(\mathrm{t}+\tau) - \phi_{\mathrm{nRF}}(\mathrm{t}))
\end{aligned}
\tag{2.1.4}
$$

where $\omega_s = 2\pi(f_s) = 2\pi[(f_2 - f_1) - (f_2 - f_1 - f_s)] = \omega_{\mathrm{LO}} - \omega$.

The phase noise of the IF signal is:

$$
\begin{aligned}
\phi_{\mathrm{nIF}}(t) &= \phi_{\mathrm{nLO}}(\mathrm{t}+\tau) - \phi_{\mathrm{nRF}}(\mathrm{t}) \\
&= \phi_{\mathrm{n1}}(\mathrm{t}+\tau) + \phi_{\mathrm{n2}}(\mathrm{t}+\tau) + \phi_{\mathrm{exLO}} - \phi_{\mathrm{n1}}(\mathrm{t}) - \phi_{\mathrm{n2}}(\mathrm{t}) - \phi_{\mathrm{exRF}} \\
&= \Delta\phi_{\mathrm{n1}} + \Delta\phi_{\mathrm{n2}} + \Delta\phi_{\mathrm{ex}}
\end{aligned}
\tag{2.1.5}
$$

where $\Delta\phi_{n1} = \phi_{n1}(t+\tau) - \phi_{n1}(t)$, $\Delta\phi_{n2} = \phi_{n2}(t+\tau) - \phi_{n2}(t)$, and $\Delta\phi_{\mathrm{ex}} = \phi_{\mathrm{exLO}} - \phi_{\mathrm{exRF}}$. In self-heterodyne detection, the same two LDs are used in both the RF and LO, therefore, the phase noises of the LDs are a common mode and the precise phase measurement of THz E-field can be realized by setting a small τ, which is controlled by adjusting the lengths of the RF and LO paths equally. Excess phase noise $\Delta\phi_{\mathrm{ex}}$ can be reduced by temperature control. From equation (2.1.4), we can obtain the amplitude and phase of THz E-field, $A(\omega)$ and $\phi(\omega)$, simultaneously by using the dual-phase lock-in detection from the measured in-phase $I(\omega)$ and quadrature-phase $Q(\omega)$, as in the following equation:

$$
\begin{aligned}
I(\omega) &= \mathrm{A}(\omega) \cos[\phi(\omega)] \\
Q(\omega) &= \mathrm{A}(\omega) \sin[\phi(\omega)] \\
&\text{or} \\
\mathrm{A}(\omega) &= \sqrt{I^2(\omega) + Q^2(\omega)} \\
\phi(\omega) &= \mathrm{Arctan}\frac{Q(\omega)}{I(\omega)}
\end{aligned}
\tag{2.1.6}
$$

The advantages of the self-heterodyne technique are that the amplitude and phase of the THz E-field can be measured in a single-shot measurement, without any delay-line modulation. Therefore, the data acquisition times by the self-heterodyne technique are faster than by the homodyne detection technique, in which two distinct measurements at different τ are required to obtain the amplitude and phase information separately. Moreover, the frequency fluctuation of LDs and common phase noise induced by the lasers can be canceled out, owing to the coherent detection of the self-heterodyne technique. Therefore, free-running CW lasers can be used in the system, instead of a stable frequency comb [2.10]. This would otherwise complicate the system and limit the frequency tunability, owing to the limitation of the bandwidth and operating frequency of EO modulators and electronic components, such as function generators and amplifiers, required to generate the frequency comb. We remarked that in the self-heterodyne technique, the THz frequency can be changed by tuning the frequency of LDs without changing the shifted frequency f_s.

2.2 EO detection techniques

2.2.1 Polarimetric technique

Figure 2.2.1 shows the principle of the EO detection technique based on a polarization modulation technique [2.4, 2.5]. This technique arises from a well-known principle: optical modulation of probe beam owing to the EO or Pockels effect [2.11] inside the EO crystal. The EO effect consists of variations in the birefringence of typical crystals induced by an E-field applied to the crystals. Generally, an optical probe beam, which has a circular polarization state, is inputted to the EO crystal through an optical circulator (port① →port② in Fig. 2.2.1). The polarization state of the optical probe beam passing through the EO crystal is modulated according to the strength of the THz field to be measured. The polarization-modulated optical probe beam from circularity to ellipticity is reflected by a high-reflectivity (HR) mirror and passes through port③ of the circulator. Then, the change in the polarization state of the optical beam can be converted to an inten-

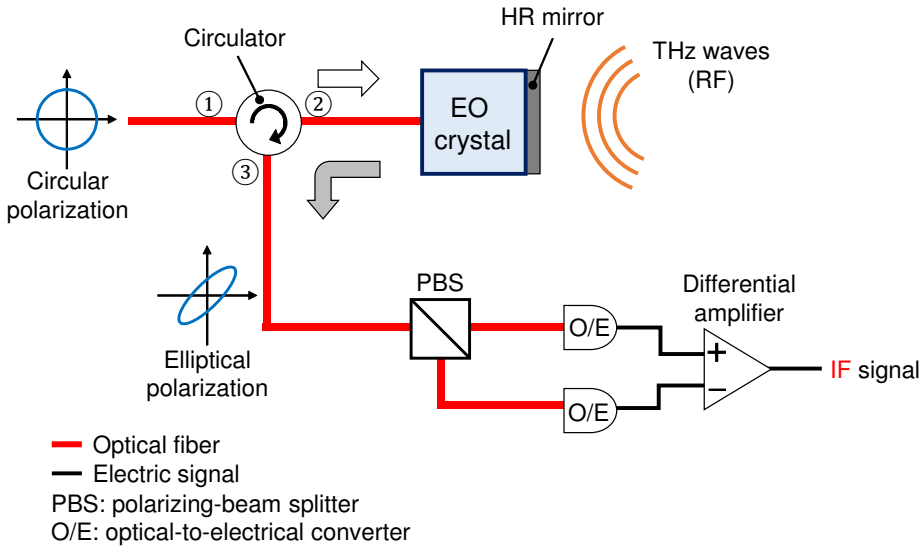

Figure 2.2.1: Schematic of polarimetric detection.

sity change by using a polarizing-beam splitter and the electronics signal by a PD, an O/E converter. A differential amplifier is used to improve the detected signal and reduce the common noise to obtain the IF signal.

The drawback of polarization modulation technique is that the polarization state of the optical probe beam inside the optical fiber and within the EO crystal can fluctuate owing to the deviations in the birefringence, which are caused by the ambient temperature fluctuation and the mechanical deviation of the optical fiber. This may lead to the fluctuation in the detected signal. This intrinsic problem of the sensitivity fluctuation in this EO detection technique limits the stability and repeatability of the measurement [2.5].

2.2.2 Nonpolarimetric technique

Figure 2.2.2 illustrates the principle of the EO nonpolarimetric detection technique applying in the self-heterodyne configuration. There are two main processes in this technique: (1) first, the THz E-field to be detected (0.1–10 THz) is up-converted to an optical frequency, e.g., 193 THz, by EO phase modulation inside the fiber-mounted EO crystal; (2) next, the generated sideband, which inherits the information of THz E-field, is down-converted to the IF signal (f_s) by optical

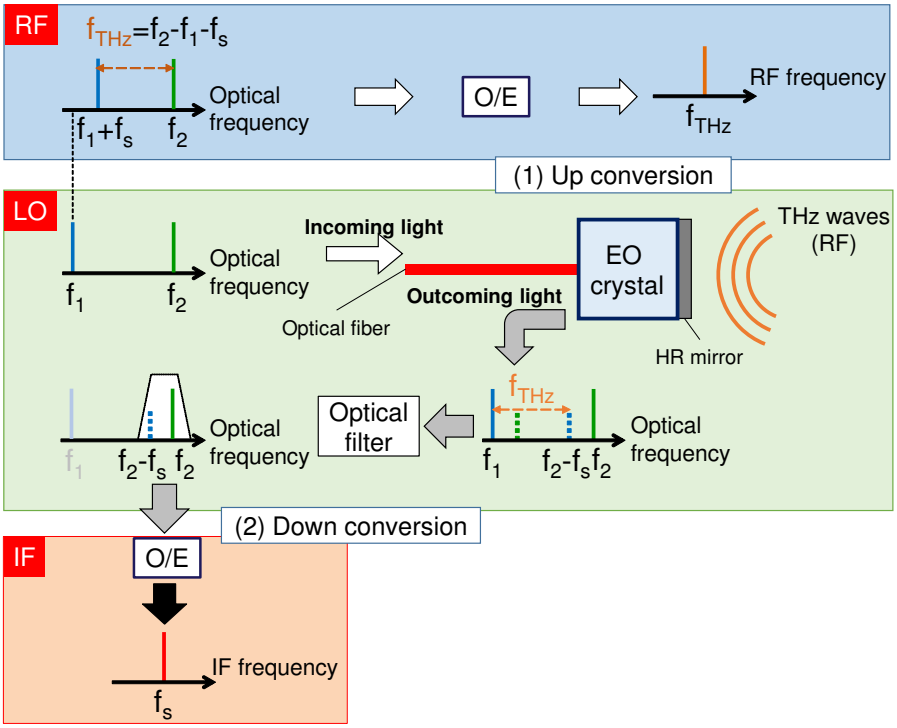

Figure 2.2.2: Nonpolarimetric detection schematic.

coherent detection. A detailed explanation of this technique is as follows.

THz waves are generated based on photonic generation at the frequency $f_{\mathrm{THz}} = f_2 - f_1 - f_s$ by converting the beat signal with the O/E converter. In the LO probe beam (incoming light), two LO carriers, which have frequencies f_1 and f_2, are fed to the EO crystal through a mounted polarization-maintaining fiber (PMF). The polarization sate of the optical probe beam is linear polarization. Note that the slow axis of the PMF is fixed parallel to the specific axis of the EO crystal [2.12]. Generally, the axis, which has a large EO coefficient, is chosen to obtain the best sensitivity. The THz E-field to be detected is up-converted to the optical frequency through the phase modulation of the probe beam inside the EO crystal based on the EO effect, i.e., the refractive index of an EO medium is varied with the applied E-field by the Pockels or Kerr effects. The reflected optical probe beam (outgoing light) from a HR mirror, which is mounted on the head of the EO crystal, consists of two LO optical carriers and the generated sidebands induced by the THz E-field. The upper sideband of carrier f_1 and the lower sideband of carrier f_2 are depicted

by the blue and green dashed lines, respectively, in Fig. 2.2.2. The frequency of the upper sideband of carrier f_1 is $f_1 + f_{\mathrm{THz}} = f_2 - f_s$ and the frequency of the lower sideband of carrier f_2 is $f_2 - f_{\mathrm{THz}} = f_1 + f_s$, because the THz frequency is $f_{\mathrm{THz}} = f_2 - f_1 - f_s$. Therefore, we obtain two carrier–sideband pairs for self-heterodyne detection: (1) f_1 carrier and the lower sideband of f_2 carrier $(f_1 + f_s)$, and (2) f_2 carrier and the upper sideband of f_1 carrier $(f_2 - f_s)$. The second pair, f_2 and the sideband $f_2 - f_s$, is extracted by an optical filter in Fig 2.2.2. The O/E converter, a slow PD, is used to down-convert the optical sideband $f_2 - f_s$ to an electric IF signal f_s (several kHz to MHz). Then, a dual-phase lock-in amplifier (LIA) can be used for the detection of both the amplitude and phase of THz waves simultaneously. Note that if the other carrier–sideband pair is extracted by the optical filter, the amplitude and phase of the THz waves can also be obtained through the the down-converted IF signal.

In this nonpolarimetric EO detection technique, an optical filter is used rather than a polarization analyzer as in the polarimetric technique. Therefore, the system is simpler because neither an active polarization compensator nor a polarization-rotated reflector [2.13–2.15] is used for stabilizing the measurement. Moreover, many types of EO materials, which have a large EO coefficient but exhibit natural birefringence, such as uniaxial and biaxial crystals, can be employed in the nonpolarimetric detection configuration. This is in spite of the fact that it was suggested that such types of EO materials should be avoided for EO sensing applications in the polarimetric detection configuration, because of the detected sensitivity fluctuation caused by the optical polarization-state fluctuation induced by the fluctuation of the natural birefringence due to the temperature fluctuation [2.4, 2.16–2.18].

2.3 Experimental setup

Figure 2.3.1 shows the nonpolarimetric self-heterodyne EO detection system [2.7], which is employed in this work. Two free-running 1.55-μm CW LDs were used as optical sources. Two erbium-doped fiber amplifiers (EDFAs) were used to amplify the optical power of the laser sources. Then, these optical signals were mixed and

converted to THz waves by an O/E converter, i.e., a UTC-PD. The THz frequency was calculated from the optical frequencies, which were measured using an optical spectrum analyzer or a wavelength counter. The frequency of THz waves can be changed by simply tuning the optical frequency of one of LDs, because free-running LDs were employed. In order to employ the self-heterodyne detection technique, the frequency of LD1 was shifted by f_s (500 kHz) using an FS, i.e., an EO phase modulator. As for the optical beam feeding to the EO probe, the frequencies of both LDs were not shifted. The THz field (RF signal) emitted from the DUT interacted with the optical LO signal in the EO probe and generated the sidebands.

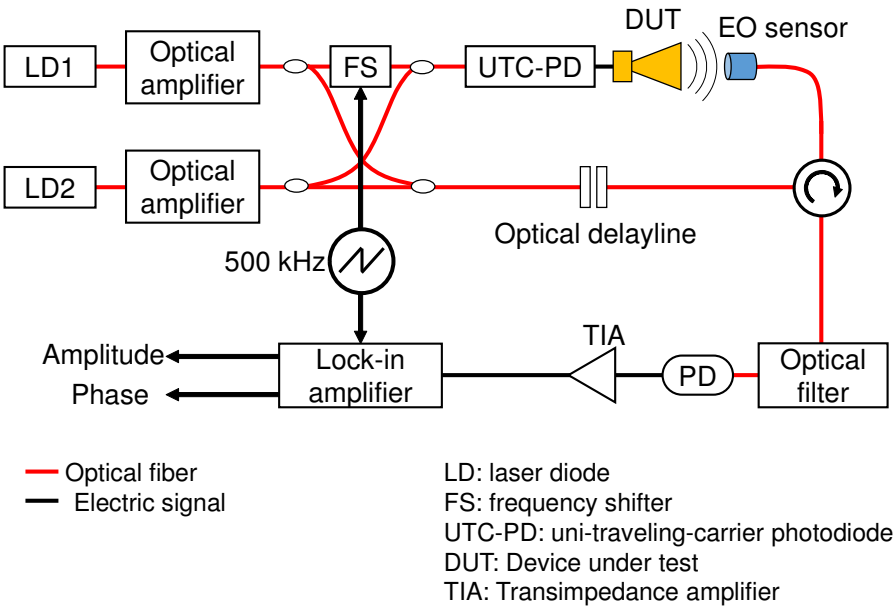

Figure 2.3.1: Experimental setup of nonpolarimetric self-heterodyne EO detection system.

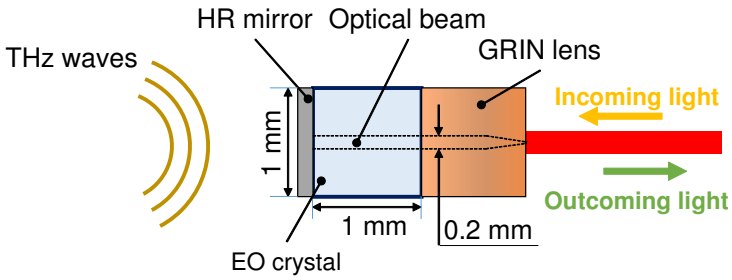

Figure 2.3.2: Structure of EO probe.

The EO probe that we used was a ZnTe EO crystal (1 mm × 1 mm × 1 mm), mounted on a PMF as shown in Fig. 2.3.2. The probe beam that passed through

the PMF was collimated into the EO crystal by a gradient index (GRIN) lens, and reflected by a HR mirror to return to the PMF. The reflected probe beam passed through an optical filter to realize the nonpolarimetric technique, and the signal was detected by the PD (Fig. 2.3.1). The spatial resolution of the EO probe was determined by the size of the optical probe beam, which was 0.2 mm as shown in Fig. 2.3.2. The amplitude and phase of the IF signal were measured by lock-in detection. An optical delay line was used to adjust the initial phase offset between the optical LO and the emitted THz waves.

In the system, the EO probe and its mounted PMF were placed on the stage for scanning, while the DUT was placed at the fixed position. In the polarimetric technique, when we move the probe in this way, the sensitivity fluctuated dramatically because the polarization state of the probe beam was required to be coherent [2.16–2.18]. In all of the experiments that will be discussed in the following chapters, the fiber-mounted EO probe was moved for the scanning, following the nonpolarimetric technique.

References

[2.1] A. Nahata and J. T. Yardley, *"Free-space electro-optic detection of continuous-wave terahertz radiation,"* Appl. Phys. Lett., **75**, pp. 2524-2526, 1999.

[2.2] S. Hisatake, G. Kitahara, K. Ajito, Y. Fukada, N. Yoshimoto, and T. Nagatsuma, *"Phase-sensitive terahertz self-heterodyne system based on photodiode and low-temperature-grown GaAs photoconductor at 1.55 μm,"* IEEE Sens. J., **13**, pp. 31-36, 2013.

[2.3] S. Hisatake and T. Nagatsuma, *"Continuous-wave terahertz field imaging based on photonics-based self-heterodyne electro-optic detection,"* Opt. Lett., **38**, pp. 2307-2310, 2013.

[2.4] F. Cecelja, B. Balachandran, M. Berwick, M. Soghomonian, and S. Cvetkovic, *"Optical sensors for the validation of electromagnetic field distributions in biological phantoms,"* Proc. SPIE Fiber Optics and Lasers Sensors XIII, **2510**, pp. 244-254, 1995.

[2.5] S. Wakana, T. Ohara, M. Abe, E. Yamazaki, M. Kishi, and M. Tsuchiya, *"Fiber-edge electrooptic/magnetooptic probe for spectral-domain analysis of electromagnetic field,"* IEEE Trans. Microw. Theory Techn., **48**, pp. 2611-2616, 2000.

[2.6] S. Hisatake and T. Nagatsuma, *"Nonpolarimetric technique for homodyne-type electrooptic field detection,"* Appl. Phys. Express, **5**, p. 012701, 2012.

[2.7] S. Hisatake, H. H. Nguyen Pham, and T. Nagatsuma, *"Visualization of the spatial-temporal evolution of continuous electromagnetic waves in the terahertz range based on photonics technology,"* Optica, **1**, pp. 365-371, 2014.

[2.8] T. Gobel, D. Schoenherr, C. Sydlo, M. Feiginov, P. Meissner, and H. L. Hartnagel, *"Continuous-wave terahertz system with electro-optical terahertz phase control,"* Electron. Lett. , **44**, pp. 863-864, 2008.

[2.9] A. Roggenbuck, K. Thirunavukkuarasu, H. Schmitz, J. Marx, A. Deninger, I. C. Mayorga, R. Gusten, J. Hemberger, and M. Gruninger, *"Using a fiber stretcher as a fast phase modulator in a continuous wave terahertz spectrometer,"* J. Opt. Soc. Am. B , **29**, pp. 614-620, 2012.

[2.10] K. Sasagawa and M. Tsuchiya, *"Modulation depth enhancement for highly sensitive electro-optic RF near-field measurement,"* Electron. Lett., **42**, pp. 1357-1358, 2006.

[2.11] F. Pockels, *"Lehrbuch der kristalloptik,"* Leipzig: Teubner, 1906.

[2.12] S. Hisatake, T. Nagatsuma, H. Uchida, *"Electro-optical probe, electromagnetic wave measurement apparatus, and electromagnetic wave measurement method,"* Japan Patent JP2017015703A, 2017 .

[2.13] M. Shinagawa, T. Nagatsuma, K. Ohno, and Y. Jin, *"A real-time electro-optic handy probe using a continuous-wave laser,"* IEEE Trans. Instrum. Meas., **50**, pp. 1076-1080, 2001.

[2.14] H. Togo, A. Sasaki, A. Hirata, and T. Nagatsuma, *"Characterization of millimeter-wave antenna using photonic measurement techniques,"* Int. J. RF and Microwave Comp. Aid. Eng., **14**, pp. 290-297, 2004.

[2.15] H. Togo, N. Kukutsu, N. Shimizu, and T. Nagatsuma, *"Sensitivity-stabilized fiber-mounted electrooptic probe for electric field mapping,"* J. Lightw. Technol., **26**, pp. 2700-2705, 2009.

[2.16] A. Garzarella, S. B. Qadri, D. H. Wu, *"Effects of crystal-induced optical incoherence in electro-optic field sensors,"* J. Electron. Mater., **39**, pp. 811-814, 2010.

[2.17] A. Garzarella, S. B. Qadri, T. J. Wieting, D. H. Wu, *"The effects of photorefraction on electro-optic field sensors,"* J. Appl. Phys., **97**, 113108, 2005.

[2.18] A. Garzarella, S. B. Qadri, T. J. Wieting, D. H. Wu, *"Spatial and temporal sensitivity variations in photorefractive electro-optic field sensors,"* Appl. Phys. Lett., **88**, 141106, 2006.

Chapter 3

Evaluation of electro-optic detection systems

In this chapter, the self-heterodyne EO detection systems [3.1, 3.2], which employ the polarimetric technique [3.3, 3.4] and nonpolarimetric technique [3.5], are experimentally evaluated in terms of the stability of measurement and the capability of near-field visualization. The THz wave emitted from an F-band (90–140 GHz) horn antenna at 125 GHz was measured and visualized by both techniques. The nonpolarimetric technique shows better stability and visualized results.

3.1 Evaluation of the stability

In the experiment to evaluate the stability of the EO detection systems, the THz frequency, which is determined by the beat frequency of the two optical frequencies of the laser diodes, was set at 125 GHz. The EO probe made from a ZnTe crystal was placed at the center and at a distance of approximately 1 mm from the surface of the F-band (90–140 GHz) horn antenna, as shown in Fig. 3.1.1. The E-field vector emitted from the horn antenna was linear and parallel to the x-axis, as depicted by the red arrow in Fig. 3.1.1.

Figures 3.1.2(a) and 3.1.2(b) show the measured amplitude and phase distributions of the THz wave at 125 GHz, without moving the EO probe by the polarimetric and nonpolarimetric techniques, respectively, employing in the self-heterodyne EO detection system. The time constant of the lock-in amplifier (LIA) was set at

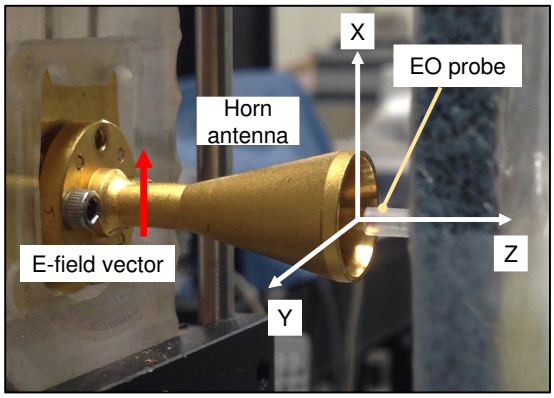

Figure 3.1.1: Position of EO probe in the experiment.

30 ms. A digital oscilloscope (Rhode & Schwarz RTO 1004) was used to measure the down-converted IF signal. The initial phase offset was set at zero by adjusting the optical delay line. The orange and blue lines represent the experimental results obtained by the polarimetric and nonpolarimetric techniques, respectively.

The value of the detected amplitude was normalized to the initial data. The amplitude of the THz wave obtained by polarimetric technique fluctuates dramatically about 48%. However, that obtained by the nonpolarimetric technique fluctuates about 22%, more than two times smaller. The percentage of the fluctuation, δ_{fluc}, is calculated by following equation:

$$\delta_{fluc} = \frac{A_{max} - A_{min}}{\mu_A}, \tag{3.1.1}$$

where A_{max}, A_{min}, and μ_A are the maximum, minimum, and average values, respectively, of the measured amplitude over 10 min.

The standard deviation of the 10-min measurement of the normalized amplitude value by the polarimetric technique ($\sigma_{pol} = 0.082$) is larger than that by nonpolarimetric technique ($\sigma_{non} = 0.032$) by approximately 2.6 times. The signal-to-noise ratio (SNR) of the amplitude measurement obtained by the nonpolarimetric technique was $SNR_{non} = 31$ dB, whereas that of the polarimetric technique was $SNR_{pol} = 24$ dB. Considering that the noise in the detected signal is white noise, the SNR can be calculated as $SNR = 20\log_{10}\frac{\mu}{\sigma}$ [3.6], where μ and σ are the average and standard deviation, respectively, of the detected signal over 60 s without moving the probe. The fluctuation of the polarization states of the probe

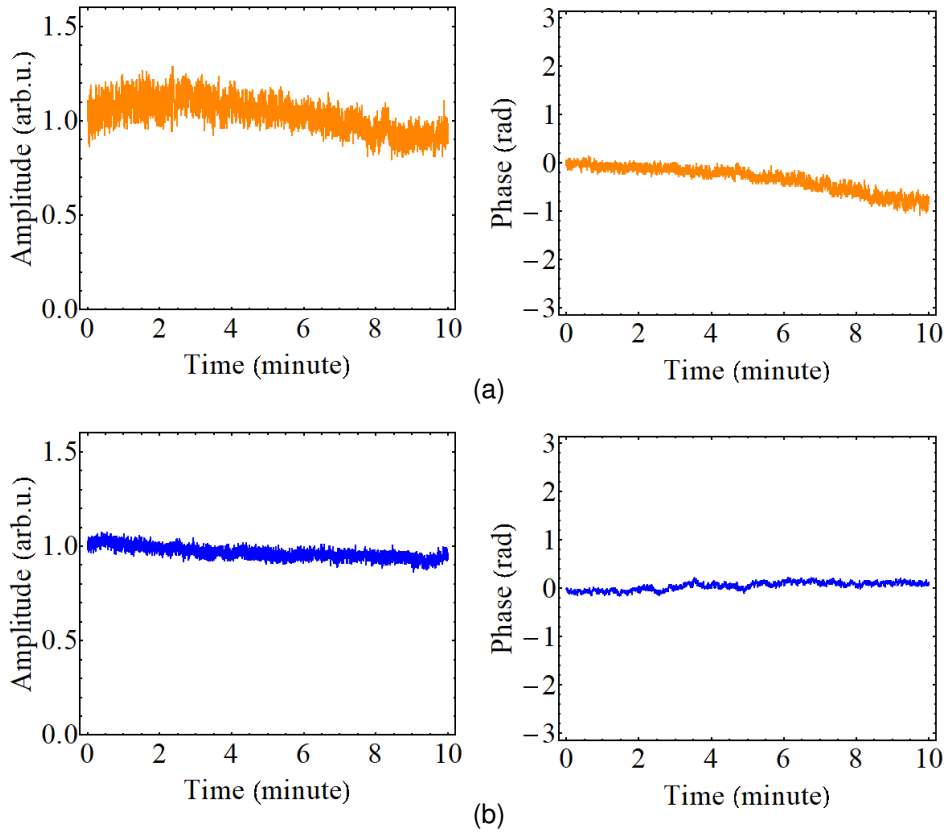

Figure 3.1.2: Amplitude and phase measurements for 10 min, obtained by (a) polarimetric and (b) nonpolarimetric EO detection techniques.

beam due to the ambient conditions affects the stability of the measurement based on the polarimetric technique.

The standard deviation of the 10-min phase measurement obtained by the polarimetric technique was 259 mrad, whereas that obtained by the nonpolarimetric technique was 81 mrad, which is smaller by a factor of 3.2. These results indicate that the nonpolarimetric technique offers a more stable measurement than the polarimetric technique, by a factor of approximately 3 for both the amplitude and phase of the THz wave.

3.2 Evaluation of the near-field measurement

We evaluate the near-field measurements obtained by the polarimetric and nonpolarimetric techniques by scanning the EO probe in the XY-, YZ-, and XZ-planes to visualize the THz wave emitted from the F-band horn antenna at 125 GHz. The

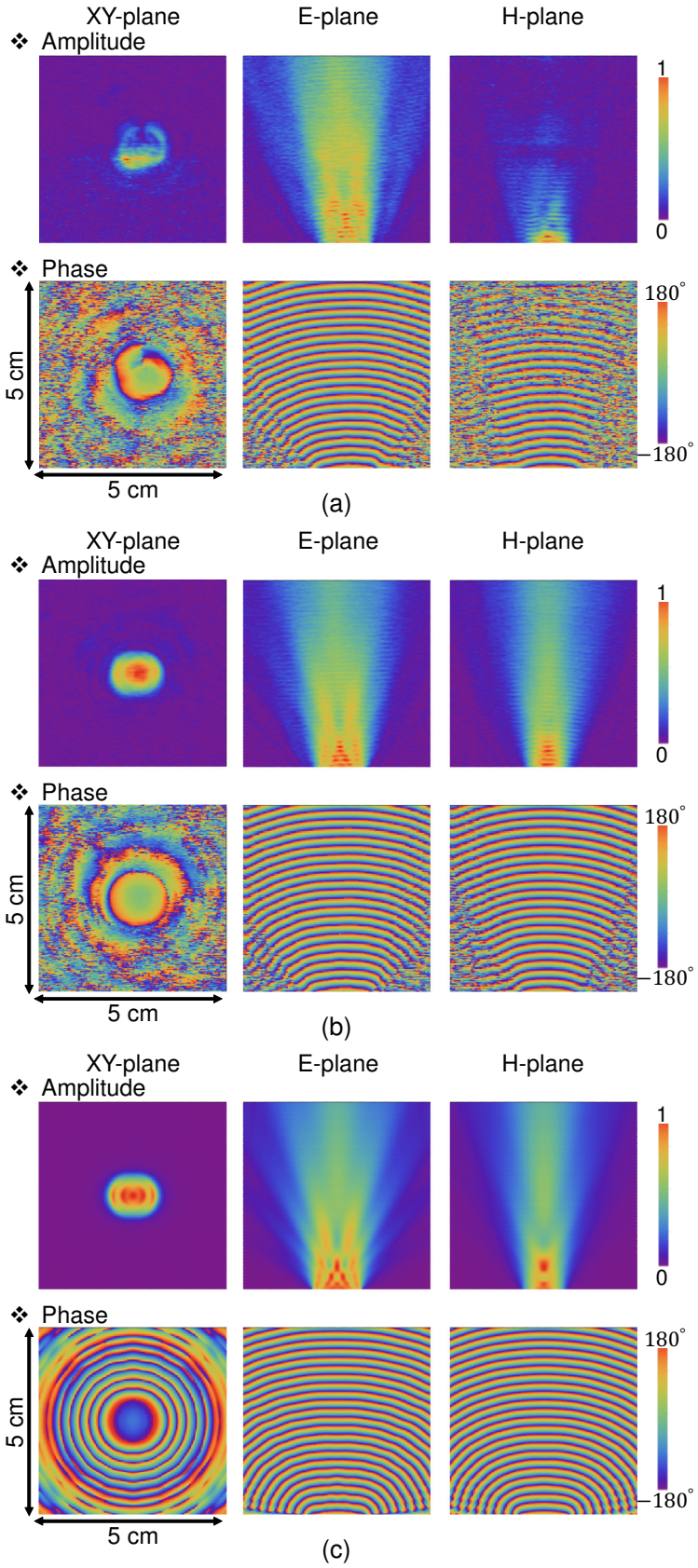

Figure 3.2.1: Experimentally visualized THz waves emitted from the horn antenna at 125 GHz by (a) polarimetric and (b) nonpolarimetric techniques; and (c) simulated results.

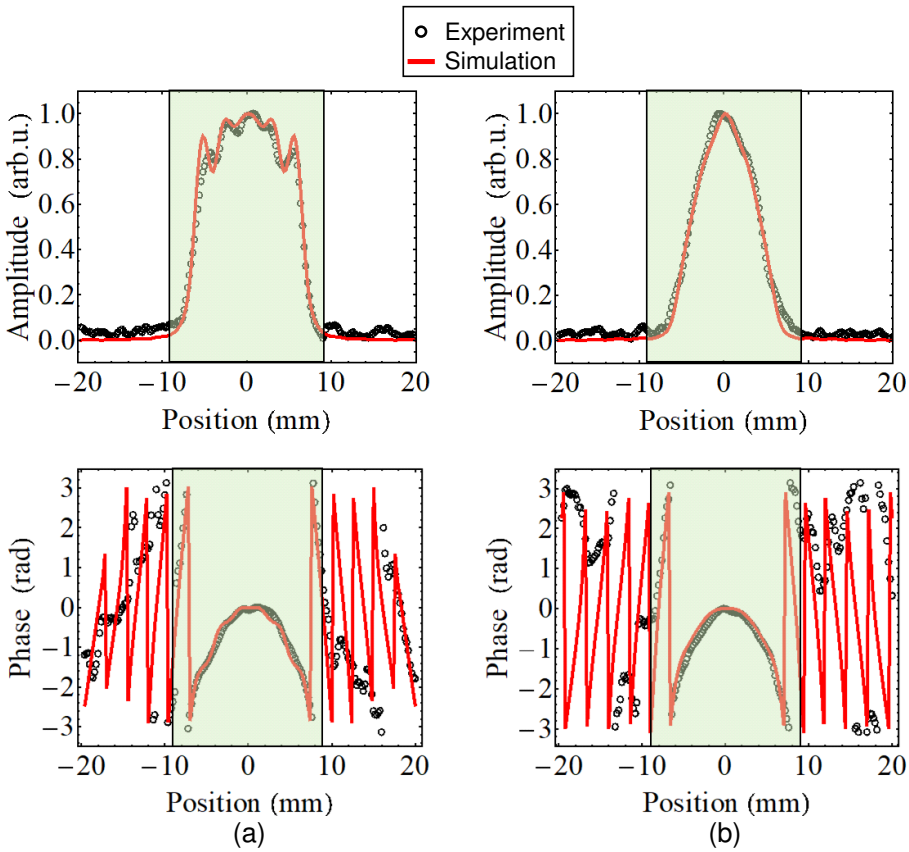

Figure 3.2.2: Experimental and simulated near-field distributions from horn antenna at 125 GHz in (a) E-plane and (b) H-plane.

measured area and sampling interval were 5 cm × 5 cm and 0.2 mm, respectively. The measurement time was approximately 30 min for each plane.

Figures 3.2.1(a) and 3.2.1(b) show the experimentally visualized amplitude and phase distributions in three planes by the polarimetric and nonpolarimetric techniques, respectively. Figure 3.2.1(c) shows the simulated results obtained by the finite integration technique using the CST Microwave Studio full-wave simulator. The dimensions of the horn antenna model in the simulation were the same as those in the experiment. The material of the antenna model was a perfect electric conductor with a thickness of 0 mm. The boundary condition in the simulation was a perfect matching layer boundary.

The obtained visualized results by the nonpolarimetric technique in Fig. 3.2.1(b) are clear in all three planes and show good agreement with the simulated results in Fig. 3.2.1(c) owing to the excellent stability of the measurement, even when the fiber-mounted EO probe is scanned. However, the visualized results by the polari-

metric technique in Fig. 3.2.1(a) are occasionally acceptable, such as the amplitude and phase images in E-plane, but they are worse in the XY- and H-planes owing to the instability of the measurement when scanning the fiber-mounted EO probe for the measurement. The unstable measurement of the EO detection system based on the polarimetric technique can cause the uncertainty of the THz device characterization and requires multiple measurements to verify the reproducibility of the E-field distributions. Therefore, the EO detection system based on the nonpolarimetric technique, in which the intrinsic problem of the sensitivity fluctuation due to the fluctuation of the polarization state is solved, is preferred for a variety of THz device characterizations.

Next, the comparison between the experimentally measured results and the simulated results in the near-field region in E- and H-planes is discussed, as illustrated in Fig. 3.2.2. The black circles and red solid line represent the experimental and simulated results, respectively. The distance between the EO probe and the horn antenna was approximately 1.2 mm (0.5 λ). The time constant of the LIA and the sampling interval were set at 30 ms and 0.2 mm, respectively. The movement speed of the EO probe was approximately 6.7 mm/s. The maximum SNR of the amplitude measurement obtained at the center of the antenna aperture was 31 dB.

The amplitude value was normalized to the maximum value in each case. As shown in Fig. 3.2.2, the measured data agree well with the simulated results within the green hatched area (-9 mm $< x, y <$ 9 mm), where the sensitivity of the EO probe is still able to detect the THz E-field. The detectable areas of the THz beam will be enlarged when the SNR is enhanced. The maximum deviation between the experimental and simulated results in the amplitude measurement was approximately 14% at the position $x = -5.2$ mm and 4% at the position $y = -1.0$ mm in the E-plane (Fig. 3.2.2(a)) and H-plane (Fig. 3.2.2(b)), respectively. These deviations are perhaps caused by the rounding of the steep change of the E-field distribution when continuously scanning the EO probe and acquiring data. Decreasing the scanning speed or the point-to-point measurements can probably reduce this effect.

3.3 Conclusion

In this chapter, the experimental evaluation of the performance of the EO detection system based on the polarization modulation and the nonpolarimetric techniques has been discussed. In particular, the stability of the measurement and the near-field visualization of the THz E-field radiated from the F-band (90–140 GHz) horn antenna have been characterized at 125 GHz. The ZnTe EO probe employing in the self-heterodyne system was used in the experiment for both techniques. The nonpolarimetric EO detection system was superior to the polarimetric EO detection system in terms of the measurement stability and near-field visualized results.

The standard deviation of the measured amplitude over 10 min without moving the EO probe by the nonpolarimetric technique was 2.6 times smaller than that by the polarimetric technique. A SNR improvement of approximately 7 dB was obtained by the nonpolarimetric technique. The visualized images by the polarimetric technique were unclear, owing to the instability that could make the obtained results be uncertain and require many repeated measurements for validation. Therefore, the nonpolarimetric EO detection system is preferred for the THz device characterization.

References

[3.1] S. Hisatake, G. Kitahara, K. Ajito, Y. Fukada, N. Yoshimoto, and T. Nagatsuma, *"Phase-sensitive terahertz self-heterodyne system based on photodiode and low-temperature-grown GaAs photoconductor at 1.55 μm,"* IEEE Sens. J., **13**, pp. 31-36, 2013.

[3.2] S. Hisatake and T. Nagatsuma, *"Continuous-wave terahertz field imaging based on photonics-based self-heterodyne electro-optic detection,"* Opt. Lett., **38**, pp. 2307-2310, 2013.

[3.3] F. Cecelja, B. Balachandran, M. Berwick, M. Soghomonian, and S. Cvetkovic, *"Optical sensors for the validation of electromagnetic field distributions in biological phantoms,"* Proc. SPIE Fiber Optics and Lasers Sensors XIII, **2510**, pp. 244-254, 1995.

[3.4] S. Wakana, T. Ohara, M. Abe, E. Yamazaki, M. Kishi, and M. Tsuchiya, *"Fiber-edge electrooptic/magnetooptic probe for spectral-domain analysis of*

electromagnetic field," IEEE Trans. Microw. Theory Techn., **48**, pp. 2611-2616, 2000.

[3.5] S. Hisatake and T. Nagatsuma, *"Nonpolarimetric technique for homodyne-type electrooptic field detection,"* Appl. Phys. Express, **5**, p. 012701, 2012.

[3.6] M. Naftaly and R. Dudley, *"Methodologies for determining the dynamic ranges and signal-to-noise ratios of terahertz time-domain spectrometers,"* Opt. Lett., **34**, pp. 1213-1215, 2009.

Chapter 4

Performance improvement techniques

In this chapter, the performance improvement techniques of the sensitivity, invasiveness, and interference issue are discussed. First, an organic EO material, 4-dimethylamino-N-metyl-4-stilbazolium tosylate (DAST), is employed to enhance the sensitivity and evaluated by comparing it with the ZnTe probe, which is one of the best inorganic EO crystals. The influence of optical components such as laser sources on the sensitivity is evaluated. A noise reduction configuration based on differential detection is introduced to reduce the excess laser noise. Second, theoretical and experimental studies of the invasiveness dependence on dimensions of the EO probe are described. A styrofoam holder is introduced to reduce the invasiveness by approximately 8 dB. Finally, the origin of the unwanted phase front appearing in the amplitude images due to the interference between signal and leaking noise is determined and solutions are proposed to reduce leaking noise power by approximately 25 dB.

4.1 Sensitivity enhancement

4.1.1 Exploitation of DAST probe

Properties of DAST

One of the methods to improve the sensitivity or signal-to-noise ratio (SNR) of the EO detection system is by exploiting a material that has a large EO coefficient as an EO probe. The exploitation of DAST crystal in the EO detection system based

Table 4.1.1: ZnTe and DAST properties.

	ZnTe	DAST
Optical feature	Isotropic	Biaxial
Refractive index @1550 nm [4.3]	$n = 2.75$	$n_1 = 2.14$
Relative permittivity @THz region [4.4]	$\varepsilon_z = 10.1$	$\varepsilon_d = 5.76$
EO coefficient (pm/V) @1535 nm [4.5]	$r_{41} = 4$	$r_{11} = 47$
Sensitivity factor	$SF_z = 8.2$	$SF_d = 80.0$

on the polarimetric technique was reported in [4.1] with the enhancement in the detected amplitude of 6 dB in comparison with a CdTe probe. In this section, we evaluate for the first time the exploitation of the DAST crystal as an EO probe in a nonpolarimetric self-heterodyne EO detection system. The evaluation method was based on a comparison with the ZnTe probe, which was known as one of the best inorganic materials for EO detection [4.2]. The sensitivity, stability, and repeatability of the measurement are evaluated at 125 GHz and 310 GHz.

The EO properties of ZnTe and DAST crystals are summarized in Table 4.1.1. The relative permittivity in the THz region and the refractive index at 1550 nm of the DAST crystal are smaller than those of the ZnTe crystal. The DAST crystal has an EO coefficient larger than that of the ZnTe crystal by approximately 12 times ($r_{41\_\mathrm{ZnTe}} = 4$ pm/V, $\mathrm{r}_{11\_\mathrm{DAST}} = 47$ pm/V). These result in the capability to enhance the sensitivity factor of the DAST crystal by approximately 9.8 times. The sensitivity factors of DAST (SF_d) and ZnTe (SF_z), which determine the sensitivity of the EO detection system based on the nonpolarimetric technique, can be calculated as [4.6]:

$$SF_d = \frac{r_{11} n_1^3}{\varepsilon_d}, \tag{4.1.1}$$

$$SF_z = \frac{r_{41} n^3}{\varepsilon_z}, \tag{4.1.2}$$

where r, n, and ε are the EO coefficient, refractive index, and relative permittivity of the EO crystal, respectively. As for the polarimetric EO detection technique, the sensitivity factor of the DAST crystal decreases, as expressed by [4.1]:

$$SF_d = \frac{|r_{11}n_1^3 - r_{21}n_2^3|}{\varepsilon_d}, \tag{4.1.3}$$

where n_1 and n_2 are the extraordinary and ordinary refractive indices of the DAST crystal, respectively.

Experimental setup

The EO detection system was modified such that we can measure the THz distribution by two probes at the same time, as shown in Fig. 4.1.1. Two free-running 1.55 µm laser diodes (LDs) were used for both the generation and detection of THz waves. The difference between optical frequencies was set at 125 GHz and 310 GHz. A frequency shifter (FS) was used to shift the frequency of LD1 by f_s = 100 kHz to realize the self-heterodyne technique. A UTC-PD was used to convert the beat-note optical frequency to THz waves. The THz power emitted from an F-band (90–140 GHz) horn antenna and J-band (220–325 GHz) horn antenna were approximately 1.3 mW and 28 µW, respectively.

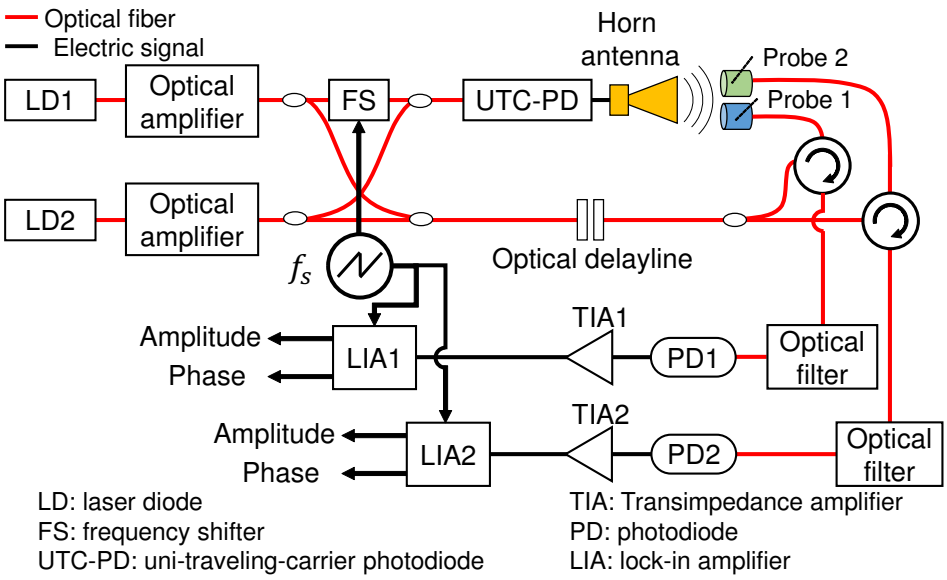

Figure 4.1.1: Experimental configuration to evaluate two probes.

In the LO path, the optical signals were divided by an optical coupler (50:50) and inputted to each EO probe through an independent optical circulator. Both

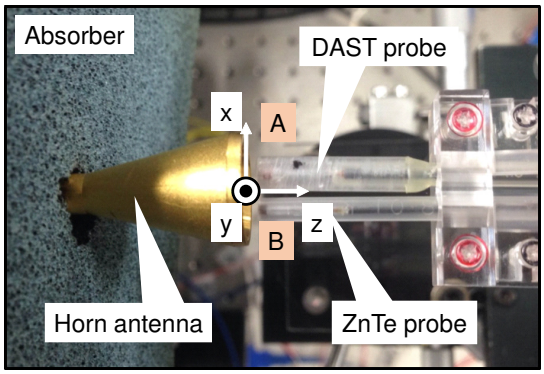

Figure 4.1.2: Position of two EO probes in the experiment.

the ZnTe and DAST crystals have the same dimensions of 1 mm × 1 mm × 1 mm and they are mounted on separate PMFs. We remark that the slow axis of the PMF was fixed parallel to the slow axis of the biaxial DAST crystal. This axis exhibits a large EO coefficient $r_{11} = 47$ pm/V. The spatial resolution of the two EO probes was 0.2 mm, which was determined by the diameter of the optical probe beam fed to these EO crystals. The modulated optical probe beam by the THz E-field from each probe is detected by different set of detection modules, including an optical filter, a photodiode (PD), a transimpedance amplifier (TIA), and a lock-in amplifier (LIA).

Figure 4.1.2 shows the position of two probes in the experiment. The origin of the measurement coordinate was set at the center surface of the F-band horn antenna. The positions of the probes (x, y, z) were A(2 mm, 0 mm, 3 mm) and B(−2 mm, 0 mm, 3 mm). The THz powers at the two positions A and B were almost the same because they were located symmetrically with respect to the center of the horn antenna. The E-field is parallel to the YZ-plane.

Evaluation at 125 GHz

Figures 4.1.3(a) and 4.1.3(b) show the measured amplitude and phase, respectively, without moving the probes for 1 min at 125 GHz by two probes simultaneously. The lock-in time constant was set at 30 ms and the photocurrent of each detecting PD was 0.9 mA. The blue and orange dots represent measured results by the DAST and ZnTe probes, respectively. The averaged detected amplitude by the

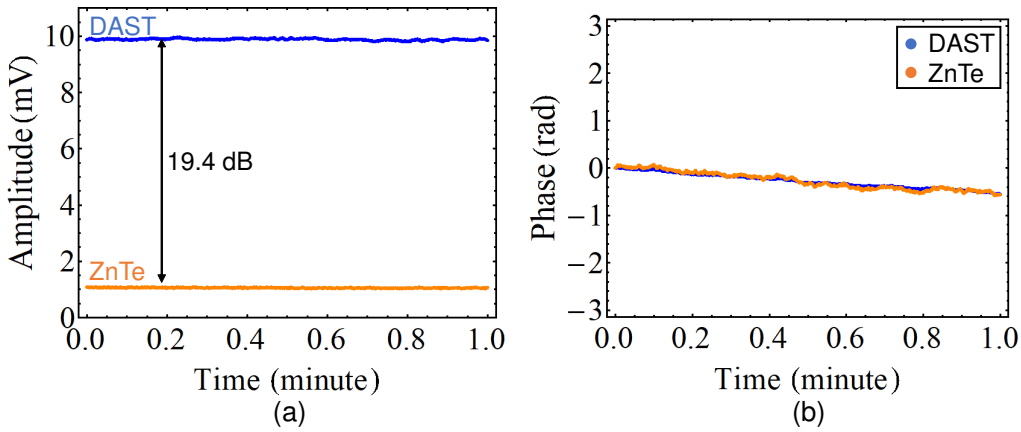

Figure 4.1.3: Measured (a) amplitude and (b) phase without moving EO probes for 1 min at 125 GHz.

DAST probe (9.9 mV) was 19.4 dB higher than that by the ZnTe probe (1.1 mV). The measured phase was stable with the a standard deviation below 0.18 rad for both probes.

The DAST and ZnTe probes were placed at position A and B, respectively, for a set of four measurements. Then, the positions of the probes were permuted for the next four measurements. The average of eight measurements of the detected amplitudes obtained by the DAST and ZnTe probes were 9.6 mV and 1.1 mV, respectively. The average of the standard deviation by the DAST and ZnTe probes were 0.03 mV and 0.01 mV, respectively. An enhancement in the SNR of greater than 10 dB was obtained for the DAST probe, from 38.89 dB to 49.72 dB. The SNR of the measurement was calculated as [4.7]:

$$SNR = 20\log_{10}\frac{\mu}{\sigma}, \tag{4.1.4}$$

where μ and σ are the mean value and the standard deviation of the measured amplitude without moving the probes for 1 min.

We define the minimum detectable E-field as the value of the E-field for which the SNR of the detected signal is 3 dB, corresponding to $\mu = 2\sigma$, which can be calculated as follows:

$$\begin{aligned} E_{\min} &= \sqrt{P_{\min}\, 120\pi}, \\ P_{\min} &= \alpha \frac{P_{\mathrm{THz}}}{10^{\frac{(SNR-3)}{10}} S_{\mathrm{spot}}} \end{aligned} \tag{4.1.5}$$

where $P_{\mathrm{THz}} = 1.3$ mW, P_{min}, and $S_{\mathrm{spot}} = 0.2 \times 0.2$ mm^2 are the emitted power of the THz wave, minimum detectable power, and area of the optical probe beam illuminated onto the EO crystal, respectively. α, which was estimated from the visualized amplitude distributions in the XY-plane, as shown later, is the ratio of the radiated THz power interacting with the EO crystal in the area S_{spot}. The distance between the EO probes and the horn antenna surface was approximately 3 mm, which was outside the reactive near-field region ($> \dfrac{\lambda}{2\pi} = 0.38$ mm). Therefore, the wave impedance can be estimated as 120π. The minimum detectable E-field obtained by the DAST probe (0.28 V/m) was 5.6 dB better than that obtained by the ZnTe probe (1.01 V/m) at 125 GHz. A summary of the detected signal including the amplitude, standard deviation (Std), SNR, and minimum detectable E-field is presented in Table 4.1.2.

Table 4.1.2: Summary of detected signal by two probes at 125 GHz.

	Amplitude (mV)	Std (mV)	SNR (dB)	Minimum detectable E-field (V/m)
DAST	9.64 ± 0.29	0.032 ± 0.004	49.72 ± 1.20	0.28 ± 0.04
ZnTe	1.06 ± 0.03	0.012 ± 0.001	38.89 ± 0.80	1.01 ± 0.09

The shot noise i_{sh}, thermal noise i_{th}, and TIA noise i_{TIA} can be calculated as:

$$\begin{aligned} i_{\mathrm{sh}} &= \sqrt{2e I_{\mathrm{ave}}\, \Delta_{BW}}, \\ i_{\mathrm{th}} &= \sqrt{4\frac{K\,T\,\Delta_{BW}}{R_{load}}}, \\ i_{\mathrm{TIA}} &= I_n \sqrt{\Delta_{BW}} \end{aligned} \tag{4.1.6}$$

where $e = 1.6 \times 10^{-19}$ C, $I_{\mathrm{ave}} = 0.9$ mA, and $\Delta_{BW} = 5.2$ Hz are the electron charge, average DC photocurrent of the detecting PD, and bandwidth of the LIA, which can be calculated from the time constant $\tau = 30$ ms with $\Delta_{BW} = \dfrac{5}{32\tau}$ as specification. $K = 1.38 \times 10^{-23}$ m^2 kg s^{-2} K^{-1}, $T = 301.75$ K, and $R_{load} = 50\ \Omega$ are the Boltzmann constant, absolute temperature of the room during the experiment, and resistance, respectively. $I_n = 1.5$ pA/$\sqrt{\mathrm{Hz}}$ is the current noise of the TIA. The root-mean-square voltage of these noises can be calculated as $V_n = i_n\, g$, where i_n and $g = 10^5$ V/A are the noises (shot, thermal, and amplifier noises) and gain

of the TIA, respectively. The calculated shot, thermal, and total noises ($V_{\text{total}} = g\sqrt{i_{\text{sh}}^2 + i_{\text{th}}^2 + i_{\text{TIA}}^2}$) were 0.004 mV, 0.004 mV, and 0.006 mV, respectively. The measured noise by the ZnTe (0.01 mV) and DAST probes (0.03 mV) are slightly higher than the estimated noise. This may be caused by the excess laser noise, the fluctuation of the RF power, and/or the fluctuation of the photocurrent of the detecting PD, which can be affected by the fluctuation of the optical signal reflected from the DAST probe owing to the imperfect alignment of the mirror mounted to the head of the DAST probe.

Overall, we obtained a SNR improvement of 10 dB by exploiting the DAST probe in the nonpolarimetric self-heterodyne EO detection system and a minimum detectable E-field of 0.28 V/m, which, to the best of our knowledge, is the best among the fiber-mounted EO probes.

Next, we evaluate the linearity of the detected signal by varying the THz output power. Figure 4.1.4 shows the dependence of the detected signal power on the THz power at 125 GHz by DAST and ZnTe probes. The blue and orange dots represent the results obtained by the DAST and ZnTe probes, respectively. The THz power was adjusted by controlling the photocurrent of the UTC-PD. The dependence of the THz power on the photocurrent of the UTC-PD was verified by a PM4 power meter. In Fig. 4.1.4, the detected intensity was normalized to the maximum detected signal by the DAST probe as follows:

$$\begin{aligned} I_D &= 20\log_{10}\frac{A_D(p)}{A_{max}}, \\ I_Z &= 20\log_{10}\frac{A_Z(p)}{A_{max}}, \end{aligned} \tag{4.1.7}$$

where I_D and I_Z are the detected intensities by the DAST and ZnTe probes, respectively. $A_D(p)$ and $A_Z(p)$ are the measured amplitude without moving the probe for 1 min at a specific THz power p by the DAST and ZnTe probes, respectively. A_{max} is the maximum detected amplitude by the DAST probe at $p = 1.46$ dBm (1.4 mW). The detected intensity at each THz power was the average of three measurements in which the DAST and ZnTe probes were placed at positions A and B, respectively, and three measurements in which the probe positions were permuted. An average enhancement in the detected intensity of 17.3 dB was ob-

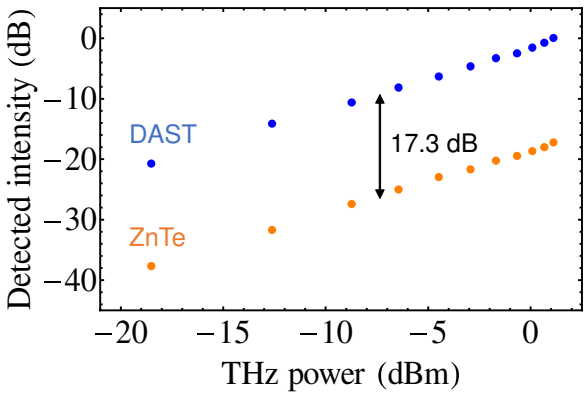

Figure 4.1.4: Dependence of detected signal power on THz power at 125 GHz by DAST and ZnTe probes.

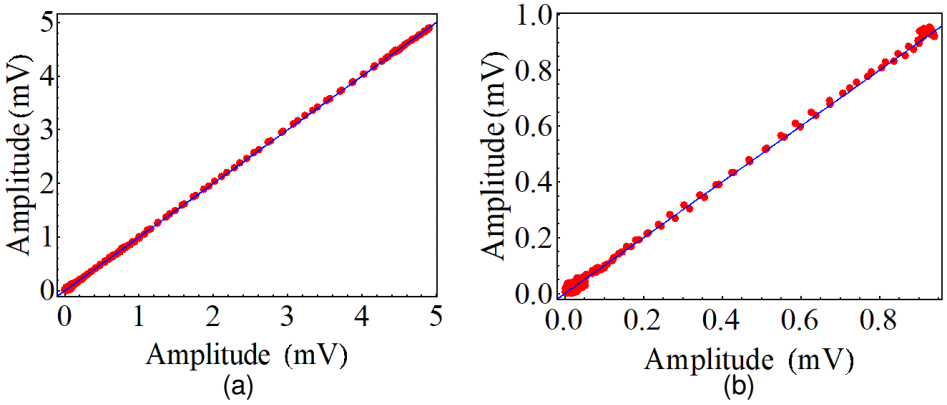

Figure 4.1.5: Typical correlation map between two independently measured amplitude distributions by (a) DAST and (b) ZnTe probes at 125 GHz.

tained by the DAST probe. A good linearity, proportional to the THz power, was also confirmed.

In another experiment, the reproducibility or repeatability of the measurements by DAST and ZnTe probes was verified. Figures 4.1.5(a) and 4.1.5(b) depict correlation maps between the detected amplitudes in two independent measurements, $A_1(x, 0, 3)$ and $A_2(x, 0, 3)$ with -50 mm $< x <$ 50 mm by DAST and ZnTe probes, respectively, when moving the probes along the x-axis. The red dots represent the experimental results, and the blue solid line has the slope of 1. The mapped data fit well to the blue solid line for both the DAST and ZnTe probes. These results indicate a good correlation between distinct measurements by both probes.

The standard deviations of the errors between two distinct measurements $A_i(x,0,3) - A_j(x,0,3)$ with $i \neq j$ were $\sigma_{mD} = 21 \pm 2$ μV and $\sigma_{mZ} = 6 \pm 1$ μV for the DAST and ZnTe probes, respectively. The standard uncertainties of the standard deviations were calculated based on 11 sets of two distinct measurements. The standard deviations of the amplitude measurements over 1 min without moving the probes were $\sigma_d = 20$ μV and $\sigma_z = 5$ μV, respectively. The standard deviations of the errors between repeated measurements coincide with the standard deviations of the measurement without moving the EO probes for both the DAST and ZnTe probes. This indicates a high repeatability of the measurement without excessive noise while scanning the fiber-mounted EO probe, even with the DAST probe in the EO detection system. Note that the slow fluctuation caused by the change in the refractive index of the EO crystals, as in equations (4.1.1) and (4.1.2), by the ambient temperature fluctuation can affect the repeatability. However, the high repeatability obtained in these experimental results proved that the ambient temperature fluctuation at the room temperature negligibly affects the repeatability of the EO measurement in this system.

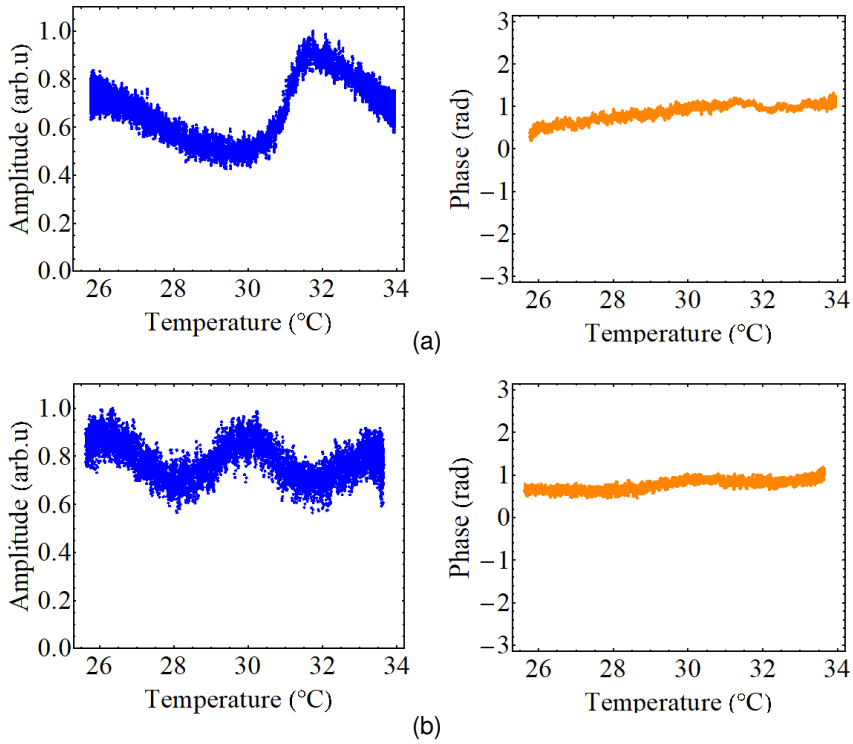

Figure 4.1.6: Experimental results of temperature dependence of detected amplitude and phase at 125 GHz by (a) DAST and (b) ZnTe probes.

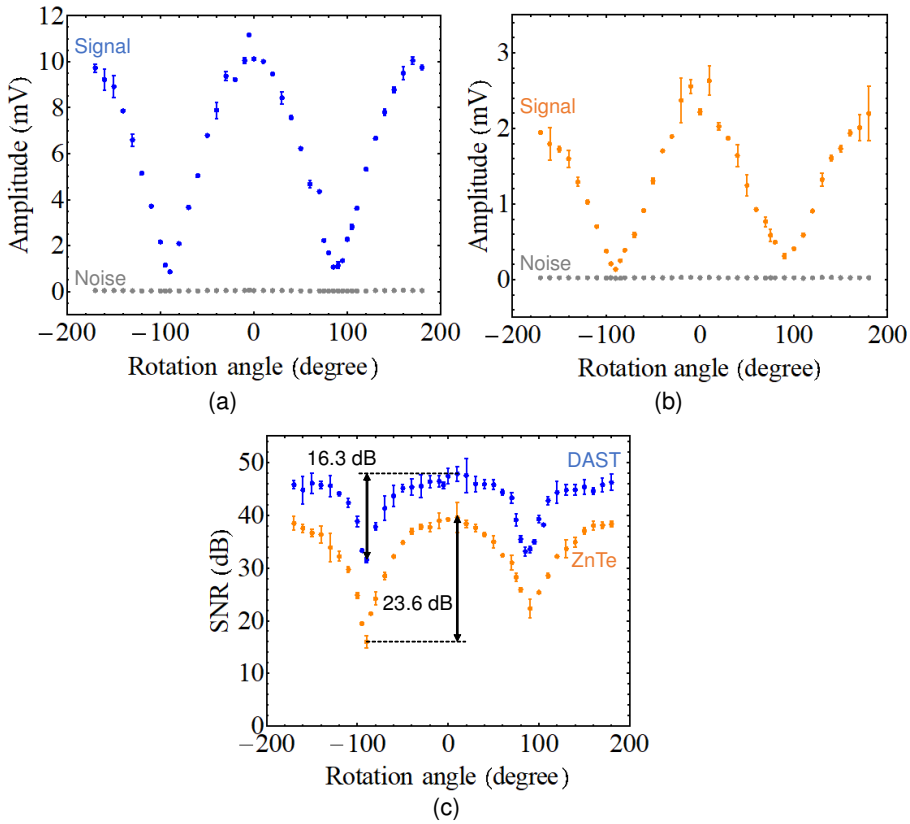

Figure 4.1.7: Measured polarization characteristics of detected signal by (a) DAST probe, (b) ZnTe probe, and (c) detected SNR at 125 GHz.

Figures 4.1.6(a) and 4.1.6(b) show the experimental results of the temperature dependence of the detected signal by the DAST and ZnTe probes, respectively, at 125 GHz. This experiment was verified inside a homemade insulated box made from styrofoam and thermistor placed close to the probes. The detected amplitudes deviated about 57% and 43% for the DAST and ZnTe probes, respectively, when increasing the temperature from 25.5 °C to 34 °C. The detected phase drifted by approximately 1.11 rad and 0.74 rad for the DAST and ZnTe probes, respectively. One possible reason of these obtained results is that the thermal variation of the refractive index and the absorption of the organic materials is generally larger than that of inorganic materials [4.8, 4.9].

Figures 4.1.7(a) and 4.1.7(b) show the polarization characteristics of the detected amplitude by the DAST and ZnTe probes, respectively, at 125 GHz. The evaluation method was based on 1-min measurements of each probe at a specific polarization. The polarization of the THz E-field emitted from the horn antenna

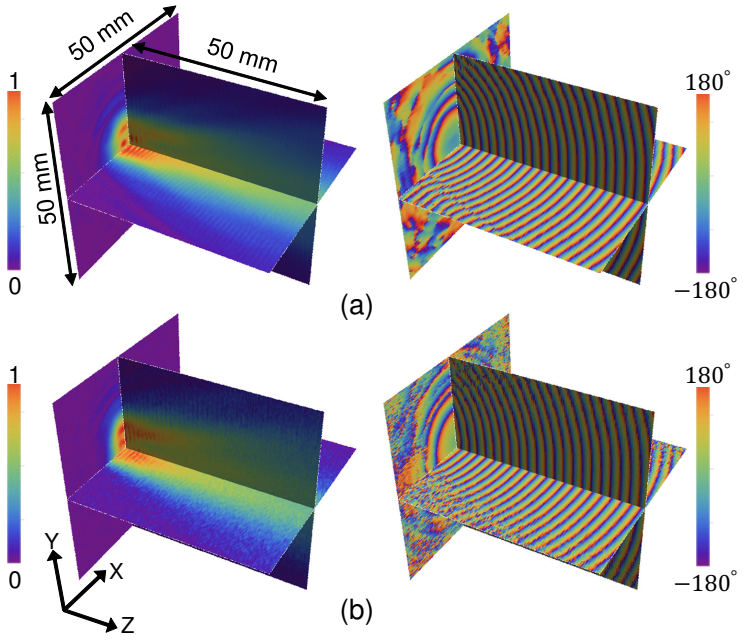

Figure 4.1.8: Visualized 3D amplitude and phase distributions of THz wave emitted from the horn antenna at 125 GHz by (a) DAST and (b) ZnTe probes.

was linear and parallel to the y-axis. Thus, each EO probe was rotated around the z-axis from $-180°$ to $180°$ in intervals of $10°$ to verify the polarization characteristics. The blue and orange dots represent the detected amplitude by the DAST and ZnTe probes, respectively, and the gray dots represent the noise or standard deviation. The standard error was calculated from three distinct measurements and the Student's t coefficient of 2.92, corresponding to a 90% two-sided confidence interval. The detected amplitudes by both probes are similar to the cosine function, as expected. The signal is highest at the center ($0°$), where the polarization of the EO probe is parallel to the y-axis, and lowest around $-90°$ and $90°$, where the polarization state of the EO probe is perpendicular to the y-axis. Figure 4.1.7(c) shows the SNR dependence on the polarization angle of the probes. The SNR obtained by the DAST probe was approximately 10 dB higher than that obtained by the ZnTe probe for every polarization angle. The extinction ratio, which is defined as the ratio between the detected SNR at two orthogonal polarization angles of the EO probe, was 16.3 dB and 23.6 dB for DAST and ZnTe probes, respectively. These results indicate that the polarization of the EO probe should be optimized to the polarization of the measured E-field to obtain the best SNR.

Figures 4.1.8(a) and 4.1.8(b) show the experimentally visualized three-dimensional (3D) amplitude and phase distributions of the THz waves emitted from the horn antenna at 125 GHz by the DAST and ZnTe probes, respectively. The amplitude value was normalized to the maximum value in each plane. The measured area and the sampling interval were 50 mm × 50 mm and 0.2 mm, respectively. The lock-in time constant was set at 30 ms and measurement time was approximately 30 min for each plane. The THz distributions were clearly visualized by both probes. The edge region was clearer when DAST probe was employed, owing to the improvement in the SNR of over 10 dB. This indicates that the DAST probe can be exploited in a nonpolarimetric self-heterodyne EO detection system with high stability, reproducibility, and sensitivity.

Evaluation at 310 GHz

The DAST probe capability is evaluated at a higher frequency of 310 GHz with a lower THz power of 28 µW. The evaluation method is similar to previous evaluation at 125 GHz: comparing the sensitivity, repeatability, and visualization with those by the ZnTe probe. Figures 4.1.9(a) and 4.1.9(b) show the measured amplitude and phase without moving the probes for 1 min at 310 GHz. Each probe was placed at the center of the J-band horn antenna to obtain the highest THz power. The lock-in time constant and photocurrent of each detecting PD were the same as for the previous experiment, i.e., 30 ms and 0.9 mA, respectively. The blue and orange dots represent the results obtained by the DAST and ZnTe probes, respectively. The detected amplitude by the DAST probe was 30.7 dB higher than that by the ZnTe probe. The phase standard deviations were 0.049 rad and 0.185 rad for the DAST and ZnTe probes, respectively.

The SNRs obtained by the DAST and ZnTe probes were 42.94 ± 0.41 dB and 15.21 ± 0.07 dB, respectively. The standard error was calculated from ten distinct measurements and the Student's t coefficient of 1.833, corresponding to a 90% two-sided confidence interval. The minimum detectable E-fields calculated by equation (4.1.5) were 0.29 ± 0.01 V/m and 3.33 ± 0.03 V/m for the DAST and ZnTe probes, respectively, at 310 GHz. The detected signals by the ZnTe and DAST

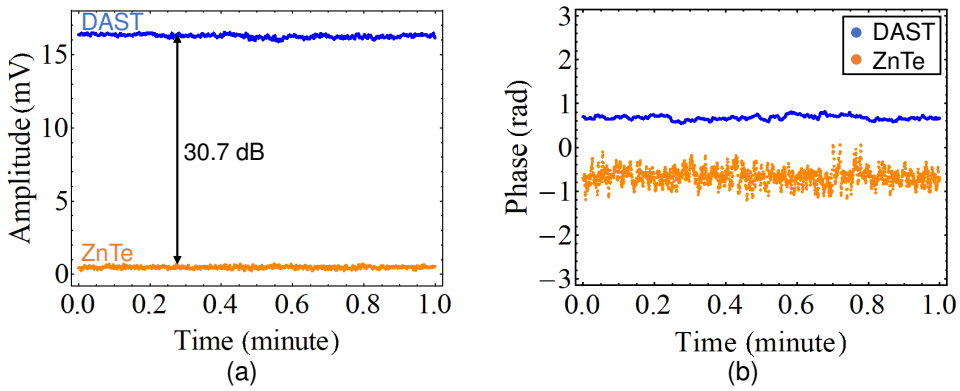

Figure 4.1.9: Measured (a) amplitude and (b) phase without moving probes in 1 minute at 310 GHz.

Table 4.1.3: Summary of detected signal by two probes at 310 GHz.

	Amplitude (mV)	Std (mV)	SNR (dB)	Minimum detectable E-field (V/m)
DAST	16.267 ± 0.044	0.116 ± 0.005	42.94 ± 0.41	0.29 ± 0.01
ZnTe	0.485 ± 0.002	0.012 ± 0.001	15.21 ± 0.07	3.33 ± 0.03

probes at 310 GHz are summarized in Table 4.1.3. These results indicate that the DAST probe offers a higher sensitivity than the ZnTe probe, even at a high THz frequency of 310 GHz, and that the best minimum detectable E-field of 0.28 V/m is maintained.

Figures 4.1.10(a) and 4.1.10(b) show the correlation map between two independently measured amplitude distributions in the x-axis by the DAST and ZnTe probes, respectively, at 310 GHz. The mapped data plotted with red dots fit well to the blue solid line, which has a slope of 1, for the DAST and ZnTe probes, even though the variation in measured data by the ZnTe probe was large as a result of the low SNR. In particular, the standard deviations of the errors between two distinct amplitude measurements were $\sigma_{mD} = 110.10 \pm 16.18$ µV and $\sigma_{mZ} = 86.03 \pm 3.55$ µV for the DAST and ZnTe probes, respectively. The standard uncertainties of the standard deviations were calculated based on 10 sets of two distinct measurements. The standard deviations of the amplitude measurements over 1 min without moving the probes were $\sigma_d = 116.32$ µV and $\sigma_z = 84.26$ µV,

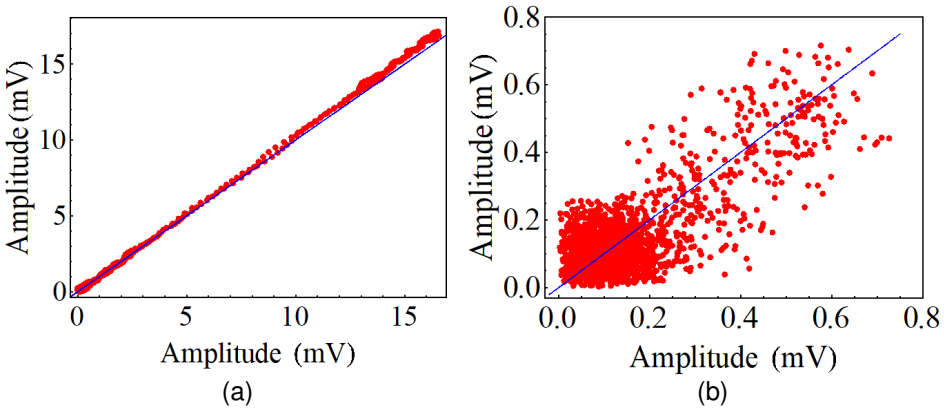

Figure 4.1.10: Typical correlation map between two independently measured amplitude distributions by (a) DAST and (b) ZnTe probes at 310 GHz.

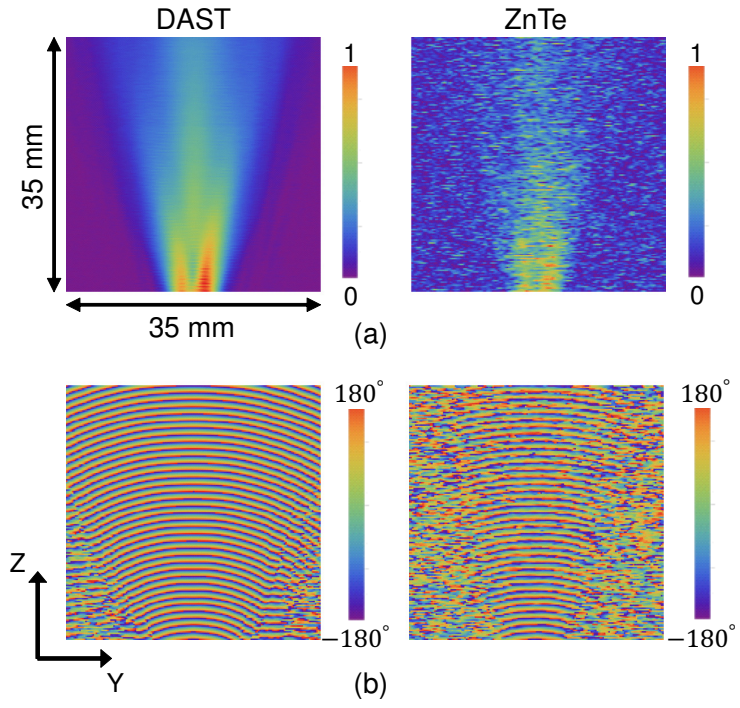

Figure 4.1.11: Experimentally visualized (a) amplitude and (b) phase distributions from the horn antenna in E-plane at 310 GHz by two probes.

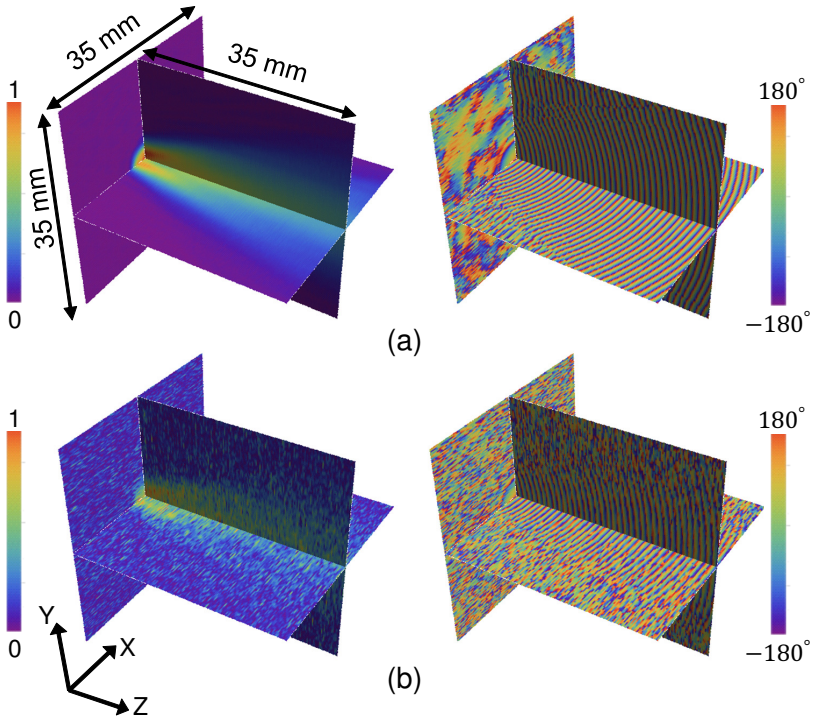

Figure 4.1.12: Experimentally visualized 3D THz distributions from the horn antenna at 310 GHz by (a) DAST and (b) ZnTe probes.

respectively. The agreement between σ_{mD} and σ_d, and σ_{mZ} and σ_z indicates that the measurements by these probes have a high repeatability without, excessive noise while moving the probes, even at 310 GHz.

Figures 4.1.11(a) and 4.1.11(b) depict the experimentally visualized amplitude and phase distributions, respectively, from the J-band horn antenna in the E-plane (YZ-plane) at 310 GHz by the DAST and ZnTe probes, respectively. The measured area and the sampling interval were 35 mm × 35 mm and 0.2 mm, respectively. The obtained results by the DAST probe were clearer than those obtained by the ZnTe probe, owing to the better sensitivity of the DAST probe. Figure 4.1.12 shows a 3D representation of the THz distribution form the J-band horn antenna by the DAST and ZnTe probes. The evaluation of the DAST probe in the nonpolarimetric self-heterodyne EO detection system shows the enhancement in the SNR of more than 10 dB with excellent stability and repeatability, which enables the characterization of THz devices at high frequencies above 100 GHz.

Issue of detected signal fluctuation of DAST probe

The initial employment of the DAST probe for the EO detection faced an issue of the fluctuation of the detected signal. In order to achieve the results described above, an investigation and solution of this issue were evaluated and proposed.

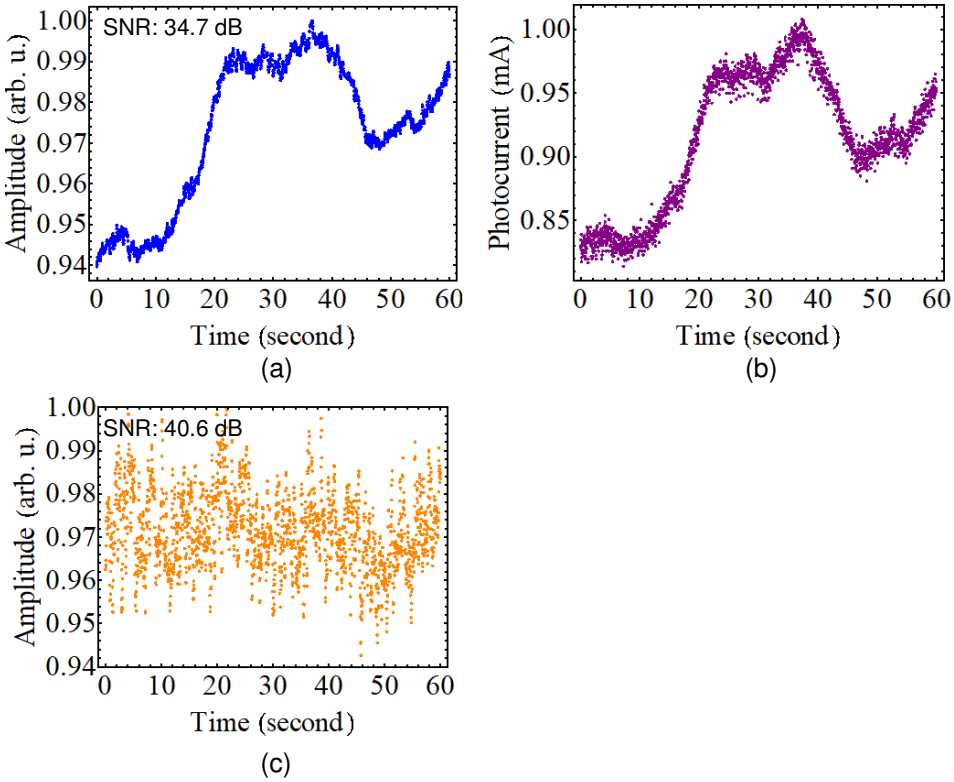

Figure 4.1.13: (a) Detected amplitude by DAST probe, (b) input photocurrent to PD of DAST probe, and (c) detected amplitude by ZnTe probe.

In the initial experiment in Fig. 4.1.1, the optical power input to each probe was approximately 12 dBm, which was the same as the input power to the single ZnTe probe used for the characterization until now. Figures 4.1.13(a), 4.1.13(b), and 4.1.13(c) show the normalized detected amplitude by the DAST probe, input photocurrent to the PD, and normalized detected amplitude by the ZnTe probe, respectively, for 1 min without moving the probes. The detected amplitude by the DAST probe fluctuated dramatically and shows a correlation with the photocurrent fluctuation. However, the detected amplitude by ZnTe shows only random noise. The obtained SNRs were 40.6 dB and 34.7 dB for the ZnTe and DAST probes, respectively.

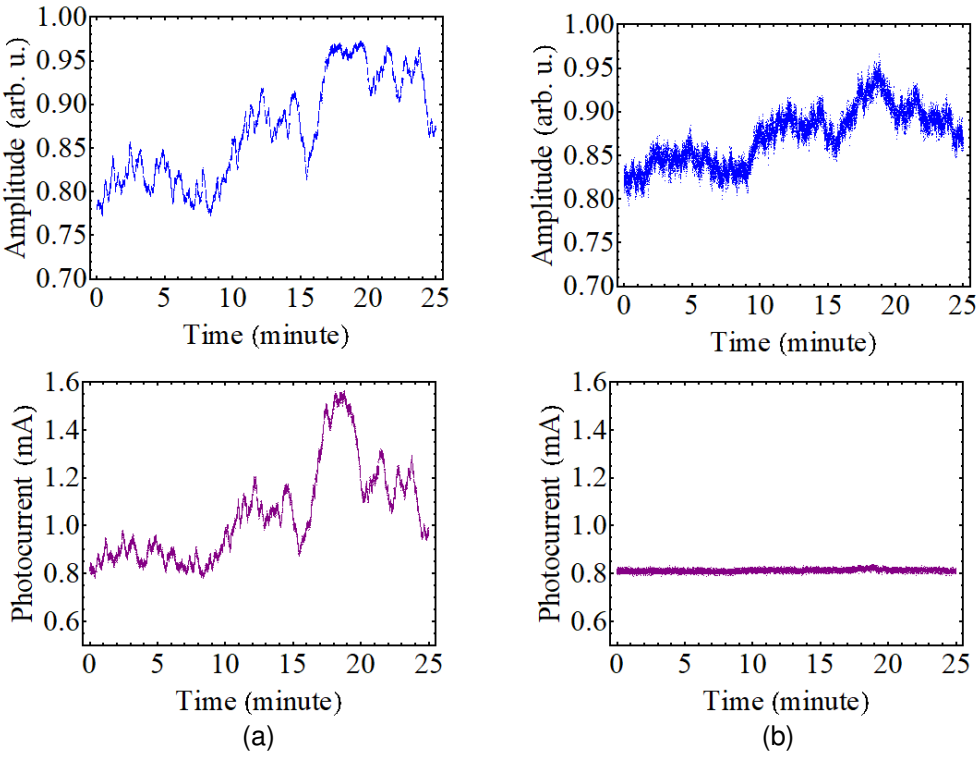

Figure 4.1.14: Detected amplitude and input photocurrent to detecting PD of (a) DAST probe and (b) ZnTe probe.

We investigate the relation between the detected amplitude and the input photocurrent to the PD of each probe over a longer time in Fig. 4.1.14. The experimental condition is same as above. In Fig. 4.1.14(a), we can observe a strong correlation between the fluctuation of the detected amplitude and the photocurrent of the DAST probe. However, the photocurrent of the ZnTe probe is stable and there is no significant correlation between the fluctuation of the detected amplitude and the photocurrent in Fig. 4.1.14(b).

The fluctuation of the photocurrent input to the detecting PD directly relates to the optical power coming back from the EO probe. Therefore, the dependence of the detected signal on the input optical LO power to the DAST probe is verified in Fig. 4.1.15. The standard error was calculated from five distinct measurements and a Student's t coefficient of 2.132, corresponding to a 90% two-sided confidence interval. The standard deviation and SNR were calculated from 1-min measurements without moving the EO probe. The detected amplitude of the DAST probe gradually increases as the input LO power increases from 6.1 dBm to 11.6 dBm in

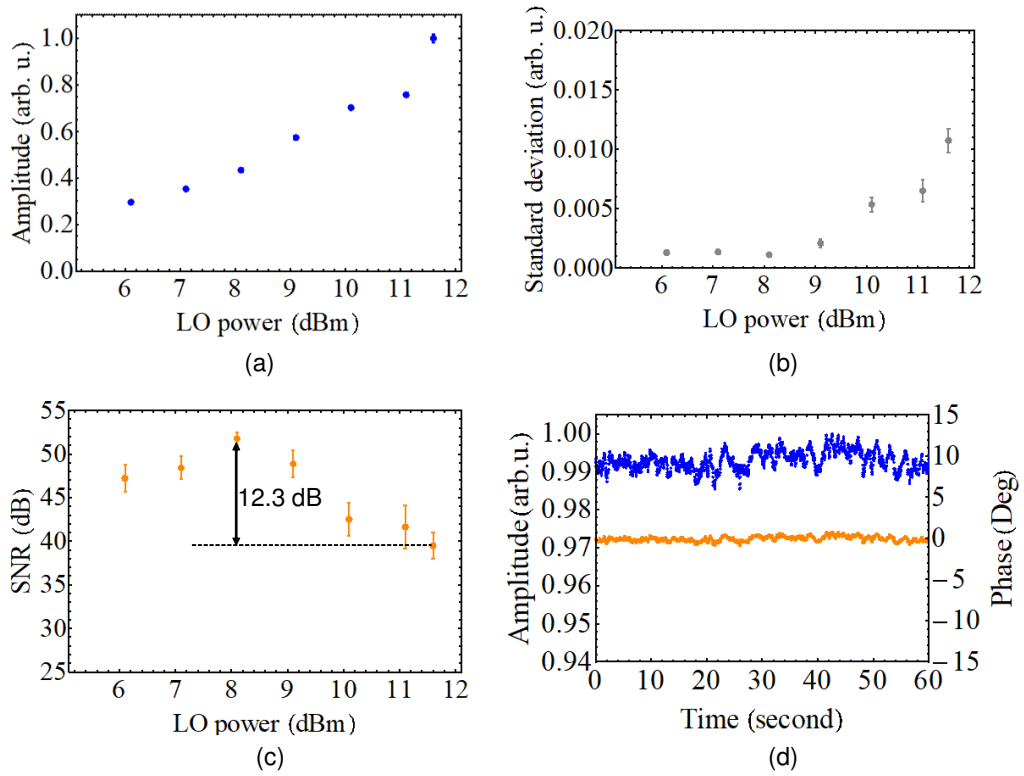

Figure 4.1.15: Dependence of (a) detected amplitude, (b) standard deviation, and (c) SNR on the optical LO power input to the DAST probe; (d) detected amplitude and phase with the optimal LO power of 8 dBm.

Fig. 4.1.15(a). The standard deviation of the amplitude value also increases as the LO power increases (Fig. 4.1.15(b)). Figure 4.1.15(c) shows the SNR dependence on the input LO power of the DAST probe. The significant degradation of the SNR can be observed when the input LO power is too large. One possible reason for this is the fluctuation of the optical signal reflected from the DAST probe, owing to the misalignment of the mirror mounted to the head of the DAST crystal or imperfection in the polishing process of the crystal and the mirror.

From this investigation, we found out that the best condition to use the DAST probe was with the input LO power of approximately 8 dBm. Figure 4.1.15(d) shows the detected amplitude and phase without moving the DAST probe for 1 min at the input LO power of 8 dBm. The SNR obtained under this condition was 51.8 dB, which was improved by 12.3 dB from the previous LO power condition and over 10 dB in comparison with the ZnTe probe, which was described initially.

4.1.2 Evaluation of optical components

Figure 4.1.16 depicts the experimental setup to evaluate the SNR dependence on the optical components of the EO detection system. Two free-running LDs, labeled LD1 and LD2, were used for both generation and detection of THz waves. A UTC-PD was used to generate the THz wave. An optical filter (Alnair Labs, BVF-300CL) extracted one pair of carrier and sideband for the down-conversion to the IF signal. First, the effect of different LDs on the SNR of the system was evaluated. Additionally, the SNR dependence on the extracted pair of the carrier and generated sideband was verified. The DAST probe was placed at the center and behind UTC-PD by approximately 5 mm. The THz frequency was set at 300 GHz. The lock-in time constant and photocurrent of detecting PD were 30 ms and 1 mA, respectively.

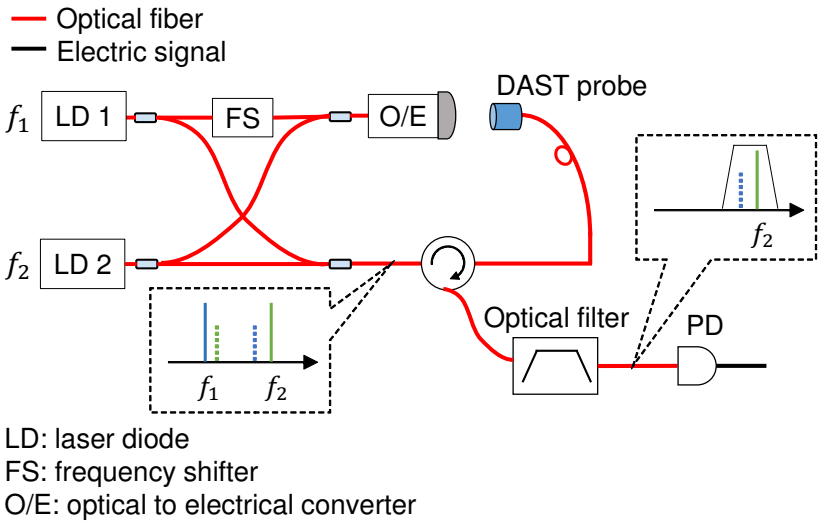

Figure 4.1.16: Experimental setup to evaluate SNR dependence on optical components of EO detection system.

Figure 4.1.17 shows the dependence of the detected signal on different LDs. The numbers (1) to (4B) denote the names of the LDs and the extracted optical carrier (carrier f_2 in Fig. 4.1.16). In particular, K601A represents Koshin LS-601A, K201A represents Koshin KLS-201A, RIO represents RIO Orion, and S510 represents Santec TSL-510. A summary of the specifications including the carrier-to-noise ratio (C/N), linewidth, side mode suppression ratio (SMSR), and relative

Table 4.1.4: Summary of specification of evaluated LDs.

	K601A	K201A	RIO	S510
C/N (dB)	65	60	70	60
Linewidth (kHz)	100	50	4	100
SMSR (dB)	50	>20	53	45
RIN (dB/Hz)	−160	−145		−145

intensity noise (RIN) of each LD is presented in Table 4.1.4. The RIO laser shows the best C/N, linewidth, and SMSR among the LDs in this experiment. The evaluation method was based on the detected signal over 1 min without moving the EO probe, under the same experimental condition. The same color in the graph denotes that the same LD was used. (#A) and (#B) denote that a different LO carrier was extracted.

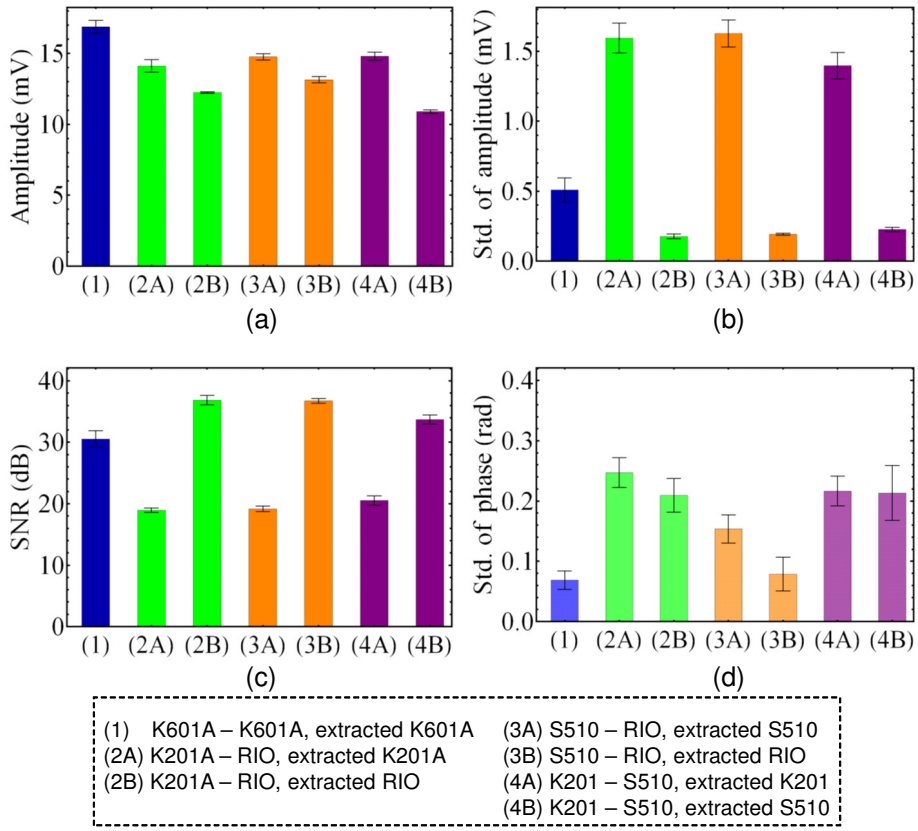

Figure 4.1.17: Dependence of (a) detected amplitude, (b) standard deviation of amplitude measurement, (c) SNR, and (d) standard deviation of phase measurement on different LDs.

The standard error was calculated from five distinct measurements. The detected amplitude using K601A is slightly higher than the other LDs in Fig. 4.1.17(a). In Fig. 4.1.17(b), the standard deviation of the amplitude measurement varied with not only the LDs but also the extracted LO carriers. Generally, the low amplitude standard deviation was obtained when the LO carrier of RIO was extracted. The best SNR of approximately 37 dB was obtained when using the best LDs and extracting its LO carrier for the nonpolarimetric detection ((2B) and (3B) in Fig. 4.1.17(c)). A standard deviation of the phase measurement below 0.25 rad was obtained for all combinations in Fig. 4.1.17(d). These results indicate that the better LDs (C/N, linewidth, SMSR, etc.) yield a better SNR of the measurement. Moreover, the optical carrier, which is extracted for the nonpolarimetric EO detection technique, should be a good LD. This is possibly because the noise in the EO measurement is significantly influenced by excessive laser noise. In the configuration in Fig. 4.1.16, LD2 should have a high C/N and stable or fixed wavelength LD, and LD1 can be tunable but not a high C/N or stable LD.

Next, the dependence of the carrier suppression ratio on the SNR of the EO detection system is verified. Here, the carrier suppression ratio γ is defined as the difference (in dB) between f_2 and f_1 optical carriers after passing through the optical filter for the nonpolarimetric detection, as depicted in Fig. 4.1.18(a). The evaluation method in this experiment was based on a 1-min measurement of collimated THz beam at 125 GHz, without moving the DAST probe. The lock-in time constant and photocurrent of detecting PD were 30 ms and 1 mA, respectively. An arbitrary tunable optical filter (Santec WSS-1000) was used to adjust the suppression ratio γ. The optical spectrum analyzer (Yokogawa AQ6370B) was used to confirm the exact value of γ, as in Fig. 4.1.19.

Figure 4.1.18(b) shows the experimental results of the measured amplitude with blue dots, and the noise or standard deviation with gray dots. The standard error was calculated from five distinct measurements. The detected amplitude increases significantly as γ increases from 0 dB to 10 dB, and increases more slowly from $\gamma = 10$ dB to $\gamma = 50$ dB. The SNR dependence on γ also shows a similar trend in Fig. 4.1.18(c). The increase in the SNR is saturated at suppression ratio $\gamma = 10$

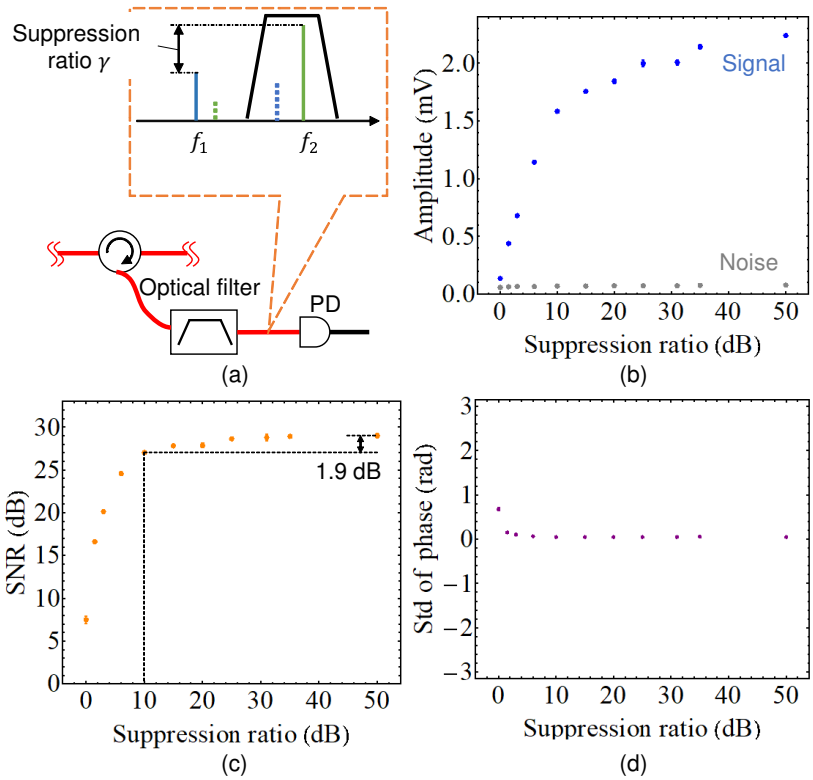

Figure 4.1.18: (a) Definition of suppression ratio γ. The dependence of (b) detected signal, (c) SNR, and (d) standard deviation of phase on γ.

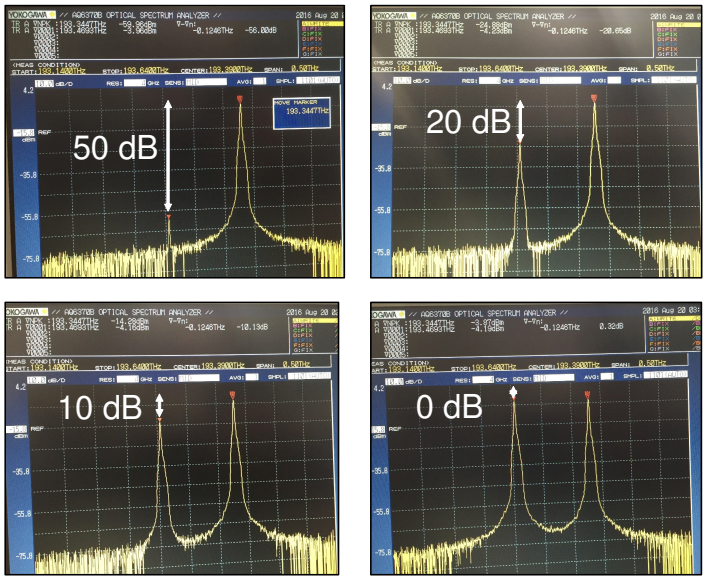

Figure 4.1.19: Carrier suppression ratio verified by optical spectrum analyzer.

dB. In particular, the difference between the SNR at $\gamma = 10$ dB and $\gamma = 50$ dB was approximately 1.9 dB. This indicates that a sharp optical filter, which is likely quite costly, does not contribute to the enhancement in the SNR of the system so much (below 2 dB). Furthermore, it indicates that this system can be employed in the low-frequency region, such as in the millimeter wave region (several tens of gigahertz), where the carrier f_2 is quite close to the carrier f_1 in Fig. 4.1.18(a) such that a large carrier suppression by an optical filter can be difficult. The phase standard deviation was also saturated at $\gamma = 10$ dB, as in Fig. 4.1.18(d).

4.1.3 Noise reduction configuration

Figure 4.1.20 shows the configuration of a noise reduction schematic (NRS) based on differential detection. In this configuration, the optical LO signal, which contains two carriers f_1 and f_2, is divided 50:50 by an optical coupler before inputting to the optical circulator. The modulated LO signal by the THz wave is reflected from the EO probe to the optical filter (OF1) through the circulator and converted to electric signal by PD1. The other divided optical LO signal, which is not directed to the EO probe, is also extracted by OF2 and converted to an electric signal by PD2. We remark that the same optical carrier f_2 is extracted by OF1 and OF2. The extracted optical signal by OF2 does not contain the generated sideband, because it does not enter the EO probe, and thus only the common laser noise is obtained from PD2. Two LIAs were used to evaluate the detected signal with and without the NRS simultaneously. The electric signal of PD1 is inputted to LIA1 for the conventional detection without NRS. The differential detection of PD1 and PD2 is realized by LIA2 for the novel EO detection with NRS. The same optical filters (Alnair Labs, BVF-300CL) and PDs were used in this experiment.

In this experiment, the ZnTe probe was used to detect the THz wave at 125 GHz. The detected amplitude and phase over 10 min without moving the EO probe are shown in Fig. 4.1.21(a) and (b), respectively. The blue and orange dots represent the results without and with NRS, respectively. The deviation of the measured data with NRS is smaller than that without NRS, for both the amplitude and phase. In particular, the standard deviations of 1-min measurements of the

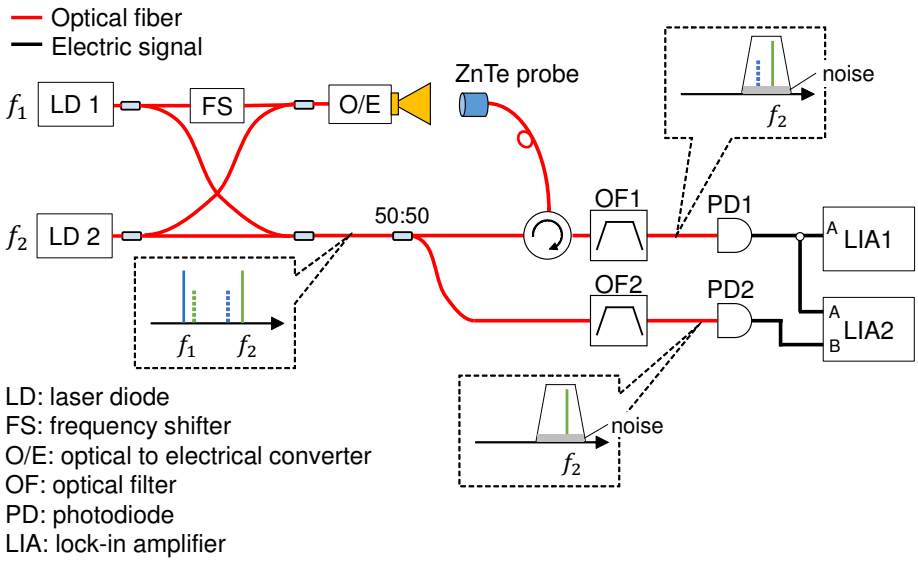

Figure 4.1.20: Experimental configuration of NRS.

amplitude and phase were 0.17 mV and 0.067 rad, respectively, in the case without NRS, and they reduced to 0.10 mV and 0.048 rad, respectively, with NRS.

Figure 4.1.22 shows the dependence of the detected signal on the THz power with and without NRS. The blue and orange dots represent the experimental results without and with NRS, respectively, which were based on 1-min measurements. The standard error was calculated from five distinct measurements. In Fig. 4.1.22(a), the detected amplitudes with and without NRS show linearity and identicalness. The noise or standard deviation of the amplitude measurement with (σ_W) and without NRS (σ_{WO}) are shown in Fig. 4.1.22(b). σ_W below 0.105 mV was obtained, whereas σ_{WO} was larger than 0.115 mV. At a THz power of 1 mW, σ_{WO} and σ_W were 0.160 ± 0.006 mV and 0.105 ± 0.002 mV, respectively. This indicates a reduction of approximately 3.6 dB noise power by this technique. This is also true when changing the THz power, as shown in Fig. 4.1.22(b).

Figures 4.1.22(c) and 4.1.22(d) show the SNR and the standard deviation of the phase measurement, respectively. At all THz powers, the SNR obtained with NRS was higher than that obtained without NRS, and the standard deviation of the phase measurement with NRS was lower than that without NRS, by approximately 0.02 rad. An improvement in the SNR of 3.6 dB was obtained with NRS. This

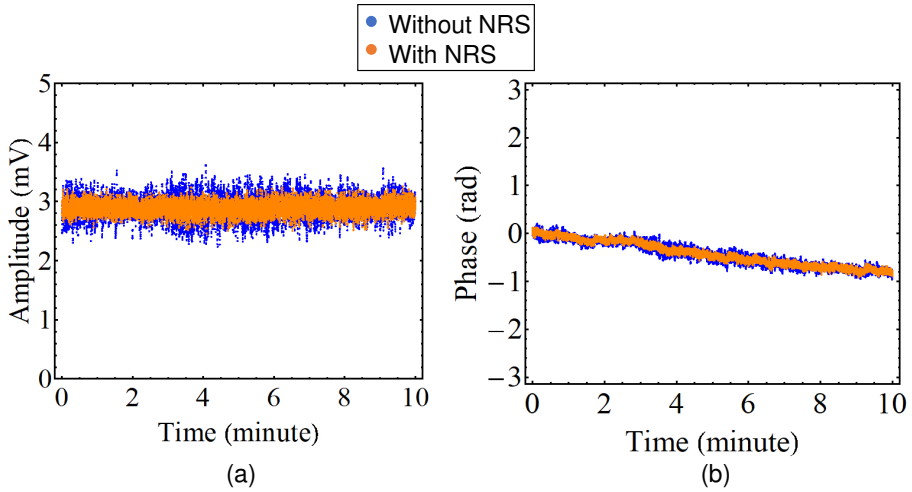

Figure 4.1.21: Measured (a) amplitude and (b) phase with and without NRS.

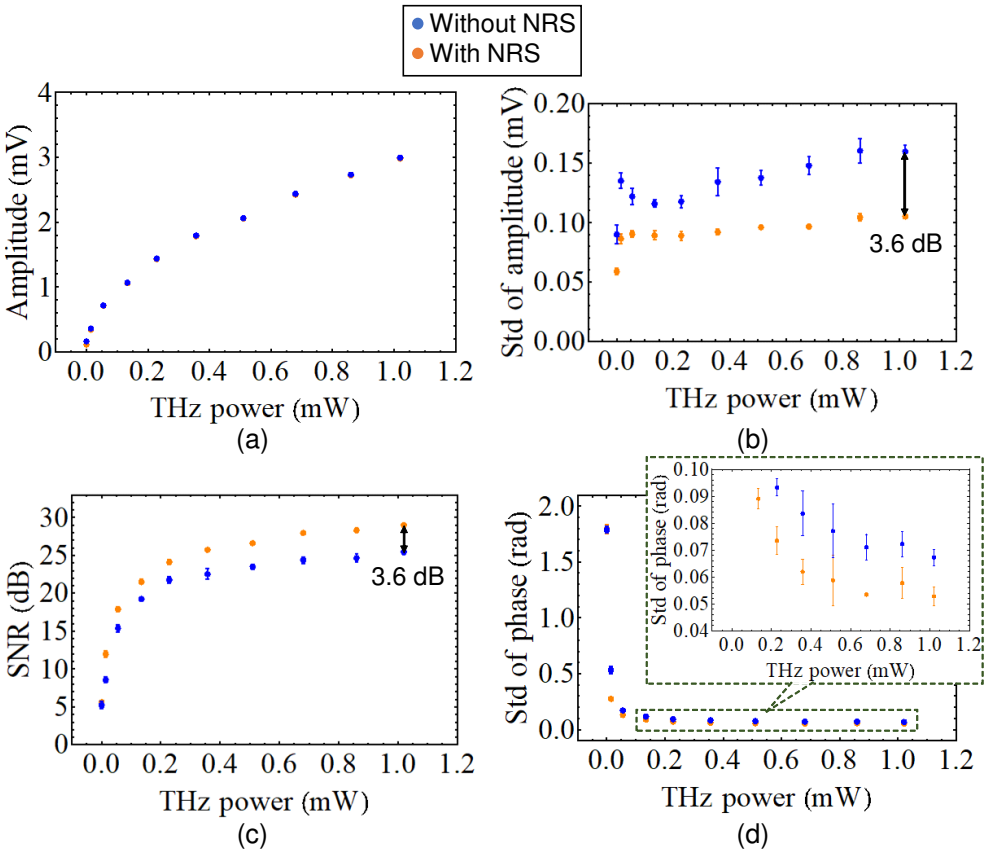

Figure 4.1.22: Dependence of detected (a) amplitude, (b) standard deviation of amplitude, (c) SNR, and (d) standard deviation of phase on the THz power with and without NRS.

indicates that the proposed noise reduction technique works effectively. We remark that the coherence between the LO part passing through the EO probe and the LO part for noise detection is important to cancel out the common laser noise in this technique.

4.2 Invasiveness reduction

4.2.1 Theoretical study

The evaluation of the invasiveness of the EO probe by simulation and experiment are discussed in this section. The evaluation method is based on verifying the standing wave phenomenon appearing between the EO probe and the DUTs, i.e., horn antennas and a Si-lens mounted device.

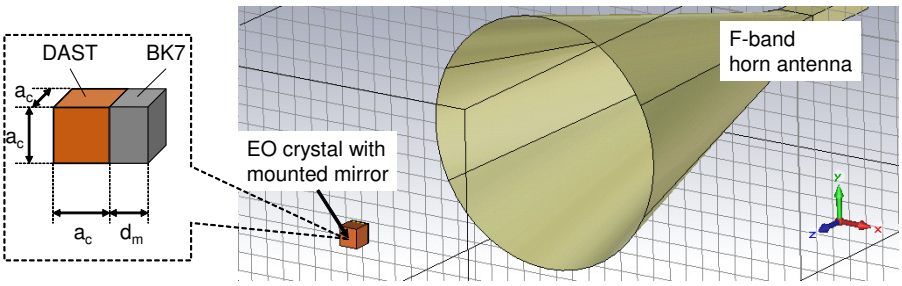

Figure 4.2.1: Simulated model of a horn antenna and a mounted-mirror cubic EO crystal to evaluate invasiveness.

Figure 4.2.1 shows the simulated model, including an F-band horn antenna and a mirror-mounted cubic EO crystal placed at the center of the horn antenna. The EO crystal has dimensions of $a_c \times a_c \times a_c$ mm^3 and is made from DAST, whose refractive index is $n_D = 2.4$ at several hundred GHz [4.4]. The attached mirror on the head of the DAST crystal is made from BK7 ($n_{BK7} = 2.5$ at 0.1–1 THz [4.10]), its width and height are the same as the crystal dimensions, and the thickness of the mirror is $d_m = 0.5$ mm. The simulation was based on the finite integration technique with the perfect matching layer boundary condition using the CST Microwave Studio full-wave simulator. The time domain solver was used with the monitor at a frequency of 125 GHz ($\lambda = 2.4$ mm). The distance between

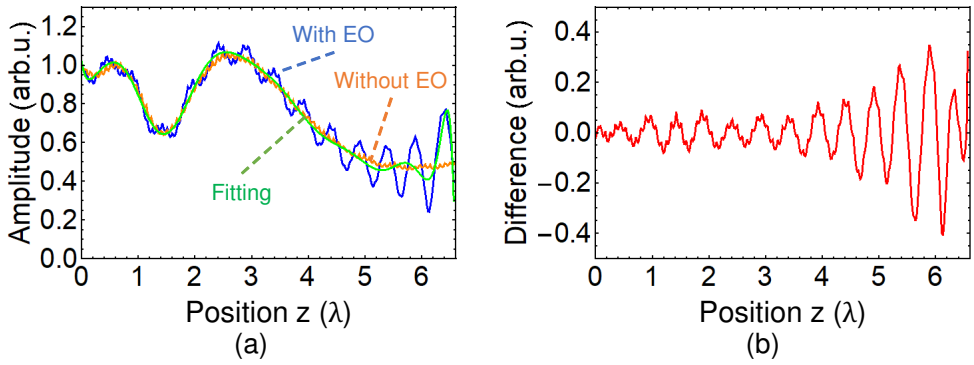

Figure 4.2.2: (a) Simulated results of the amplitude distribution and fitting line along z-axis at the center of the horn antenna with a 1 mm^3 DAST probe, and (b) difference between amplitude distribution and fitting line.

the horn antenna surface and the mirror was set at 16 mm (6.67 λ).

Figure 4.2.2(a) shows the simulated results of the amplitude distribution, where the EO probe is plotted with the blue line, the fitting line with the green line, and the ideal amplitude distribution without EO probe with the orange line, at the center of the horn antenna along the z-axis. $z = 0\lambda$ is the position at the surface of the horn antenna. The dimensions of the DAST crystal were set at $a_c = 1$ mm in this simulated result. We can observe the standing wave appearing in the amplitude distribution with the EO probe (blue line), i.e., the periodical peak appearing at every $\frac{\lambda}{2}$ position. This standing wave is caused by the Fresnel reflection due to the refractive index difference between the EO crystal or the mirror and the surrounding medium. However, the ideal amplitude distribution without the EO probe (orange line) does not show any standing wave.

The fitting line (green line) of the amplitude distribution with the EO probe agreed well with the ideal orange line, because it shows the average amplitude distribution along the z-axis. The fitting line here is used for the evaluation in this study because it is difficult to simulate all conditions exactly similar to those of the experiment for the investigation. A polynomial regression model of a 15th-degree polynomial was used for the fitting line, because the amplitude distribution from the horn antenna in the near-field region does not degrade exponentially as a normal Gaussian beam.

Figure 4.2.2(b) shows the normalized difference (Dif) between the amplitude

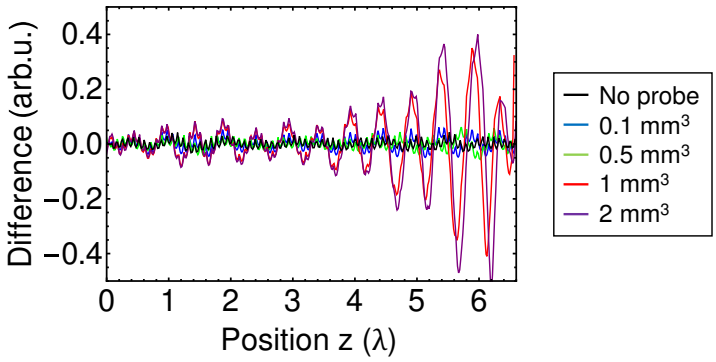

Figure 4.2.3: Dependence of standing wave on dimensions of DAST probe.

distribution (A(z)) and the fitting line (A_{fit}(z)), which is calculated as $Dif = \frac{A(\text{z}) - A_{\text{fit}}(\text{z})}{A_{\text{fit}}(\text{z})}$. We define the peak-to-peak deviation as $Dev = \frac{Dif_{\max} - Dif_{\min}}{2}$, where $Dif_{\max}$ and $Dif_{\min}$ are the maximum and minimum values of the differences, respectively. The deviation was $Dev = 0.38$ for 1-mm^3 DAST crystal.

Figure 4.2.3 shows the simulated results of the difference between the amplitude distribution and the fitting line when changing the dimensions of the EO probe from 0.1 mm^3 to 2 mm^3. As for dimensions smaller than 0.5 mm^3 (0.21 λ), the standing wave is relatively small and comparable to ideal case without the EO probe. In particular, the deviation was $Dev = 0.06$ for 0.1-mm^3 and 0.5-mm^3 crystals, whereas it was $Dev = 0.04$ for the ideal case. However, the deviations increased significantly to $Dev = 0.38$ and $Dev = 0.46$ for 1-mm^3 (0.42 λ) and 2-mm^3 ((0.83 λ)) crystals, respectively. These results indicate that the DAST probe with dimensions smaller than 0.2 λ allows negligible invasiveness to the measured E-field with the wavelength λ. Increasing the dimensions of the DAST probe by a factor of two, from 1 mm^3 to 2 mm^3 or relatively increasing the THz frequency 2 times leads to an increase in the invasiveness or standing wave by 21% ($Dev = 0.38$ to $Dev = 0.46$).

Next, the improvement in the invasiveness of the DAST probe based on an anti-reflective (AR) coating method by simulation is verified. The idea is that the mirror mounted on the head of the EO probe is also engineered to function as the AR-coating. The refractive index n_m and thickness d_m of the mirror can be calculated based on thin single layer AR coating technique [4.11–4.13] as follows:

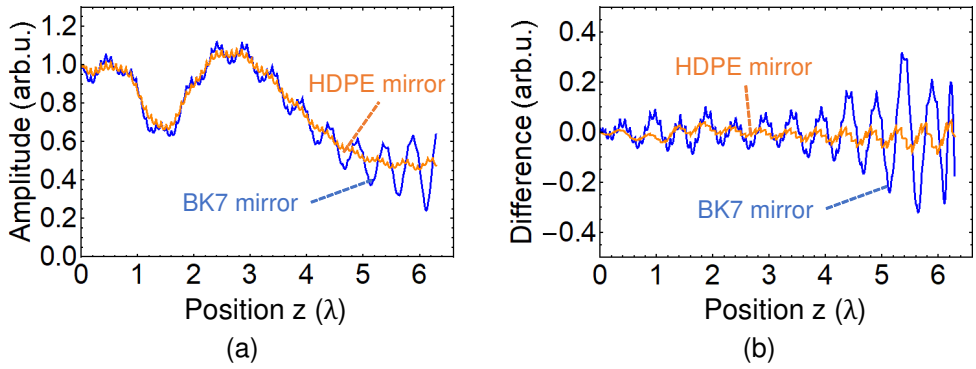

Figure 4.2.4: (a) Simulated results of amplitude distribution and (b) the differences between it and the fitting line of the DAST probe associated with BK7 mirror and AR-coating HDPE mirror.

$$\begin{aligned} n_m &= \sqrt{n_1\, n_D}, \\ d_m &= \frac{(2j+1)\lambda}{4n_m} \quad (j = 0,\ 1,\ 2, ...) \end{aligned} \tag{4.2.1}$$

where $n_1 = 1$, $n_D = 2.4$, and $\lambda = 2.4$ mm are the refractive indices of the air, DAST crystal, and the free space wavelength of the THz wave, which is considered at 125 GHz, respectively. The first equation in (4.2.1) ensures the same reflectance from the air–mirror and mirror–crystal, and the second equation in (4.2.1) realizes the destructive interference of the reflected waves. The obtained refractive index and thickness of the mirror are $n_m = 1.549$ and $d_m = 0.387$ mm. High-density polyethylene (HDPE), which has a refractive index of approximately 1.55 and a low absorption coefficient below 2 cm^{-1} at THz frequencies from 0.1 THz to 2 THz [4.10], is one of the suitable materials for the mirror of the EO probe.

A 1 mm^3 DAST crystal mounted on a 0.39-mm-thick HDPE mirror is verified. The simulated conditions were the same as the previous ones. Figure 4.2.4(a) shows the simulated results of the amplitude distribution along the z-axis, at the center of the horn antenna surface at 125 GHz. The blue and orange lines represent the results with the mirror made from conventional 0.5-mm thick BK7 and AR-coating HDPE mirror, respectively. The standing wave effect shows a significant reduction when using the HDPE mirror. Figure 4.2.4(b) shows the difference between the amplitude distribution and the polynomial fitting line in each case. The peak-to-peak deviation in the case of HDPE mirror decreases by 81.6% to 0.07 in comparison with 0.38 in the case of BK7 mirror. Additionally, a broadband

AR coating mirror for the EO probe in the THz region can be also expected by employing multilayer or gradient index AR coating techniques [4.12].

4.2.2 Experimental study

Next, we experimentally investigate the invasiveness of the DAST probe without cover as shown in Fig. 4.2.5(b) by verifying the standing wave at different frequencies from 24 GHz to 490 GHz when scanning the probe in z-axis as shown in Fig. 4.2.5(a). We remarked that using another EO probe to measure the standing wave between the DAST probe and the antenna is probably better for the comparison with the simulated results, but we only considered the experimental results this time owing to the difficulty of performing the experiment by two probes. Changing THz frequency is similar to changing the dimensions of the DAST probe at a specific frequency. Absorbers were placed around the antenna, the probe, and the surrounding area to reduce unwanted multiple reflection. Figure 4.2.5(a) shows the experimental configuration of invasiveness investigation at 24 GHz. A 1 mm^3 DAST crystal mounted on a 0.5-mm-thick BK7 mirror was placed on an acrylic holder, which has the measured refractive index of approximately 1.59 at 125 GHz. The EO probe was placed at the center and close to the antenna surface. Owing to the bandwidth limitation of the antenna and waveguide, we employed a K-band (18–27 GHz) horn antenna, F-band (90–140 GHz) horn antenna, and Si-lens-mounted UTC-PD (over 1 THz bandwidth).

Figures 4.2.6 and 4.2.7 show the experimental results of the invasiveness evaluation of the DAST probe at frequencies from 24 GHz to 140 GHz and from 260 GHz to 490 GHz, respectively. In particular, in Fig. 4.2.6(a) and Fig. 4.2.7(a), the blue line represents the amplitude distribution at the center of the antenna along the z-axis, and the yellow line represents its fitting line based on a 15th-degree polynomial regression model. The amplitude distribution was the average of 12 measurements. The difference between the amplitude distribution and its fitting line is shown in Fig. 4.2.6(b) and Fig. 4.2.7(b). The calculation method is the same as the simulated results in Fig. 4.2.2(b). The peak-to-peak deviation Dev of the difference between the amplitude distribution and its fitting line at each

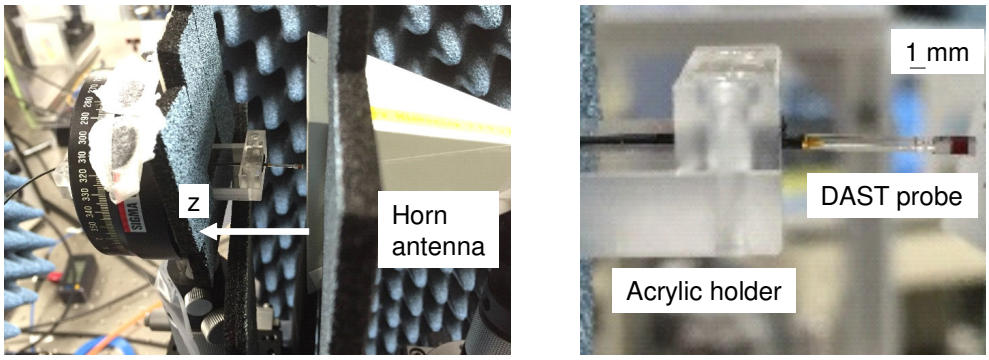

Figure 4.2.5: (a) Experimental configuration of invasiveness investigation of DAST probe at 24 GHz, and (b) 1 mm^3 DAST crystal mounted 0.5-mm-thick BK7 mirror on acrylic holder.

Table 4.2.1: Experimental peak-to-peak deviations and the standard deviation of the differences between amplitude distribution and its fitting line.

Frequency (GHz)	24	90	125	140	260	310	390	490
Dev (arb. u.)	0.134	0.199	0.196	0.116	0.114	0.123	0.130	0.130
Std (arb. u.)	0.055	0.065	0.062	0.036	0.038	0.049	0.051	0.054

frequency is summarized in Table 4.2.1.

The effect of the DAST probe on the standing wave should be negligibly small at low frequencies (24 GHz and 90 GHz), and become larger at frequencies two to three times higher than 125 GHz (260–490 GHz). However, in the experiment, *Dev* was almost the same for every frequency, excluding 90 and 125 GHz, where they were slightly higher. The standard deviation of the difference at each frequency was almost unchanged. These experimental results indicate that the standing wave or invasiveness in the EO detection system is probably not caused by the 1 mm^3 EO probe itself, but rather by another factor. The acrylic holder, which has larger dimensions (10 mm × 30 mm) and a refractive index of 1.59, could probably cause the invasiveness to the E-field measurement.

Figures 4.2.8(a) and 4.2.8(b) show the experimental configurations and schematics with 2 cm × 8 cm × 1 cm acrylic holder and 20 cm × 15 cm × 3 cm styrofoam holder, respectively. The measured refractive index of the styrofoam was 1.02 (close to air) at 125 GHz. The DAST probe was covered in a thin plastic cylinder

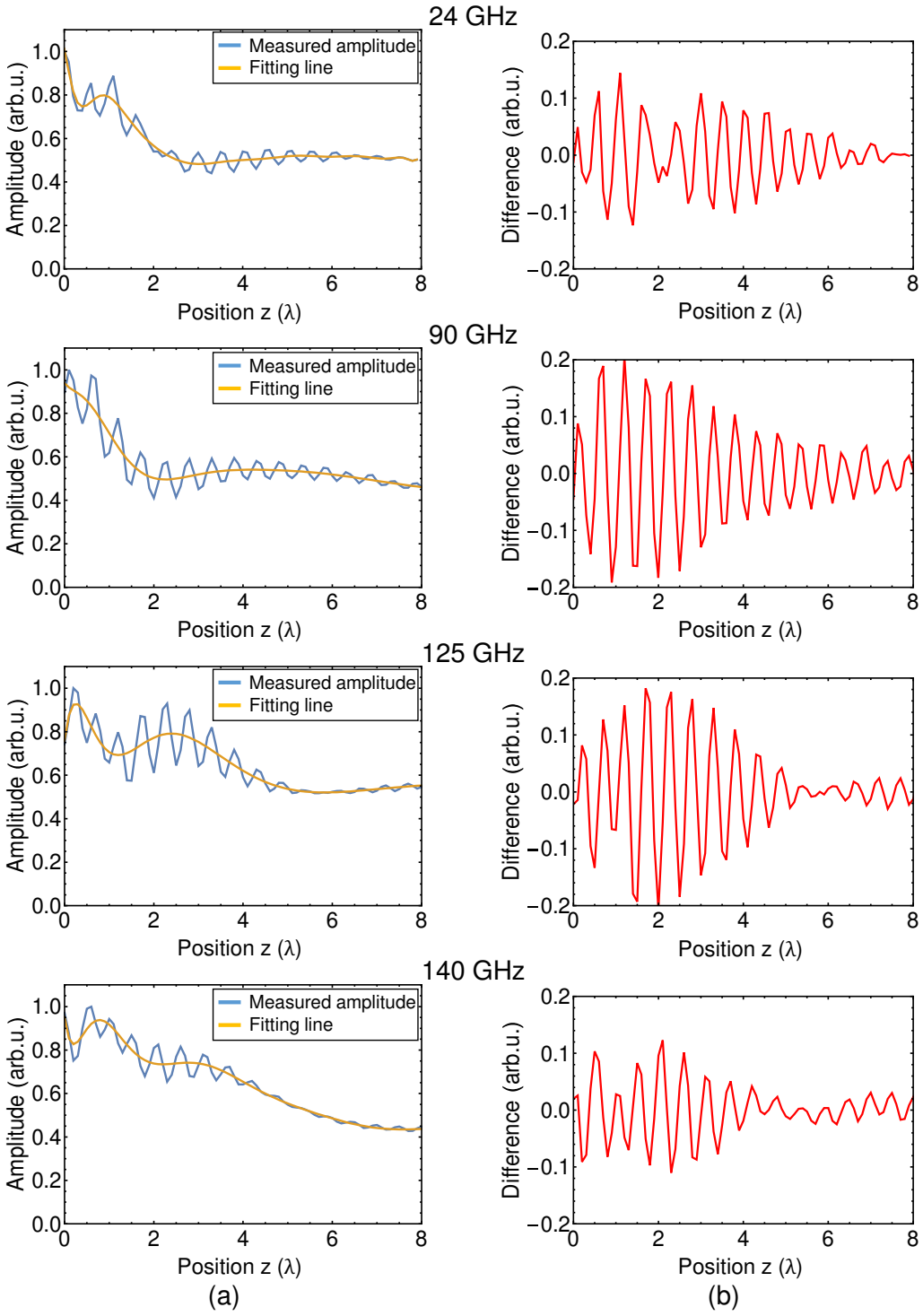

Figure 4.2.6: (a) Measured amplitude distribution along z-axis by DAST probe in acrylic holder at different frequencies from 24 GHz to 140 GHz, and (b) difference between it and fitting line.

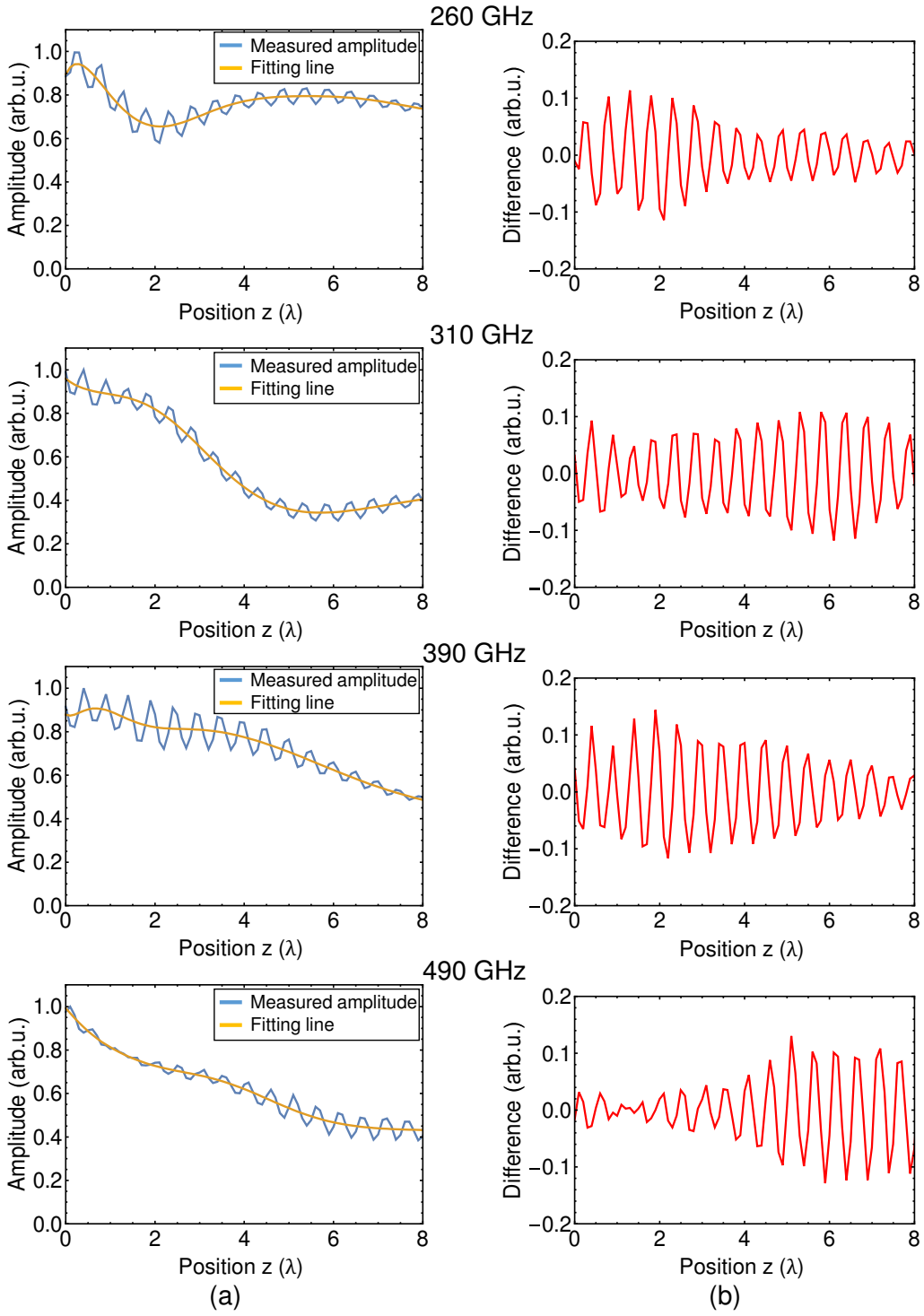

Figure 4.2.7: (a) Measured amplitude distribution along z-axis by DAST probe in acrylic holder at different frequencies from 260 GHz to 490 GHz, and (b) difference between it and fitting line.

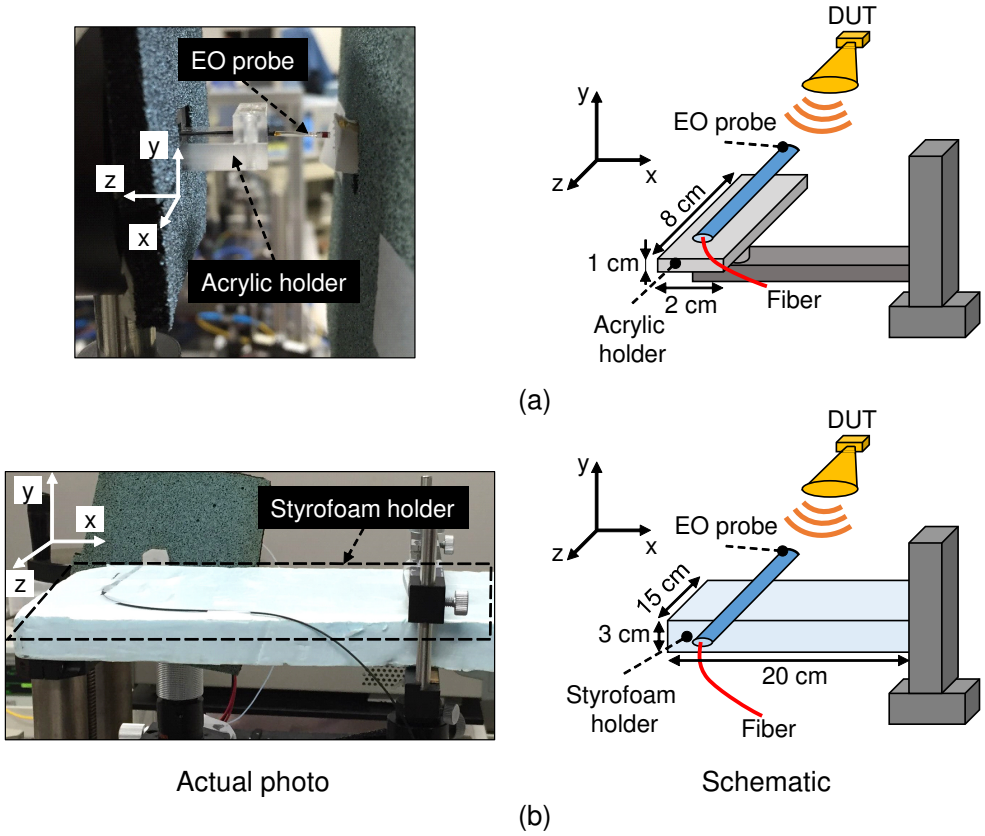

Figure 4.2.8: Experimental configurations and simplified schematics with (a) acrylic holder and (b) styrofoam holder.

for mechanical protection and placed on the styrofoam holder. The experimental measured amplitude distribution along z-axis and its fitting line at F-band frequencies are shown in Fig. 4.2.9(a). The difference between them at each frequency is shown in Fig. 4.2.9(b). The reduction in the standing wave can clearly observed in those experimental results in comparison with the results for the acrylic holder in Fig. 4.2.6. The quantitative evaluation of the peak-to-peak deviation *Dev* and the standard deviation of the differences are summarized in Table 4.2.2. In particular, *Dev* decreases to 59%, 54%, and 60% at frequencies of 90 GHz, 125 GHz, and 140 GHz, respectively, in comparison with the acrylic holder. The standard deviation of the difference also decreases to 40%, 39%, and 56% at frequencies of 90 GHz, 125 GHz, and 140 GHz, respectively. A reduction in the invasiveness of approximately 8 dB was obtained. This indicates the superior low E-field invasiveness of the styrofoam holder compared to the conventional acrylic holder.

Figure 4.2.10 shows the experimentally visualized amplitude distribution from the horn antenna in the E-plane at 125 GHz by the DAST probe placed in acrylic

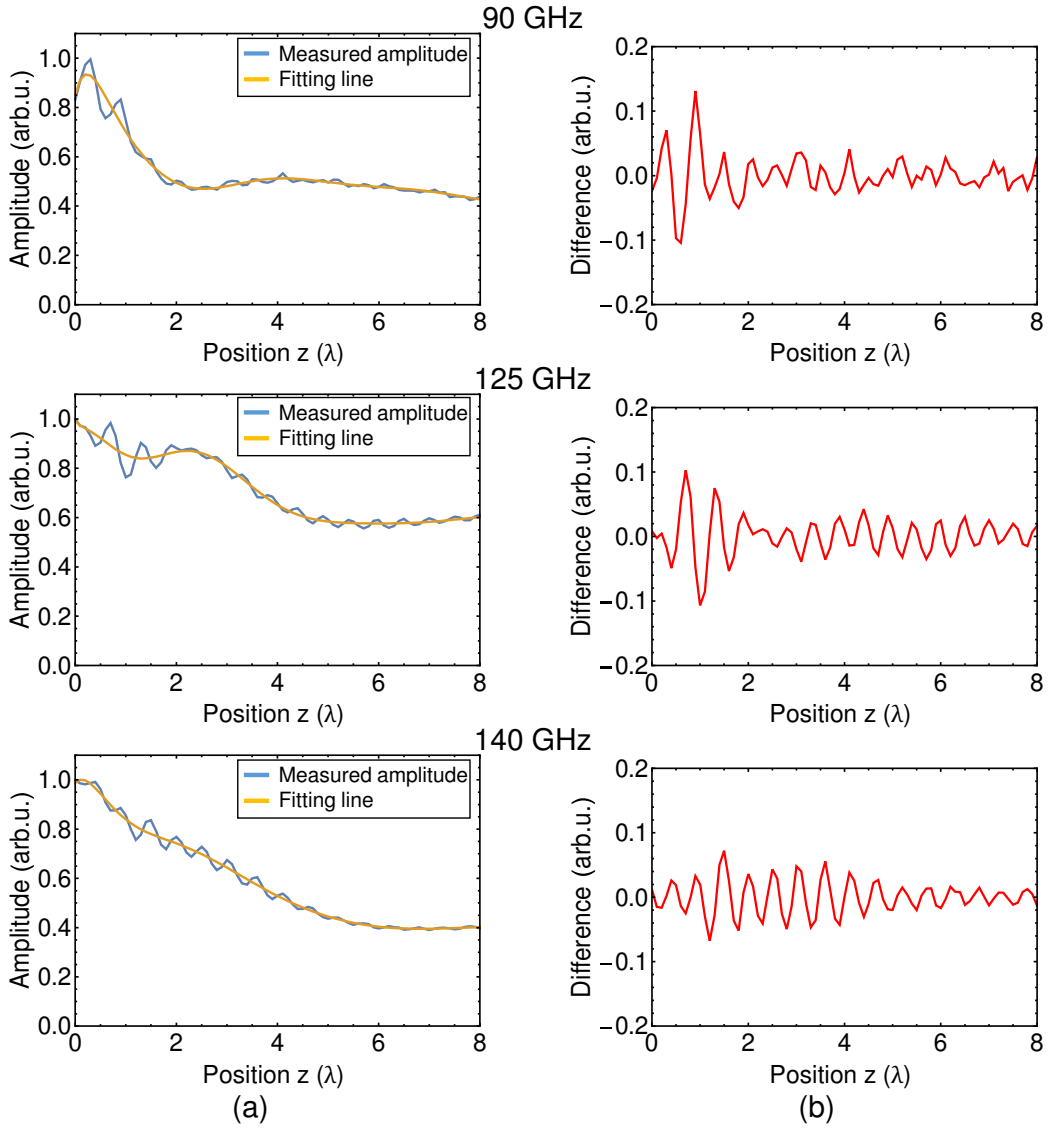

Figure 4.2.9: (a) Measured amplitude distribution along z-axis by DAST probe in styrofoam holder at different frequencies from 90 GHz to 140 GHz, and (b) difference between it and fitting line.

Table 4.2.2: Experimental peak-to-peak deviations and the standard deviation of the differences between amplitude distribution and its fitting line with styrofoam holder.

Frequency (GHz)	90	125	140
Dev (arb. u.)	0.118	0.105	0.070
Std (arb. u.)	0.026	0.024	0.020

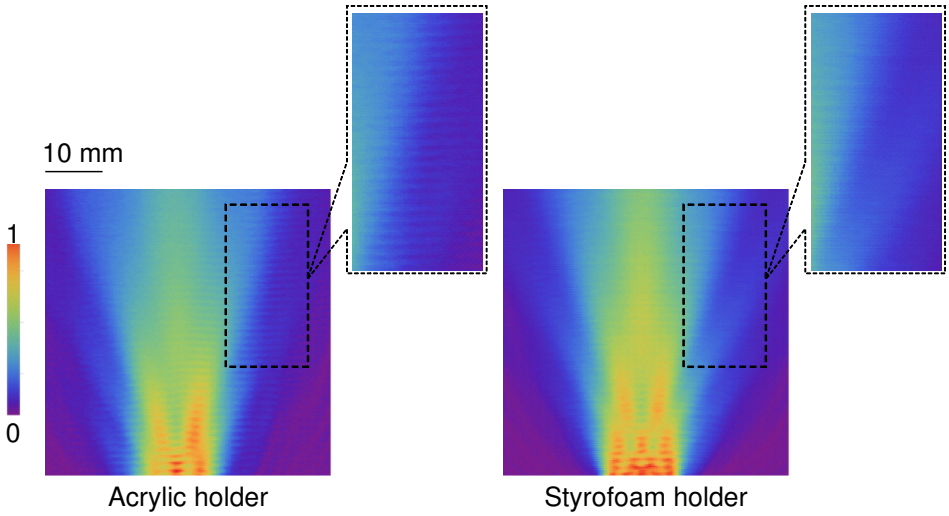

Figure 4.2.10: Experimentally visualized amplitude distribution from the horn antenna in E-plane at 125 GHz by two holders.

and styrofoam holders. The standing waves shown in the dashed boxes clearly indicate the degradation of this effect when using the styrofoam holder.

4.3 Issue of unwanted phase front appearing in amplitude images

4.3.1 Problem and its origin

We faced an issue of unwanted phase front distribution appearing in the experimental amplitude images, as shown in the raw data of Fig. 4.3.1 and Fig. 4.3.2(a) when characterizing THz devices with the EO detection system. The characterized devices were a metal hole array (MHA) (Fig. 4.3.1) and Terajet (4.3.2). The details of the introduction and characterization of these devices are described in Chapter 5. This issue occurred occasionally in the experiment, but not every time, when using the EO detection system. Therefore, it is a significant problem. In this section, we clarify the origin of this issue and propose two solutions by a signal processing method and by reducing the ground group effect based on hardware improvement.

Figure 4.3.3 shows the amplitude and phase distributions with the MHA at the center line in the E-plane (z-axis), the dashed-line in Fig. 4.3.1, before and after

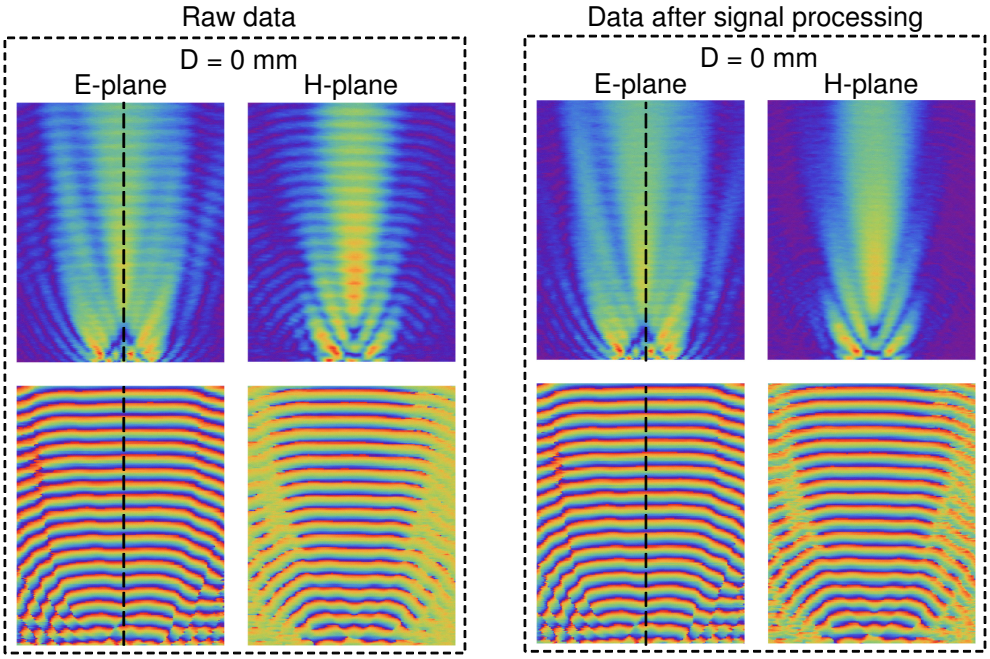

Figure 4.3.1: Issue of unwanted phase front appearing in the amplitude images of MHA and the solution by signal processing method.

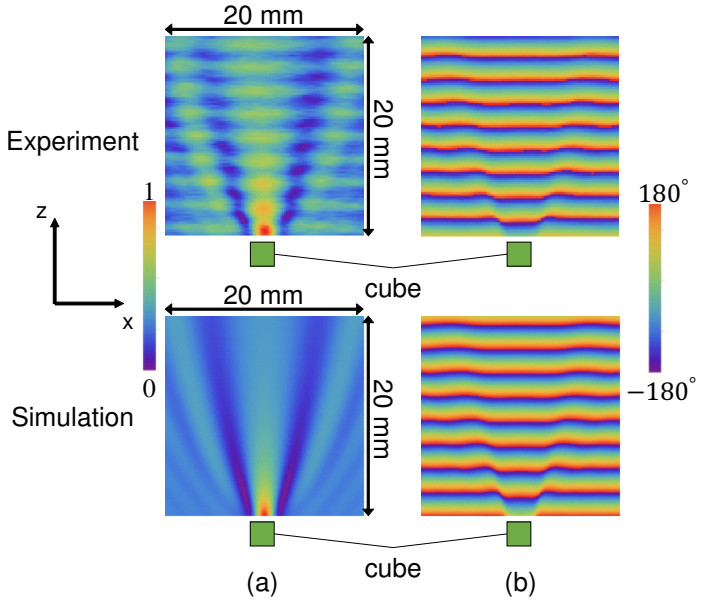

Figure 4.3.2: Issue of unwanted phase front distribution appearing in the amplitude images of Terajet-generating device with (a) amplitude and (b) phase distributions.

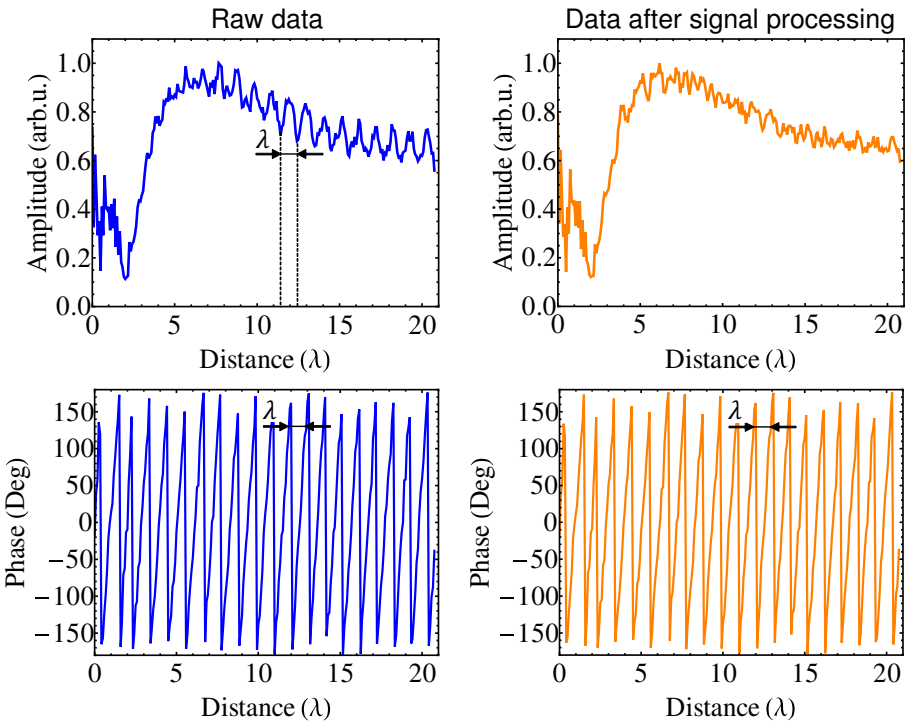

Figure 4.3.3: Amplitude and phase distributions at the center of the E-plane before and after signal processing in Fig. 4.3.1.

signal processing. In the raw data of Fig. 4.3.3, we can see the periodic deviation in the amplitude increasing from the position $z = 5\lambda$ to $z = 21\lambda$. The period of this deviation in the amplitude is equal to a wavelength or the period of the phase distribution along the z-axis. This issue can be probably explained by the interference between the actual signal and the unwanted leaking signal in the lock-in detection of the EO measurement system. We remark that the leaking signal can cause significant error, especially in the near-field measurement, as discussed elsewhere [4.14].

Figure 4.3.4 shows the phasor diagrams in lock-in detection of the ideal case and leaking case. In the ideal case, the measured amplitude A_M and measured phase ϕ_M are equal to the actual amplitude A and phase ϕ, depicted as a blue vector. Thus, there is no mutual effect of the phase distribution on the amplitude distribution and vice versa. However, in the leaking case, apart from the actual amplitude A and phase ϕ, there is an unwanted leaking signal represented by the orange dotted-vector, which has the leaking amplitude A_L and phase δ. In this condition, the measured vector (green arrow), which has the amplitude A_M and

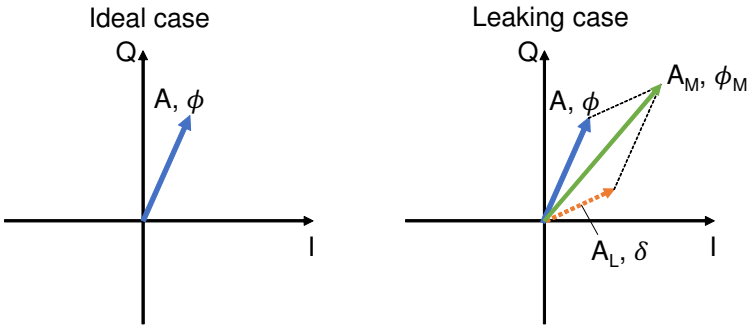

Figure 4.3.4: Phasor diagram of detected signal in lock-in detection.

measured phase ϕ_M, is the summation of the actual vector (blue arrow) and leaking vector (orange dotted-arrow), and can be expressed as:

$$\begin{aligned} &A_M \sin(\omega_L t + \phi_M) = A \sin(\omega_L t + \phi) \ + \ A_L \sin(\omega_L t + \delta) \\ &\Rightarrow \begin{cases} A_M = \sqrt{A^2 + A_L^2 + 2A\,A_L \cos\phi_{dif}} \\ \phi_M = \arctan \dfrac{A_L \sin\phi_{dif}}{A + A_L \cos\phi_{dif}} \end{cases} \end{aligned} \tag{4.3.1}$$

where ω_L and $\phi_{dif} = \delta - \phi$ are the angular frequency of the lock-in frequency and the phase difference between the leaking phase and the actual phase, respectively. When the EO probe is scanned for the visualization, the actual amplitude and phase have a spatial variation, but the variation of the A_L and δ are spatially independent. This leads to the unwanted phase front distribution appearing in the amplitude images, because the A_M contains both the A and ϕ, as in equation (4.3.1).

The origin of the issue of the unwanted phase front appearing in the amplitude images was theoretically explained by a leaking signal above. Next, the experimental evidence of this origin is described. Figure 4.3.5 (a) shows the normalized amplitude distribution to its maximum value along the z-axis at the center (blue dots) and its exponential fitting line (green dots) of the experimentally visualized results in Fig. 4.3.2. The function of fitting line is $a_1\ e^{-(a_2 z)} + a_3$, where the coefficients $a_1 = 0.523$, $a_2 = 0.044$, and $a_3 = 0.467$, were found using the software Mathematica (Wolfram Research). Figure 4.3.5(b) shows the difference between the amplitude distribution and fitting line in Fig. 4.3.5(a). The average peak deviation was approximately 0.15 or 15%.

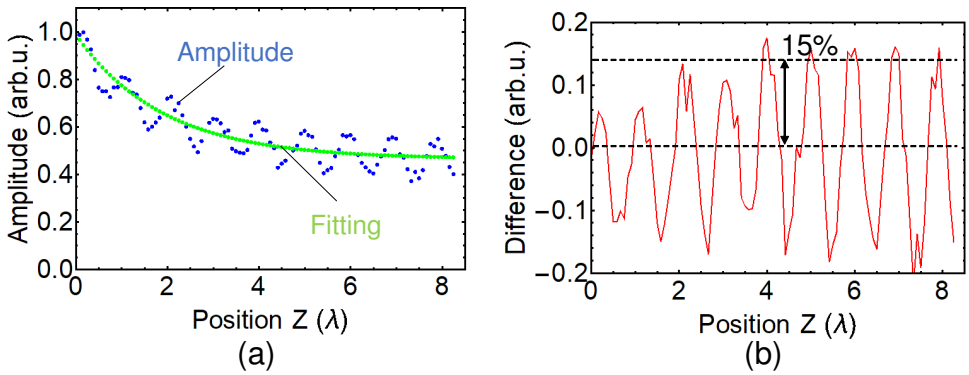

Figure 4.3.5: (a) Amplitude distribution in the center line along z-axis and the fitting line in Fig. 4.3.2; and (b) its difference.

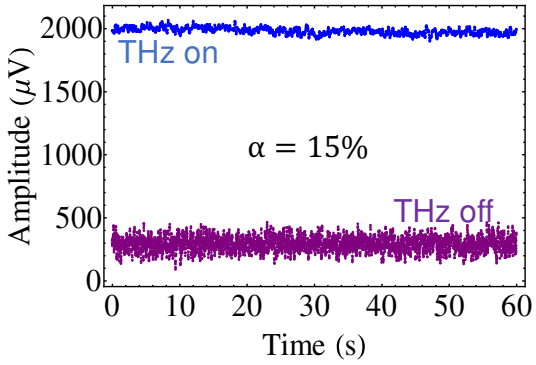

Figure 4.3.6: Detected amplitude with and without THz wave.

Fig. 4.3.6 shows the detected amplitude without moving the EO probe for 60 s with (blue dots) and without THz wave (purple dots). The leaking signal is defined as the detected signal without the THz wave. The leaking ratio can be calculated as $\alpha = \dfrac{A_{\text{off}}}{A_{\text{on}}}$, where A_{off} and A_{on} are the average of the detected amplitude for 60 s when the THz radiation is turned off and turned on, respectively. In Fig. 4.3.6, $A_{\text{on}} = 1987$ μV, $A_{\text{off}} = 297$ μV, and the leaking ratio was $\alpha = 15\%$, which is equivalent to the deviation in Fig. 4.3.5(b). Therefore, these experimental results indicate that the issue of the unwanted phase front distribution appearing in the amplitude images relates to the leaking signal in the detection process.

4.3.2 Solution by signal processing method

In order to solve this problem, a signal processing method to reconstruct the actual amplitude A and phase ϕ is proposed to obtain results, as shown in Fig. 4.3.1.

The measured in-phase I_{M} and quadrature Q_{M} components in the lock-in de-

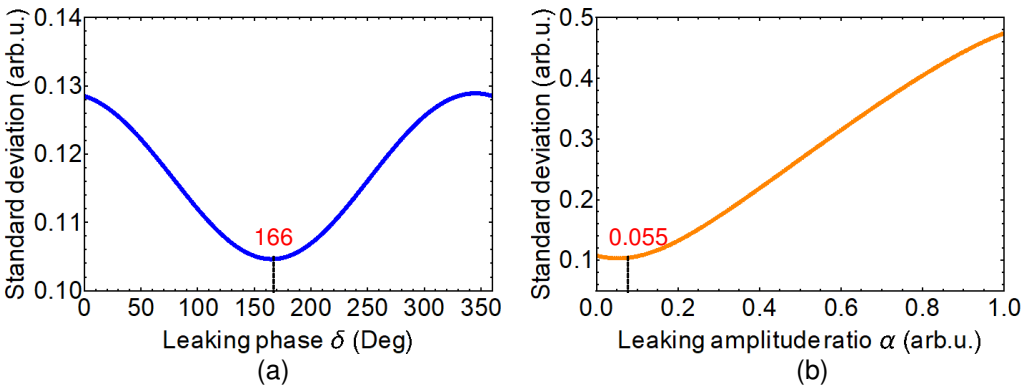

Figure 4.3.7: Relation between standard deviation of 1D amplitude distribution along z-axis and (a) leaking phase, and (b) leaking amplitude ratio.

tection in the leaking case are the summation of the actual and leaking in-phase components (I and I_{L}), and the actual and leaking quadrature components (Q and Q_{L}), as follows:

$$\begin{cases} I_{\mathrm{M}} = I + I_{\mathrm{L}} \\ Q_{\mathrm{M}} = Q + Q_{\mathrm{L}} \end{cases} \Rightarrow \begin{cases} \mathrm{A_M} \sin\phi_{\mathrm{M}} = \mathrm{A} \sin\phi + \mathrm{A_L} \sin\delta \\ \mathrm{A_M} \cos\phi_{\mathrm{M}} = \mathrm{A} \cos\phi + \mathrm{A_L} \cos\delta \end{cases}$$
$$\Rightarrow \begin{cases} \mathrm{A} \sin\phi = \mathrm{A_M} \sin\phi_{\mathrm{M}} - \alpha\, \mathrm{A_{maxM}} \sin\delta \\ \mathrm{A} \cos\phi = \mathrm{A_M} \cos\phi_{\mathrm{M}} - \alpha\, \mathrm{A_{maxM}} \cos\delta \end{cases} \tag{4.3.2}$$

where α and $\mathrm{A_{maxM}}$ are the ratio of the leaking amplitude and the maximum value of the measured 1D amplitude distribution in the z-axis, respectively.

We can find the optimal α and δ such that the effect of the mutual relation between the phase and the amplitude distributions is minimal, i.e., the standard deviation of the 1D amplitude distribution in the z-axis from $\mathrm{z} = 4.5\lambda$ to $\mathrm{z} = 21\lambda$ is minimal. Figures 4.3.7(a) and 4.3.7(b) show the relation between this standard deviation and the leaking phase δ, and the relation between it and the leaking amplitude ratio α, respectively, for the data depicted in Fig 4.3.3. We can obtain the optimal values of $\delta = 166°$ and $\alpha = 0.055$, as shown in Fig. 4.3.7. The actual 1D amplitude and phase distributions can be reconstructed from these δ and α values, to obtain the results as shown in Fig. 4.3.3, data after signal processing. The periodic deviation of the amplitude distribution, which is mutually related to the phase front distribution, is reduced significantly. This algorithm is employed for

each 1D measured data in the z-axis direction and clearer images can be obtained, as shown in Fig. 4.3.1, data after signal processing.

4.3.3 Solution by hardware improvement

The cause of the leaking signal was investigated by considering the detection module of the EO detection system, as shown in the dashed box in Fig. 4.3.8(a). The specific details of the detection module are presented in Fig. 4.3.8(b). A function generator (nF WF1946B) was used to generate a 500 kHz signal to the FS and to input In2 of the frequency extender (nF 5571) to down-convert the 500 kHz signal to 20 kHz, because the upper limitation of the lock-in frequency of the LIA (LI5640) is 100 kHz. The down-converted 20 kHz signal from output Out2 of the frequency extender is connected to the reference port of the LIA. The detected signal from the EO probe is converted to an electric signal at 500 kHz by a PD and inputted to In1 of the frequency extender. This signal is also down-converted to 20 kHz and inputted to the signal port of the LIA.

The effect of the lock-in frequency on the leaking issue and SNR is verified by changing the lock-in frequency from 10 kHz to 3.5 MHz. The gain of the TIA was set at 10^5V/A. From 10 kHz to 100 kHz, the frequency extender was not used, the reference and signal were connected directly to the LIA, as depicted in Fig. 4.3.8(c). In this experiment, the SNR and leaking ratio were calculated from the 1-min measurement without moving the EO probe.

Figure 4.3.9 shows the experimental results of the dependence of the detected SNR (blue dots) and leaking ratio (orange dots) on the lock-in frequency. At lock-in frequencies lower than 50 kHz, the SNR degraded significantly below 20 dB and the leaking ratio was dramatically larger than 0.5 or 50%. This is probably due to the pink noise and the lower limitation of approximately 10 kHz of the bias T, which is used to cut the DC component of the signal after the PD. At frequencies above 100 kHz, from 200 kHz to 1 MHz, in which the frequency extender was used, the SNR degrades by approximtely 3.5 dB and the leaking ratio increases by approximately 1.33 times from 0.03 (3%) to 0.04 (4%). At frequencies above 1 MHz, the leaking ratio significantly increases over 7%. This is probably due to the

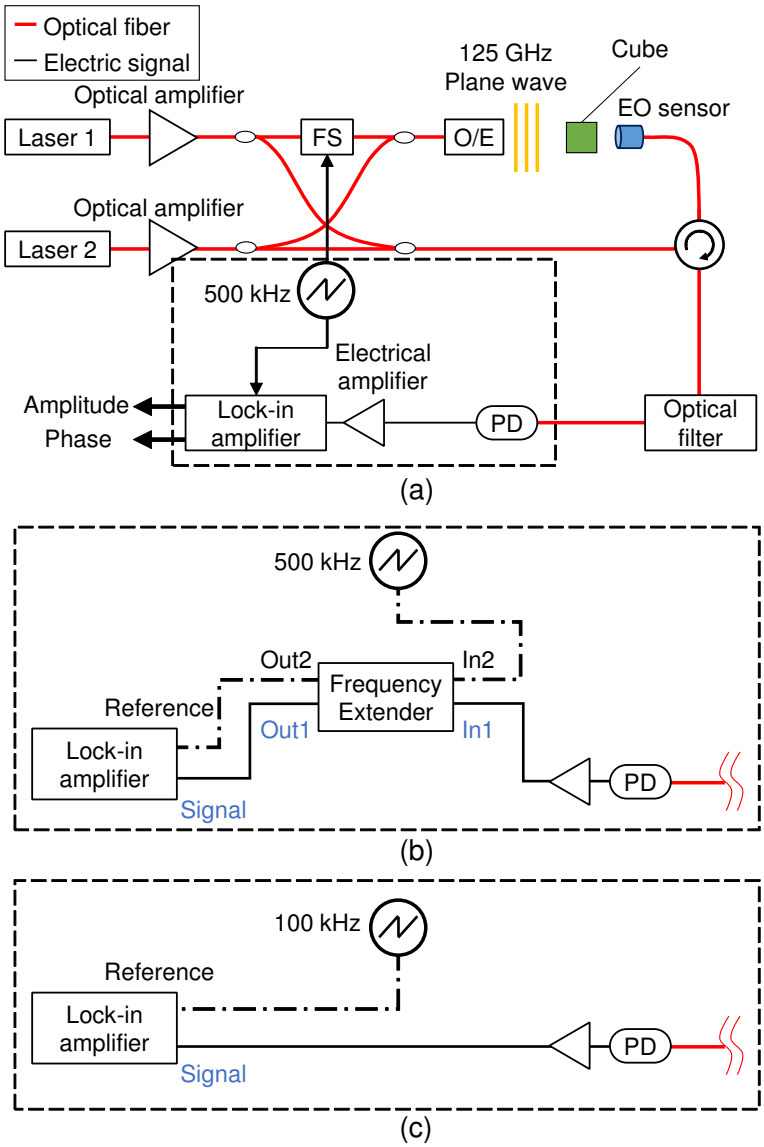

Figure 4.3.8: (a) Schematic of the EO detection system, (b) specific schematic of the detection module, and (c) optimized detection module.

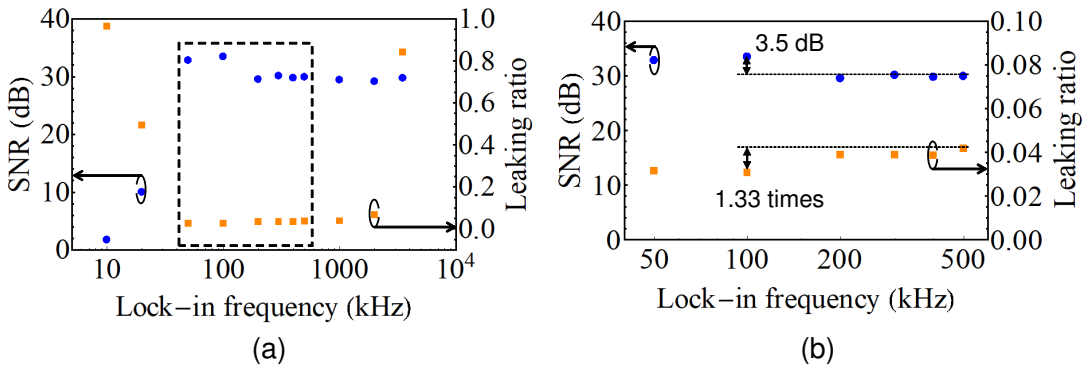

Figure 4.3.9: (a) Dependence of detected SNR and leaking ratio on lock-in frequency and (b) zoomed-in graph from 50 kHz to 500 kHz.

ground group effect and the strong radiation of the EM wave in the MHz-region. From these results, we found out that the optimal lock-in frequency was 100 kHz without the frequency extender (Fig. 4.3.8(c)). We remark that as coaxial cables, which are used to transmit electronic signal among devices, of as short lengths as possible are employed to reduce the ground group effect. In this condition, the A_{off} was 17.2 µV. This corresponds to a reduction in the leaking power of approximately 25 dB compared to that in Fig. 4.3.2.

4.4 Conclusion

In this chapter, we discussed and evaluated techniques to improve the performance of the EO detection system, including the sensitivity, the invasiveness, and the issue of the phase front appearing in the amplitude. First, a fiber-mounted one-cubic-millimeter DAST crystal was employed to enhance the sensitivity. The DAST was evaluated by comparing simultaneously with a ZnTe probe, one of the best inorganic EO materials. A SNR enhancement of more than 10 dB was obtained by the DAST probe with the minimum detectable E-field of approximately 0.28 V/m at both 125 GHz and 310 GHz. However, that obtained by the ZnTe probe was 1.01 V/m and 3.33 V/m at 125 GHz and 310 GHz, respectively. The stability and reproducibility of the measurement by the DAST probe was confirmed to be the same as those by the ZnTe probe. The THz E-field distribution from the J-band (220–325 GHz) horn antenna at 310 GHz with the output power of 28 µW, was successfully visualized by the DAST probe, whereas the results obtained by the ZnTe probe were unclear owing to the lack of sensitivity. The effect of the optical components on the SNR was experimentally evaluated. The obtained results indicate the excess laser noise significantly affects the SNR of the measurement. A noise reduction configuration based on differential detection was proposed and demonstrated to reduce the laser noise power by 3.6 dB.

Second, the invasiveness of the EO probe was studied by experiment and simulation. Theoretically, decreasing the dimensions of the EO probe or decreasing the THz frequency can reduce the invasiveness. Nevertheless, the experimental results

revealed that the acrylic holder of the EO probe caused a significant invasiveness compared to the EO probe itself. A styrofoam holder, which has a refractive index close to air, was employed to reduce the invasiveness by approximately 8 dB.

Finally, the origin of the issue of the unwanted phase front appearing in the amplitude images was theoretically investigated and experimentally verified. The interference between the actual signal and leaking signal is the reason. Two solutions based on a signal processing method and hardware improvement by reducing the ground group effect were proposed to solve the problem. A reduction in leaking noise power of approximately 25 dB was obtained.

References

[4.1] H. Togo, H. Uchida, H. Yokota, A. Izumi, T. Nagatsuma, and N. Fukasaku, *"Highly sensitive optical electric-field sensor using DAST and its applications,"* Proceedings of the European Microwave Association Special Issue on Microwave Photonics, **4**, pp. 294-301, 2008.

[4.2] C. Winnewisser, P. U. Jepsen, M. Schall, V. Schyja, and H. Helm, *"Electro-optic detection of THz radiation in $LiTaO_3$, $LiNbO_3$ and ZnTe,"* Appl. Phys. Lett., **70**, pp. 3069-3071, 1997.

[4.3] B. Cai, T. Hattori, H. H. Deng, K. Komatsu, C. Zawadzki, N. Keil, and T. Kaino, *"Refractive index control and grating fabrication of 4'-N,N-dimethylamino-N-methyl-4-stilbazolium tosylate crystal,"* Jpn. J. Appl. Phys., **40**, pp. L964-L966, 2001.

[4.4] M. Walther, K. Jensby, and S. R. Keiding, *"Far-infrared properties of DAST,"* Opt. Lett., **25**, pp. 911-913, 2000.

[4.5] F. Pan, G. Knopfle, C. Bosshard, S. Follonier, R. Spreiter, M. S. Wong, and P. Gunter, *"Electro- optic properties of the organic salt 4-N,N-dimethylamino-4'-N'-methyl-stilbazolium tosylate,"* Apply. Phys. Lett., **69**, 1996.

[4.6] S. Hisatake and T. Nagatsuma, *"Nonpolarimetric technique for homodyne-type electrooptic field detection,"* Appl. Phys. Express, **5**, p. 012701, 2012.

[4.7] M. Naftaly and R. Dudley, *"Methodologies for determining the dynamic ranges and signal-to-noise ratios of terahertz time-domain spectrometers,"* Opt. Lett., **34**, pp. 1213-1215, 2009.

[4.8] T. Matsukawa, H. Hoshina, A. Hoshikawa, C. Otani, and T. Ishigaki, *"Temperature dependence of crystal structure and THz absorption spectra of organic nonlinear optical stilbazolium material for high-output THz-wave generation,"* J. Infrared Milli. Terahz. Waves, **37**, pp. 540-550, 2016.

[4.9] R. T. Bailey, G. H. Bourhill, F. R. Cruickshank, D. Pugh, J. N. Sherwood, G. S. Simpson, and K. B. R. Varma, *"Linear electro- optic effect and temperature coefficient of birefringence in 4- nitroâĂŞ4'- methylbenzylidene aniline single crystals,"* J. Appl. Phys., **71**, pp. 2012-2014, 1992.

[4.10] M. Naftaly and R. E. Miles, *"Terahertz time-domain spectroscopy for material characterization,"* Proc. IEEE, **95**, pp. 1658-1665, 2007.

[4.11] A. J. Gatesman, J. Waldman, M. Ji, C. Musante, and S. Yngvesson, *"An anti-reflection coating for silicon optics at Terahertz frequencies,"* IEEE Microw. Guided Wave Lett., **10**, pp. 264-266, 2000.

[4.12] H. K. Raut, V. A. Ganesh, A. S. Nair, and S. Ramakrishna, *"Anti-reflective coatings: A critical, in-depth review,"* Energy Environ. Sci., **4**, pp. 3779-3804, 2011.

[4.13] H. A. Macleod, *"Thin-film optical filters,"* CRC Press, 4th edition, p. 130, 2010.

[4.14] A. C. Newell and G. Hindman, *"Techniques for reducing the effect of measurement errors in near-field antenna measurements,"* The 2nd European Conference on Antennas and Propagation (EuCAP), 2007.

Chapter 5

Device characterization by EO measurement

In this chapter, the characterization of THz devices based on the EO detection system is presented, including an antenna, a wavefront manipulating device, a spherical-wave generation device, and a near-field localization device. For each device, the motivation, the experimental results, and the impact of obtained results are discussed.

5.1 Antenna

5.1.1 Motivation

An antenna is a device used to transform the EM field guided in a waveguide to radiated EM waves in free space or vice versa. It is one of the most important components in any THz system, for applications such as wireless communication, nondestructive imaging, and spectroscopy, because the radiation direction of THz waves is determined by the antenna. Studies and research on antennas in the THz region for practical applications have attracted much interest. For example, the Cassegrain antenna was introduced for long-distance transmission over 800 m [5.1], and the plate-laminated waveguide slot array antenna was proposed for short-link transmission (several millimeters to 2.5 m) [5.2, 5.3]. The needs for broad-bandwidth antenna characterization are increasing in the THz region. In

particular, the identification of the 3-dB beamwidth and sidelobe positions of the far-field patterns plays an important role in antenna characterization, because they relate to the antenna gain and the directions of the radiation [5.4]. Both near-field and far-field radiation patterns need to be characterized.

Generally, in order to characterize the far-field patterns of an antenna, the far-field measurement based on electronic technique with a metallic probe is used. The electronic technique associated with the metallic probe and coaxial cables cannot be used for near-field measurement because they interfere with the EM field and cause EM disturbances that affect the accuracy of the characterization [5.5]. However, the EO measurement based on photonic techniques and optical fibers can offer minimal invasiveness and disturbance to the EM field, owing to the all-dielectric material probe [5.6, 5.7]. Moreover, the large detectable bandwidth makes the EO measurement a strong candidate to characterize antennas. The EO measurement was used to characterize the near-field patterns at 10 GHz [5.8] and 60 GHz [5.9]. The far-field patterns can also be measured in the far-field by the EO measurement at 60 GHz [5.9].

In higher-frequency regions such as the sub-THz and THz bands, the output power of the sources decreases owing to either saturation conditions or thermal effects [5.10–5.12]. An alternative method to characterize antenna far-field patterns is based on the near-field transformation [5.13, 5.14]. Not only the information of the amplitude distribution but also the accurate phase distribution in the near-field region is required. Owing to the capability to measure both amplitude and phase distributions as well as the negligible EM disturbance of the nonpolarimetric self-heterodyne EO detection system, the antenna can be characterized. In this section, the experimental characterization of an F-band (90–140 GHz) standard horn antenna based on EO near-field measurement, in which the probe was made from a ZnTe crystal mounted on an optical fiber, is discussed.

5.1.2 Near-to-far-field transformation technique

The antenna regions can be roughly divided into three regions: reactive near-field, radiating near-field, and far-field, as shown in Fig. 5.1.1. The far-field region

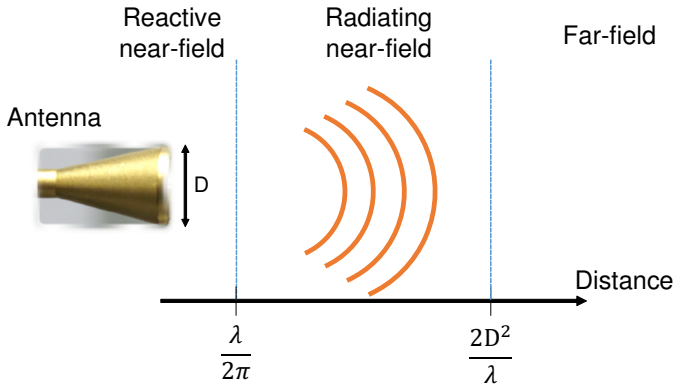

Figure 5.1.1: Definition of three regions surrounding an antenna.

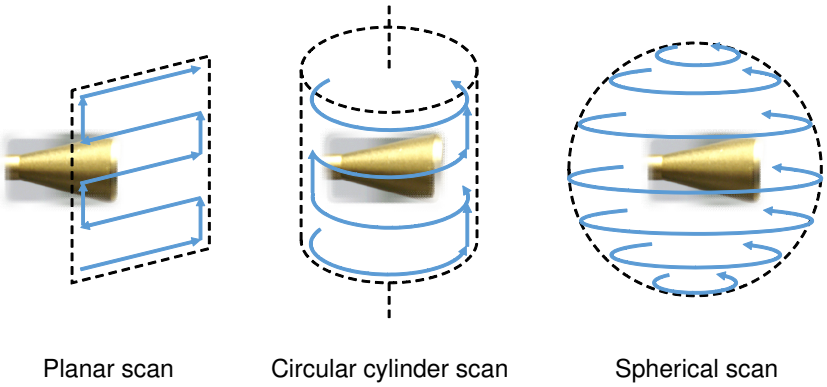

Figure 5.1.2: Near-field scanning methods.

is defined at a distance above $\frac{2D^2}{\lambda}$ from the antenna surface, also named the Fraunhofer distance [5.13], where D and λ are the largest dimension of the antenna aperture and the wavelength of the radiated EM wave in free space, respectively. The angular distribution of the radiated EM wave measured in the far-field region is essentially independent of the distances to the observation point. The near-field region includes reactive and radiating components. The reactive near-field is the region where the reactive component predominates. The strength of the reactive component decays rapidly with distance from the antenna. Commonly, the reactive region is within $\frac{\lambda}{2\pi}$ from the antenna surface. The radiating near-field region is located between $\frac{\lambda}{2\pi}$ and $\frac{2D^2}{\lambda}$. The radiating near-field region is used for the determination of far-field patterns from the near-field measurement. This technique can be named the near-to-far-field transformation technique.

The initial study of the near-to-far-field transformation technique was reported in the microwave region, in which the direct far-field measurement required a large

space, long acquisition time, and a bulky anechoic chamber [5.13]. For example, a 1.22-m paraboloid antenna operated at 5.45 GHz requires a far-field measurement beyond 54 m. In the THz region, the direct far-field measurement is also difficult owing to the low emission power or low signal-to-noise ratio (SNR). Therefore, the near-to-far-field transformation technique is sufficient for the antenna characterization in the THz region.

Generally, three types of near-field scanning methods can be employed: planar, circular cylinder, and spherical types, as shown in Fig 5.1.2. The planar scan is generally preferred for characterizing a high-gain antenna [5.13], owing to its simplicity and fast measurement. In this work, the planar scan was employed to measure the near-field E-field distribution from the horn antenna, because this is a high-gain antenna, which is preferred for wireless communication applications.

The E-field distribution $E(x, y, z)$, in which z-axis is the propagation direction, can be expressed as:

$$E(x, y, z) = A(x, y, z)\, e^{j\varphi(x,y,z)}, \tag{5.1.1}$$

where $A(x, y, z)$ and $\varphi(x, y, z)$ are the measured amplitude and phase distributions in Cartesian coordinates in the near-field, respectively. The spatial frequency spectrum for planar scan can be expressed as:

$$F(k_x, k_y) = \frac{1}{2\pi} \int_{-\infty}^{\infty} \int_{-\infty}^{\infty} E(x, y, z_0)\, e^{-jk_x x}\, e^{-jk_y y}\, dxdy, \tag{5.1.2}$$

$$\begin{aligned} k_x &= k \sin\theta \cos\phi, \\ k_y &= k \sin\theta \sin\phi \end{aligned} \tag{5.1.3}$$

where $E(x, y, z_0)$, k_x, and k_y are the E-field distribution over a scanning surface at $z = z_0$ and the wavenumber components in the x- and y-directions, respectively. θ and ϕ are the polar and azimuthal angles in the spherical coordinate representation, respectively. $k = \dfrac{2\pi}{\lambda}$ is the wavenumber.

The spatial frequency spectrum $F(k_x, k_y)$ can be converted to an angular spectrum $F(\theta, \phi)$ through equation (5.1.3), and then the far-field radiation patterns can be obtained. In the experiment, the distance between the antenna under test

Table 5.1.1: Boundary of near- and far-field regions of characterized antenna.

D (mm)	Frequency (GHz)	$\frac{\lambda}{2\pi}$ (mm)	$\frac{2D^2}{\lambda}$ (mm)
13	90∼140	0.5∼0.3	101∼158

(AUT) and the EO probe was $z_0 = 1.0$ mm ($\frac{\lambda}{2\pi} < z_0 < \frac{2D^2}{\lambda}$), which was located in the radiating near-field region (Table 5.1.1). When a conventional horn antenna or waveguide probe are used, a complex antenna compensation is required. Even though it has been suggested [5.15] that no compensation is needed when using a minimally invasive EO probe, we carefully measured the EO-probe patterns for the probe compensation.

5.1.3 F-band horn antenna characterization

Figures 5.1.3(a) and 5.1.3(b) show the experimental configuration and its side view, respectively. The E-plane was parallel to the x-axis and the H-plane was parallel to the y-axis. The EO probe was placed at a distance of approximately 1 mm from the horn antenna surface. An absorber was used to reduce unwanted E-field disturbance from the holder of the EO probe. The experimentally verified absorption rate of the absorber was above 20 dB.

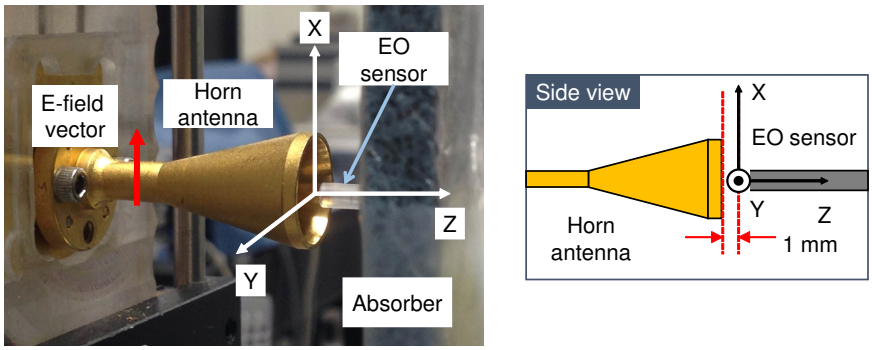

Figure 5.1.3: (a) Experimental configuration and (b) its side view.

Figure 5.1.4 depicts the experimentally visualized THz wave distribution in the XY-plane from the horn antenna at 125 GHz. The amplitude image was normalized to the maximum value. The initial phase offset was set to zero at the center

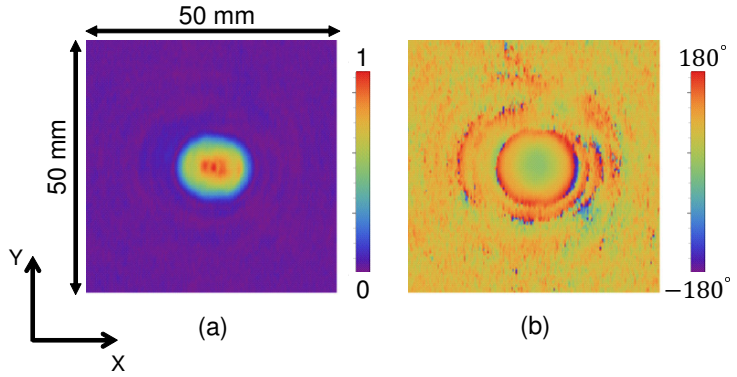

Figure 5.1.4: Experimentally visualized (a) amplitude and (b) phase distribution from the horn antenna in XY-plane at 125 GHz.

of the horn antenna. The measured area was 50 mm × 50 mm, corresponding to 250 × 250 data points. The sampling interval was $\Delta x = \Delta y = 0.2$ mm. The half-wavelength of the THz frequency in the F-band (90–140 GHz) is $\frac{\lambda}{2} = 1.07$ mm ~ 1.67 mm. Therefore, the sampling interval in the measurement satisfied the Nyquist criterion in all frequencies within the F-band ($\Delta x < \frac{\lambda}{2}, \Delta y < \frac{\lambda}{2}$). The time constant was set as 30 ms.

The THz power, which was measured by a PM4 power meter, emitted from the horn antenna was 1.3 mW (1.13 dBm) at 125 GHz. The optical power of the LO probe beam fed to the EO probe was 19 mW (12 dBm). The SNR is defined as the ratio of the signal power to the noise power. The measured signal at time t is considered as $h(t) = S + n(t)$, where S and $n(t)$ are the signal and white noise, respectively. In this condition, the SNR can be calculated as [5.16]:

$$\text{SNR} = 20 \log_{10}(\frac{\mu}{\sigma}), \tag{5.1.4}$$

where $\mu = \frac{1}{T}\int_0^T A(t)\,dt$ and σ are the mean value and the standard deviation, respectively, of the measured amplitude signal for $T = 1$ min without moving the EO probe, and $A(t)$ is the measured amplitude at time t. The maximum SNR of the amplitude measurement obtained at the center of the horn antenna surface was approximately 40 dB.

The planar scan only requires the E-field component, and thus one measurement by one probe is sufficient for the near-to-far-field transform technique [5.13]. In contrast, the spherical scan requires both the electric and magnetic fields, and

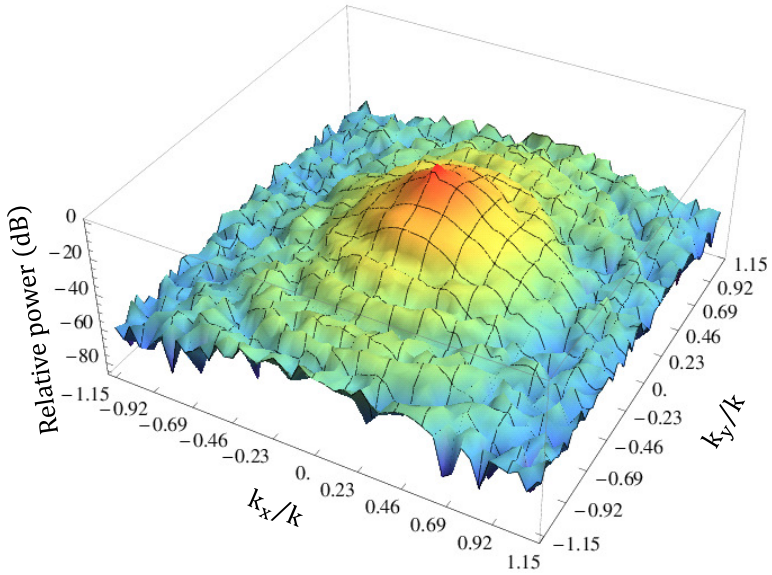

Figure 5.1.5: Experimentally measured 3D representation of radiation pattern of the horn antenna at 125 GHz.

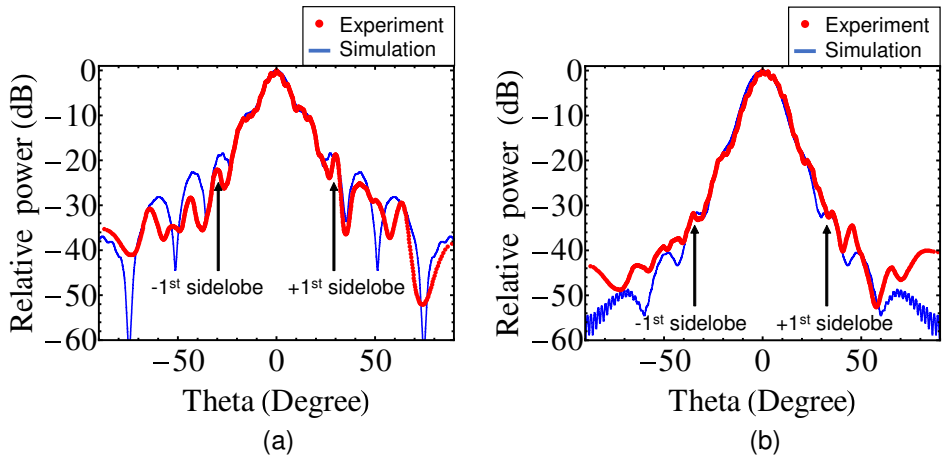

Figure 5.1.6: Radiation patterns in (a) E-plane and (b) H-plane at 125 GHz without probe compensation.

thus two measurements by two probes are probably necessary [5.13, 5.14]. In addition, some AUTs might require two measurements by two probes to obtain the horizontal and vertical polarization of the E-field. However, the horn antenna has one major linear polarization (parallel to the x-axis). Therefore, the far-field patterns were estimated from one measurement by one probe in the experiment. It is probable that the far-field patterns calculated from two measurements consisting of both polarizations would provide similar or better results.

The E-field value at each data point was calculated by equation (5.1.1). Then, the spatial frequency spectrum was calculated through a 2D Fourier transform,

as in equation (5.1.2). Figure 5.1.5 shows the obtained 3D representation of the radiation pattern. The cross-sections in the E- and the H-planes are shown in Fig. 5.1.6. The red and blue lines present the experimental and simulated results, respectively. The experimental discrete data of the radiation patterns in the E- and H-planes can be interpolated by the 2D zero padding method of the measured near-field before performing the transformation, or the summation of the sinc function at each data point [5.17], because the sampling interval in the measurement satisfied the Nyquist criterion for the sampling theorem.

In Fig. 5.1.6, the main lobes of the estimated patterns in the experiment agree well with those in the simulation for both the E- and H-planes. The experimental 3-dB beamwidths, which are calculated for the average of five measurements, are 11.2° and 12.4° in the E- and H-planes, respectively, whereas those in the simulated results are 11.5° and 13.6°, respectively. The differences between the experiment and the simulation in the 3-dB beamwidths are 0.3° and 1.2° for the E- and H-planes, respectively.

The positions of the first sidelobes in the experiment are also similar to those in the simulation. As shown in Fig. 5.1.6, the first sidelobes of the E-plane are located at $-28.4°$ and $+27.9°$ in the experiment, and at $\pm 27.3°$ in the simulation. In the H-plane, they are respectively located at $-32.5°$ and $+34.6°$ in the experiment, and at $\pm 33.9°$ in the simulation. The average differences in the positions between the experimental and simulated results are 0.9° and 1.1° in the E- and H-planes, respectively.

The finite integration technique (FIT) was used for the simulation. The dimensions of the horn antenna model in the simulation were the same as that in the experiment. The material of the antenna model is perfect electric conductor with a thickness of 0 mm. The boundary condition in the simulation was the perfect matching layer (PML) boundary. The mesh density was set at 15 lines per wavelength and the number of cells was optimized by the optimizing-mesh method, perfect boundary approximation (PBA) in the simulator, CST Microwave Studio. In the simulation, the complicated constructions at back side of the horn antenna, such as holders, were not added. That is perhaps one of possible reasons

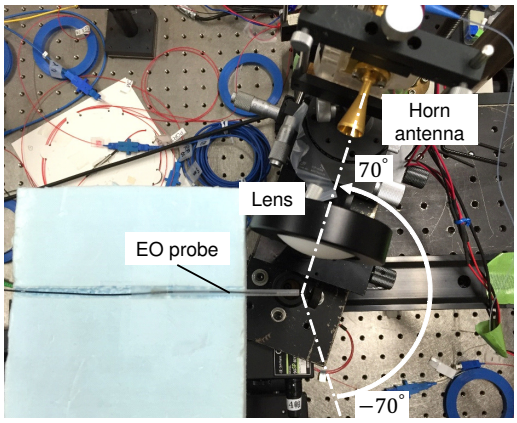

Figure 5.1.7: Configuration to verify angular characteristic of EO probe.

for the slight difference in intensity value of the sidelobes between experiment and simulation. In the near-field measurement results, the absence of minor E-field polarization in the y-axis is another possible reason for this difference.

The probe compensation is usually needed for the estimation of radiation patterns of the AUT [5.18]. Therefore, we characterize the angular characteristics of the ZnTe probe by experimental configuration in Fig. 5.1.7. The collimated beam by the F-band horn antenna and a lens was rotated around the head of the EO probe using an automated rotation stage from $-70°$ to $70°$ with the angular interval of $0.5°$. The distance between the lens and the EO probe was 4.5 cm.

Figures 5.1.8 and 5.1.9 show the measured angular characteristics of the ZnTe probe in E- and H-planes, respectively. In Figs. 5.1.8(a) and 5.1.9(a), the intensity power (orange dots) and noise (gray dots) at each angle were calculated from the mean value of the measured amplitude and standard deviation over 6 s with the lock-in time constant of 30 ms. The intensity and noise were normalized to the maximum value of the intensity. The SNRs at each angle were also calculated from the measured amplitude over 6 s by equation (5.1.4). The standard error was calculated from three distinct measurements and a Student's t coefficient of 2.92, corresponding to a 90% two-sided confidence interval. The specific calculation of the standard error is shown later. The ZnTe probe shows isotropic patterns in both the E- and H-planes. The 3-dB beamwidths were approximately $90°$ from $-55°$ to $35°$ and $100°$ from $-50°$ to $50°$ in the E- and H-planes, respectively.

We can compensate the radiation patterns of the AUT from the measured

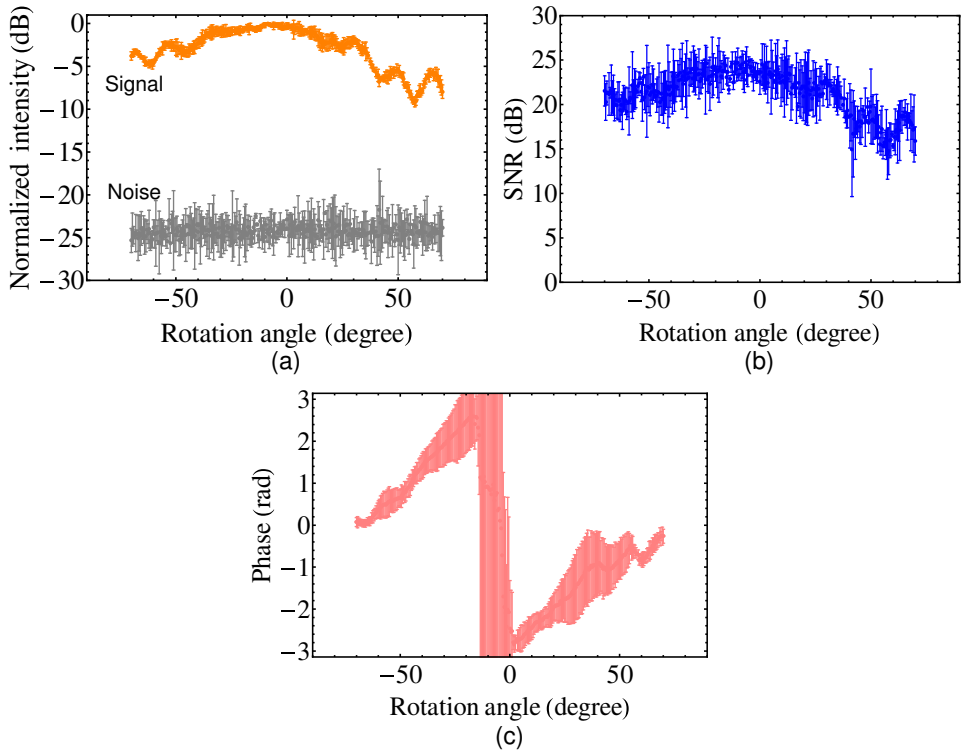

Figure 5.1.8: Angular characteristics of ZnTe probe in E-plane (a) detected power, (b) SNR, and (c) phase.

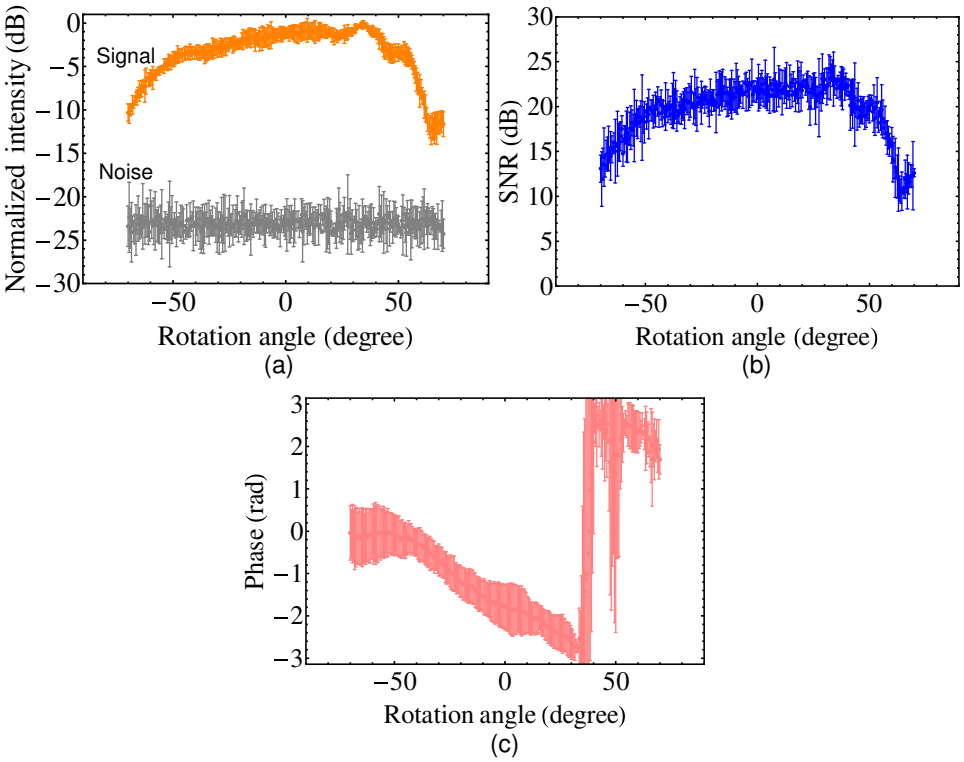

Figure 5.1.9: Angular characteristics of ZnTe probe in H-plane (a) detected power, (b) SNR, and (c) phase.

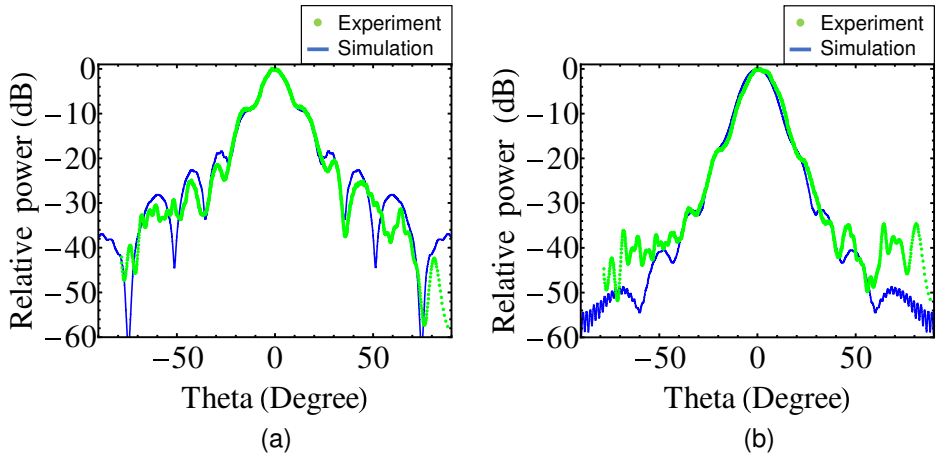

Figure 5.1.10: Radiation patterns in the (a) E-plane and (b) H-plane at 125 GHz with probe compensation.

angular characteristics of the EO probe as [5.18, 5.19]:

$$E_{\mathrm{Eaut}}(\theta) = \cos\theta \, \frac{E_{\mathrm{Em}}(\theta)}{P_{\mathrm{E}}(-\theta)},$$
$$E_{\mathrm{Haut}}(\theta) = \cos\theta \, \frac{H_{\mathrm{Hm}}(\theta)}{P_{\mathrm{H}}(-\theta)}, \tag{5.1.5}$$

where $E_{\mathrm{Eaut}}(\theta)$ and $E_{\mathrm{Haut}}(\theta)$ are the compensated radiation patterns of the AUT in the E- and H-planes, respectively. $E_{\mathrm{Em}}(\theta)$ and $E_{\mathrm{Hm}}(\theta)$ are the measured radiation patterns of the AUT before probe compensation in the E- and H-planes, respectively. $P_{\mathrm{E}}(-\theta)$ and $P_{\mathrm{H}}(-\theta)$ are the angular characteristics of the EO probe in the E- and H-planes, respectively. Note that all of the radiation patterns are in the complex E-field representation $A(\theta)\, e^{j\,\varphi(\theta)}$.

Figure 5.1.10 shows the obtained radiation patterns of the F-band horn antenna at 125 GHz by the near-to-far-field transformation technique with the probe compensation in the E- and H-planes. The green dots and blue solid line denote the experimentally compensated radiation patterns and simulated results, respectively. The experimental results are in a good agreement with the simulated results for both the 3-dB beamwidths and the position of the first sidelobes. The compensated results in Fig. 5.1.10 are also similar to the obtained results before the probe compensation Fig. 5.1.6, owing to the isotropic characteristic of the EO probe.

We measured the E-field distribution from the horn antenna at the same scanning plane within the full F-band (90–140 GHz), with a frequency interval of 10 GHz. The frequency of the THz wave can be tuned by changing laser frequencies,

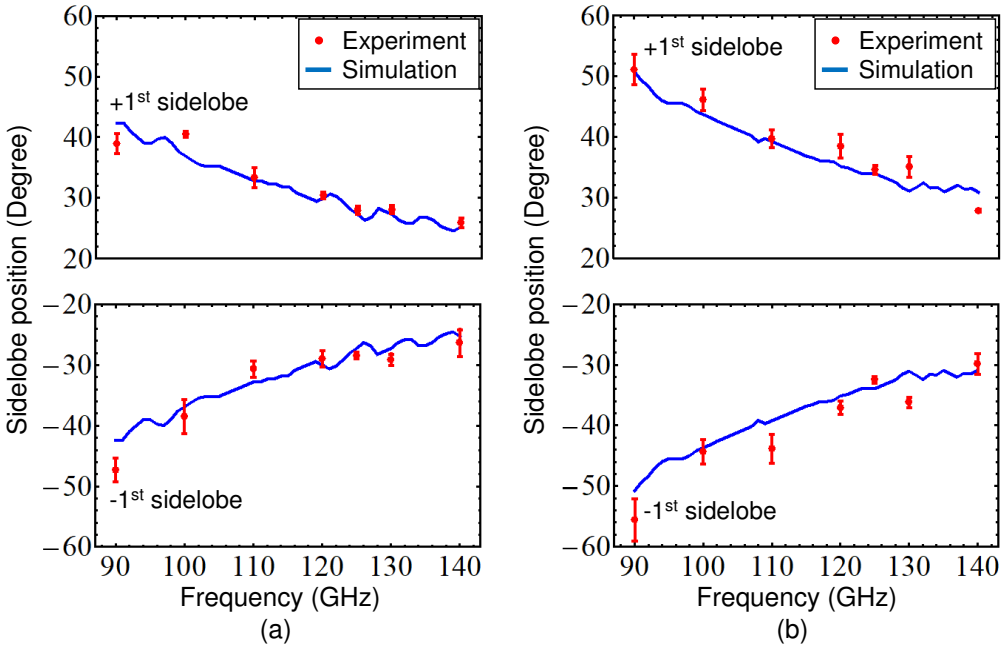

Figure 5.1.11: Frequency characteristics of the positions of the first sidelobes of the horn antenna in (a) E-plane and (b) H-plane.

owing to the free-running lasers used in the experiment. The probe compensation process was reduced in this experiment.

Figures 5.1.11(a) and 5.1.11(b) show the frequency characteristics of the first sidelobe positions in the E- and H- planes, respectively. The red dots and the blue solid line represent the experimental and simulated results, respectively. The simulated results were estimated from the far-field patterns of the full F-band with a 1-GHz step. The measured standard error at each frequency in Figs. 5.1.11, 5.1.12, and 5.1.13 is calculated from five measurements and expressed as follows:

$$\begin{aligned} \sigma_{err} &= t_{a,n-1}\frac{\sigma}{\sqrt{n}}, \\ \sigma &= \sqrt{\frac{\sum_{i=1}^{n}(x_i-\mu)^2}{n-1}}, \end{aligned} \tag{5.1.6}$$

where σ_{err}, $t_{a,n-1}$, σ, and μ are the standard error, the Student's t distribution at $a\,\%$ confidence interval value, standard deviation, and the average of n measurements, respectively. $n = 5$ for each frequency and $t = 1.533$, corresponding to a one-sided confidence interval of 90%.

The simulated first sidelobe positions at 90 GHz are $\pm 42.4°$ and $\pm 50.8°$ in the E- and H-planes, respectively. At 140 GHz, they are respectively $\pm 25.3°$ and $\pm 30.9°$.

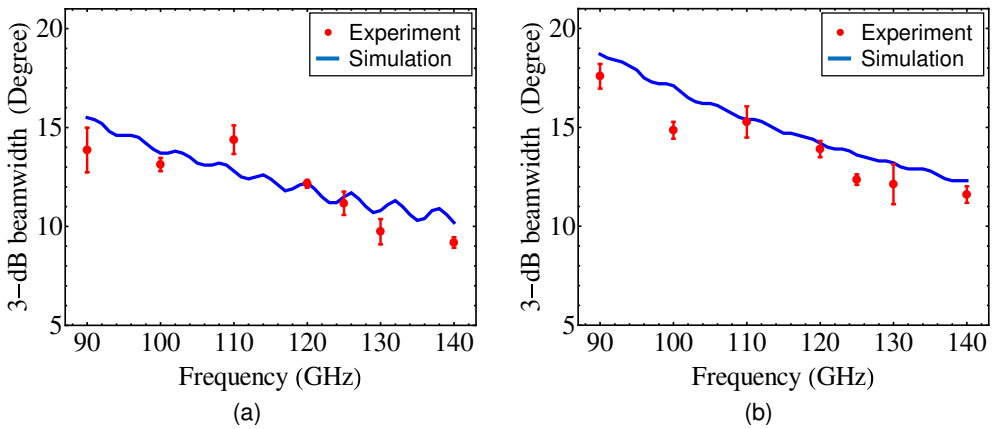

Figure 5.1.12: Frequency characteristics of the 3-dB beamwdith of the horn antenna in (a) E-plane and (b) H-plane.

Therefore, the differences between the first sidelobe positions at 90 GHz and 140 GHz are approximately 17.0° and 20.0° in the E- and the H-planes, respectively. The first sidelobe positions tend to be closer to the center (0°) as the THz frequency increases for both E- and H-planes. The experimental results agree well with the simulated results and also show this trend.

Figure 5.1.12 shows the frequency characteristics of the 3-dB beamwidths of the radiation patterns in the E- and H-planes. The red dots and blue solid line represent the experimental and simulated results, respectively. The 3-dB beamwidths in both planes decrease as the THz frequency increases. The simulated 3-dB beamwidths at 90 GHz are 15.5° and 18.7° for the E- and H-planes, respectively. At 140 GHz, they are respectively 10.2° and 12.3° for the E- and H-planes, respectively. Thus, the differences in the 3-dB beamwidths between 90 GHz and 140 GHz in the E- and H-planes are 5.3° and 6.4°, respectively. Figure 5.1.12 shows that we can clearly resolve these differences in the experimental results. The largest standard error of the 3-dB beamwidths and first sidelobe position are 1.1° and 3.5° at a frequency of 90 GHz. One possible reason for the large standard error at 90 GHz is that the SNR at this frequency was the lowest (SNR = 24.5 dB). In order to reduce the standard error, the number of measurements and the SNR of the EO detection system should be increased.

Figure 5.1.13 depicts the frequency characteristics of the gain of the F-band horn antenna. The red dots and blue solid line show the experimental and simulated results, respectively. The antenna gain can be calculated from the measured

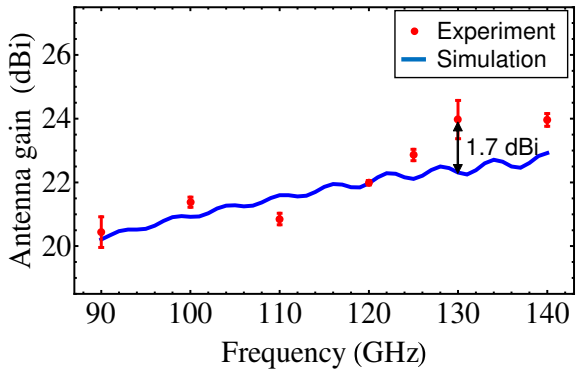

Figure 5.1.13: Frequency characteristics of the gain of the horn antenna.

3-dB beamwidths by approximating the antenna pattern as an elliptical area, as follows [5.20]:

$$D = \frac{P}{P_{iso}} = \frac{\text{Area}_{sphere}}{\text{Area}_{antenna}} = \frac{4\pi r^2}{\frac{\pi\ r^2\ \sin\theta_{BW}\ \sin\phi_{BW}}{4}} = \frac{16}{\sin\theta_{BW}\ \sin\phi_{BW}},$$
$$G = 10\ \log_{10}(\eta\ D) = 10\ \log_{10}(\eta \frac{16}{\sin\theta_{BW}\ \sin\phi_{BW}}), \tag{5.1.7}$$

where D, P, and P_{iso} are the antenna directivity, radiation intensity in a given direction, and radiation intensity averaged over all isotropic directions, respectively. G, θ_{BW}, and ϕ_{BW} are the antenna gain, 3-dB beamwidth in the E-plane and H-plane, respectively. The antenna efficiency is $\eta = 0.5$ for the standard horn antenna.

At 125 GHz, the antenna gain is 22.9±0.2 dBi and 22.1 dBi for the experimental and simulated results, respectively. The calculated antenna gains are 20.4±0.5 dBi and 24.0±0.2 dBi at 90 GHz and 140 GHz, respectively. The simulated results are 20.2 dBi and 22.9 dBi at 90 GHz and 140 GHz, respectively. The results in Fig. 5.1.13 indicated that the obtained antenna gains of the horn antenna agree well with those of the simulated results within 1.7 dBi in the full F-band.

In summary, we employed the near-to-far-field transformation technique by the EO measurement to characterize the F-band horn antenna. The obtained results agreed well with the simulated results. This indicates the impact of this technique for the THz antenna characterization. This technique has the advantages of compact and fast measurement compared to conventional direct far-field measurement.

5.2 Wavefront manipulating device

5.2.1 Motivation

Wavefront manipulating devices are often used to change the radiating beam. A lens is a common example of these devices. Lenses are usually used to change a spherical wavefront to a planar wavefront, also called a collimated beam, or change a collimated beam to a compressed beam in the microwave and photonic regions. In the THz region, the wavefront manipulating device is widely used in many practical systems. Therefore, an increasing number of designs and studies of these devices are being reported [5.21–5.23]. In these studies, the amplitude distributions were measured for the characterization. However, the characterization of the phase front distribution is also essential to understand the E-field behavior after passing through such devices.

A metal hole array (MHA) is another wavefront manipulating device. It is a planar device, which has periodic subwavelength holes on a metallic substrate. Generally, EM waves have extremely low transmittance through an aperture smaller than the incident wavelength, owing to diffraction. Nevertheless, an extraordinary transmission through subwavelength hole arrays was found experimentally [5.24] at a specific resonant frequency by a spectroscopy system in the optical region. This interesting phenomenon has attracted much research interest [5.25–5.27]. The mechanism of the resonant transmission through MHA can be explained by surface plasmon polaritons [5.28], which are localized at the metal–dielectric interface, and cylindrical waves, which are surface waves that can be excited on a perfect conductor surface [5.25, 5.29]. Until now, the MHA was studied theoretically through simulation and their transmittance properties were studied experimentally by spectroscopy systems.

In this section, we characterize a commercially available lens made from polytetrafluoroethylene (PTFE) Telfon and a homemade MHA by visualizing both the amplitude and phase distributions of THz waves after interacting with these devices using the EO detection system.

5.2.2 Characterization of a lens

Figures 5.2.1(a) and 5.2.1(b) show the experimental setup to characterize the lens and the front view of the lens, respectively. The lens had a focal length of 10 cm and diameter of 50 mm. The lens was placed at a distance of 10 cm from the F-band horn antenna. The EO probe was set at the center and behind the lens by 1.5 cm. An absorber was used to eliminate unwanted reflection on the EO probe. The E-field was parallel to the XZ-plane. The photocurrent inputted to the UTC-PD was 6 mA and the output THz power was approximately 1.3 mW.

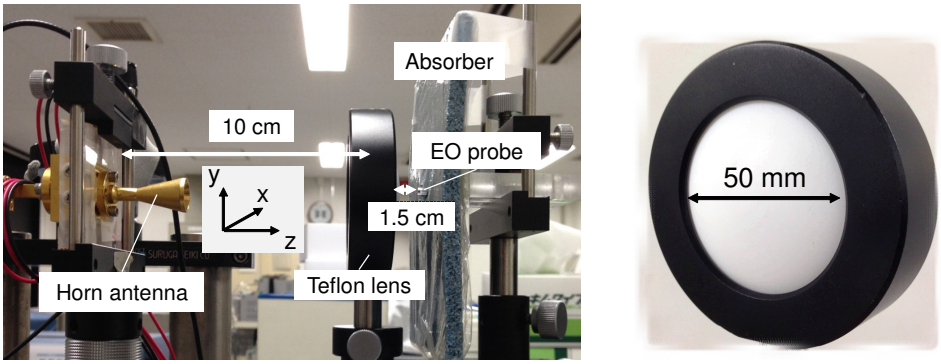

Figure 5.2.1: (a) Experimental setup to characterize a lens at 125 GHz, and (b) PTFE Teflon lens of diameter 50 mm.

Figure 5.2.2 shows the experimentally visualized results of the amplitude and phase distributions from the lens at 125 GHz ($\lambda = 2.4$ mm) in the XZ-, YZ-, and XY-planes. The 3D representations are shown in Fig. 5.2.3. The measured area was 50 mm $\times$ 50 mm and the sampling interval was set at 0.2 mm. The lock-in time constant was 10 ms and the measured time was approximately 12 min for each plane. The amplitude image was normalized to the maximum value in each plane. The SNR of the measurement at the center of the lens was 27 dB.

Figure 5.2.4 shows the experimentally visualized amplitude and phase distributions at a distance of approximately 1 mm from the surface of the F-band horn antenna at 125 GHz for the comparison. In the amplitude images, the beam is collimated for the lens (Fig. 5.2.2), whereas it is diverged for the horn antenna (Fig. 5.2.4). The quantitative comparison is evaluated based on the intensity distribution, I, which is calculated as follows:

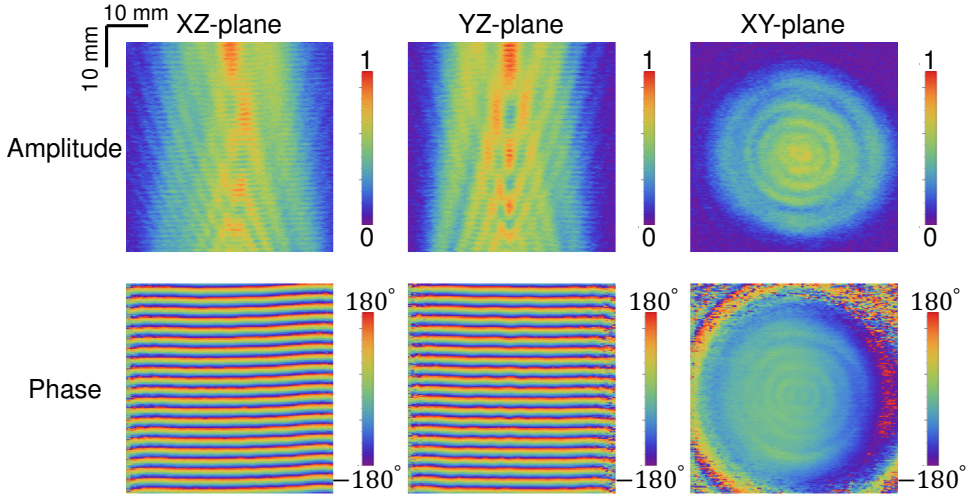

Figure 5.2.2: Visualized results of amplitude and phase distributions of collimated THz beam by lens in each plane at 125 GHz.

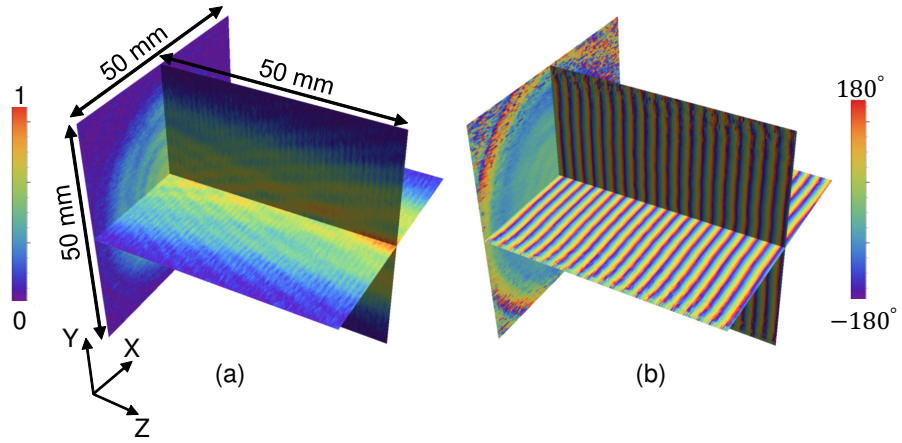

Figure 5.2.3: Visualized 3D representations of (a) amplitude and (b) phase distributions of collimated THz beam by the lens at 125 GHz.

$$I_E(x) = 20\log_{10}\frac{A_E(x)}{A_{Emax}},$$
$$I_H(y) = 20\log_{10}\frac{A_H(y)}{A_{Hmax}} \tag{5.2.1}$$

where $I_E(x)$, $A_E(x)$, and A_{Emax} are the 1D intensity distribution (1-line scanning), measured amplitude distribution of 1-line scanning, and its maximum value in the XZ-plane. Similarly, $I_H(y)$, $A_H(y)$, and A_{Hmax} are those in the YZ-plane. From the intensity distributions, the 10-dB beamwidths along propagation direction (z-axis) of the lens and the horn antenna are characterized in both the E- and H-planes in Fig. 5.2.5. The 10-dB beamwidths are the full width at position where the

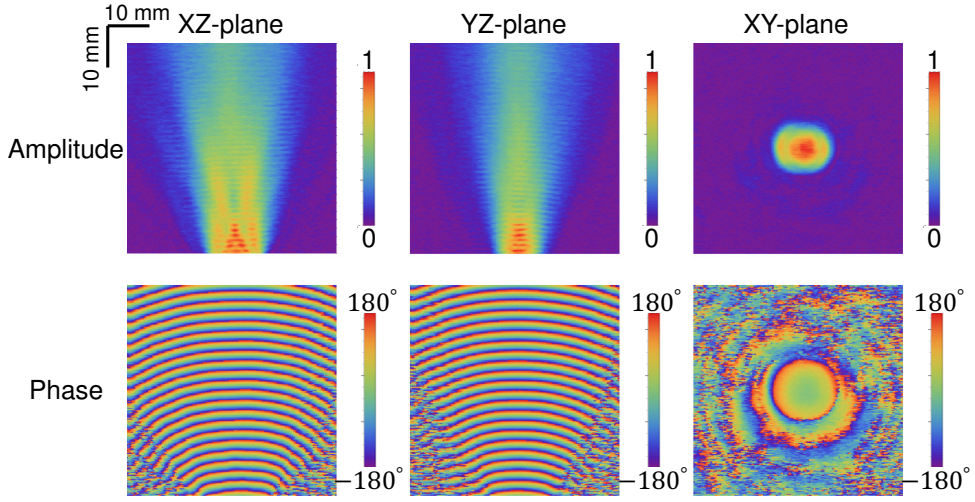

Figure 5.2.4: Visualized THz distribution from horn antenna at 125 GHz.

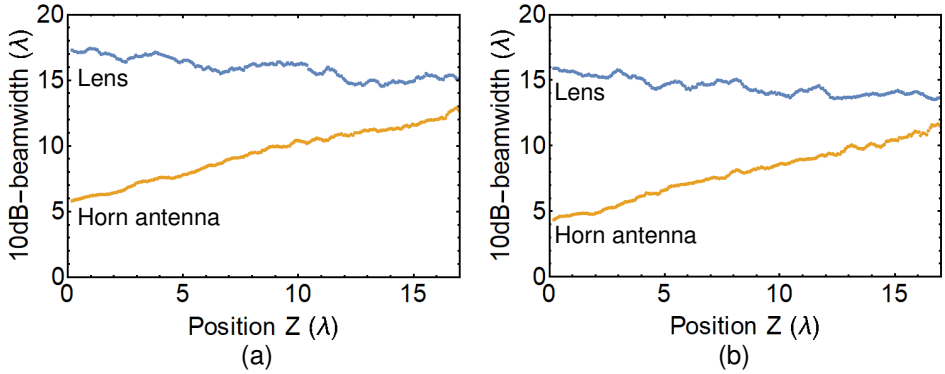

Figure 5.2.5: 10-dB beamwidths along z-axis of lens and horn antenna at 125 GHz in (a) XZ-plane and (b) YZ-plane.

intensity is equal to −10 dB of the maximum intensity distribution in each 1D scanning line.

In Fig. 5.2.5, the data are calculated based on moving average of six data points. The 10-dB beamwidths show the flatness for the lens, whereas they increase gradually for the horn antenna in both the E- and H-planes. In the E-plane, the 10-dB beamwidths of the lens are 17.1 λ and 15.1 λ at position z = 0.5 λ and z = 17.0 λ, respectively, whereas those of the horn antenna are 6.0 λ and 12.7 λ at position z = 0.5 λ and z = 17.0 λ, respectively. In the H-plane, the 10-dB beamwidths of the lens are 15.7 λ and 13.7 λ at position z = 0.5 λ and z = 17.0 λ, respectively, whereas those of the horn antenna are 4.6 λ and 11.5 λ at position z = 0.5 λ and z = 17.0 λ, respectively.

Moreover, the planar phase front can be observed clearly in the phase images

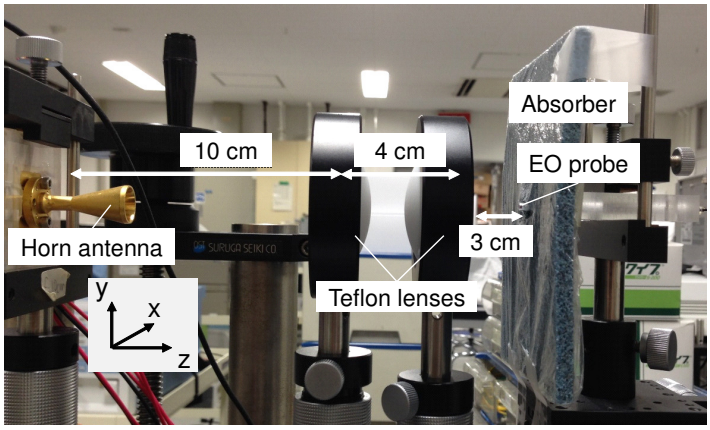

Figure 5.2.6: Experimental setup to characterize focused THz beam.

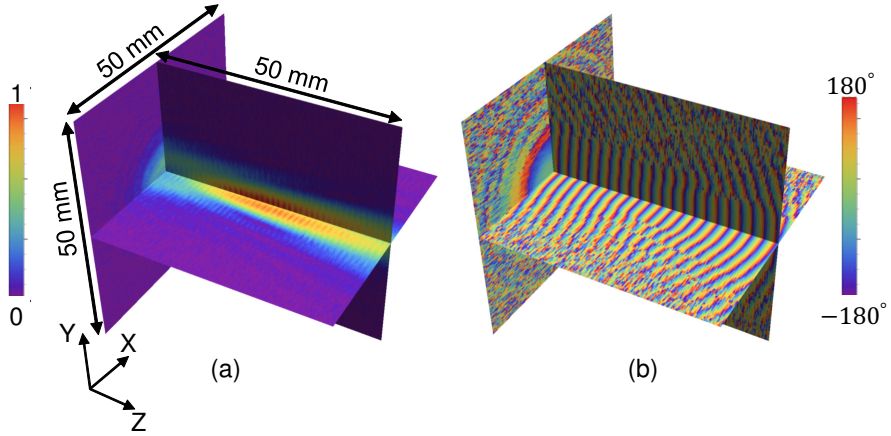

Figure 5.2.7: 3D representations of (a) amplitude and (b) phase distributions of focused THz beam by the lens at 125 GHz.

with the lens in Fig. 5.2.2. Nevertheless, the spherical phase front can be observed from the horn antenna in the phase images of Fig. 5.2.4. These results indicate that THz waves are collimated by the lens and that the phase distribution is converted from a spherical to planar phase front.

Next, we characterize the conversion of the collimated THz beam to focused THz beam by placing another lens behind the first lens at a distance of approximately 4 cm from the first lens, as shown in configuration Fig. 5.2.6. The EO probe was placed behind the second lens by approximately 3 cm.

Figure 5.2.7 shows the experimentally visualized results in 3D representations of amplitude and phase distributions of the focused THz beam. In the amplitude image, we can observe clearly that the THz beam is more narrow and the intensity is focused at the middle position in the z-axis. The measurement conditions are the same as for the collimated case.

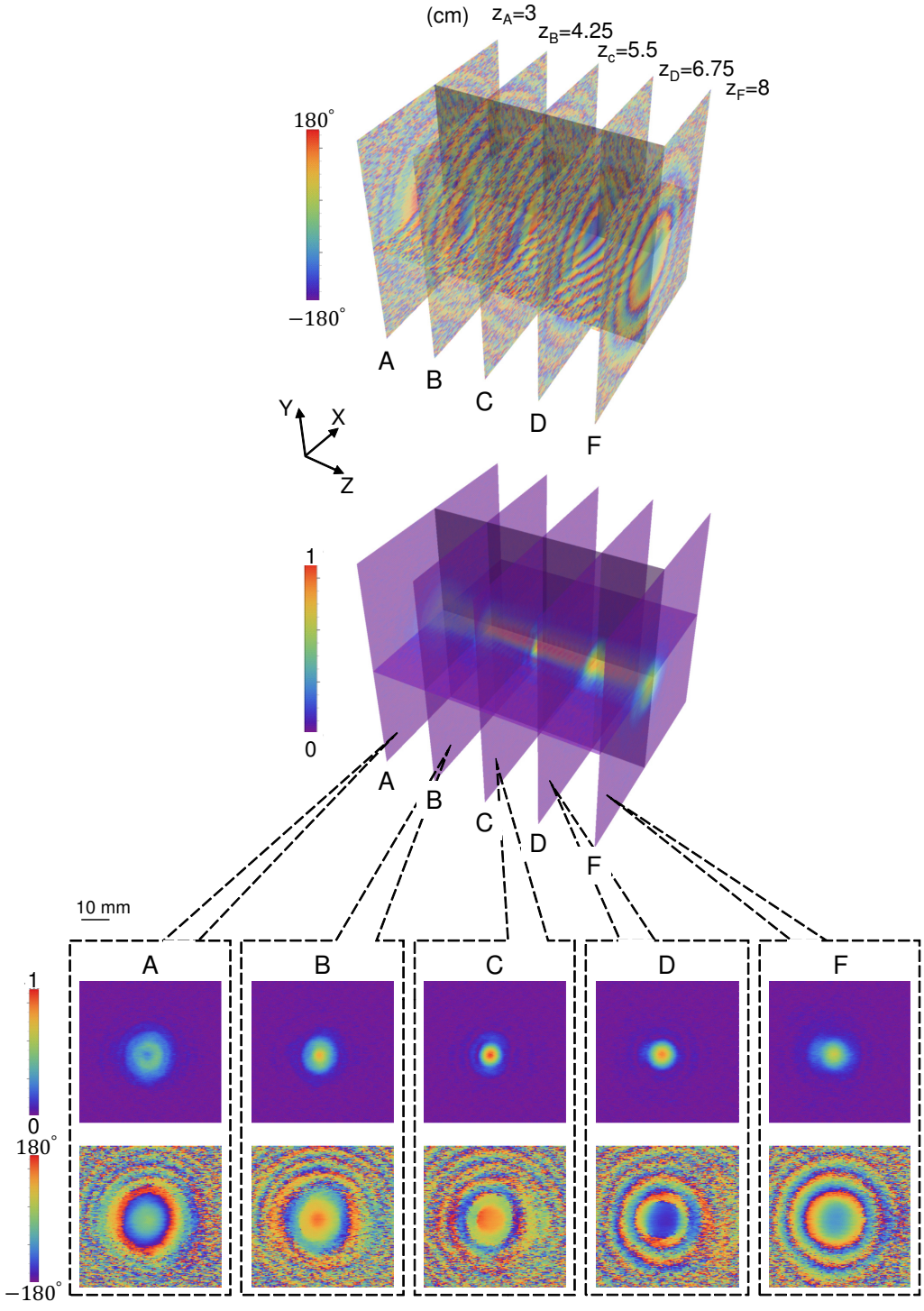

Figure 5.2.8: Visualized amplitude and phase distribution of focused THz beam in the XY-plane at different positions in z-axis.

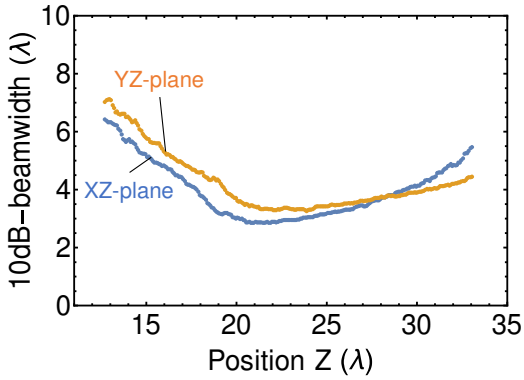

Figure 5.2.9: 10-dB beamwidths along z-axis of focused beam at 125 GHz.

Figure 5.2.8 shows the visualized THz distribution in the XY-plane at five different positions in the z-axis, i.e., A-, B-, C-, D-, and F-planes corresponding to $z_A = 3$ cm, $z_B = 4.25$ cm, $z_C = 5.5$ cm, $z_D = 6.75$ cm, and $z_F = 8$ cm. The amplitude images were normalized to the maximum value in the five planes. These are the point spread functions (SPFs) at each position when employed in THz imaging applications. As we can see in Fig. 5.2.8, the SPF is gradually smaller from the A-plane to the C-plane, and larger from the C-plane to the F-plane. This indicates the focal point of the second lens is around the C-plane.

Figure 5.2.9 shows the 10-dB beamwidths of the focused THz beam along the z-axis in the XZ- and YZ-planes. They are also calculated based on a moving average of six data points. The 10-dB beamwidths decrease gradually to a minimum of 2.85 λ at position $z = 21.5$ λ (5.2 cm) in the E-plane, and 3.26 λ at position $z = 23.9$ λ (5.7 cm) in the H-plane. The slight difference between the positions of the minimum 10-dB beamwidths in the E- and H-plane is probably due to a slight misalignment of the lenses.

5.2.3 Characterization of metal hole array

Figure 5.2.10 shows the experimental configuration to characterize the MHA. The MHA was made from a 40 mm × 40 mm aluminum plate with the thickness of 1 mm and hole arrays with a periodic triangular pattern, in which the diameter of the hole is $d = 1.5$ mm (subwavelength) and the lattice constant is $p = 2.5$ mm (Fig. 5.2.10(b)). This MHA was designed to exhibit an extraordinary transmission at the frequency of approximately 125 GHz by the simulation and fabricated by

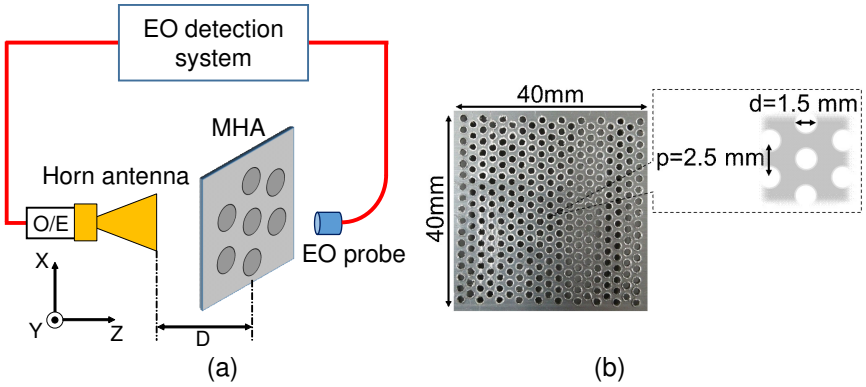

Figure 5.2.10: (a) Experimental configuration to characterize (b) MHA.

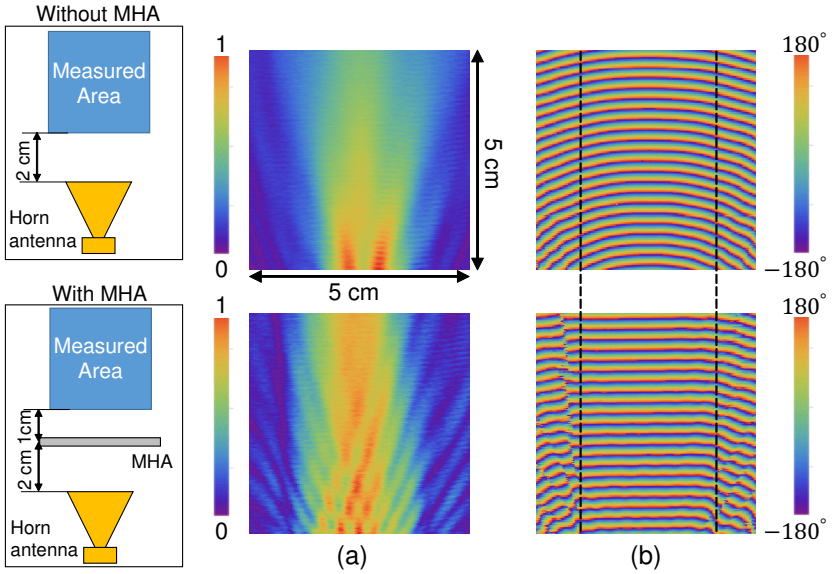

Figure 5.2.11: Visualized results of (a) amplitude and (b) phase distributions with and without MHA in the E-plane at 125 GHz.

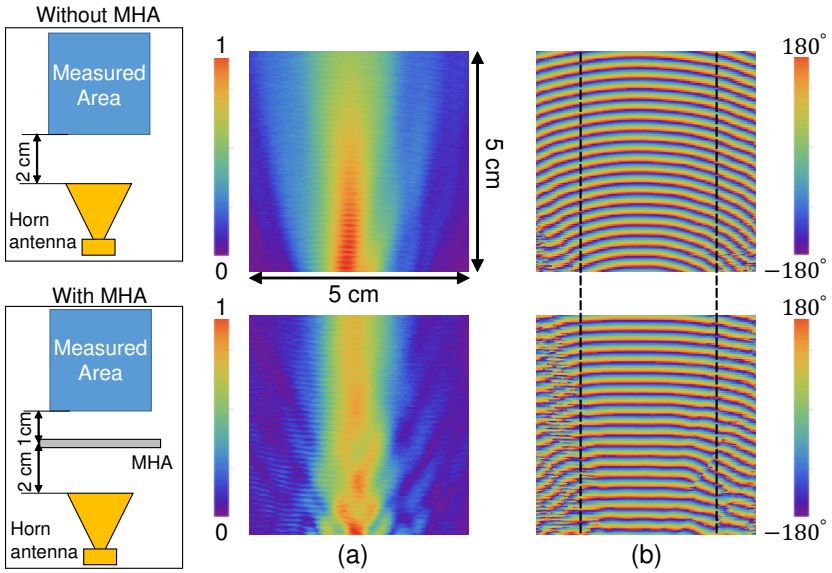

Figure 5.2.12: Visualized results of (a) amplitude and (b) phase distributions with and without MHA in the H-plane at 125 GHz.

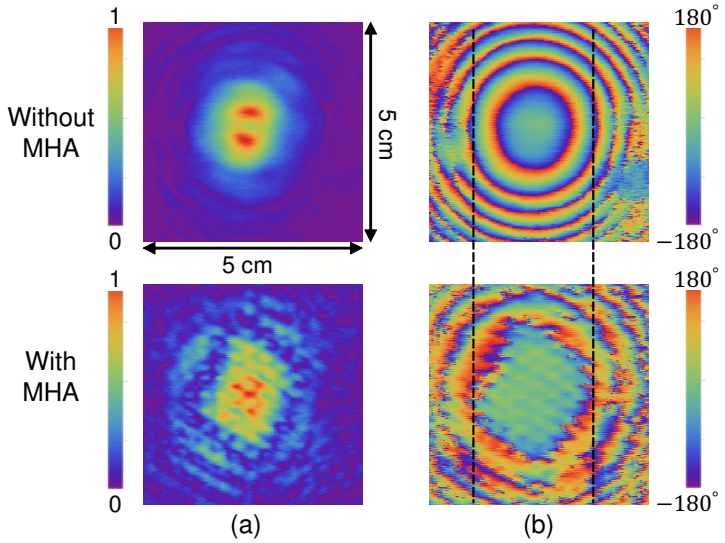

Figure 5.2.13: Visualized results of (a) amplitude and (b) phase distributions with and without MHA in the XY-plane at 125 GHz.

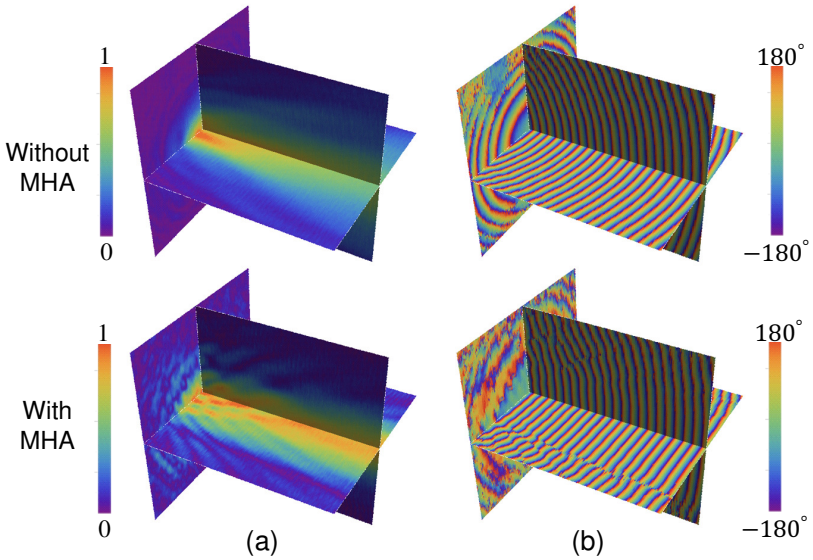

Figure 5.2.14: Visualized 3D representations of (a) amplitude and (b) phase distributions with and without MHA at 125 GHz.

a mini Computer Numerical Control Cobra 2520 machine. The MHA was placed at a distance of D mm behind the horn antenna surface. Both ZnTe and DAST probes were employed to visualize the THz wave distribution after interacting with the MHA. The E-field of THz waves is parallel to the XZ-plane in Fig. 5.2.10(a), which is also the longer side of the hole patterns.

Figure 5.2.11 shows the experimentally visualized results of the amplitude and phase distributions with and without the MHA in the E-plane at 125 GHz. The distance between the MHA and the horn antenna was D = 2 cm in this case. The measured area was 5 cm × 5 cm. In Fig. 5.2.11, the upper images and lower

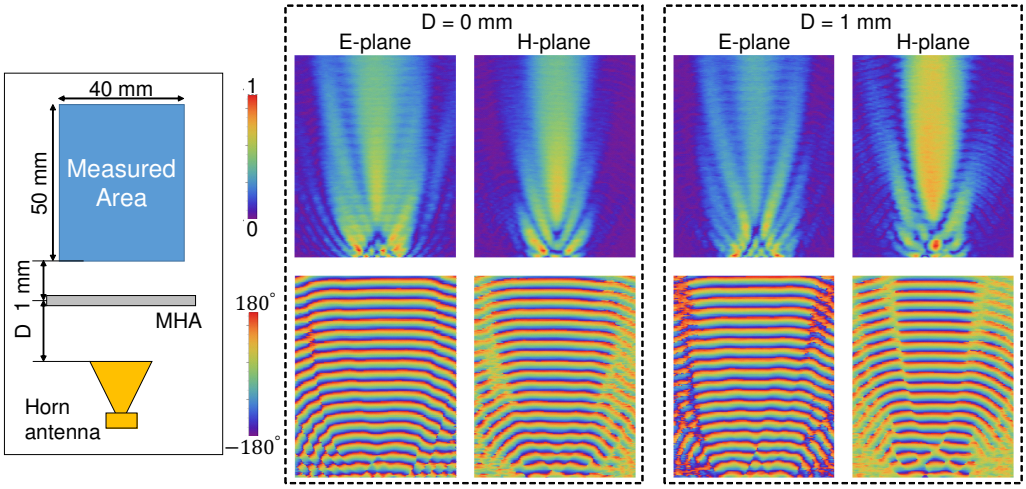

Figure 5.2.15: Visualized results of collimated THz beam by MHA with D = 0 mm and D = 1 mm at 125 GHz.

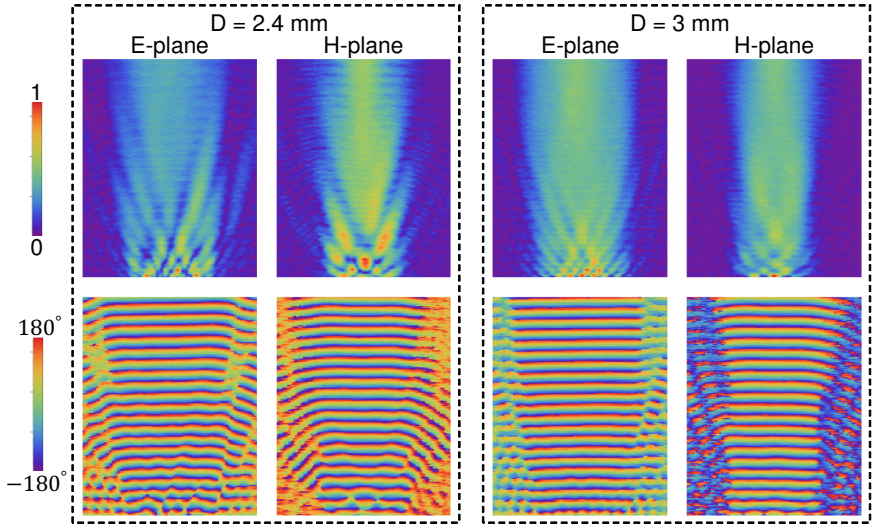

Figure 5.2.16: Visualized results of collimated THz beam by MHA with D = 2.4 mm and D = 3 mm at 125 GHz.

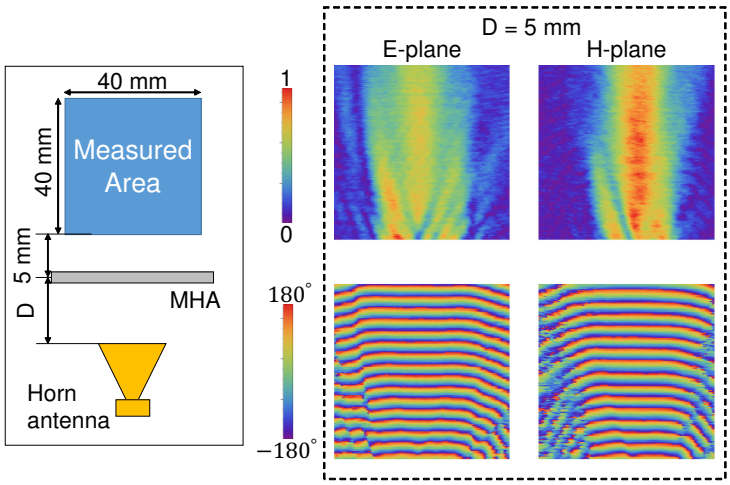

Figure 5.2.17: Visualized results of collimated THz beam by MHA with D = 5 mm at 125 GHz.

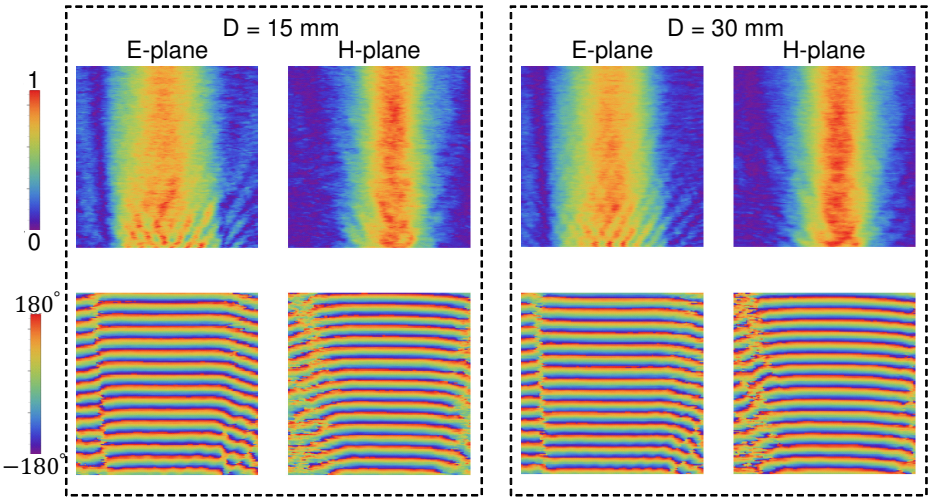

Figure 5.2.18: Visualized results of collimated THz beam by MHA with D = 15 mm and D = 30 mm at 125 GHz.

images are without and with the MHA, respectively. The divergent THz beam and the spherical phase front can be observed in the amplitude and phase images without the MHA, respectively. However, with the MHA, the THz distribution is similar to a collimated beam in the amplitude image. In particular, the phase front with the MHA shows a planar distribution between the dashed lines. This indicates that the spherical phase front of the THz wave emitted from the horn antenna was converted to a planar phase front after interacting with the MHA. The phase-front-converting phenomenon by the MHA was also confirmed in the H-plane, as shown in Fig. 5.2.12, in the XY-plane as depicted in Fig. 5.2.13, and in 3D representation in Fig. 5.2.14.

Next, we characterize the MHA working under different distances D from the horn antenna, particularly D = 0 mm, i.e., MHA attached to the horn antenna, to D = 30 mm (12.5 λ). The EO probe was place behind the MHA by 1 mm for distance D < 3 mm, and 5 mm for the others. Figure 5.2.15 shows the visualized results in the E- and H-planes with D = 0 mm and D = 1 mm. The phase images in both planes indicate that the phase front becomes planar when the THz waves pass through the MHA, even in the case in which the MHA is close to the horn antenna. The amplitude images also show that the THz beam is gradually collimated as propagating father from the MHA. The collimating effect tends to occur earlier even at the position near the MHA when D is longer, as shown in

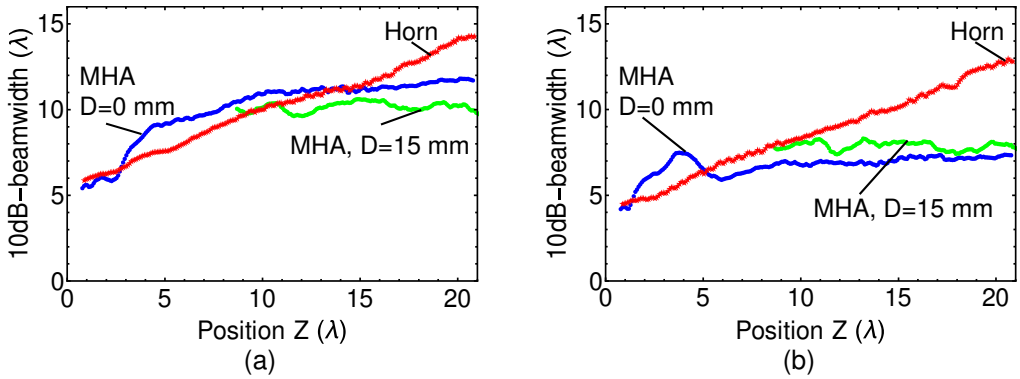

Figure 5.2.19: 10-dB beamwidths along z-axis of collimated beam by MHA at 125 GHz in the (a) E-plane and (b) H-plane.

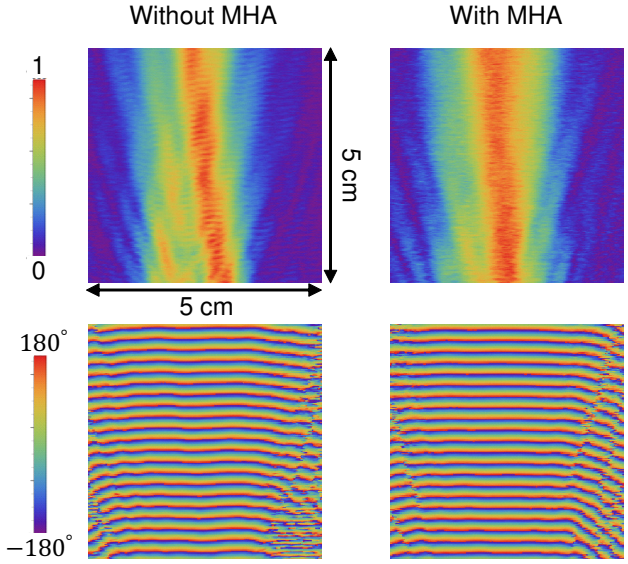

Figure 5.2.20: Visualized results of THz distribution in H-plane when illuminating the MHA by a collimated beam at 125 GHz.

the case D = 2.4 mm and D = 3 mm in Fig. 5.2.16. Figures 5.2.17 and 5.2.18 show the experimental results with D longer than a wavelength (5 mm, 15 mm, and 30 mm). The collimating effect and the planar phase front distributions are maintained for different distances D.

The quantitative evaluation of 10-dB beamwidths with and without the MHA along the propagation direction in the z-axis is depicted in Fig. 5.2.19. The red line represents the 10-dB beamwidths without the MHA, i.e., the diverged beam from the horn antenna. The blue and green lines show the 10-dB beamwidths with the MHA placed behind the horn antenna at a distance D = 0 mm and D = 15 mm, respectively. The beamwidths without the MHA increase gradually with a slope of 0.46 and 0.42 in the E- and H-planes, respectively. However, the beamwidths

with the MHA are flat from the position z $\geq 9\lambda$. The average beamwidths with the MHA at distance D = 0 mm are 11.3 λ and 7.1 λ in the E- and H-planes, respectively; those with the MHA at distance D = 15 mm are 10.1 λ and 7.9 λ in the E- and H-planes, respectively. These results indicate that the MHA can work as a wavefront-collimating device with a flexible "focal length", i.e., the distance between the MHA and the antenna is flexible.

An interesting difference between the MHA and a common lens is that the MHA converts a diverged beam to collimated beam, but not vice versa. Figure 5.2.20 shows the visualized THz distribution in the H-plane after a collimated beam illuminated to the MHA. A planar phase front distribution of the incident beam can be confirmed in the phase image without the MHA. The planar phase front was also obtained with the MHA, as shown in the phase image in Fig. 5.2.20. This indicates that the MHA does not convert the collimated beam to the focused beam like the lens.

5.2.4 Frequency characteristics and physical mechanism of MHA

In order to evaluate the transmittance efficiency of the MHA, we measured the THz distribution with and without the MHA in the XY-plane at the same position in the z-axis, i.e., 26 mm from the horn antenna surface, as shown in Fig. 5.2.21. The measured area was 50 mm × 50 mm, corresponding to 250 × 250 data points. The transmittance power efficiency, T, was calculated as follows:

$$T = 10 \log_{10} \frac{\sum_{i=1}^{N} A_{w,i}^2}{\sum_{i=1}^{N} A_{wo,i}^2} \tag{5.2.2}$$

where N, $A_{w,i}$, and $A_{wo,i}$ are the total number of measured points (N = 62500 points in this case), and measured amplitude at each point in XY-plane with and without the MHA, respectively. The obtained transmittance efficiency of the MHA is 35.07 % at 125 GHz. We evaluate the transmittance power by the same method at different frequencies from 105 GHz to 130 GHz within the F-band. The frequency characteristic of the transmittance power of the MHA is shown in Fig. 5.2.22. The transmittance power above 50% was obtained at frequencies 115 GHz

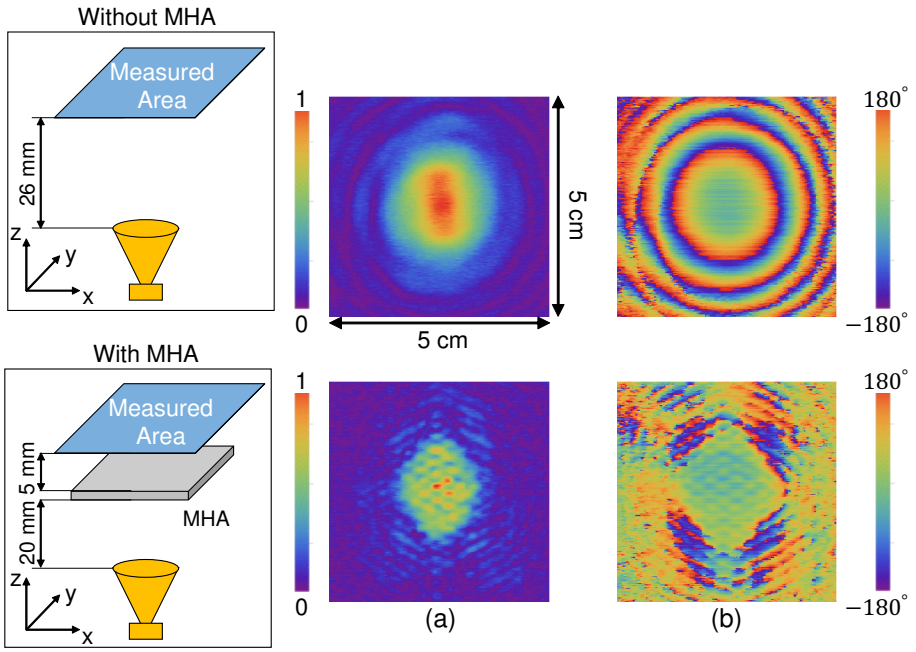

Figure 5.2.21: Visualized (a) amplitude and (b) phase in XY-plane with and without MHA at 125 GHz to evaluate the transmittance efficiency.

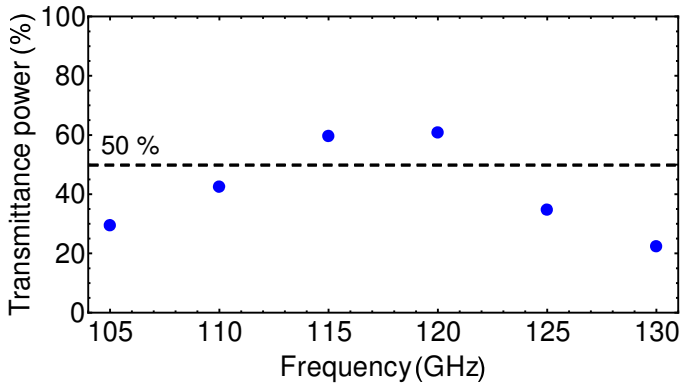

Figure 5.2.22: Frequency characteristic of transmittance power of the MHA.

and 120 GHz. The maximum transmittance power of 61.15 % was obtained at 120 GHz, instead of at the designed frequency of 125 GHz. This slight difference is probably caused by limitations of the fabrication process.

Finally, we experimentally investigate the physical mechanism of the MHA through the radiation patterns. The THz distribution in the XY-plane was measured with a 0.1 mm sampling interval in three cases: horn antenna, collimated beam by the lens, and collimated beam by the MHA at 125 GHz. The distances between the DAST probe the devices mentioned above were, respectively, 2 cm (8.3 λ), 1 cm (4.2 λ), and 2 cm (8.3 λ). These positions were located in the radiating

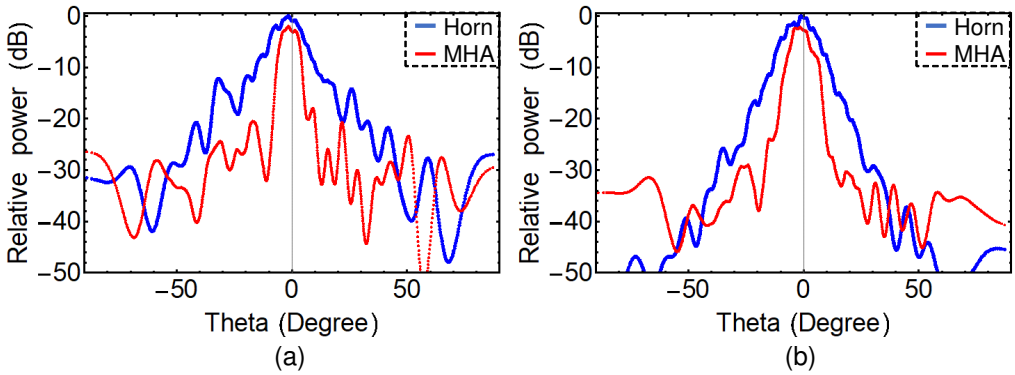

Figure 5.2.23: Radiation patterns in the (a) E- and (b) H-planes of the MHA and horn antenna at 125 GHz.

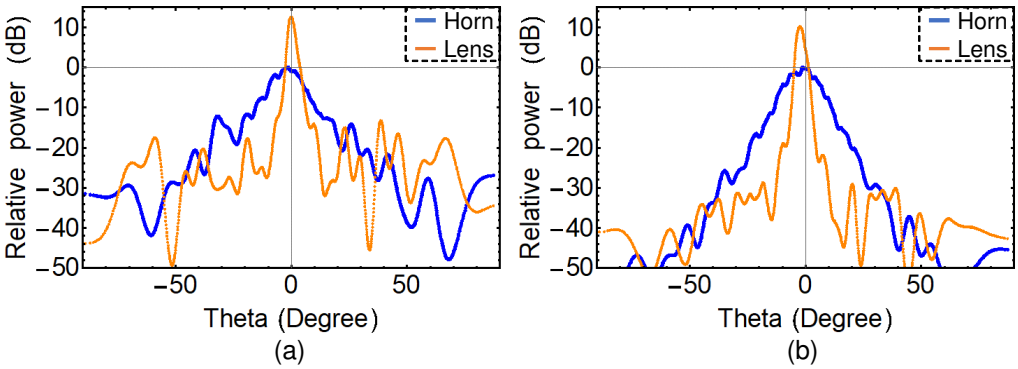

Figure 5.2.24: Radiation patterns in the (a) E- and (b) H-planes of lens and horn antenna at 125 GHz.

near-field region. Therefore, the near-to-far-field transformation technique can be applied to estimate the radiation patterns. Note that the experimental conditions such as the THz output power and input photocurrent to the detecting photodiode (PD) were the same in those cases.

Figure 5.2.23 shows the radiation patterns in the E- and H-planes of the MHA and the horn antenna. The blue and red lines represent the results of the horn antenna and the MHA, respectively. The data are normalized to the maximum value of radiation patterns of the horn antenna in each plane. The peak power reduced by approximately 2 dB for the MHA. The beamwidths of the radiation patterns of the MHA are smaller than those of the horn antenna. In particular, the 3-dB beamwidths and 10-dB beamwidths are approximately 8° and 12° for the MHA, respectively; and those are 13° and 26° for the horn antenna in the E-plane as summarized in Table 5.2.1. The difference of the 10-dB beamwidths between the MHA and the horn antenna ($26° - 13° = 13°$) is much larger than the difference of 3-dB beamwidths ($12° - 8° = 4°$) between them. This indicates that

the MHA probably exhibits a k-vector filtering property, which allows the k-vector normal to the MHA pass through it but not for other k-vectors. This is probably the physical mechanism of the collimating phenomenon in the MHA.

Figure 5.2.24 shows the radiation patterns of the horn antenna with the blue line and the collimated beam by the lens with the orange line, respectively, in the E- and H-planes at 125 GHz. The data are also normalized to the maximum value of the radiation patterns of the horn antenna in each plane. A peak power enhancement of approximately 12.6 dB by the lens was obtained. The 3-dB beamwidths and 10-dB beamwidths of the lens are also the narrowest among the three cases, as shown in Table 5.2.1. The enhancement in the peak power also indicates the lens does not exhibit the k-vector filtering effect like the MHA.

Table 5.2.1: Summary of radiation patterns of MHA, lens and horn antenna.

Beamwidth		MHA	Lens	Horn
E-plane	3-dB beamwidth	8.09°	2.64°	12.66°
	10-dB beamwidth	11.66°	5.20°	25.74°
H-plane	3-dB beamwidth	7.60°	3.06°	12.07°
	10-dB beamwidth	16.23°	6.11°	24.45°
Maximum power		−2.0 dB	12.6 dB	0 dB

In summary, we experimentally verified the beam collimating phenomenon in the MHA at 125 GHz for the first time based on the visualized results of both amplitude and phase distribution. The collimating beam by the MHA was characterized by comparing it with that by the lens. The experimentally obtained radiation patterns help us to understand the physical mechanism of the MHA. The MHA exhibits a k-vector filtering effect, whereas the lens exhibits gain-enhancement effect.

5.3 Spherical-wave generation device

5.3.1 Motivation

One of the attractive features of the THz band for research and industrial applications is its ultrabroad bandwidth in comparison with the microwave band. For example, a 300-GHz band can employ over 50 GHz bandwidth for radio commu-

nications with a demonstration of 50-Gbit/s data transmission [5.30]. Moreover, in spectroscopy applications for material and biological inspection [5.31, 5.32], a broader bandwidth from 0.2 THz to over 1 THz was employed.

Initially, the THz time-domain spectroscopy was studied owing to the development of femto- and picosecond pulse lasers [5.33, 5.34]. Recently, the frequency-domain spectroscopy has attracted increased research interest owing to its advantages such as no requirement of mechanical scanning delay line, higher frequency resolution, selectable frequency-scan length and resolution, and higher spectral density and SNR at a given frequency [5.35]. Generally, the photomixing technique, in which a fast PD or photoconductive switch is used to convert the beat of two optical signals to a THz wave, is employed for frequency-domain spectroscopy [5.35–5.37].

A Si-lens-mounted antenna, such as a log-periodic spiral antenna, is used for those broadband devices to generate spherical waves. We name it a spherical-wave generation device. Generally, the THz power of the spherical-wave generation device is characterized by focusing the radiation into the power meter by optical mirrors or lenses. To the best of our knowledge, the characterization of this device based on the visualization of the THz distribution has not been done before. The E-field distribution in the near-field region and how it radiates from the device are still uncertain. It is necessary to characterize the THz wave distribution to verify its operation in a broad bandwidth.

In this section, we employ the EO detection system to characterize a Si-lens-mounted UTC-PD. It is a commercially available device, which is used in frequency-domain THz spectroscopy systems and can operate at over 1 THz. The THz power emitted from this broadband UTC-PD was below 10 µW. Therefore, the DAST probe was exploited.

5.3.2 Experimental characterization

First, the THz output power from the Si-lens-mounted UTC-PD was measured by a PM4 power meter. Figure 5.3.1 shows the configuration to measure the THz power emitted from the spherical-wave generation device. For frequencies above

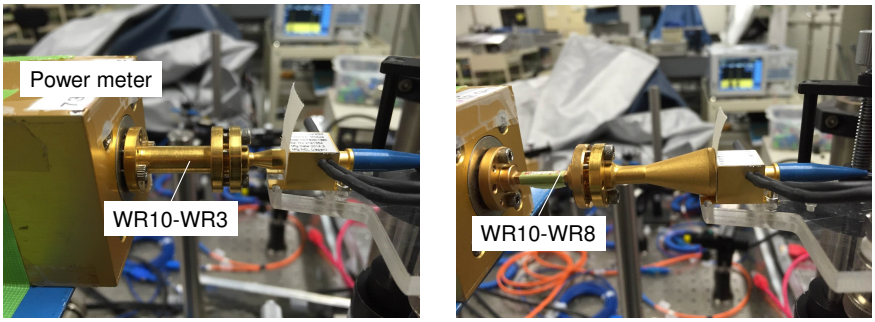

(a) (b)

Figure 5.3.1: Configuration to measure the THz power emitted from the broadband UTC-PD at frequency (a) 200–600 GHz, and (b) below 150 GHz.

200 GHz, a waveguide WR10-WR3 and a J-band (220–325 GHz) horn antenna were employed, as in Fig. 5.3.1(a). For frequencies below 200 GHz, a waveguide WR10-WR8 and the F-band (90–140 GHz) horn antenna were used, as in Fig. 5.3.1(b). The horn antenna was placed as close as possible to the spherical-wave generation device such that all of the radiated THz power could be harvested.

The UTC-PD converts the beat optical signal (1.55 µm) to the THz wave. However, this type of broadband UTC-PD has an issue of leaking optical signal: the optical power is radiated in addition to the THz radiation. The THz wave can pass through a paper with negligible loss, whereas a paper can prevent the optical signal significantly. Therefore, we measure the frequency characteristics of the THz power emitted from the spherical-wave generation device with and without inserting the paper as shown in Fig. 5.3.2. The results were obtained at a bias voltage of −1 V with a UTC-PD photocurrent of 4 mA. The blue and orange dots represent the results without and with the paper, respectively. The difference between the measured power with and without the paper varies from 5.4 dB to 16.8 dB. The difference become larger as the THz frequency increased. The THz power (with paper) was generally below −18 dBm (15.8 µW) and degraded as the THz frequency increased. The THz powers were −21.6 dBm (6.9 µW) and −29.2 dBm (1.2 µW) at frequencies of 300 GHz and 500 GHz, respectively.

Figure 5.3.3 shows the relationship between the measured output power and photocurrent of the broadband UTC-PD at 300 GHz with and without the paper. The difference in THz power between with and without the paper was approximately 8–9 dB. The blue and orange dots represent the results without and with

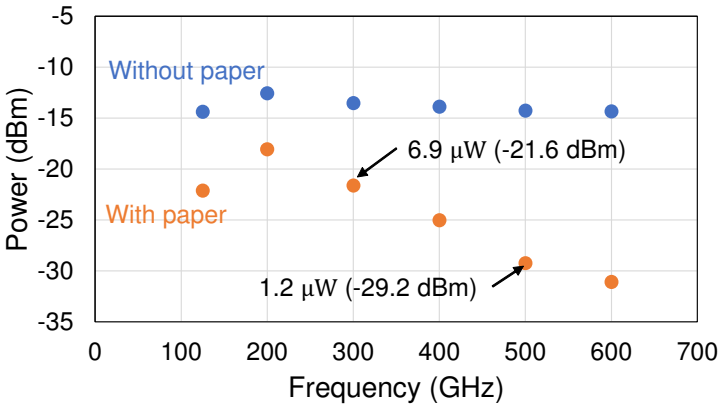

Figure 5.3.2: Frequency characteristics of the radiated THz power from the broadband UTC-PD with and without inserting the paper.

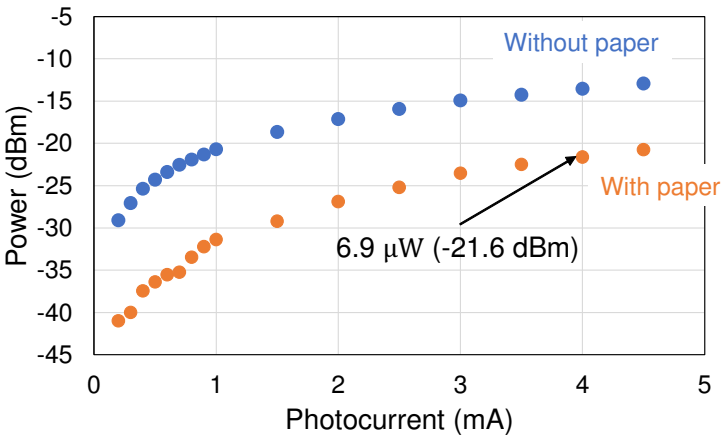

Figure 5.3.3: Relationship between the measured output power and photocurrent of the broadband UTC-PD at 300 GHz.

the paper, respectively. The THz power with the paper was nearly saturated at a photocurrent of 4 mA. Therefore, we visualize the THz distribution from this device with a photocurrent of 4 mA.

Figure 5.3.4 shows the experimental configuration to visualize THz waves distribution from the spherical-wave generation device. The DAST probe was placed at a distance of approximately 5 mm from the Si-lens surface. A paper sheet was attached on the head of the Si-lens to reduce the optical leaking signal from the UTC-PD. The amplitude and phase distributions were visualized in three planes XY-, YZ-, XZ-planes at different frequencies from 30 GHz to 600 GHz. The accurate THz frequency setting was verified by measuring the difference between two optical-carrier frequencies by the optical spectrum analyzer (Yokogawa AQ6370B), which has a minimum frequency resolution of 4 GHz, as shown in Fig. 5.3.5.

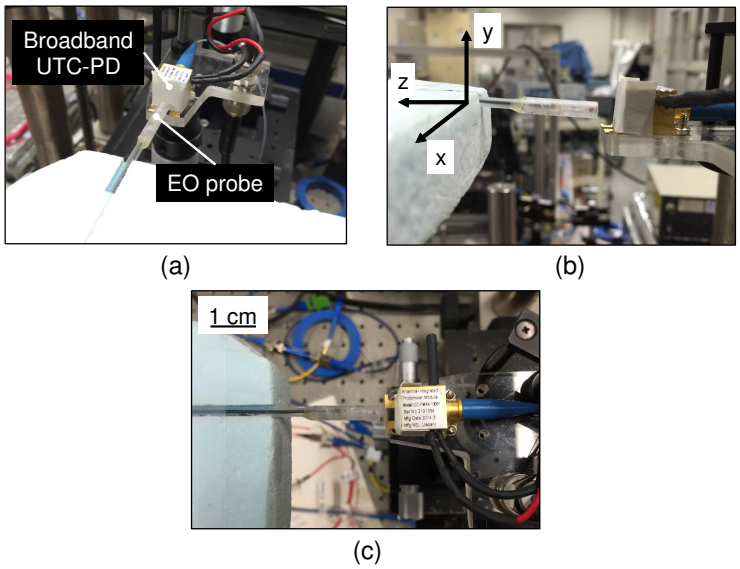

Figure 5.3.4: Experimental configuration of to visualize THz distribution from spherical-wave generation device by DAST probe: (a) front view, (b) side view, and (c) top view.

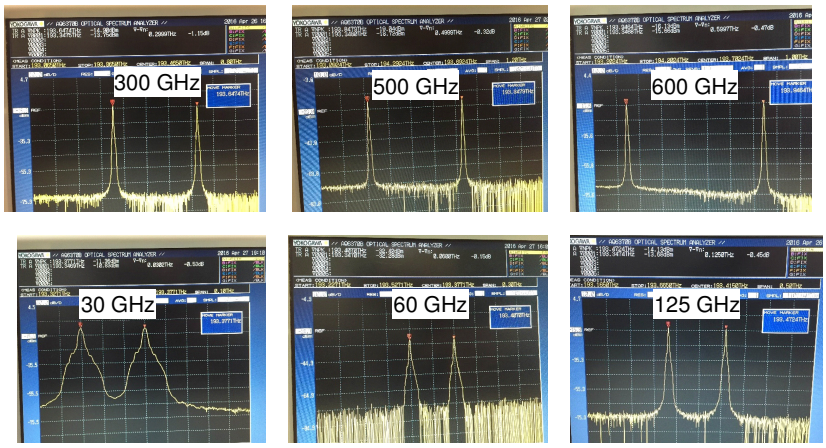

Figure 5.3.5: THz frequency verified by measuring the beat optical frequencies using optical spectrum analyzer.

Figures 5.3.6, 5.3.7, 5.3.8, 5.3.9, and 5.3.10 show the experimentally visualized results of amplitude and phase distributions from the spherical-wave generation device at frequencies of 30 GHz, 60 GHz, 125 GHz, 300 GHz, and 500 GHz, respectively. The sampling interval was set at 0.2 mm for frequencies below 500 GHz ($\lambda = 0.6$ mm) and 0.1 mm for frequencies equal to or higher than 500 GHz. The lock-in time constant was set at 30 ms. The gain of a low-noise transimpedance amplifier was set at 1 MV/A. We have successfully visualized the amplitude and phase distributions of THz radiation in free-space from the broadband spherical-wave generation device in three planes.

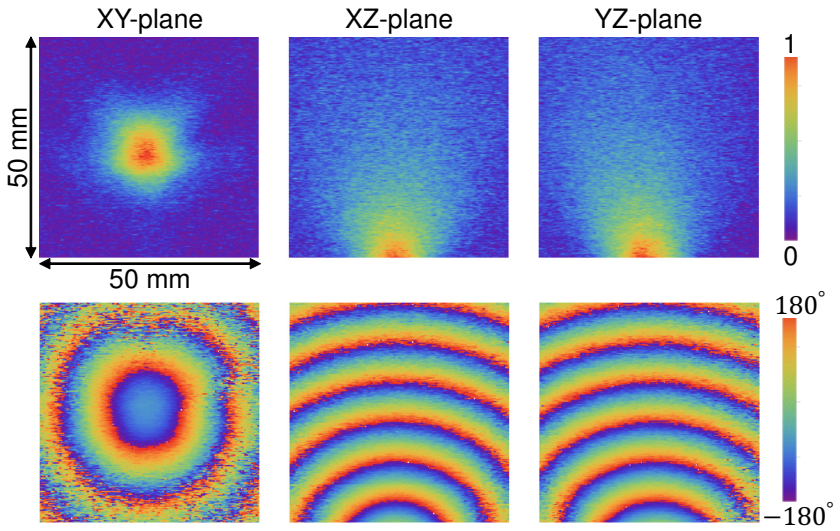

Figure 5.3.6: Visualized THz distributions from the device at 30 GHz.

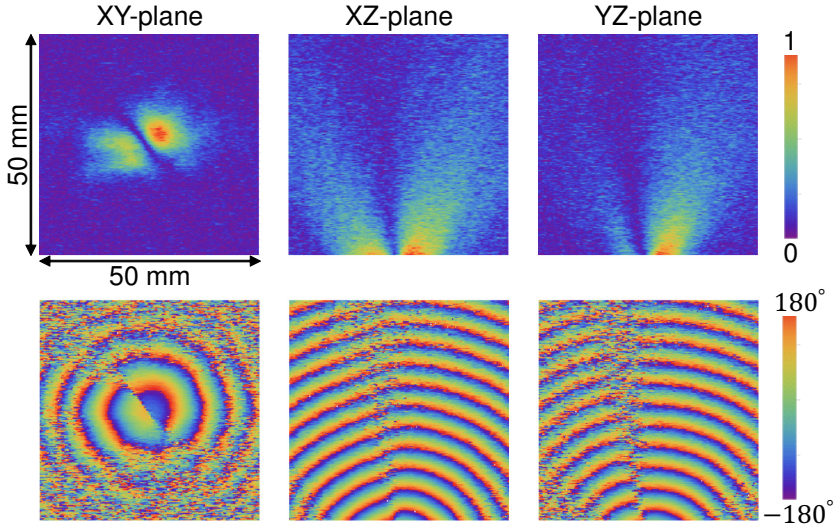

Figure 5.3.7: Visualized THz distributions from the device at 60 GHz.

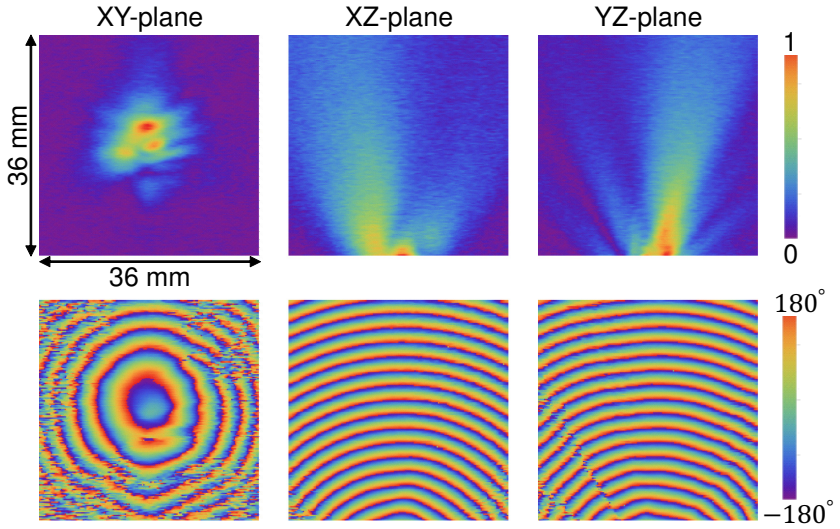

Figure 5.3.8: Visualized THz distributions from the device at 125 GHz.

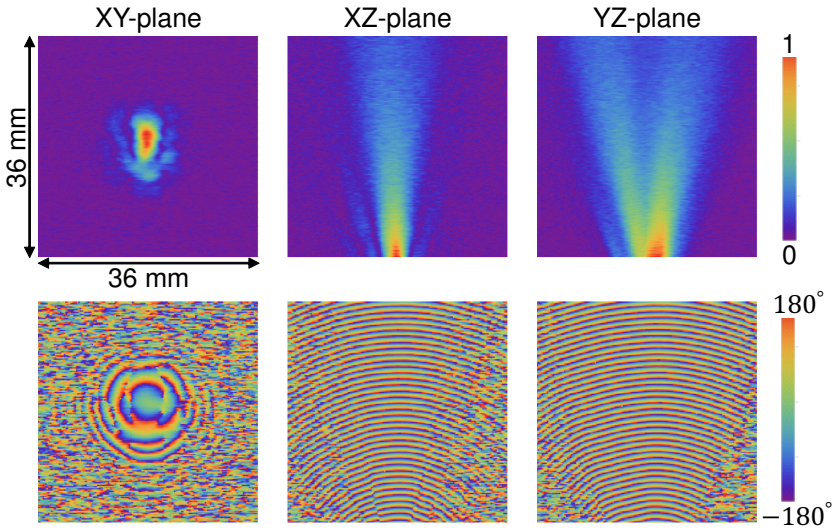

Figure 5.3.9: Visualized THz distributions from the device at 300 GHz.

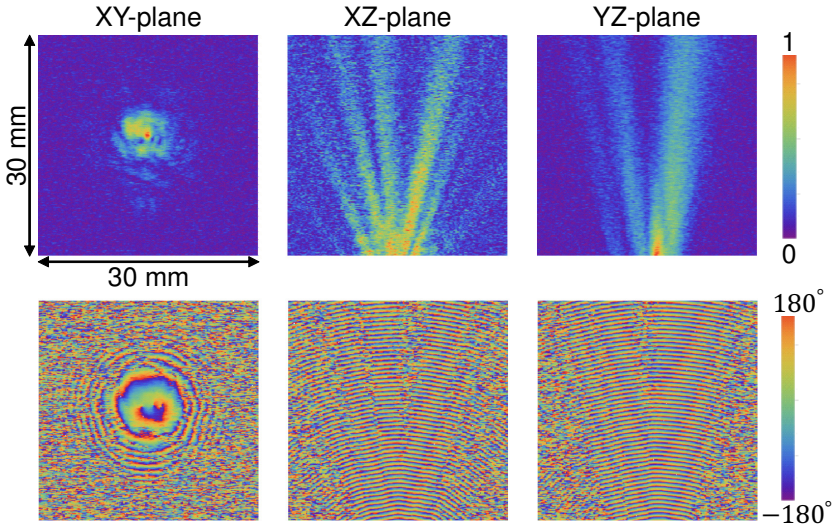

Figure 5.3.10: Visualized THz distributions from the device at 500 GHz.

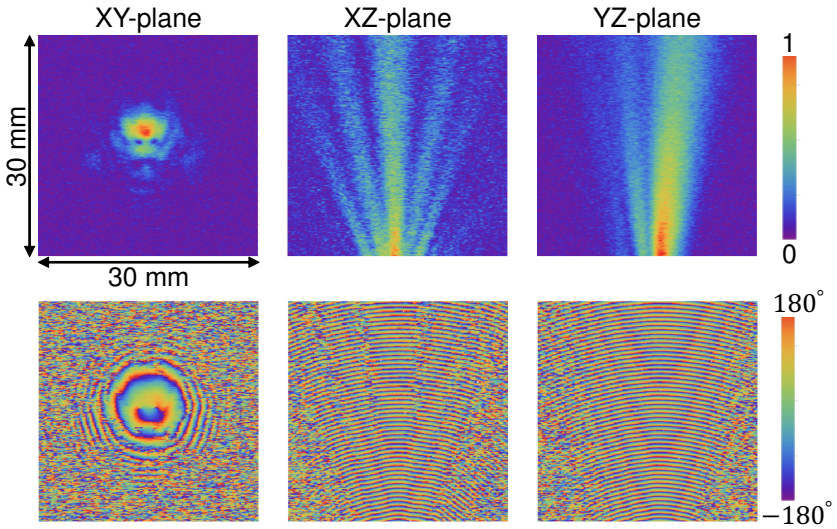

Figure 5.3.11: Visualized THz distributions from the device at 500 GHz without attaching paper.

At 30 GHz, the THz distribution was nearly isotropic (Fig. 5.3.6). At 60 GHz, it has a diagonal breaking (Fig. 5.3.7). At 125 GHz, the phase distribution was spherical, but the amplitude was disturbed (Fig. 5.3.8). At 300 GHz, the THz radiation showed a good directivity and spherical phase front distribution (Fig. 5.3.9). At 500 GHz, the THz radiation disturbed in a different direction (Fig. 5.3.10). Overall, the THz radiations were different at different frequencies. The malfunction of this device at high frequency (500 GHz) was discovered due to the visualized results. A misalignment of the antenna and the Si-lens can be one of possible reasons. This indicates the importance of experimentally visualizing the THz distribution for practical applications and giving feedback to the production of such types of broad-bandwidth-operating devices. The EO detection system, which exploited the DAST probe, shows the capability to meet this need.

The mean value of detected amplitude in V_{RMS} and SNR without moving the DAST probe for 1 min at the center of the Si-lens at each frequency are summarized in Table 5.3.1. The standard errors were calculated from three distinct measurements. The lowest SNR was approximately 17.5 ± 0.1 dB at 500 GHz, in which the THz power was 1.2 µW (−29.2 dBm). The highest SNR was 33.0 ± 1.9 dB at 300 GHz, in which the THz power was 6.9 µW (−21.6 dBm). The decreasing of the SNR of the measurement coincides with that of the THz output power.

Table 5.3.1: Detected amplitude and SNR without moving DAST probe at different frequencies.

Frequency	30 GHz	60 GHz	125 GHz	300 GHz	500 GHz
Signal (mV)	1.322 ± 0.062	0.428 ± 0.002	3.395 ± 0.020	3.588 ± 0.088	0.477 ± 0.002
SNR (dB)	26.6 ± 0.6	17.7 ± 0.2	33.1 ± 0.6	33.0 ± 1.9	17.5 ± 0.1

The THz distribution from this device was also visualized at 600 GHz with the power of −31.1 dBm, but the sensitivity was insufficient to obtain reliable images. One possible reason for this is that THz frequency has a strong absorption of vapor around 600 GHz [5.38, 5.39]. We verified the THz distribution with and without attaching paper at 500 GHz, owing to the enhanced output power when removing the paper, as shown in Fig. 5.3.2. Figure 5.3.11 shows the experimentally visualized amplitude and phase distributions at 500 GHz without attaching paper. A slight difference between the amplitude images without and with the paper (Fig.

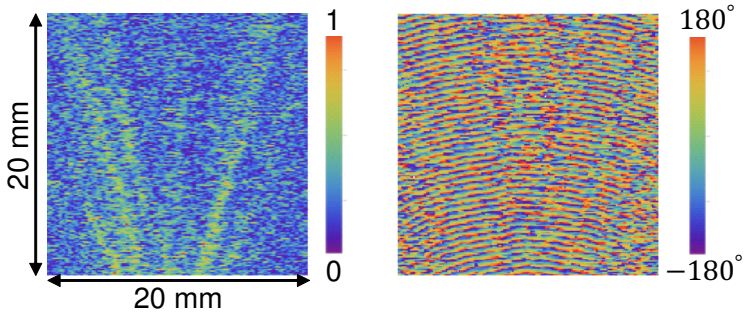

Figure 5.3.12: Visualized THz distributions from the device in XZ-plane at 600 GHz without attaching paper.

5.3.10) can be observed owing to the disturbance caused by leaking optical signal from the device, but the overall radiation can be estimated without the paper.

Figure 5.3.12 shows the experimentally visualized THz distribution at 600 GHz without paper. The detected amplitude and SNR at this frequency were 0.188 ± 0.004 mV and 8.8 ± 0.3 dB, respectively. Owing to the limitation of the SNR, the obtained visualized results are not clear. However, the general radiation diverging in different directions and the malfunction of the spherical phase front distribution can be resolved.

In summary, we have successfully characterized, for the first time, the broadband Si-lens-mounted UTC-PD from 30 GHz to 600 GHz with the minimum output power of 1.2 µW by visualizing the THz distribution in the near-field region using the EO detection system. The focused THz beam into an EO plate at 500 GHz was imaged by measuring the only amplitude by a CCD camera [5.40], but this system cannot scan the EO probe freely for device characterizations. To the best of our knowledge, there have been no reports to date of visualizing the THz radiation in free space for both amplitude and phase distributions at such high frequency and low power by EO measurement. The diagnosis of the malfunction of this device at high frequency can also be obtained by the EO measurement.

5.4 Near-field localization device “Terajet”

5.4.1 Motivation

Terajet [5.41]—the generation of the photonic nanojets [5.42–5.44] in the THz region—is the subject of a growing number of studies owing to its capability of obtaining a subwavelength localization EM field applicable to high-resolution imaging and

microscopy applications [5.45]. The photonic nanojets also exhibit the backscattering enhancement effect that can be applied to detect nanoparticles [5.46], e.g., in optical data storage applications [5.47, 5.48], lithography, and nanopatterning applications [5.49, 5.50].

Initial studies on the generation of photonic nanojets from a mesoscale—a wavelength-dimension—particle, which has the shapes of spheroids and cylinders, was conducted theoretically and experimentally in the light waves region based on the well-known Mie scattering theory [5.42, 5.51, 5.52]. Later, certain experimental studies were demonstrated in the microwave and millimeter wave regions (8–30 GHz) [5.53–5.55] based on an S-parameter measurement or power measurement.

In the THz region, the Terajet has been studied mainly by simulation from cuboids and other shapes [5.56–5.59]. The direct observation and experimental characterization of this phenomenon at the THz frequency are important for the exploitation of these Terajet-generating devices in practical applications. It can also fulfill the academic studies of the Terajet in the EM spectrum from the microwave to light wave regions.

In order to characterize a near-field localization device such as a Terajet, a precise near-field measurement at the THz frequency is necessary. Therefore, the EO detection system was employed to characterize the Terajet generated from a dielectric cube. Among various shapes of Terajet-generating devices, a cube was chosen for the characterization, owing to the simplicity of fabrication and alignment in the experiment. Moreover, dielectric cubes have certain advantages over dielectric spherical particles [5.60]: spheroids generate more elliptical jets than cuboids; with increasing cuboid size and spheroid diameter, the length of the jet increases for cuboids and decreases for spheroids; cuboids allow the attainment of jets with minimal dimensions of $0.5 \times 0.5 \times 0.5$ times the wavelength, but spheroids can produce jets with a minimal diameter of one wavelength. Consequently, these properties of cubes can be exploited in practical applications.

5.4.2 Characterization of Terajet generation

Before the experimental study, we characterized the Terajet generation with different dimensions d_T and refractive index n of the dielectric cube by simulation at 125

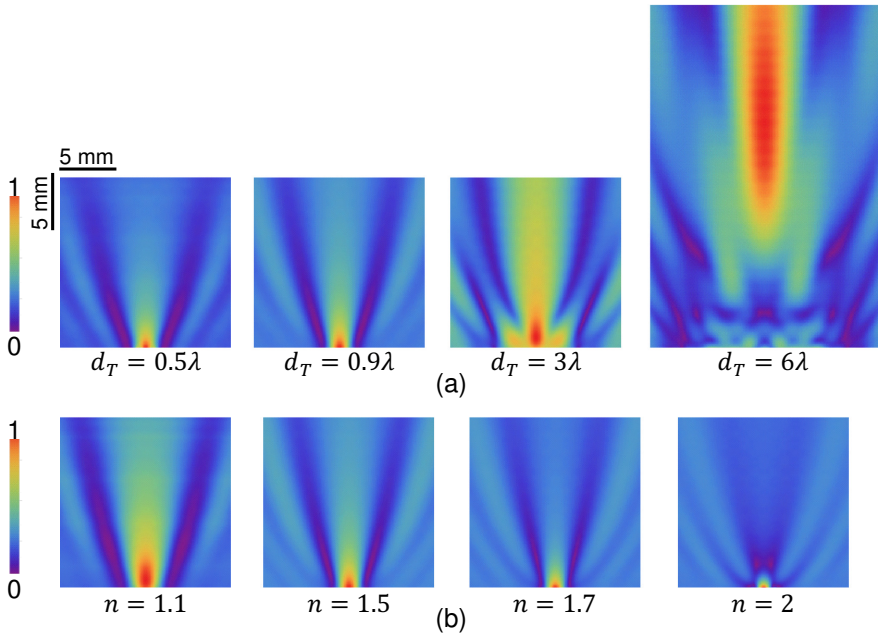

Figure 5.4.1: Simulated 2D amplitude distribution from cube under planar incidence in the E-plane when (a) changing cube dimension with fix refractive index of 1.46 and (b) changing cube refractive index with fix dimension of 1 λ.

GHz to choose the optimal material and dimensions of the cube. The FIT technique with the PML boundary condition by the CST Microwave Studio full-wave simulator was used. The mesh density was optimized by PBA. Figures 5.4.1(a) and 5.4.1(b) show the simulated results of 2D amplitude distributions from the cube in the E-plane under planar incidence when changing d_T with fixed $n = 1.46$ and changing n with fixed $d_T = 1\lambda$, respectively. The Terajet, the red hotspot in each image, tends to move farther from the cube as the size increases and the refractive index of the cube decreases. The size of the hotspot increases as the cube dimensions increase and decreases with increasing refractive index.

The quantitative characterization of the generated Terajet is depicted in Fig. 5.4.2. The length of the Terajet is defined as the distance from the cube surface to the position where the intensity degrades to -3 dB to the maximum intensity in the propagation direction, the z-axis. The focus position is defined as the position that has the maximum intensity; the full width at half maximum (FWHM) is defined as the diameter of the beam where the intensity degrades to half of maximum intensity (-3 dB), respectively. These parameters of the Terajet are illustrated in Fig. 5.4.2(a). The refractive index dependence of the FWHM, focus

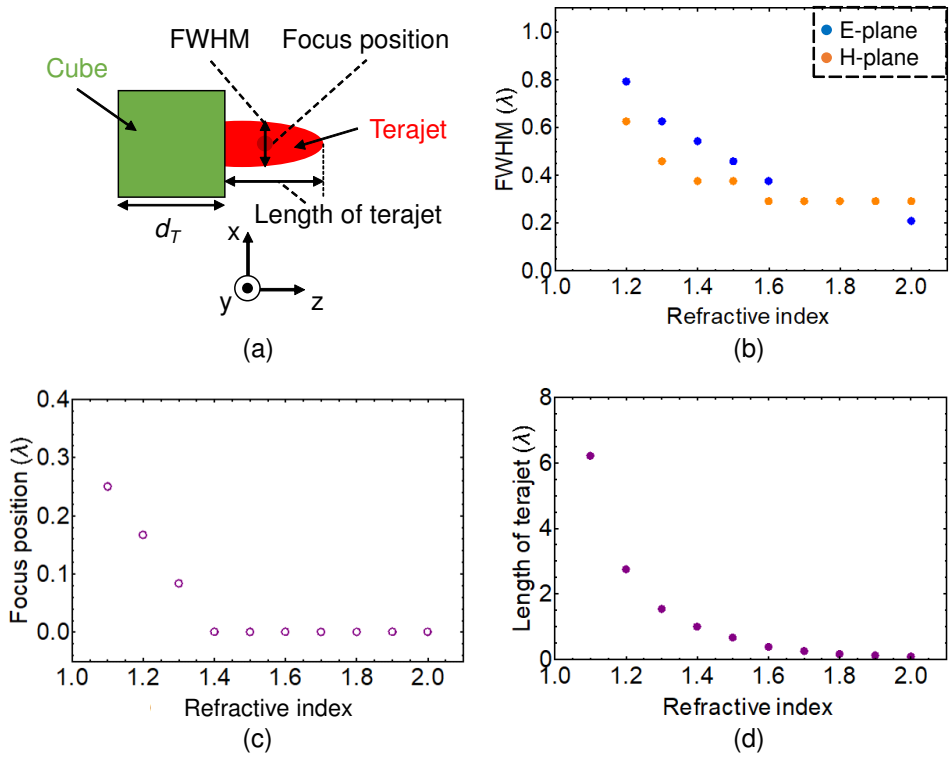

Figure 5.4.2: (a) Definitions and simulated results of (b) FWHM, (c) focus position, and (d) length of Terajet when changing the refractive index of the cube.

position, and length of the Terajet are shown in Figs. 5.4.2(b), 5.4.2(c), and 5.4.2(d), respectively. Note that the dimensions of the cube are fixed at $d_T = 1\lambda$. The obtained FWHM is less than one wavelength and gradually decreases as the refractive index increases, which is an advantageous property for high-resolution imaging applications. However, the focus position and the length of the Terajet also decrease and approach the cube surface as the refractive index increases. A short Terajet length might limit the imaging samples in practical applications. The refractive index of approximately 1.46 was selected, because the length of the Terajet is close to one wavelength and the FWHM is approximately 0.5λ.

Figure 5.4.3 shows the simulated results of the generated Terajet with a refractive index of 1.46 and changing dimensions d_T from 0.5 λ to 6 λ. The FWHM, focus position, and length of the Terajet in Figs. 5.4.3(a), 5.4.3(b), and 5.4.3(c) gradually increase with increasing cube dimensions d_T. In particular, for d_T above 5 λ, the subwavelength FWHM is no longer maintained, the focus position and length of the Terajet also increase such that the cube functions more similarly to a common lens than a Terajet-generating device. Figures 5.4.3(d), 5.4.3(e), and

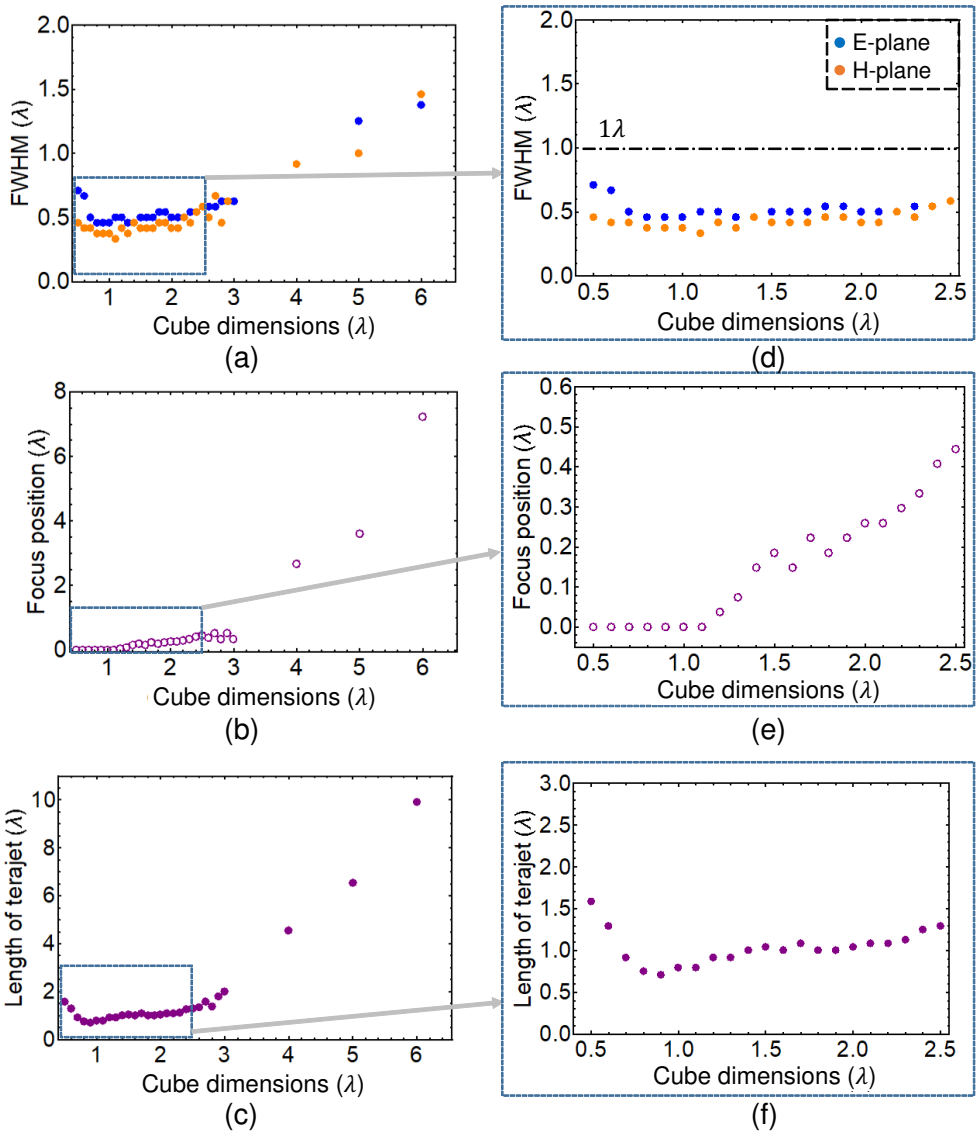

Figure 5.4.3: Simulated results of (a) FWHM, (b) focus position, and (c) length of Terajet when changing the dimensions of the cube; (d), (e), (f): zoomed in graphs of the dashed boxes.

5.4.3(f) show the zoomed in view of the dashed box area. The FWHM below one wavelength was obtained for cube dimensions from 0.5 λ to 2.5 λ. These results indicate that the subwavelength-beam focusing ability of the Terajet generated from the cube can operate in a broad bandwidth, because changing the cube dimensions is equivalent to changing the THz frequency. A cube with dimensions of one wavelength was selected.

A PTFE Teflon was chosen as the material for the cube. The measured refractive index of the Teflon at 125 GHz was approximately 1.46. Figure 5.4.4 shows the homemade cube from the PTFE Teflon, which has the dimensions of $d_T \times d_T \times d_T$

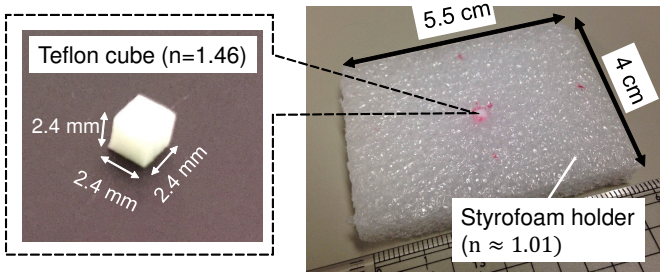

Figure 5.4.4: Homemade Teflon cube placed in a styrofoam holder.

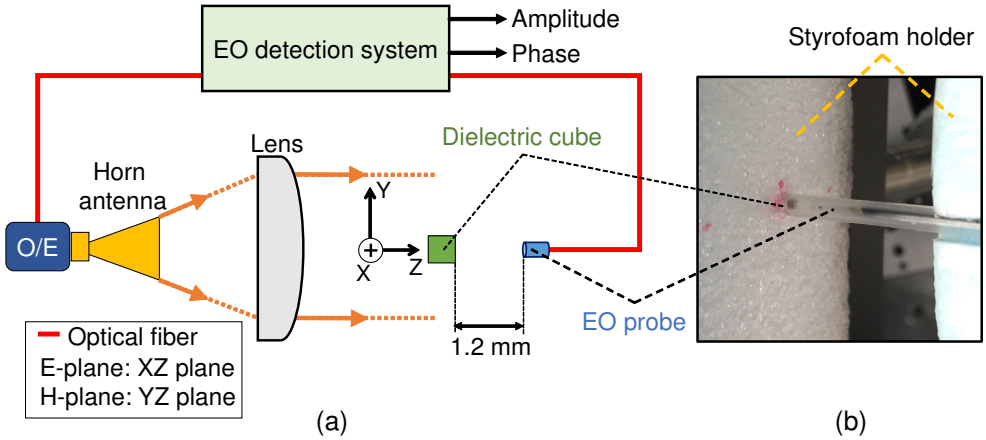

Figure 5.4.5: (a) Experimental setup to characterize Terajet generated from dielectric cube and (b) photograph of the EO probe placed close to the cube.

with $d_T = 2.4$ mm $= \lambda$ at 125 GHz. The cube was placed in a holder made from styrofoam, which has the measured refractive index of 1.01 at 125 GHz. Figures 5.4.5(a) and 5.4.5(b) show the experimental setup to characterize the Terajet generating from the cube and a photograph of the EO probe placed close to the cube. The THz wave generating from the F-band horn antenna at 125 GHz is collimated by the lens and illuminated to the cube. The EO probe was placed at a distance of approximately 0.5–1.2 mm from the cube surface. The E-plane and H-plane are parallel to XZ- and YZ-planes, respectively.

Figures 5.4.6(a) and 5.4.6(b) show the experimentally visualized results of the amplitude and phase distributions at 125 GHz in the XY-, E-, and H-planes with and without the cube, respectively. Figure 5.4.7 depicts their 3D representations. The measured area in each plane was 20 mm × 20 mm, corresponding to $8.3\lambda \times 8.3\lambda$. The sampling interval was set at 0.1 mm (0.04 λ) and the lock-in time constant was 30 ms. The amplitude results in each plane were normalized to the maximum value in the case of the cube. The generation of the Terajet from the center of

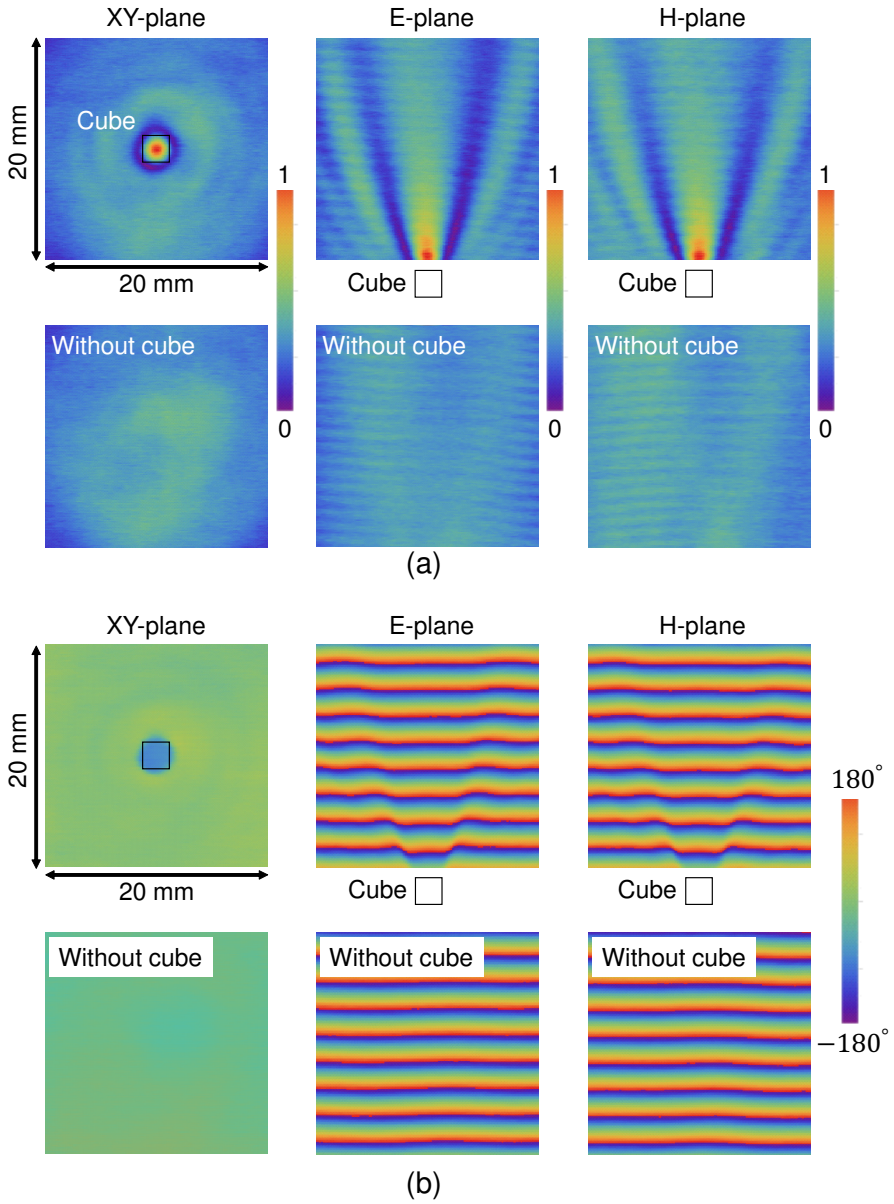

Figure 5.4.6: Visualized (a) amplitude and (b) phase distributions with and without the cube at 125 GHz.

the cube surface can be clearly observed in the amplitude images in the three planes. In the phase images in Fig. 5.4.6(b), the collimated incident beam can be confirmed because the phase front distribution in the XY-plane is the same, and a planar phase front is observed in the E- and H-planes without the cube. Moreover, the Gouy phase shift phenomenon [5.61], which exists in any wave passing through the focus [5.62], was observed at the location where the Terajet was generated.

Figure 5.4.8 shows the experimental images of the intensity enhancement by the cube in each plane. The value in each plane is calculated as follows:

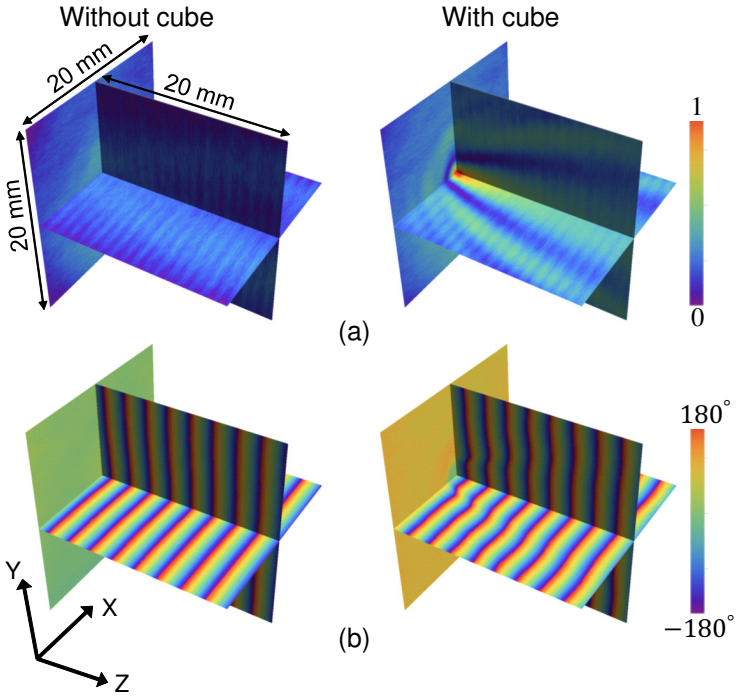

Figure 5.4.7: Visualized 3D representation of THz wave distribution with and without the cube: (a) amplitude and (b) phase.

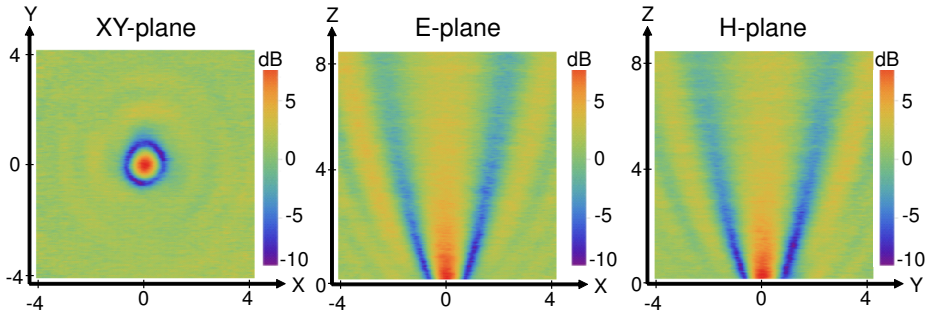

Figure 5.4.8: Visualized results of intensity enhancement by the cube.

$$I_{en} = 20 \log_{10} \frac{A_w}{A_{wo}} \tag{5.4.1}$$

where I_{en} is the intensity enhancement in the THz power. A_w and A_{wo} are the amplitude detected with and without the presence of the cube, respectively. A significant enhancement in the THz power can be observed at the position where the Terajet was generated. Figure 5.4.9 shows the intensity enhancement along the z-axis at the center surface of the cube. The blue solid line and the orange dots denote the simulated and experimental results, respectively. The simulated model of the cube also has dimensions of 2.4 mm × 2.4 mm × 2.4 mm and refractive index of 1.46, as the actual cube. The experimental results are in a good agreement with

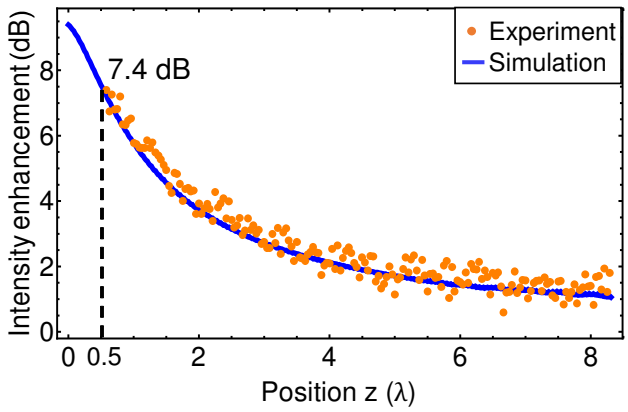

Figure 5.4.9: Intensity enhancement along z-axis.

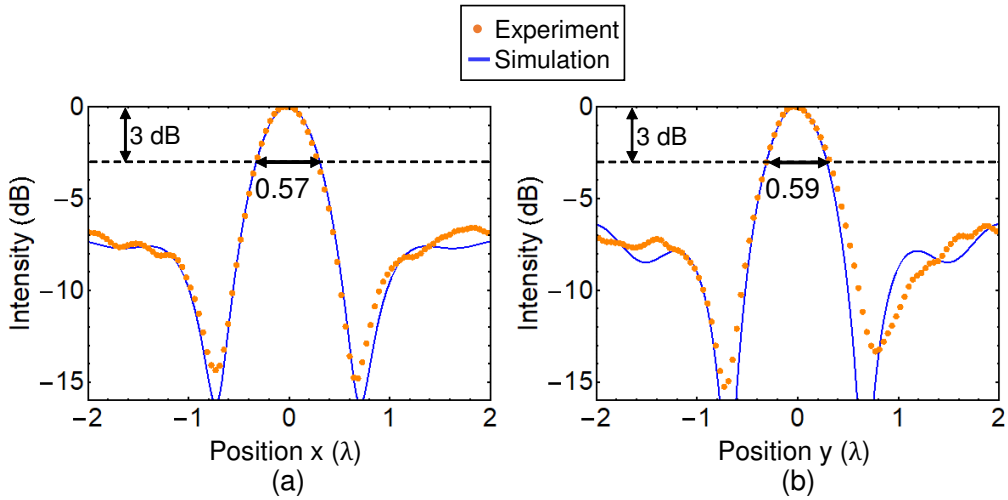

Figure 5.4.10: Beam profile of Terajet in the (a) E- and (b) H-planes.

the simulated results, and show a maximum enhancement of 7.4 dB at a distance of 0.5 λ from the cube, which exponentially decreases.

Figures 5.4.10(a) and 5.4.10(b) show the beam profile along the x- and y-axes, corresponding to E- and H-planes, respectively, at position Z = 0.5 λ. The experimental results shown with the orange dots agree well with the simulated results shown by the blue solid line for both the E- and H-planes. The slight difference between the experimental and simulated results at position $Y > 0.5\,\lambda$ in Fig. 5.4.10(b) is possibly due to a slight misalignment of the cube in the H-plane. The FWHM smaller than 0.6 λ was obtained in both planes. These results indicate that the generation of the Terajet with the subwavelength beam waist was experimentally verified at the THz frequency.

Figure 5.4.11 shows the phase distribution at a distance of 1.2 mm from the cube in the E- and H-planes. A good agreement was obtained between the experimental

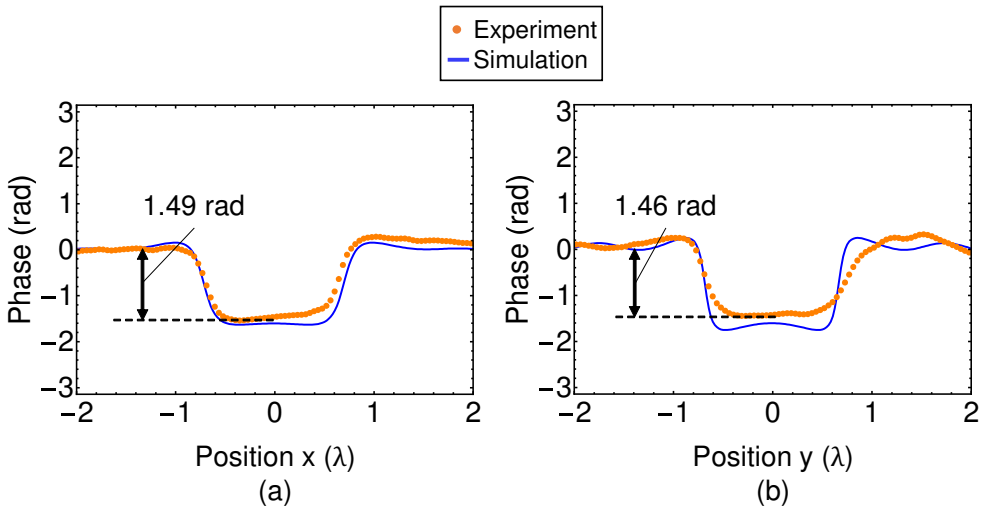

Figure 5.4.11: Phase distribution at a distance of 1.2 mm from cube in (a) E- and (b) H-planes.

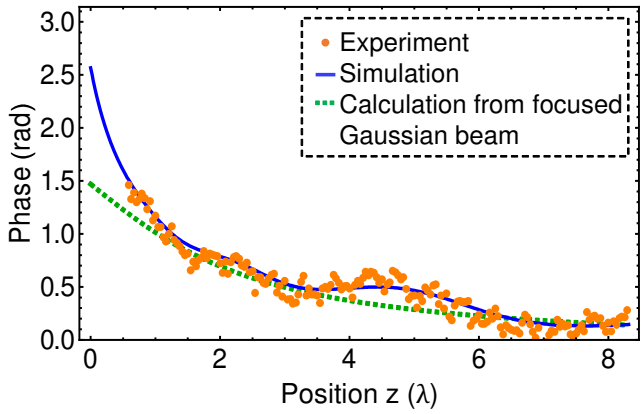

Figure 5.4.12: Gouy phase shift along z-axis of generated Terajet.

results, shown by the orange dots, and the simulated results, shown by the blue solid line. In particular, a Gouy phase shift of approximately 1.5 rad (0.48π) can be observed in the region where the Terajet was generated ($-0.5\,\lambda < X < 0.5\,\lambda$ and $-0.5\,\lambda < Y < 0.5\,\lambda$).

We quantitatively evaluate the Gouy phase shift phenomenon along the z-axis in Fig. 5.4.12. The experimental and simulated results are depicted by the orange dots and blue solid line, respectively. The green dash line depicts the calculated results of the accumulated phase of the focused Gaussian beam with respect to the beam waist. The Gouy phase shift for a focused Gaussian beam by a lens can be calculated by the following equation [5.63]:

$$\phi(Z) = -\arctan\frac{Z}{Z_R} \tag{5.4.2}$$

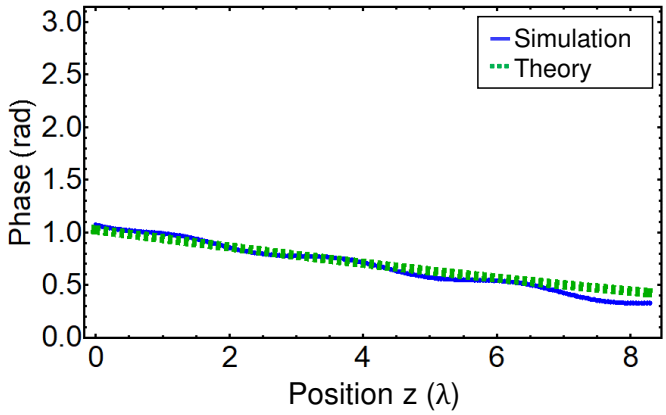

Figure 5.4.13: Simulated Gouy phase shift along z-axis by lens.

where $Z_R = \frac{\pi w_0^2}{\lambda}$ is the Rayleigh range, and $w_0 = 1.25$ mm is the waist size estimated from the experimental amplitude information.

The experimental and simulated results are calculated as follows:

$$\phi_{dif}(Z) = \phi_{cen}(Z) - \phi_{ed}(Z) \tag{5.4.3}$$

where $\phi_{cen}(Z)$ and $\phi_{ed}(Z)$ denote the phase distribution along z-axis at the position center (X = 0) and the edge of the measured area (X = -4.15λ), respectively. We remark that a planar phase front distribution was observed at the edge of the measured area in the phase image with the cube shown in Fig. 5.4.6(b); hence, this area was not affected by the Terajet phenomenon. The experimental results agree with the simulated results. The Terajet Gouy phase shift (blue solid line) is slightly different from the Gouy phase shift of the focused Gaussian beam by the lens (green dashed line) in Fig. 5.4.12. This difference is also observed and confirmed in the experimental results.

Figure 5.4.13 shows the Gouy phase shift along z-axis of the focused beam, which has beam waist of 3.05 mm, by a lens. The simulated result in a blue solid line agrees well with the calculated result theoretically by equation (5.4.2). Therefore, a calculation model of the Gouy phase shift based on focused Gaussian beam by a lens cannot explain the Gouy phase shift of the focused beam by the Terajet. Another model is possibly needed to explain the Terajet Gouy phase. These results indicate that a focused beam based on the Terajet is different from a focused beam by a lens. A precise experimental verification by visualizing both the

amplitude and phase distributions in the THz region are essential to characterize the properties of the Terajet.

5.4.3 Angular characteristics of Terajet

Angular variation is one of the characteristics determining the angular scanning property of an imaging system. The Terajet generated from a spheroid particle does not change with variation in the angle of the incident illumination, owing to its point-symmetric structure. In contrast, the cube does not exhibit a point-symmetric structure. Therefore, the characteristics of the Terajet generated from the cube under oblique illumination need to be investigated for practical imaging applications. A theoretical simulation of a Terajet under oblique illumination based on the amplitude distribution was investigated [5.59]. In this study, the characteristics of Terajets generated from different angles of illuminations are characterized experimentally by the EO detection system.

In particular, the Gouy phase anomaly of the Terajet was examined carefully. We remark that the Gouy phase anomaly has attracted considerable attention owing to its importance in many applications, including imaging [5.64]. The exploitation of the Gouy phase anomaly to enhance the depth resolution of a THz tomography system based on the destructive interferometry technique was proposed [5.65]. The study of the variation of the Gouy phase anomaly can have an impact on those imaging applications when employing the generation of the Terajet to enhance the spatial resolution in such systems.

Figures 5.4.14(a), 5.4.14(b), and 5.4.14(c) show the photograph of the experimental setup to characterize the angular characteristic of the generated Terajet, its front view, and a simplified schematic, respectively. In the experiment, the collimated beam produced by the F-band horn antenna and the lens was rotated around the same cube in the previous section. The THz distribution in the XZ-plane (E-plane) were measured by the EO probe at 125 GHz. The u-axis is parallel to the propagation direction of the incident beam and the v-axis is perpendicular to the u-axis or parallel to the E-field vector of the incident beam. When the E-field of the incident beam is parallel to the rotation plane, we define it as TM excitation,

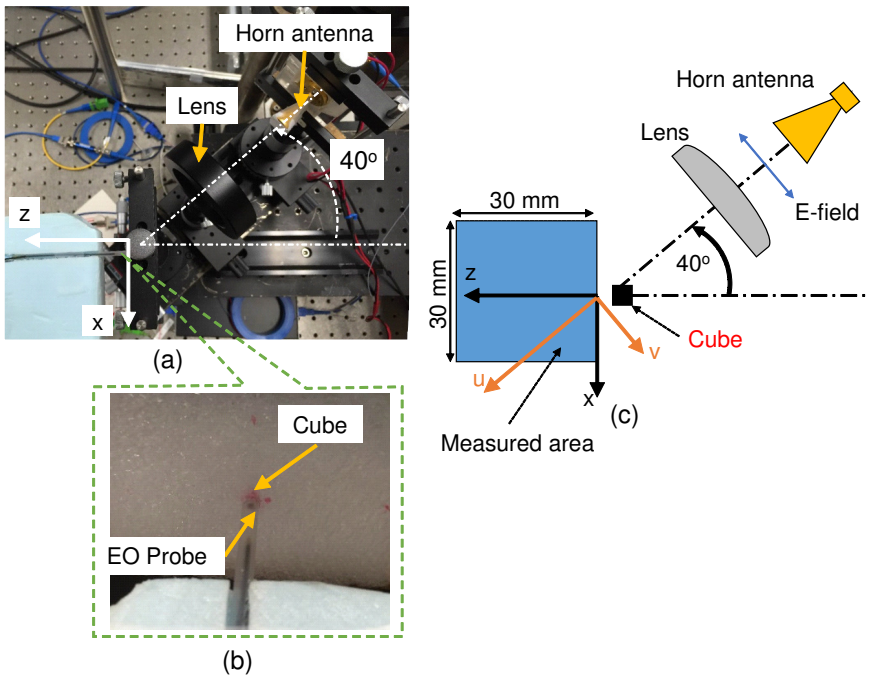

Figure 5.4.14: (a) Experimental setup photograph to characterize angular characteristic of the Terajet, (b) front view, and (c) simplified schematic.

and when the E-field of the incident beam perpendicular to the rotation plane, we define it as TE excitation. In the experiment, the E_x component of the E-field was detected by the EO probe by adjusting the polarization of the EO probe parallel to x-axis, and the cube was excited by the TM excitation. The counterclockwise and clockwise rotations are defined by positive and negative angles, respectively. The EO probe was placed at a distance of approximately 1 mm (0.4 λ) from the cube surface.

Figures 5.4.15(a) and 5.4.15(b) show the experimentally visualized phase and amplitude distributions with the cube under incident angle of 40°. The measured area was 30 mm × 30 mm and the sampling interval was 0.2 mm (0.08 λ). The maximum SNR and phase standard deviation, measured at the center of the cube, were 33 dB and 0.04 rad, respectively. We can clearly observe a hotspot and phase anomaly at the position where the Terajet was generated.

Figure 5.4.16(a) depicts the measured phase difference between two cases, with and without the cube at an incident angle of 40°. This is the experimental 2D image of the Gouy phase anomaly of the generated Terajet under oblique incidence. The

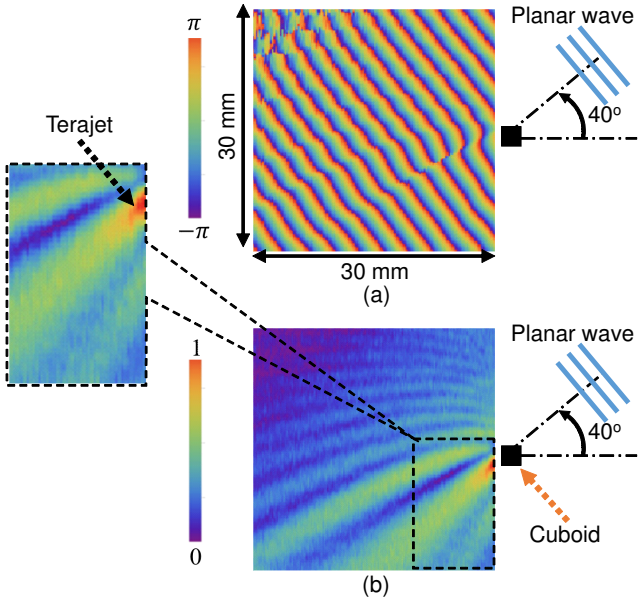

Figure 5.4.15: Visualized (a) phase and (b) amplitude distributions of generated Terajet at an incident angle of 40° at 125 GHz.

phase difference at the position near the cube (around line A) is large (blue color) and decreases (green color) at the position farther from the cube (around line B).

The cutting lines at positions corresponding to line A ($u_A = 2\,\lambda$) and line B ($u_B = 6\,\lambda$) are shown in Figs. 5.4.16(b) and 5.4.16(c), respectively. The orange dots and the blue solid line represent the experimental and simulated results, respectively. The experimental results show a good agreement with the simulated results for both positions at lines A and B. At the position crossing the hotspot at line A in Fig. 5.4.16(b) ($-\lambda < v < \lambda$), an asymmetric phase distribution of the Gouy phase anomaly can be observed. In particular, $\phi_A(v_1) = -1.12$ rad at position $v_1 = -0.7\,\lambda$ and $\phi_A(v_2) = -0.67$ rad at position $v_2 = 0.7\,\lambda$. The phase difference is $\Delta\phi(A) = |\phi_A(v_2) - \phi_A(v_1)| = 0.45$ rad. However, the phase distribution of the Gouy phase anomaly at line B is more symmetric. In particular, at the same position on the v-axis at line B in Fig. 5.4.16(c), $\phi_B(v_1) = -0.41$ rad for $v_1 = -0.7\,\lambda$ and $\phi_B(v_2) = -0.34$ rad for $v_2 = 0.7\,\lambda$. The phase difference is $\Delta\phi(B) = |\phi_B(v_2) - \phi_B(v_1)| = 0.07$ rad. This result indicates that the asymmetric Gouy phase anomaly occurs at the point where the hotspot is generated. Subsequently, at positions farther from the focus region, the Gouy phase anomaly becomes symmetric.

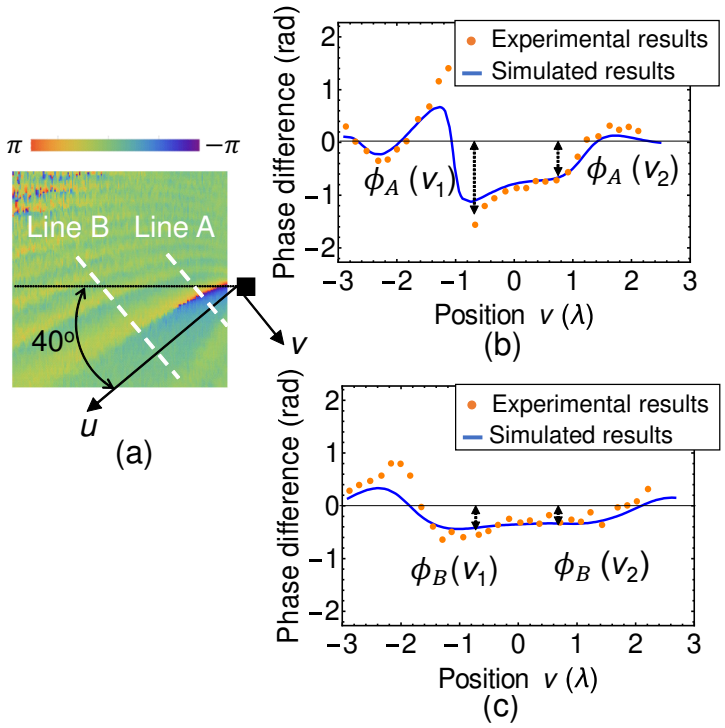

Figure 5.4.16: (a) Measured phase difference with and without the cube at an incident angle of 40°; 1D results (b) at line A, and (c) at line B.

Figures 5.4.17(a) and 5.4.17(b) illustrate the observed Gouy phase anomaly of the Terajet under normal incidence to the cube surface (Fig. 5.4.11) and under oblique incidence (Fig. 5.4.16), respectively. In this figure, the k-axis is denoted as the axis perpendicular to the phase distribution of the Gouy phase anomaly between positions v_1 and v_2. α is defined as the deviation angle between the k-axis and the u-axis. In the case of normal incidence to the cube surface, the phase difference between positions v_1 and v_2 is 0 (Fig. 5.4.17(a)), which means that the deviation angle α is 0°. However, in the case under oblique incidence in Fig. 5.4.17(b), α is not 0°, which means that there is a deviation between the k- and u-axes. We refer the asymmetry of the phase distribution here as the asymmetric Gouy phase anomaly. When considering the phase distribution of the Gouy phase anomaly over the position range of $v_1 < v < v_2$ as linear, we can calculate the deviation angle α between the k-axis, which is normal to the slope of the phase distribution over the range $v_1 < v < v_2$, and the u-axis based on a simple geometric equation as follows:

$$\alpha = \mathrm{Arctan}\frac{\Delta\phi}{L\,\frac{2\pi}{\lambda}} \tag{5.4.4}$$

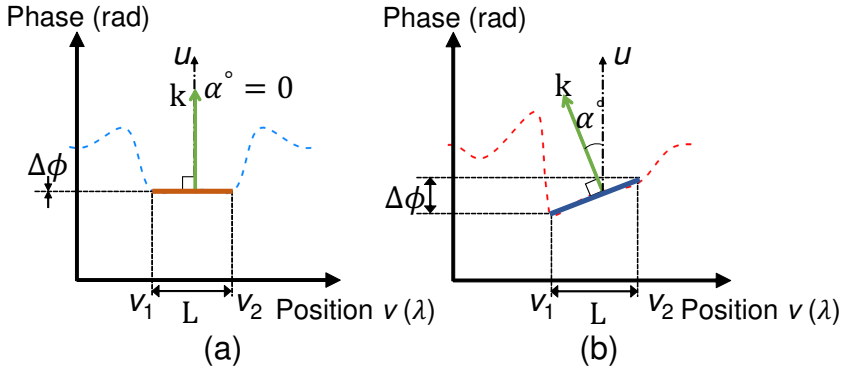

Figure 5.4.17: Illustration of the Gouy phase anomaly in a Terajet under (a) normal illumination and (b) oblique illumination.

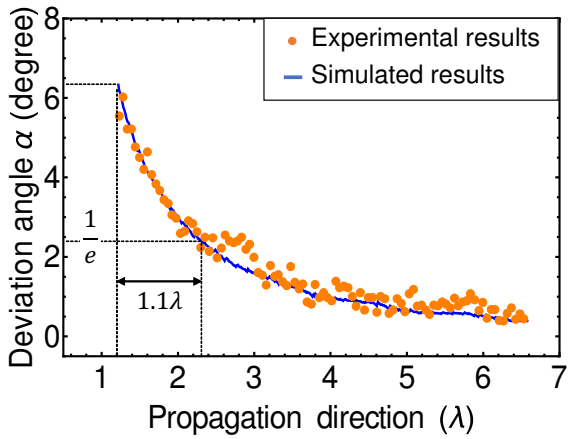

Figure 5.4.18: Experimental deviation angle α between k-axis and u-axis along the propagation direction of the Terajet at an incident angle of 40°.

where $\Delta\phi$ and $L = |v_2 - v_1|$ denote the phase difference between positions v_1 and v_2, and the distance between these positions, respectively.

We quantitatively evaluated the asymmetric Gouy phase anomaly experimentally and by simulation. Figure 5.4.18 shows the deviation angle α along the propagation direction, u-axis, of the Terajet at an incident angle of 40°. The orange dots and blue solid line represent the experimental and simulated results, respectively. The experimental results are in a good agreement with the simulated results. At the position $u = 1.3\,\lambda$ from the cube, the experimental deviation angle is approximately 6°. The deviation angle decreases exponentially as the waves propagate farther from the cube, and it has decreased by a factor of $\frac{1}{e}$ by the position $u = 2.4\,\lambda$. This result indicates that the asymmetric Gouy phase anomaly occurs in the hotspot (approximately two wavelengths away from the cube). Sub-

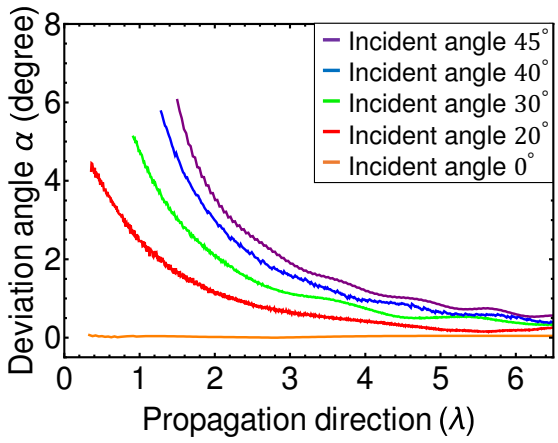

Figure 5.4.19: Angular characteristics of the deviation angle α between k-axis and u-axis.

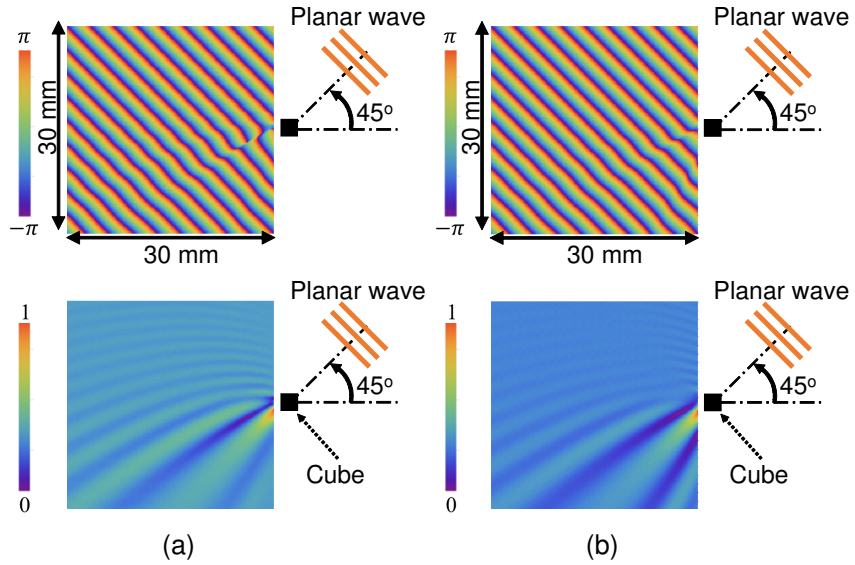

Figure 5.4.20: Simulated results of the Terajet generated under 40° oblique illumination of (a) E_x and (b) E_v components.

sequently, the deviation angle α approaches 0°, which means that the direction of the phase distribution of the generated Terajet becomes parallel to the direction of the incident planar waves.

The simulated results of the deviation angle α along the propagation direction as a function of the angle of the incident illumination on the cube from 0° to 45° of the E_x component is shown in Fig. 5.4.19. At the incident angle of 0°, the deviation angle is almost 0°, which means that Gouy phase anomaly is symmetric for normal illumination. The slopes of these deviations increase as the angle of the incident beam increases. This result indicates that Gouy phase anomalies are

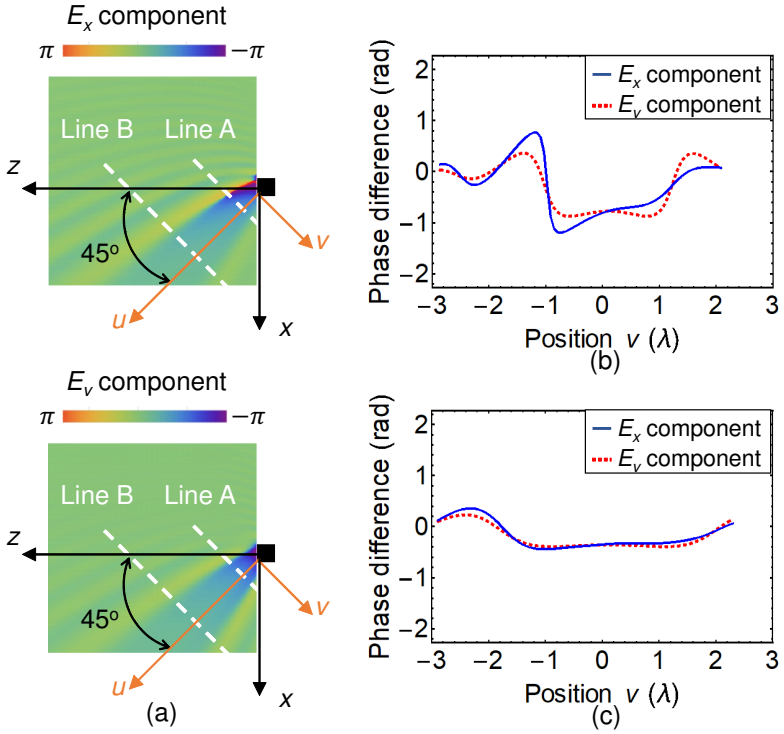

Figure 5.4.21: (a) Simulated phase difference with and without the cube under 40° oblique illumination of E_x and E_v components; 1D results at (b) line A, and (c) line B.

more asymmetric when the angle of the incidence increases from 0° to 45°. After a deviation of approximately 6° at positions near the cube ($u < 2\,\lambda$), the deviation angle decreases $\frac{1}{e}$ times when propagating about $1\,\lambda$ for all cases.

The above results are the results when considering E_x component of the E-field. When considering the E_v component, we obtained different results. Figures 5.4.20(a) and 5.4.20(b) show the simulated amplitude and phase distributions of the E_x and E_v components of the generated Terajet under an incident angle of 45°. The generation of the Terajet can be confirmed in the amplitude images in both cases. However, the phase distributions are different.

The 2D Gouy phase anomalies of E_x and E_v components are shown in Fig. 5.4.21(a), and the cutting lines at line A and line B are depicted in Figs. 5.4.21(b) and 5.4.21(c), respectively. The blue solid line and red dashed line represent the phase of the E_x and E_v components, respectively. The asymmetric phase can be observed for the E_x component (Fig. 5.4.21(b)), in contrast to the phase of the E_v component, which is symmetric. After propagating several distances, the phases

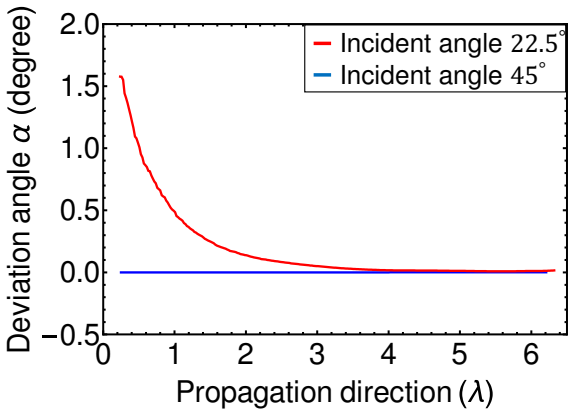

Figure 5.4.22: Simulated deviation angle α between k-axis and u-axis along propagation direction of the E_v component under 22.5° and 45° oblique illumination.

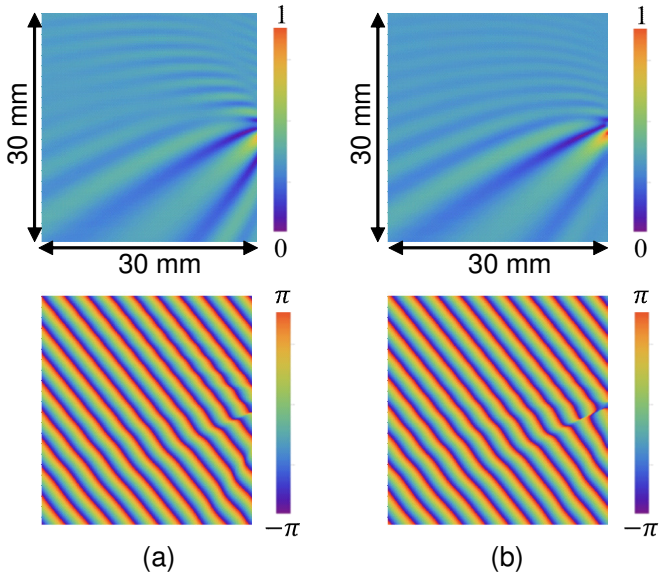

Figure 5.4.23: Simulated results of the Terajet generated under 40° oblique (a) TE and (b) TM excitations.

of two components are the same and become symmetric (Fig. 5.4.21(c)).

Figure 5.4.22 shows the simulated deviation angle α along the propagation direction of the E_v component under 22.5° (red line) and 45° (blue line) oblique incidences. At an illumination angle of 22.5°, α larger than 0° can be observed. This indicates that the E_v component also exhibits the asymmetric Gouy phase anomaly. At an illumination angle of 45°, in contrast with large deviation angle α of the E_x component (purple line in Fig. 5.4.19), the E_v component shows the symmetric Gouy phase anomaly and the deviation angle is almost 0° (purple line in Fig. 5.4.22). The reason is that at the incident point of the cube, there is

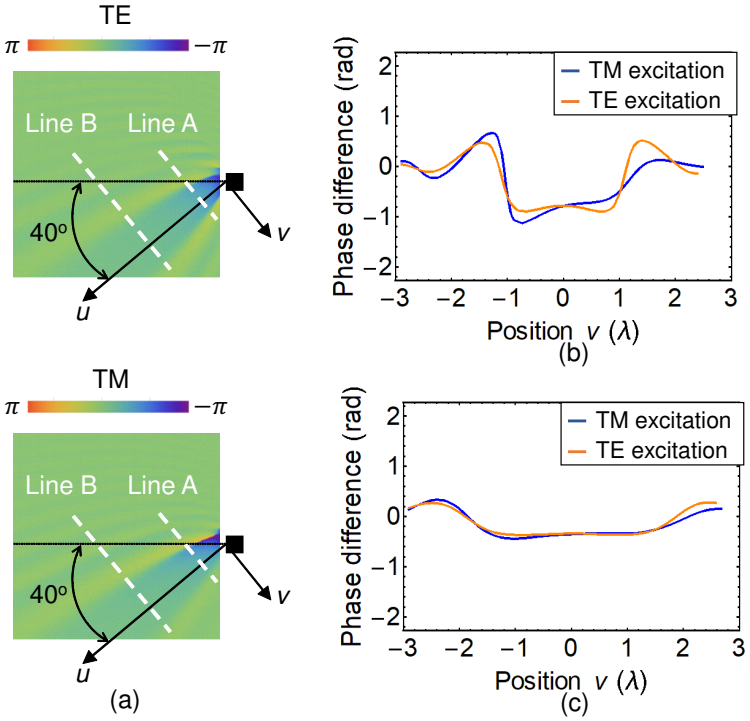

Figure 5.4.24: (a) Simulated phase difference with and without cube under 40° oblique TE and TM excitations; 1D results at (b) line A, and (c) line B.

no boundary of the refractive index in the polarization of the E-field E_v at the illumination angle of 45°.

We have examined the asymmetric Gouy phase anomaly of the Terajet under TM excitation. Next, we verify this phenomenon under TE excitation of the E_x component. Figure 5.4.23 shows the simulated amplitude and phase distributions of the generated Terajet under 40° oblique TE and TM excitations. In the amplitude images, the Terajet generation can be confirmed for both excitations.

In the phase images, the Gouy phase anomaly shows the difference between two types of excitations. We evaluate the phase difference with and without the cube under TE and TM excitations in Fig. 5.4.24. The cutting lines at line A and line B in Fig. 5.4.24(a) are shown in Fig. 5.4.24(b) and Fig. 5.4.24(c), respectively. The Gouy phase anomaly was asymmetric for TM excitation but symmetric for TE excitation (Fig. 5.4.24(b)).

Figure 5.4.25 shows the simulated results of the deviation angle α along the propagation direction of the u-axis of two exciting modes at an incident angle of 40°. The blue and red lines denote the TM and TE excitations, respectively. As

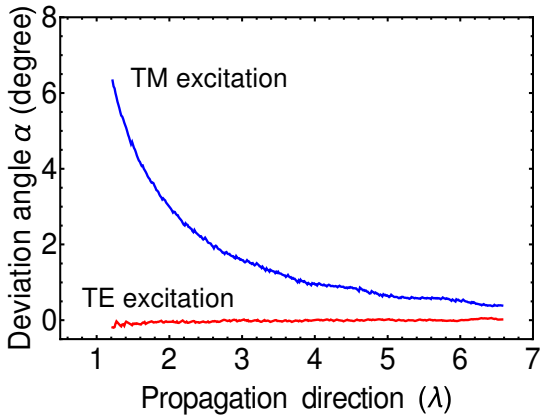

Figure 5.4.25: Simulated deviation angle α between k-axis and u-axis along propagation direction of Terajet under 40° oblique TE and TM excitations.

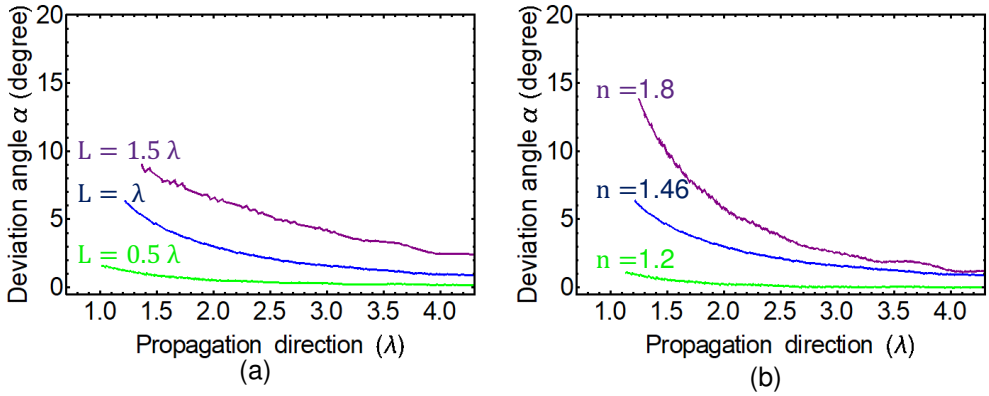

Figure 5.4.26: Simulated results of dependences of deviation angle α on (a) cube dimension and (b) refractive index at incident angle of 40°.

for the TE excitation, α is 0° in contrast with the TM excitation. This indicates that the asymmetric Gouy phase anomaly occurs for the TM excitation but not for the TE excitation.

The dependences of the deviation angle α along the propagation direction on the dimensions and the refractive indices of the cube are numerically evaluated at the illumination angle of 40° at 125 GHz in Figs. 5.4.26(a) and 5.4.26(b), respectively. In Fig. 5.4.26(a), the refractive index is fixed at 1.46. α increases gradually as the cube size increases from 0.5 λ to 1.5 λ. In Fig. 5.4.26(b), the cube size is fixed at $d_T = \lambda$. The slope of the deviation angle increases significantly as the refractive index increases from 1.2 to 1.8.

We summarize the found conditions in which the asymmetric Gouy phase anomaly occurs in this study in Fig. 5.4.27. The Gouy phase anomaly is symmetric

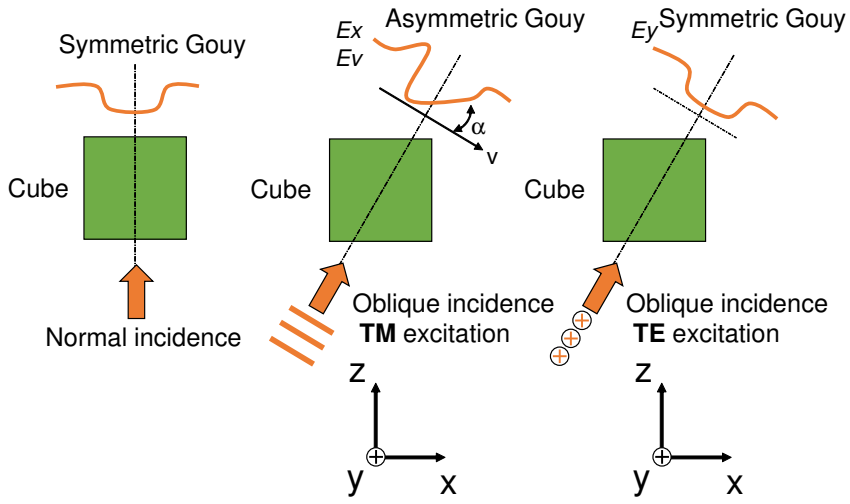

Figure 5.4.27: Summary of the conditions in which the asymmetric Gouy phase anomaly occurs.

for Terajet generated under normal incidence perpendicular to the cube surface; under TM-mode 45° oblique incidence with an E_v component; and under TE-mode oblique incidence. The Gouy phase anomaly is asymmetric for Terajet generated under TM-mode oblique incidence with both E_x and E_v components. From these results, it can be said that the asymmetric Gouy phase anomaly, which is found for both E_x and E_v components of the Terajet generated from the dielectric cube under the TM-mode oblique illuminations, relates to the presence of the boundary of the refractive index in the polarization direction of the E-field at the incident point.

Finally, the beam profiles of the generated Terajet under different oblique incidences are evaluated by experiment and simulation. Figure 5.4.28 shows the experimentally visualized 2D amplitude and phase distributions with and without the cube at different incident angles from $-45°$ to $40°$. The measured area was 30 mm $\times$ 30 mm and the sampling interval was 0.2 mm. The amplitude images with and without the cube at each incident angle were normalized to the maximum value with the cube. We can clearly observe the generation of the Terajet in all cases and its direction also changes when changing the incident angle. The phase images without the cube are planar for all cases, which confirms the precise planar wave illumination at each angle.

Figure 5.4.29 shows the beam profiles at a distance of approximately 0.5 λ from

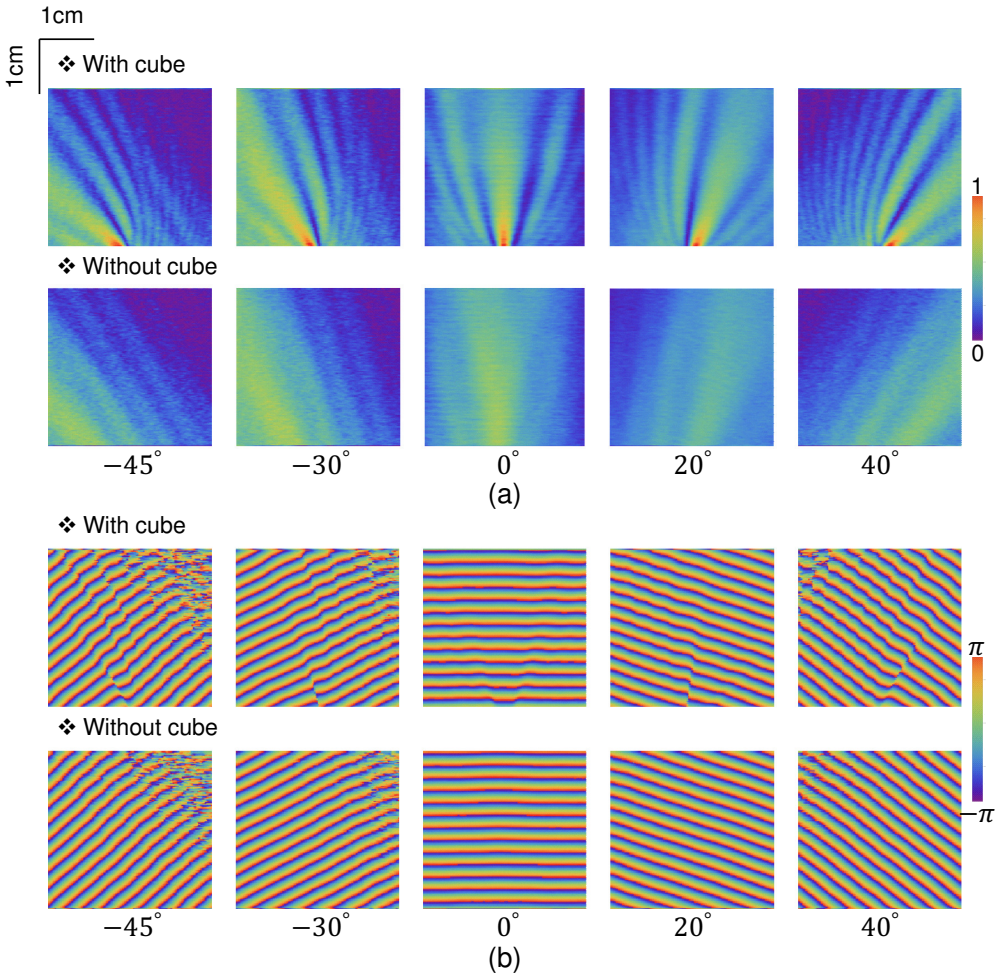

Figure 5.4.28: Visualized (a) amplitude and (b) phase distributions with and without cube at different illumination angles from −45° to 40°.

the cube of the generated Terajet under different illumination angles. Equation (5.4.1) was used to calculate the beam profiles from the measured amplitude. The calculated intensity distribution was normalized to the maximum value in each case of the oblique illumination. The solid line and dots represent the simulated and experimental results, respectively. Different colors denote different incident angles. The experimental results agree well with the simulated results, and the position of the peak intensity are varied within two wavelengths as the illumination angles change from −45° to 40°.

The angular dependence of the output angle of the generated Terajet and its FWHM are characterized in Fig. 5.4.30. The output angle of the generated Terajet

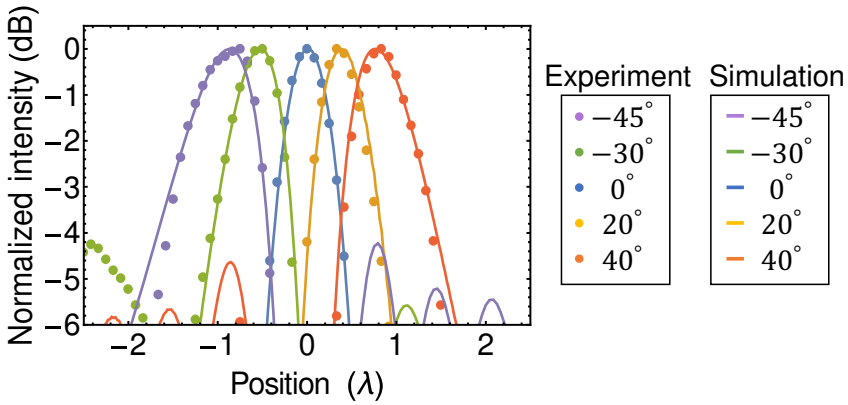

Figure 5.4.29: Experimental and simulated results of the beam profiles of the generated Terajets under different illumination angles.

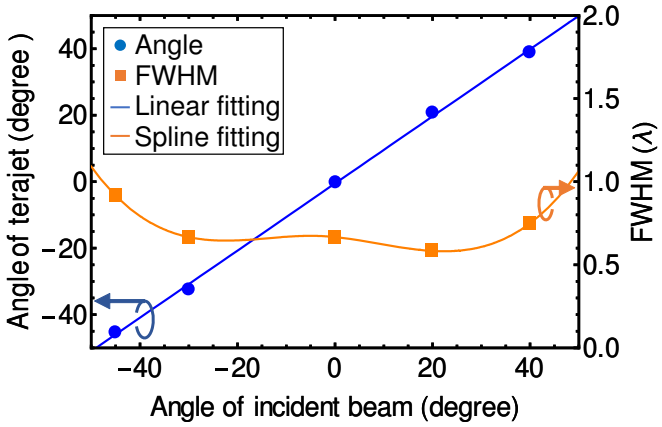

Figure 5.4.30: Experimental results of the angular characteristic of the output angle and FWHM of the generated Terajet.

was evaluated based on the peak values of the measured 2D amplitude distribution in the E-plane in Fig. 5.4.28. The linearity and the identicalness of the angle between the generated Terajet and the incident beam were confirmed. The FWHM value of less than one wavelength was obtained within an incident angle of ±45° at a distance of approximately 0.5λ from the cube. This result indicates that the subwavelength focusing capability of the Terajet is maintained with different incident angles. Here, we note that the common experimental standard error when evaluating the FWHM is approximately 0.05 λ.

5.5 Conclusion

In this chapter, we have employed the EO detection system to practically characterize different THz devices, including an antenna, MHA, spherical-wave generation device, and Terajet. The motivation and necessity of characterizing these devices, as well as the impact of the EO measurement were described.

The near-to-far-field transformation technique was exploited to obtain the radiation patterns of the antenna. The experimental results agreed well with the simulated results. This indicates the reliability of this technique. The benefits of compact and fast measurement can be achieved by this technique for the THz antenna characterization.

We experimentally verified the beam collimating phenomenon in the MHA for the first time. The MHA showed the collimating ability with a flexible focal length. The physical mechanism of the MHA was experimentally explained based on the consideration of the radiation patterns for the first time. The MHA exhibits a k-vector filtering effect, in which the k-vector perpendicular to its surface can transmit, but other k-vectors are filtered.

The characterization of the spherical-wave generation device was the first THz device characterization up to 500 GHz. The obtained results indicated the impact of the EO measurement to diagnose malfunctions of this device in a broad bandwidth.

The Terajet generation phenomenon was experimentally visualized for the first time. The details experimental and simulated studies of this phenomenon at different illumination conditions were described. The asymmetric Gouy phase anomaly was also characterized. The subwavelength FWHM of 0.6 λ was experimentally verified. Moreover, this property is maintained for a wide incident angle of $\pm 45^{\circ}$. It indicated that the Terajet-generating device can work as a novel flat focusing device. The practical applications of the Terajet are discussed in the next chapter.

References

[5.1] A. Hirata, R. Yamaguchi, T. Kosugi, H. Takahashi, K. Murata, T. Nagatsuma, N. Kukutsu, Y. Kado, N. Iai, S. Okabe, S. Kimura, H. Ikegawa, H.

Nishikawa, T. Nakayama, and T. Inada, *"10-Gbit/s wireless link using InP HEMT MMICs for generating 120-GHz-band millimeter-wave signal,"* IEEE Trans. Microw. Theory Techn., **57**, pp. 1102-1109, 2009.

[5.2] D. Kim, J. Hirokawa, K. Sakurai, M. Ando, T. Takada, T. Nagatsuma, J. Takeuchi and A. Hirata, *"Design and measurement of the plate laminated waveguide slot array antenna and its feasibility for wireless link system in the 120 GHz band,"* IEICE Trans. Commun., **E96-B**, pp. 2102-2111, 2013.

[5.3] T. Nagatsuma, K. Oogimoto, Y. Inubushi, and J. Hirokawa, *"Practical considerations of terahertz communications for short distance applications,"* Nano Commun. Netw., **10**, pp. 1-12, 2016.

[5.4] C. A. Balanis, *"Antenna theory: analysis and design,"* Third Edition, Wiley, 2005.

[5.5] N. Hidaka, K. Kobayashi, H. Sugama, R. Usui, Y. Tanabe, and O. Hashimoto, *"Log-periodic dipole antenna arary-type optical electric field sensor,"* IEICE Trans. Electron., **E88-C**, pp. 98-104, 2005.

[5.6] F. Cecelja, B. Balachandran, M. Berwick, M. Soghomonian, and S. Cvetkovic, *"Optical sensors for the validation of electromagnetic field distributions in biological phantoms,"* SPIE Proc. Fiber Optics and Laser Sensors XIII, **2510**, pp. 244-254, 1995.

[5.7] S. Wakana, T. Ohara, M. Abe, E. Yamazaki, M. Kishi, and M. Tsuchiya, *"Fiber-edge electrooptic magnetooptic probe for spectral-domain analysis of electromagnetic field,"* IEEE Trans. Microw. Theory Techn., **48**, pp. 2611-2616, 2000.

[5.8] T. Ohara, M. Abe, S. Wakana, M. Kishi, M. Tsuchiya and S. Kawasaki, *"Two-dimensional field mapping of microstrip lines with a band pass filter or a photonic bandgap structure by fiber-optic EO spectrum analysis system,"* Proc. IEEE Topical Meeting Microw. Photonics, pp. 210-213, 2000.

[5.9] H. Togo, A. Sasaki, A. Hirata, and T. Nagatsuma, *"Characterization of millimeter-wave antenna using photonic measurement techniques,"* International Journal of RF and Microwave Computer-Aided Engineering, **14**, pp. 290-297, 2004.

[5.10] T. Nagatsuma, H. Ito, and T. Ishibashi, *"High-power RF photodiodes and their applications,"* Laser & Photon. Rev., **3**, pp. 123-137, 2009.

[5.11] T. Ishibashi, Y. Muramoto, T. Yoshimatsu, and H. Ito, *"Unitraveling-carrier photodiodes for terahertz applications,"* IEEE J. Sel. Topics Quantum Electron., **20**, 3804210, 2014.

[5.12] E. R. Brown, F. W. Smith, and K. A. Mclntosh, *"Coherent millimeter-wave generation by heterodyne conversion in low-temperature-grown GaAs photoconductors,"* J. Appl. Phys., **73**, pp. 1480-1484, 1993.

[5.13] R. C. Johnson, H. A. Ecker, and J. S. Hollis, *"Determination of far-field antenna patterns from near-field measurements,"* Proc. IEEE., **61**, pp. 1668-1694, 1973.

[5.14] A. D. Yaghjian, *"An overview of near-field antenna measurements,"* IEEE Trans. Antennas Propag., **AP-34**, pp. 30-45, 1986.

[5.15] D. J. Lee and J. F. Whitaker, *"An optical-fiber-scale electro-optic probe for minimally invasive high-frequency field sensing,"* Opt. Express, **16**, pp. 21587-21597, 2008.

[5.16] M. Naftaly and R. Dudley, *"Methodologies for determining the dynamic ranges and signal-to-noise ratios of terahertz time-domain spectrometers,"* Opt. Lett., **34**, pp. 1213-1215, 2009.

[5.17] E. T. Whittaker, *"On the functions which are represented by the expansions of interpolation-theory,"* Proc. Roy. Soc. Edinburgh, **35**, pp. 181-194, 1915.

[5.18] D. T. Paris, W. M. Leach, Jr., and E. B. Joy, *"Basic theory of probe-compensated near-field measurements,"* IEEE Trans. Antennas Propag., **AP-26**, pp. 373-379, 1978.

[5.19] P. J. Chiu, D. C. Tsai, and Z. M. Tsai, *"Fast near-field antenna measurement technique,"* Proceedings of European Microwave Conference (EuMC), pp. 594-597, 2015.

[5.20] C. A. Balanis, *"Antenna theory; analysis and design,"* Wiley, Third Edition, pp. 66-68, 2005.

[5.21] J. He, J. Ye, X. Wang, Q. Kan, and Y. Zhang, *"A broadband terahertz ultrathin multi-focus lens,"* Sci. Rep., **6**, p. 28800, 2016.

[5.22] R. Mendis, M. Nagai, Y. Wang, N. Karl, and D. M. Mittleman, *"Terahertz artificial dielectric lens,"* Sci. Rep., **6**, p. 23023, 2016.

[5.23] N. V. Chernomyrdin, M. E. Frolov, S. P. Lebedev, I. V. Reshetov, I. E. Spektor, V. L. Tolstoguzov, V. E. Karasik, A. M. Khorokhorov, K. I. Koshelev, A. O. Schadko, S. O. Yurchenko, and K. I. Zaytsev, *"Wide-aperture aspherical lens for high-resolution terahertz imaging,"* Rev. Sci. Instrum., **88**, p. 014703, 2017.

[5.24] T. W. Ebbesen, H. J. Lezec, H. F. Ghaemi, T. Thio, and P. A. Wolf, *"Extraordinary optical transmission through sub-wavelength hole arrays,"* Nature, **391**, pp. 667-669, 1998.

[5.25] F. Miyamaru, M. Kamijyo, K. Takano, M. Hangyo, H. Miyazaki, and M. W. Takeda, *"Characteristics and generation process of surface waves excited on a perfect conductor surface,"* Opt. Express, **18**, pp. 17576-17583, 2010.

[5.26] F. Beijnum, P. J. Veldhoven, E. J. Geluk, M. J. A. Dood, G. W. Hooft, and M. P. Exter, *"Surface plasmon lasing observed in metal hole arrays,"* Phys. Rev. Lett., **110**, p. 206802, 2013.

[5.27] R. Gordon, A. G. Brolo, D. Sinton, and K. L. Kavanagh, *"Resonant optical transmission through hole-arrays in metal films physics and applications,"* Laser & Photon. Rev., **4**, pp. 311-335, 2010.

[5.28] F. J. Garcia-Vidal, L. Martin-Moreno, and J. B. Pendry, *"Surfaces with holes in them new plasmonic metamaterials,"* J. Opt. A Pure Appl. Opt., **7**, pp. S97-S101, 2005.

[5.29] H. Lic and P. Lalanne, *"Microscopic theory of the extraordinary optical transmission,"* Nature, **452**, pp. 728-731, 2008.

[5.30] T. Nagatsuma, S. Hisatake, M. Fujita, H. H. Nguyen Pham, K. Tsuruda, S. Kuwano, and J. Terada, *"Millimeter-wave and Terahertz-wave applications enabled by photonics,"* IEEE J. Quantum Electron., **52**, p. 0600912, 2016.

[5.31] J. Y. Kim, H. J. Song, M. Yaita, A. Hirata, and K. Ajito, *"CW-THz vector spectroscopy and imaging system based on 1.55-μm fiber-optics,"* Opt. Express, **22**, pp. 1735-1741, 2014.

[5.32] M. Kato, S. R. Tripathi, K. Murate, K. Imayama, and K. Kawase, *"Non-destructive drug inspection in covering materials using a terahertz spectral imaging system with injection-seeded terahertz parametric generation and detection,"* Opt. Express, **24**, pp. 6425-6432, 2016.

[5.33] K. P. Cheung and D. H. Auston, *"A novel technique for measuring far-infrared absorption and dispersion,"* Infrared Phys., **26**, pp. 23-27, 1986.

[5.34] D. Grischkowsky, S. Keiding, M. V. Exter, and Ch. Fattinger, *"Far-infrared time-domain spectroscopy with terahertz beams of dielectrics and semiconductors,"* J. Opt. Soc. Am. B, **7**, pp. 2006-2015, 1990.

[5.35] J. R. Demers, R. T. Logan Jr., N. J. Bergeron, and E. R. Brown, *"A coherent frequency-domain THz spectrometer with a signal-to-noise ratio 60 dB at 1 THz,"* Proc. SPIE Defense Security, **6949**, p. 694909, 2008.

[5.36] T. Nagatsuma, A. Kaino, S. Hisatake, K. Ajito, H. J. Song, A. Wakatsuki, Y. Muramoto, N. Kukutsu, and Y. Kado, *"Continuous-wave Terahertz spectroscopy system based on photodiodes,"* PIERS Online, **6**, pp. 390-394, 2010.

[5.37] A. Roggenbuck, H. Schmitz, A. Deninger, I. C. Mayorga, J. Hemberger, R. Gusten, and M. Gruninger, *"Coherent broadband continuous-wave terahertz spectroscopy on solid-state samples,"* New J. Phys., **12**, p. 043017, 2010.

[5.38] J. F. Federici, B. Schulkin, F. Huang, D. Gary, R. Barat, F. Oliveira, and D. Zimdars, *"THz imaging and sensing for security applications–explosives, weapons, and drugs"* Semicond. Sci. Technol., **20**, pp. S266-S280, 2005.

[5.39] T. Yuan, H. B. Liu, J. Z. Xu, F. Al-Douseri, Y. Hu, and X. C. Zhan, *"Terahertz time-domain spectroscopy of atmosphere with different humidity"* Proc. of SPIE, Terahertz for Military and Security Applications, **5070**, pp. 28-37, 2003.

[5.40] A. Nahata, J. T. Yardley, and T. F. Heinz, *"Two-dimensional imaging of continuous-wave terahertz radiation using electro-optic detection"* Appl. Phys. Lett., **81**, pp. 963-965, 2003.

[5.41] V. Pacheco-Pena, M. Beruete, I. V. Minin, and O. V. Minin, *"Terajets produced by dielectric cuboids,"* Appl. Phys. Lett., **105**, p. 084102, 2014.

[5.42] A. Heifetz, S. C. Kong, A. V. Sahakian, A. Taflove, and V. Backman, *"Photonic nanojets,"* J. Comput. Theor. Nanosci., **6**, pp. 1979-1992, 2009.

[5.43] M. S. Kim, T. Scharf, S. Muhlig, C. Rockstuhl, and H. P. Herzig, *"Gouy phase anomaly in photonic nanojets,"* Appl. Phys. Lett., **98**, p. 191114, 2011.

[5.44] I. Minin and O. Minin, *"3D diffractive lenses to overcome the 3D Abbe subwavelength diffraction limit,"* Chin. Opt. Lett., **12**, p. 060014, 2014.

[5.45] H. Yang, R. Trouillon, G. Huszka, and M. A. M. Gijs, *"Super-resolution imaging of a dielectric microsphere is governed by the waist of its photonic nanojet,"* Nano Lett., **16**, pp. 4862-4870, 2016.

[5.46] S. Yang, A. Taflove, and V. Backman, *"Experimental confirmation at visible light wavelengths of the backscattering enhancement phenomenon of the photonic nanojet,"* Opt. Express, **19**, pp. 7084-7093, 2011.

[5.47] S. C. Kong, A. Sahakian, A. Taflove, and V. Backman, *"Photonic nanojet-enabled optical data storage,"* Opt. Express, **16**, pp. 13713-13719, 2008.

[5.48] S. C. Kong, A. V. Sahakian, A. Heifetz, A. Taflove, and V. Backman, *"Robust detection of deeply subwavelength pits in simulated optical data-storage disks using photonic jets,"* Appl. Phys. Lett., **92**, p. 211102, 2008.

[5.49] W. Guo, Z. B. Wang, L. Li, D. J. Whitehead, B. S. Lukyanchuk, and Z. Liu, *"Near-field laser parallel nanofabrication of arbitrary-shaped patterns,"* Appl. Phys. Lett., **90**, p. 243101, 2007.

[5.50] W. Wu, A. Katsnelson, O. G. Memis, and H. Mohseni, *"A deep sub-wavelength process for formation of highly uniform arrays of nanoholes and nanopillars,"* Nanotechnology, **18**, p. 485302, 2007.

[5.51] D. S. Benincasa, P. W. Barber, J. Z. Zhang, W. F. Hsieh, and R. K. Chang, *"Spatial distribution of the internal and near-field intensities of large cylindrical and spherical scatterers,"* Appl. Opt., **26**, pp. 1348-1356, 1987.

[5.52] P. Ferrand, J. Wenger, A. Devilez, M. Pianta, B. Stout, N. Bonod, E. Popov, and H. Rigneault, *"Direct imaging of photonic nanojets,"* Opt. Express, **16**, pp. 6930-6940, 2008.

[5.53] L. Zhao and C. K. Ong, *"Direct observation of photonic jets and corresponding backscattering enhancement at microwave frequencies,"* J. Appl. Phys., **105**, p. 123512, 2009.

[5.54] A. Heifetz, K. Huang, A. V. Sahakian, X. Li, A. Taflove, and V. Backman, *"Experimental confirmation of backscattering enhancement induced by a photonic jet,"* Appl. Phys. Lett., **89**, p. 221118, 2006.

[5.55] B. Ounnas, B. Sauviac, Y. Takakura, S. Lecler, B. Bayard, and S. Robert, *"Single and dual photonic jets and corresponding backscattering enhancement with tipped waveguides: direct observation at microwave frequencies,"* IEEE Trans. Antennas Propag., **63**, pp. 5612-5618, 2015.

[5.56] I. V. Minin, O. V. Minin, V. Pacheco-Pena, and M. Beruete, *"All-dielectric periodic Terajet waveguide using an array of coupled cuboids,"* Appl. Phys. Lett., **106**, p. 254102, 2015.

[5.57] I. V. Minin, O. V. Minin, V. Pacheco-Pena, and M. Beruete, *"Localized photonic jets from flat, three-dimensional dielectric cuboids in the reflection mode,"* Opt. Lett., **40**, pp. 2329-2332, 2015.

[5.58] I. V. Minin, O. V. Minin, and Y. E. Geints, *"Localized EM and photonic jets from non-spherical and non-symmetrical dielectric mesoscale objects: brief review,"* Ann. Phys., **527**, pp. 491-497, 2015.

[5.59] V. Pacheco-Pena, M. Beruete, I. V. Minin, and O. V. Minin, *"Multifrequency focusing and wide angular scanning of Terajets,"* Opt. Lett., **40**, pp. 245-248, 2015.

[5.60] I. V. Minin and O. V. Minin,*"Diffractive optics and nanophotonics: Resolution below the diffraction limit,"* Springer, 2016.

[5.61] M. S. Kim, T. Scharf, S. Muhlig, C. Rockstuhl, and H. P. Herzig, *"Gouy phase anomaly in photonic nanojets,"* Appl. Phys. Lett., **98**, p. 191114, 2011.

[5.62] S. Feng and H. G. Winful, *"Physical origin of the Gouy phase shift,"* Opt. Lett., **26**, pp. 485-487, 2001.

[5.63] L. G. Gouy, *"Sur une propriete nouvelle des ondes lumineuses,"* C.R. Acad. Sci. Paris, **110**, p. 1251, 1890.

[5.64] X. Pang, T. D. Visser, and E. Wolf, *"Phase anomaly and phase singularities of the field in the focal region of high-numerical aperture systems,"* Opt. Commun., **284**, pp. 5517-5522, 2011.

[5.65] J. L. Johnson, T. D. Dorney, and D. M. Mittleman, *"Enhanced depth resolution in terahertz imaging using phase-shift interferometry,"* Appl. Phys. Lett., **78**, pp. 835-837, 2001.

Chapter 6

Applications of characterized Terajet device

In this chapter, applications of the Terajet phenomenon, which was characterized in Chapter 5, are proposed and demonstrated. The first application is to enhance the sensitivity of the EO probe by concentrating THz wave into the EO probe by the cube. The second application is to enhance the spatial resolution of THz imaging systems based on the subwavelength beam-compressing property of the Terajet. Subwavelength resolution imaging of an integrated circuit (IC) card using a cube was demonstrated and the impact of this resolution-enhancing technique was illustrated.

6.1 Sensitivity enhancement of EO probe

6.1.1 Concept and experimental verification

The schematic of the configuration to enhance the sensitivity of the EO probe by employing the Terajet phenomenon is shown in Fig. 6.1.1. The idea of this configuration is to exploit a dielectric cube that has a small size and low invasiveness to concentrate the radiating THz waves into the EO crystal to increase the intensity of signal to be measured, such that the signal-to-noise ratio (SNR) can be improved. The Terajet generated from a Teflon cube, which has dimensions equal to the wavelength of the THz wave at 125 GHz ($\lambda = 2.4$ mm), is employed,

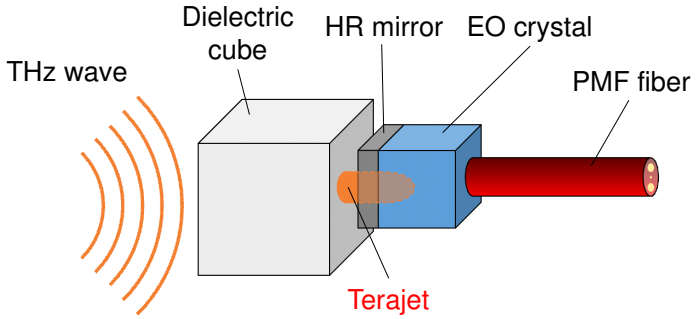

Figure 6.1.1: Configuration of sensitivity enhancement based on Terajet.

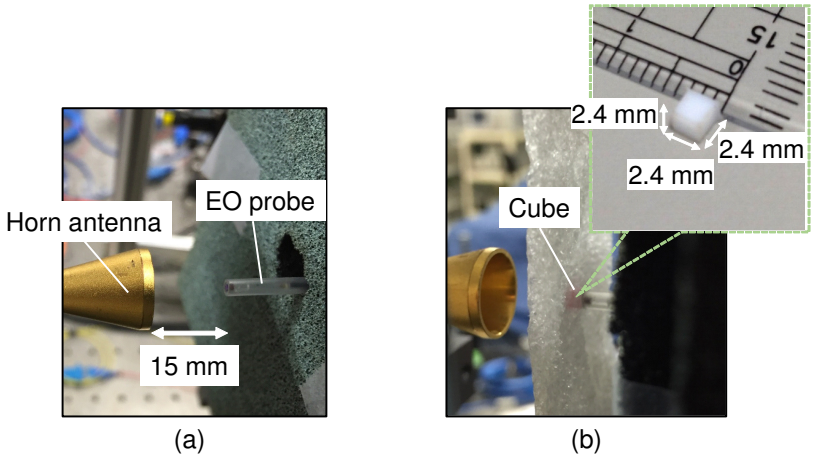

Figure 6.1.2: Experimental configuration (a) without and (b) with the cube.

as shown in Fig. 6.1.2. In the proof-of-concept experiment, the cube was placed as close as possible to the head of the ZnTe probe. The F-band horn antenna was placed at a distance of approximately 15 mm from the EO probe. The THz frequency was set at 125 GHz. The horn antenna was moved to visualize the THz E-field distribution.

Figures 6.1.3(a) and 6.1.3(b) show the measured amplitude and phase at the center of the horn antenna without moving the antenna, respectively. The lock-in time constant and photocurrent of the detecting photodiode were 30 ms and 1 mA, respectively. The blue and orange dots represent measured data without and with the cube. The measured amplitude with the cube was 6.62 ± 0.05 mV, which was 6 dB higher than that without the cube 3.29 ± 0.02 mV. The standard error was calculated from five distinct measurements and a Student's t coefficient of 2.132, corresponding to a 90% two-sided confidence interval. The standard deviations of the amplitude measurement were 0.120 ± 0.005 mV and 0.096 ± 0.001 mV for the

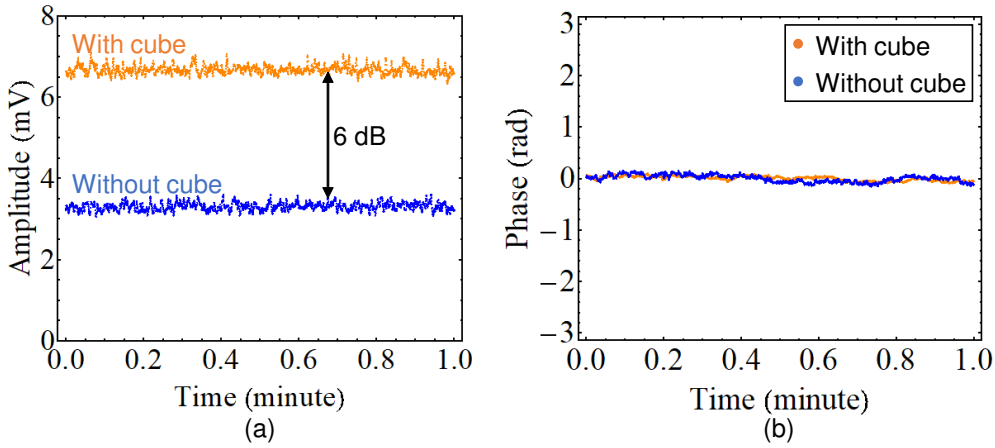

Figure 6.1.3: Measured (a) amplitude and (b) phase with and without the cube at 125 GHz.

cases with and without the cube, respectively. The slight multiple reflection of THz wave between the cube and the EO probe owing to unwanted air gap between them may be one of the possible reasons for a slight increase in the standard deviation or noise with the cube. Overall, the obtained SNR with the cube was 34.8 ± 0.4 dB and that without the cube was 30.7 ± 0.1 dB. The standard deviations of phase measurement were 0.042 ± 0.004 rad and 0.054 ± 0.011 rad for the cases with and without the cube, respectively. These results indicate that the proposed technique can enhance the detected THz intensity of 6 dB and the SNR of at least 4 dB.

6.1.2 Application to visualization

We apply the proposed sensitivity enhancement technique to the practical visualization of THz waves radiated from the F-band horn antenna. The experimentally visualized THz distributions from the horn antenna in three planes at 125 GHz without and with the cube are shown in Fig. 6.1.4(a) and Fig. 6.1.4(b), respectively. The measured area and the sampling interval were 4 cm $\times$ 4 cm and 0.2 mm, respectively. The visualized results indicate that the attached-cube EO probe can visualize the THz distribution with negligible invasiveness. The reproducibility of the measured results were confirmed in three distinct measurements.

In Fig. 6.1.4(b), the obtained amplitude image with the cube in the XY-plane is slightly blurry compared to that without the cube. The degradation of the spatial resolution with the cube, which has a dimension of one wavelength, is probably

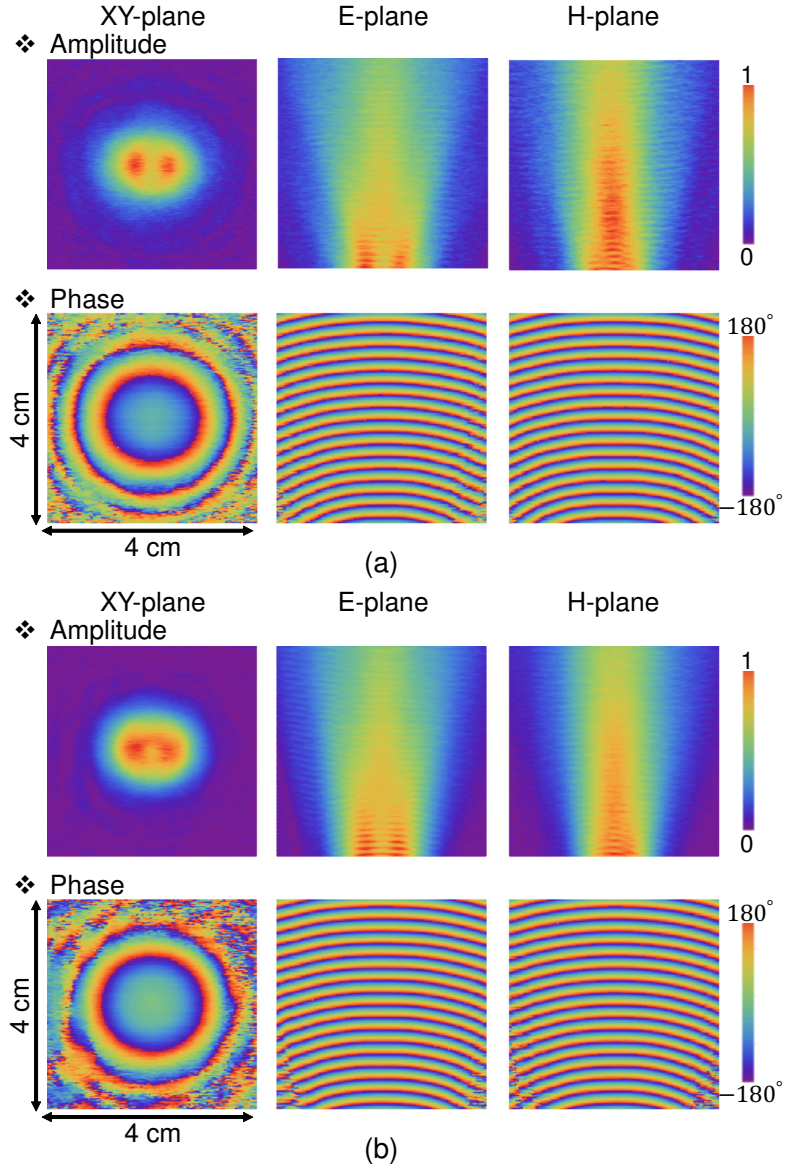

Figure 6.1.4: Experimental results of THz distributions from the horn antenna in three planes at 125 GHz (a) without and (b) with the cube.

one of the reasons. We remark that the resolution of the EO probe without the cube was 0.2 mm (0.08 λ), which was determined by the diameter of the optical probe beam.

Figures 6.1.5(a) and 6.1.5(b) show far-field patterns, which are obtained from the near-to-far-field transformation technique [6.1], of the horn antenna at 125 GHz without and with the cube, respectively. The details of this technique are explained in Chapter 5. The red dots and blue solid line represent the experimental and simulated results, respectively. The simulated results were based on the

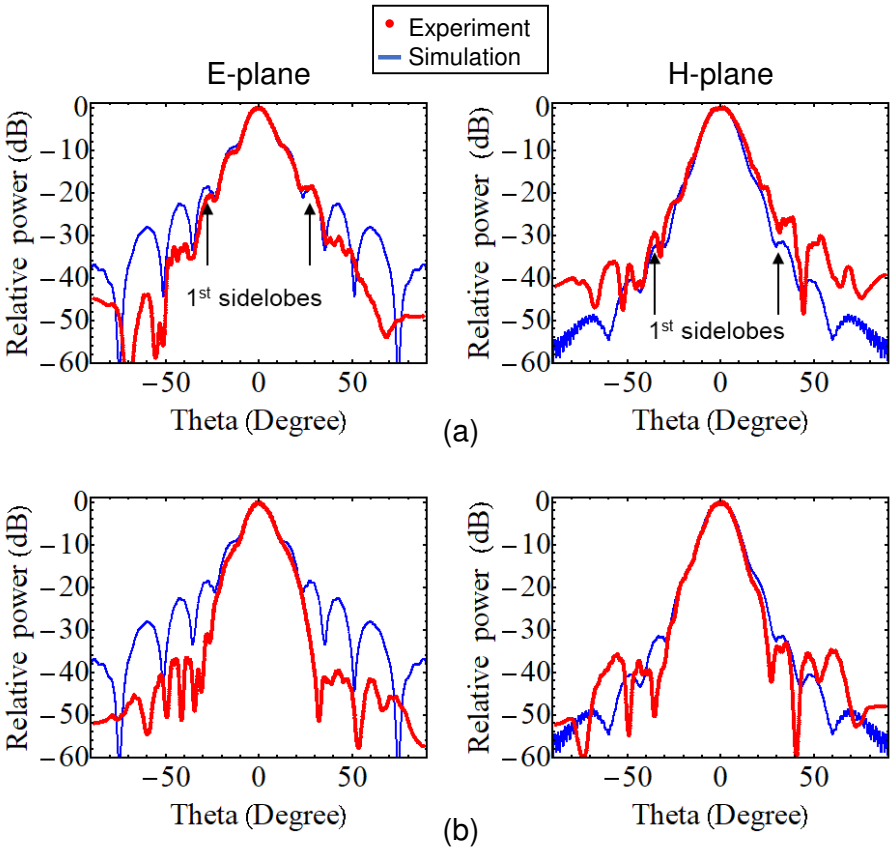

Figure 6.1.5: Far-field patterns calculated from the near-field measurement (a) without and (b) with the cube.

finite integration technique technique with the perfect matching layer boundary condition using the CST Microwave Studio full-wave simulator. Without the cube, the experimental results agree well with the simulated results up to the first sidelobe positions. Whereas, with the cube, the experimental results agree well with the simulated results within ±22°, and the first sidelobes could not be identified. The lack of spatial resolution could be one of the reasons. A smaller cube could be used to improve the spatial resolution, although the SNR enhancement can degrade. There is a trade-off between the resolution and the SNR enhancement when employing this proposed technique. Nevertheless, the main lobes of the far-field patterns with and without the cube show a good agreement with the simulated results. In particular, the measured 3-dB beamwidths with the cube were 12.1° and 13.0° in the E- and H-planes, respectively. Those without the cube were 11.9° and 14.6° in the E- and H-planes, respectively. Those of the simulated results were 11.5° and 13.6° in the E- and H-planes, respectively. This indicates that the

proposed sensitivity-enhancement technique can be used to characterize antenna, which has a high-directivity and negligible sidelobes.

6.2 Resolution enhancement of THz imaging

6.2.1 Characterize Terajet under focused incidence

The experimental characterizations of the generated Terajet from the dielectric cube by the EO measurement indicated that the cube is a promising candidate for a flat focusing devices, which can be exploited to enhance the spatial resolution of the practical THz imaging system. The configuration of a common imaging system based on focusing device without the cube and the proposed technique with the cube are depicted in Figs. 6.2.1(a) and 6.2.1(b), respectively. Generally, the imaging point in any imaging system should be small to obtain the high spatial resolution. The lens and/or parabolic mirrors are used to compress the beam. In order to verify the resolution enhancement technique based on the cube, the EO probe was used to characterize the THz wave distribution when placing the cube at the imaging point like in Fig. 6.2.1(b).

Figure 6.2.2 shows the experimental setup to characterize the Terajet generation from the cube under focused incidence by a lens. Two commercially available Teflon lenses were used to collimate and focus the THz wave radiated from the F-band horn antenna at 125 GHz (λ = 2.4 mm). The dielectric cube was the same as the previous experiment, and placed at the focal position of the lens. The measured focal length of the lens, which focuses the THz beam to the cube, was f_L = 6.7 cm. The EO probe was placed behind the cube at a distance of

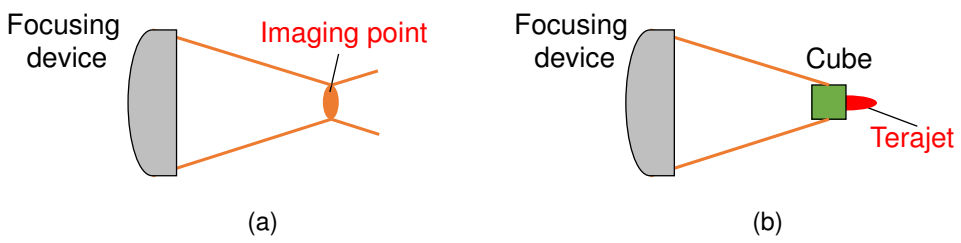

Figure 6.2.1: Configuration of imaging based on (a) a focusing device without the cube and (b) the proposed technique with the cube.

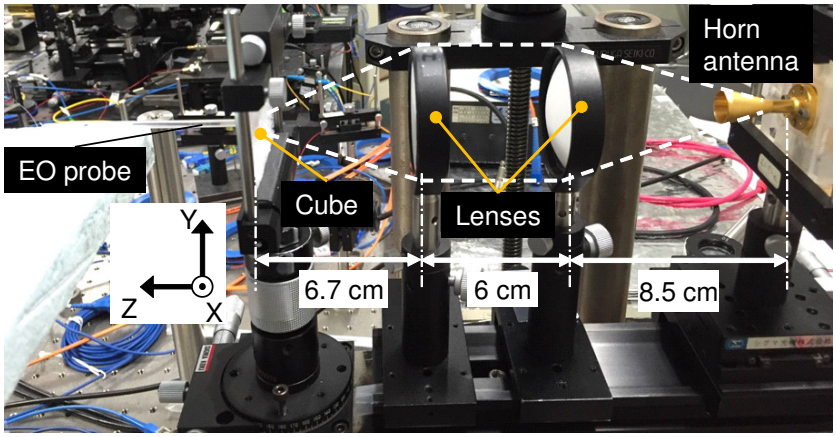

Figure 6.2.2: Experimental setup to characterize the Terajet generation from the cube under focused incidence by a lens.

approximately 0.5 mm. The E-plane was parallel to the XZ-plane.

Figure 6.2.3 shows the experimentally visualized amplitude distribution of focused beam without and with the cube at 125 GHz. The amplitude value was normalized to the maximum value with the cube in each plane. The measured area and the sampling interval were 18 mm × 18 mm and 0.1 mm, respectively. The generation of the Terajet can be confirmed in all three planes when placing the cube at the focused position of the lens.

In Fig. 6.2.4, the brown and purple dots represent the beam profile of the imaging point with and without the cube, respectively, in the XZ-plane. The THz intensities with (I_w) and without the cube (I_{wo}), respectively, were normalized to the maximum amplitude obtained without the cube on each plane (A_{max_wo}) by the following equations:

$$\begin{aligned} I_w &= 20\log_{10}\frac{A_w}{A_{max\_wo}}, \\ I_{wo} &= 20\log_{10}\frac{A_{wo}}{A_{max\_wo}}, \end{aligned} \tag{6.2.1}$$

where A_w and A_{wo} are the measured amplitude distributions with and without the cube, respectively. The intensity enhancement of 6.4 dB and the full width at half maximum (FWHM) of 0.5 λ —a subwavelength resolution —were obtained with the cube. The FWHM, however, was 1.8 λ for the focused beam by the lens without the cube.

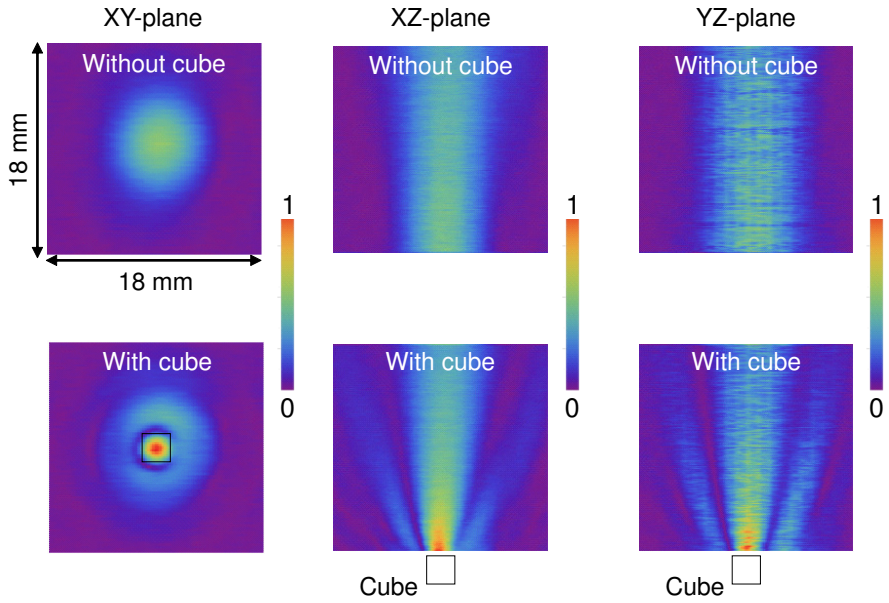

Figure 6.2.3: Experimentally visualized amplitude distribution of focused beam without and with cube at 125 GHz.

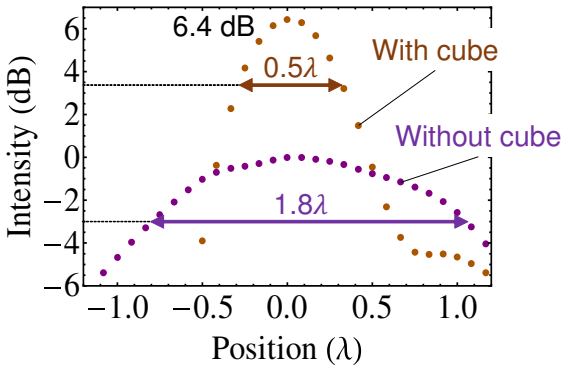

Figure 6.2.4: Measured beam profiles of imaging point with and without cube at a distance of 0.5 mm from the cube.

The resolution at a certain frequency or wavelength is generally limited by the numerical aperture (NA) of the focusing device based on the diffraction limit described by the well-known Rayleigh [6.2] and Abbe criteria [6.3]. The minimum FWHM (FWHM_{limit}) imposed by the diffraction limit in a coherent illumination system [6.4] is expressed as:

$$\text{FWHM}_{limit} = 0.67\frac{\lambda}{\text{NA}}, \tag{6.2.2}$$

$$\text{NA} \approx n\frac{D}{2f_L}, \tag{6.2.3}$$

where n, D, and f_L are the refractive index of the surrounding medium, the diam-

eter of the collimated incident beam, and the focal length of the focusing device, respectively. Note that the FWHM is approximately 0.82 of the radius of the Airy disk first dark-ring, and that the coefficient based on Abbe criterion in Ref. [6.4] is 0.82, which leads to the 0.67 coefficient in equation (6.2.2) ($0.82 \times 0.82 = 0.67$). In Fig. 6.2.4, the measured $\frac{1}{e^2}$ beamwidth of the incident collimated beam to the lens was $D = 49$ mm. Therefore, the actual NA of the lens is NA = 0.38 that leads to the $\text{FWHM}_{limit} = 1.76\,\lambda$ by equation (6.2.2). This value coincides with the experimental measured FWHM without the cube in Fig. 6.2.4. It can be said that the FWHM obtained by the cube is better than the diffraction-limited FWHM of the lens.

6.2.2 Employ Terajet in THz imaging system

We characterize the Terajet generated from the cube, which can be considered as a resolution enhancer, when placing it in a practical THz imaging system. First, we precisely construct and align the components of the THz imaging system in reflection-mode by visualizing THz distribution using EO measurement.

Figures 6.2.5(a) and 6.2.5(b) show the configuration of the THz imaging system and its actual photograph. THz waves at 125 GHz emitted from the F-band horn antenna were collimated by a lens and split by a beam splitter. The THz beam was widened by the next lens and Mirror1, which has a specification $\text{NA}_1 = 0.5$. It was then compressed by Mirror2 with a larger specification $\text{NA}_2 = 0.75$. The actual NA_2 estimated by measuring the $\frac{1}{e^2}$ beamwidth of the incident collimated beam and the focal length was 0.55. The difference between the specification NA and the measured NA results from the fact that the diameter of the collimated beam entering the mirror is smaller than the diameter of the mirror. The actual measured value $\text{NA}_2 = 0.55$ is used in the discussion and evaluation presented in this study. The cube was placed at the focal point of Mirror2 and the imaging sample was placed behind the cube at a distance of approximately 0.5 mm. The hatched-areas numbered from 1 to 4 in Fig. 6.2.5(a) were visualized for the alignment of the imaging system. The E-plane was parallel to the XZ-plane.

Figure 6.2.6 shows the experimentally visualized results of the area hatched-1.

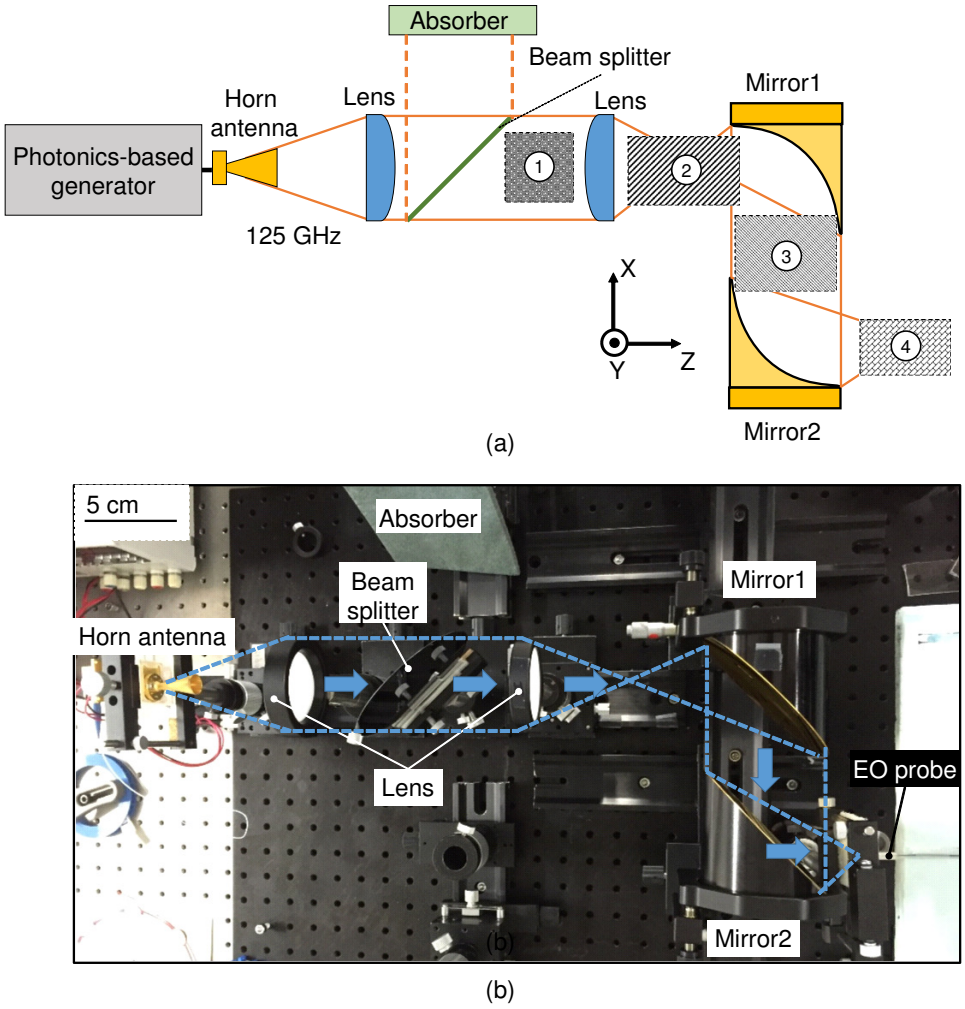

Figure 6.2.5: (a) Configuration of THz imaging system in reflection-mode with hatched areas needed to be verified and (b) its actual photograph.

The collimated THz beam can be confirmed in both XZ- and YZ-planes because the phase front distributions are planar. This indicates that the horn antenna was set at the right focal point of the lens. Figure 6.2.7 shows the experimentally visualized results of the area hatched-2. The second lens was used to compress and diverge the THz beam to get a larger beam diameter entering Mirror1. The compressed THz beam in the amplitude images and the direction of the phase front in the phase images can confirm that the THz beam was compressed and propagated straight.

Figures 6.2.8 and 6.2.9 show the experimentally visualized results of the hatched-3 and hatched-4 areas in the XZ- and YZ-planes, respectively. The amplitude images in each plane were normalized to the maximum value of the amplitude

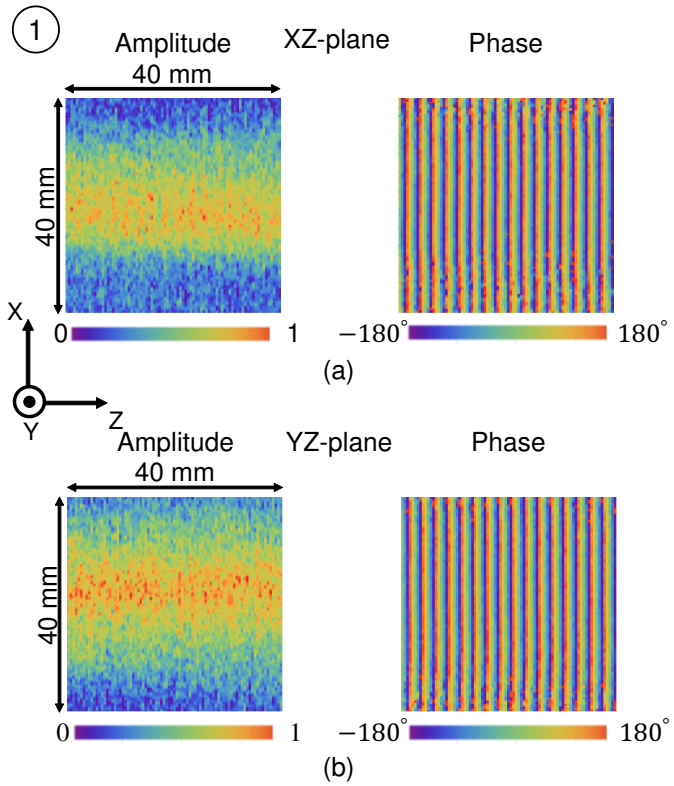

Figure 6.2.6: Experimentally visualized results of hatched-1 area in (a) XZ-plane and (b) YZ-plane.

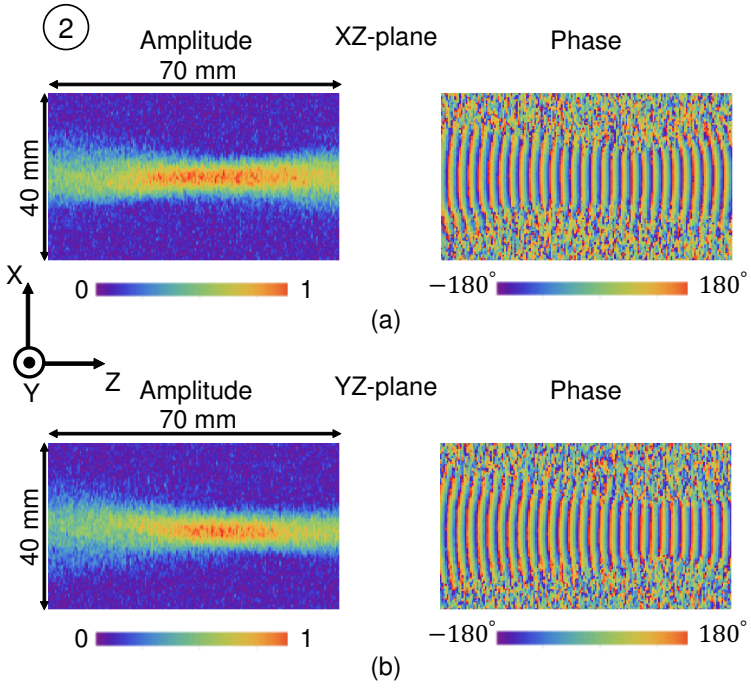

Figure 6.2.7: Experimentally visualized results of hatched-2 area in (a) XZ-plane and (b) YZ-plane.

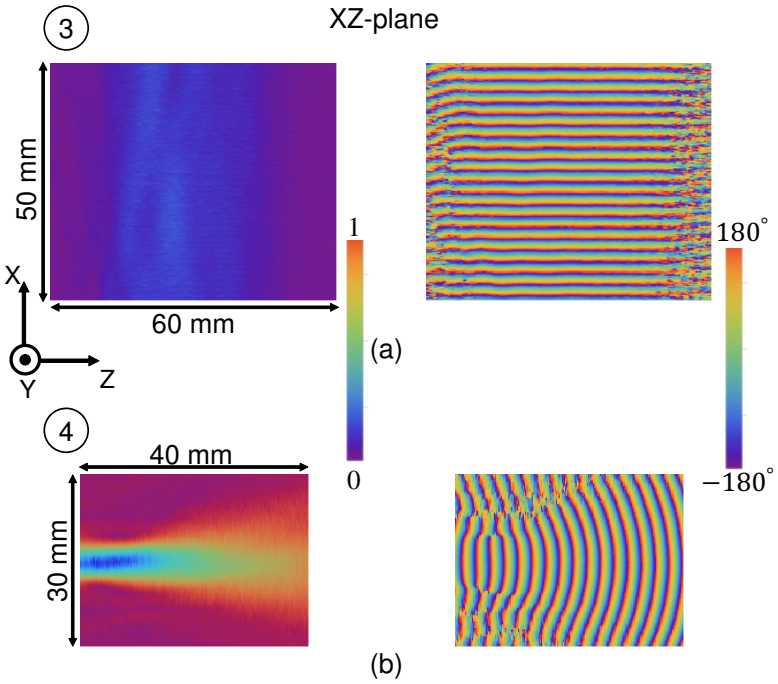

Figure 6.2.8: Experimentally visualized results in XZ-plane of (a) hatched-3 and (b) hatched-4 areas.

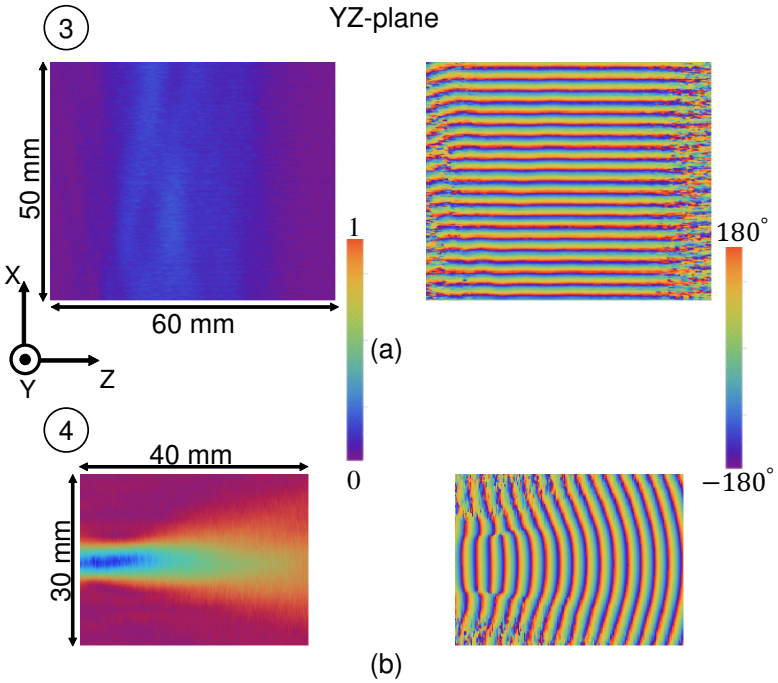

Figure 6.2.9: Experimentally visualized results in YZ-plane of (a) hatched-3 and (b) hatched-4 areas.

distribution in area hatched-4. A strong focusing beam can be observed in the amplitude images in area hatched-4 for both planes. The collimating THz beam in the hatched-3 area can be confirmed through the planar phase front distributions in the phase images for both planes. These results indicate that each component of the THz imaging system was aligned precisely, thanks to the EO measurement. We remark that the phase front distribution is essential to accurately verify the wave planarity and the focal lengths of the focusing devices when constructing the THz system.

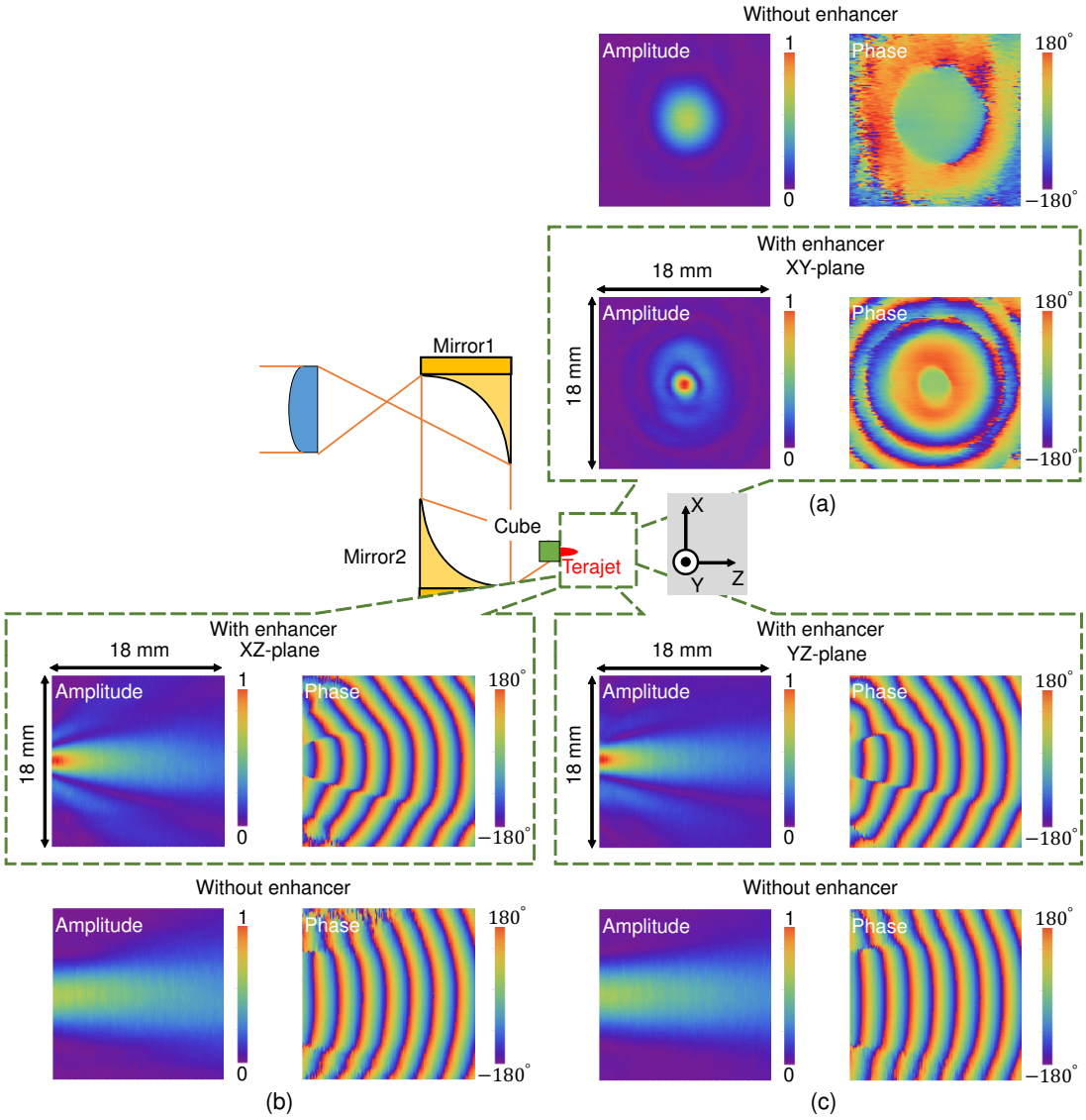

Figure 6.2.10: Visualized THz radiations with and without placing cube at focal point of Mirror2 in (a) XY-plane, (b) XZ-plane, and (c) YZ-plane.

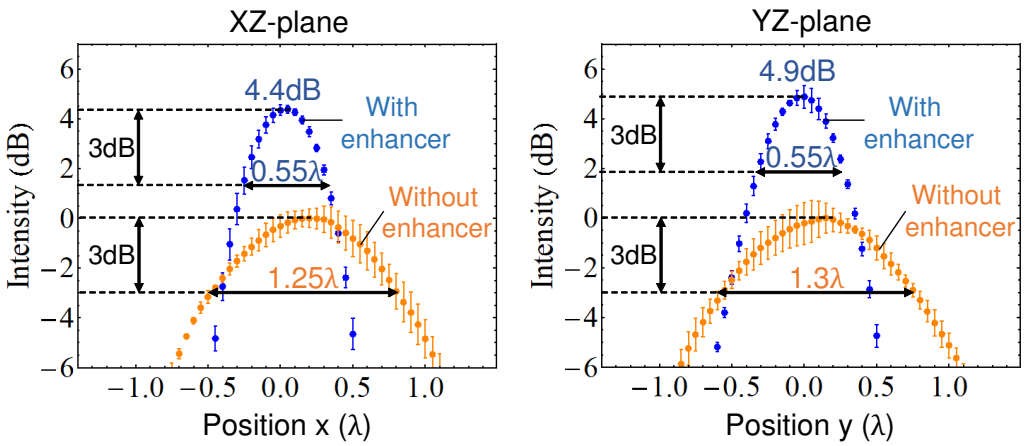

Figure 6.2.11: Measured beam profiles with and without enhancer in XZ- and YZ-planes.

Figure 6.2.10 shows experimentally visualized results of the THz wave distribution with and without placing the cube at the focal point of Mirror2 in the XY-, XZ-, YZ-planes. The amplitude values were normalized to the maximum value with the cube in each plane. The measurement area was 18 mm × 18 mm, corresponding to 150 × 150 measurement points. The sampling interval was set at 0.12 mm (0.05λ). The maximum SNR obtained at the center and 0.5 mm behind the cube was 33.8 ± 0.4 dB. The Terajet generated from the cube, the enhancer, placed at the focal point of Mirror2 is clearly shown in all of three planes in the amplitude images in Fig. 6.2.10. The total THz power in the XY-plane (Fig. 6.2.10(a)), which was calculated from the summation of the square of the measured amplitude, with the enhancer was about 88% (or −0.6 dB) of that without the enhancer. This slight degradation of THz power is possibly due to a small absorption and reflection of the dielectric cube.

The subwavelength hotspot property of the generated Terajet was quantitatively characterized by evaluating the FWHM of the beam profiles with and without the enhancer in the XZ- and YZ-planes. Figure 6.2.11 shows the point spread function or the beam profile of the imaging system with and without the enhancer. The blue and orange dots represent the measured beam profiles with and without the enhancer, respectively. The intensity was calculated from the measured amplitude distribution at a distance of 0.5 mm from the enhancer surface by equation (6.2.1). Intensity enhancements of approximately 4.4 dB and 4.9 dB were

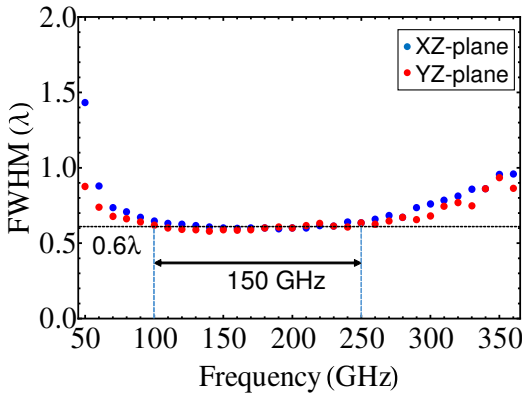

Figure 6.2.12: Simulated frequency characteristics of FWHM of generated Terajet from the enhancer under normal planar incidence.

obtained in the XZ- and YZ-plane, respectively. A slight difference in the observed intensity enhancement values in two planes is probably caused by a slight misalignment in the horizontal and vertical directions (approximately $0.2\,\lambda$) when placing the enhancer. The standard error was calculated from three distinct measurements and a Student's t coefficient of 2.92, corresponding to a 90% two-sided confidence interval. The FWHMs obtained without the enhancer were $1.25 \pm 0.05\,\lambda$ (3.00 ± 0.12 mm), and $1.30 \pm 0.17\,\lambda$ (3.12 ± 0.41 mm) in the XZ- and YZ-planes, respectively. These FWHM values almost reached the diffraction limited FWHM of approximately $1.22\,\lambda$, calculated by equation (6.2.2), of the focusing device with the actual NA = 0.55.

The FWHM obtained with the enhancer is $0.55 \pm 0.05\,\lambda$ (1.32 ± 0.12 mm), which is two times better in both the XZ- and YZ-planes. The FWHM obtained with the enhancer is even better than that obtained by a focusing device with an ideal maximum value of NA in air (NA = 1, $\mathrm{FWHM_{limit}} = 0.67\,\lambda$). Using the enhancer at 125 GHz in the THz imaging system, we have successfully obtained a diffraction-limited FWHM without the enhancer at 275 GHz, a 2.2 times higher frequency.

This result is associated with the results obtained previously with the Terajet generated under planar incidence (FWHM = $0.6\,\lambda$), which can be considered as an NA = 0 focusing device, and the Terajet generated under focused beam (FWHM = $0.5\,\lambda$) by the NA = 0.38 lens, indicates that the mesoscale dielectric cubes can enhance the spatial resolution to the subwavelength region by simply being placed

at the focused imaging points of continuous-wave (CW)-THz imaging systems with different NA values. A slight misalignment of the enhancer position (approximately $0.2\,\lambda$) when placing the enhancer at the focused imaging point shows no significant effect on the subwavelength FWHM of the hotspot. It should be noted that placing the enhancer at the focal point of focusing devices with small NAs leads to an inefficient use of THz power because the diameter of the imaging point of small-NA focusing devices is larger than the dimensions of the enhancer (one wavelength).

Figure 6.2.12 shows the simulated frequency characteristics of the subwavelength FWHM of the generated Terajet from the enhancer under planar incidence. The dimensions of the enhancer ($d_T = 2.4$ mm) are the same as the wavelength of the desire center frequency at $f_0 = 125$ GHz. The simulated results for both the XZ-plane (blue dots) and YZ-plane (red dots) in Fig. 6.2.12 indicate that a subwavelength FWHM better than $0.6\,\lambda$ was maintained for a wide bandwidth, from 100 GHz to 250 GHz ($0.8f_0$–$2f_0$), located among F, D, and G-bands. Moreover, the enhancer can be exploited in other frequency bands by scaling the dimensions of the enhancer accordingly to the wavelength of the frequency of interest [6.5–6.7]. This indicates a wide usability of this resolution enhancer in the THz region.

Figure 6.2.13 shows the intensity distributions along the z-axis, the propagation direction. The depth of field, Δz(FWHM), is defined as the beam length where the intensity is within 3 dB of the maximum intensity, as shown by the arrows in Fig. 6.2.13. As shown in the graphs, with the enhancer, the values of Δz(FWHM) are $0.97 \pm 0.05\,\lambda$ (2.33 ± 0.12 mm) and $0.98 \pm 0.05\,\lambda$ (2.35 ± 0.12 mm) in the XZ- and YZ-planes, respectively; the corresponding values without the enhancer are $3.48 \pm 0.13\,\lambda$ (8.35 ± 0.31 mm) and $3.32 \pm 0.74\,\lambda$ (7.97 ± 1.78 mm) in the XZ- and YZ-planes, respectively. Therefore, the depth of field when using the enhancer is approximately 3.4 times smaller than that obtained without the enhancer. A small depth of field will be beneficial when imaging samples that have layers of different reflectivity, where it is required to image those layers separately.

Figures 6.2.14(a) and 6.2.14(b) show the configuration of the constructed THz imaging system and its actual photograph. The reflected THz signal from the imaging sample, which is placed behind the cube at a distance of approximately

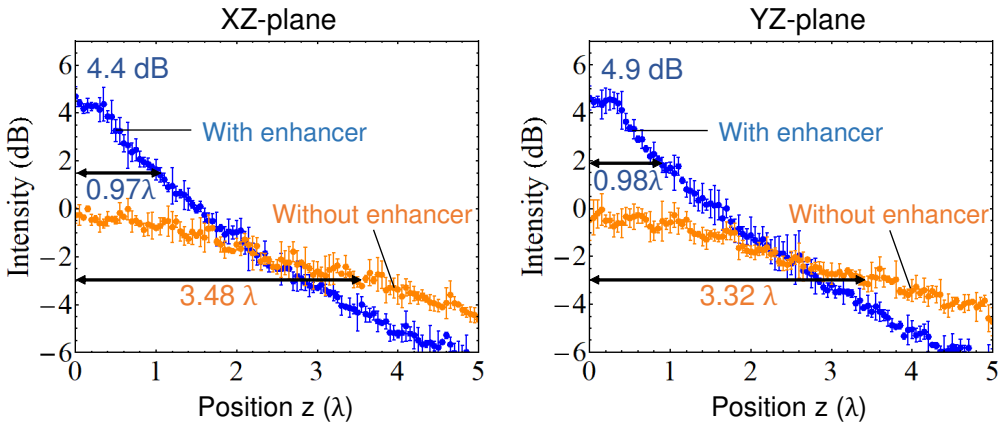

Figure 6.2.13: Intensity distribution along the z-axis with and without the enhancer in the XZ- and YZ-planes.

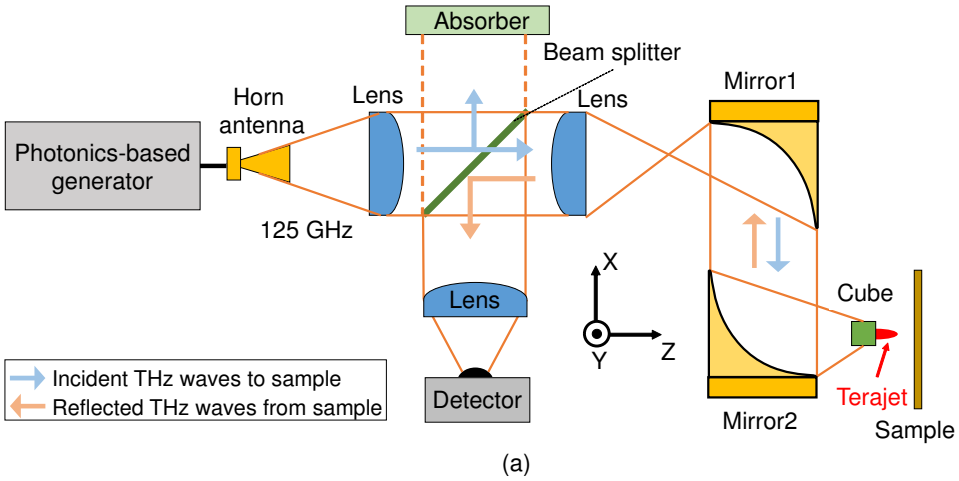

(a)

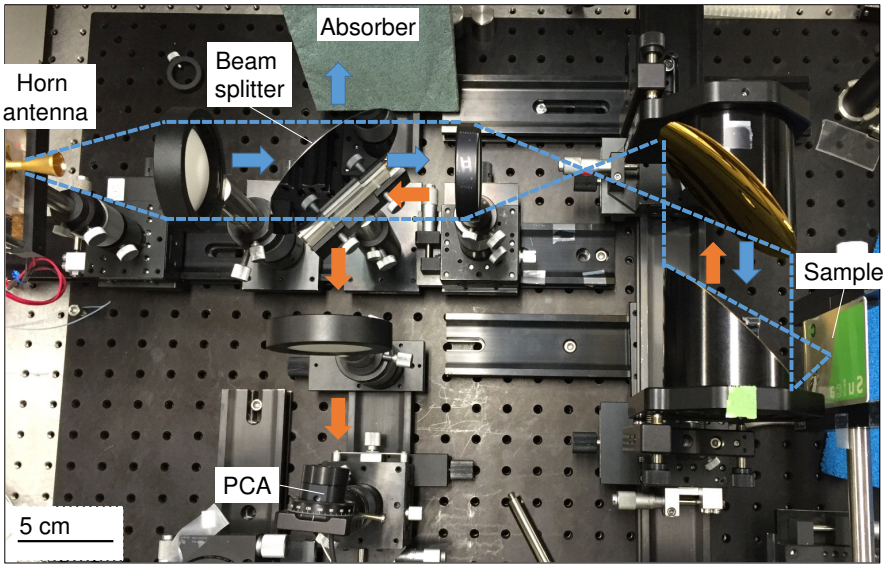

(b)

Figure 6.2.14: (a) Configuration of the THz imaging system and (b) its actual photograph. PCA: photoconductive antenna, a detector.

0.5 mm, was focused to the detector by a lens. A photoconductive antenna (PCA) was used as a detector. In Fig. 6.2.14, the blue and orange arrows depict the direction of the incident THz waves and reflected THz waves, respectively. An absorber was placed on the opposite site of the PCA to eliminate unnecessary interference.

Figure 6.2.15 shows the imaging samples: an aluminum plate with 1.5 mm ($0.63\,\lambda$) trenches and a 1.5 mm ($0.63\,\lambda$) diameter hole (Fig. 6.2.15(a)), and a Suica IC card—a common fare card used for trains in Japan (Fig. 6.2.15(b)). The thickness of both samples was 1 mm ($0.42\,\lambda$). The electronic circuitry inside the IC card includes four metal lines with an approximate width of 0.85 mm ($0.35\,\lambda$), placed around the border of the card (Fig. 6.2.15(c)).

The amplitude and phase images of the aluminum plate sample obtained with and without the enhancer are shown in Fig. 6.2.16(a). The measured area was 20 mm × 20 mm, and the sampling interval was 0.1 mm. Without the enhancer, the trenches and the hole were blurred because of the lack of resolution. In contrast, three trenches and the hole could be clearly observed when the enhancer was used. The cross-sections at the center of the amplitude images are shown in Fig. 6.2.16(b), for both cases. The blue and orange dots represent the measured amplitudes with and without the enhancer, respectively. The amplitude values were normalized by their maximum value in each case, and the standard errors were calculated from three distinct measurements. The dips in the graph correspond to the positions of the trenches and the hole, where the reflected signal was smaller than that of the surrounding metal area. Four blue dips were clearly resolved when using the enhancer, whereas only three orange dips could be resolved without the enhancer. The image contrast is defined as $\dfrac{A_{max} - A_{min}}{A_{max} + A_{min}}$, where A_{max} and A_{min} are the maximum and minimum detected amplitudes, respectively [6.8]. Without the enhancer, the obtained contrast was 0.14, and it was increased by approximately 4.4 times to 0.62 when the enhancer was used.

Figure 6.2.17 shows the results of nondestructive imaging of the IC card with and without the enhancer at 125 GHz. The measured area was 56 mm × 88 mm, and the sampling interval was set at 0.2 mm. The circuitry details were more

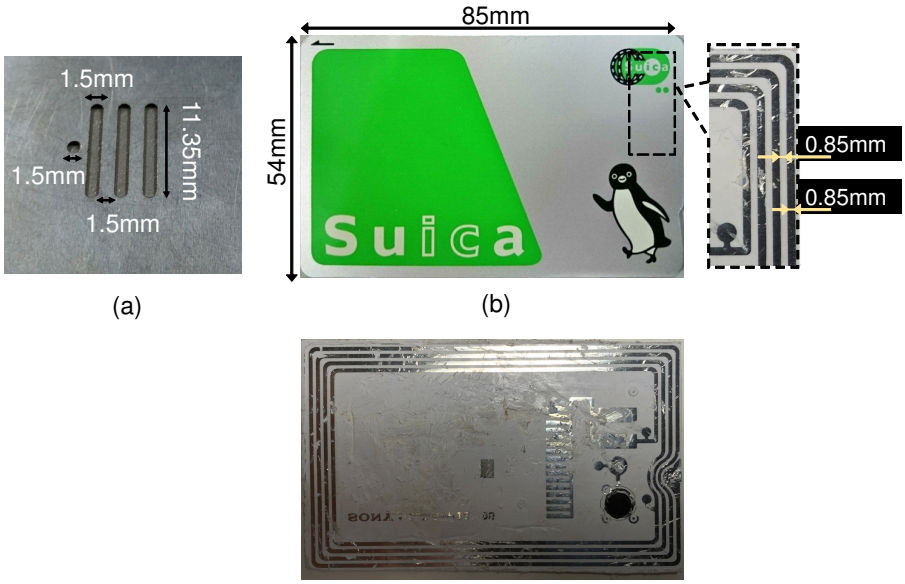

Figure 6.2.15: Imaging samples: (a) an aluminum plate, (b) a common IC card used for trains in Japan, and (c) the electronic circuitry inside it.

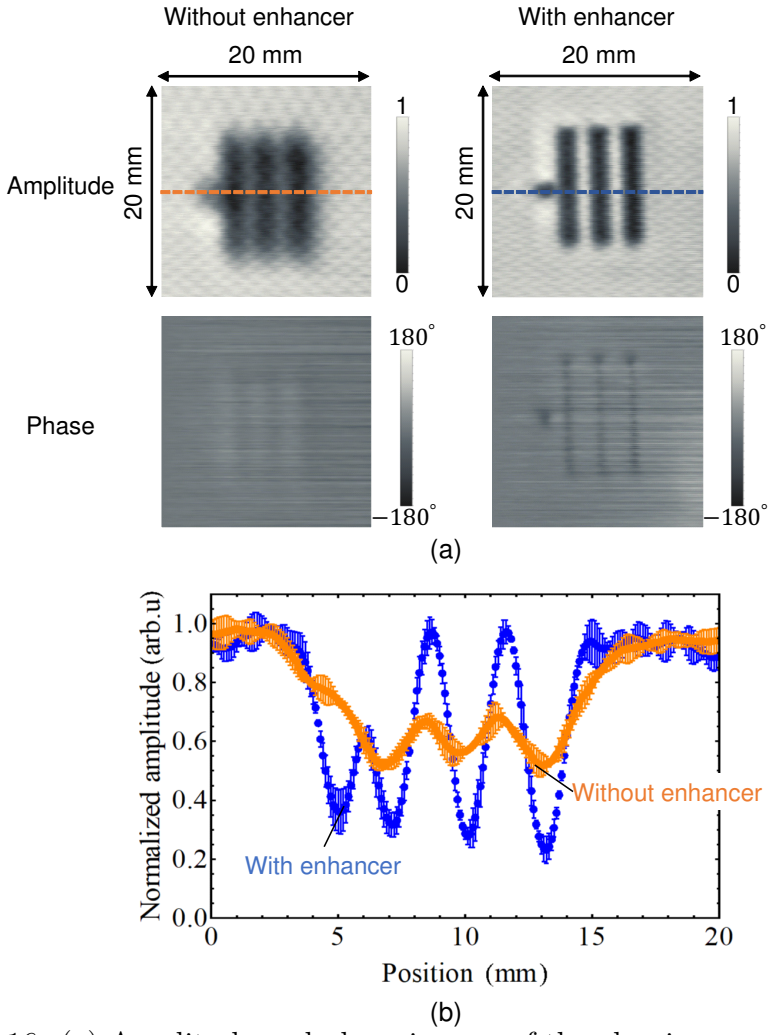

Figure 6.2.16: (a) Amplitude and phase images of the aluminum sample obtained with and without the enhancer. (b) Central cross-section of amplitude images.

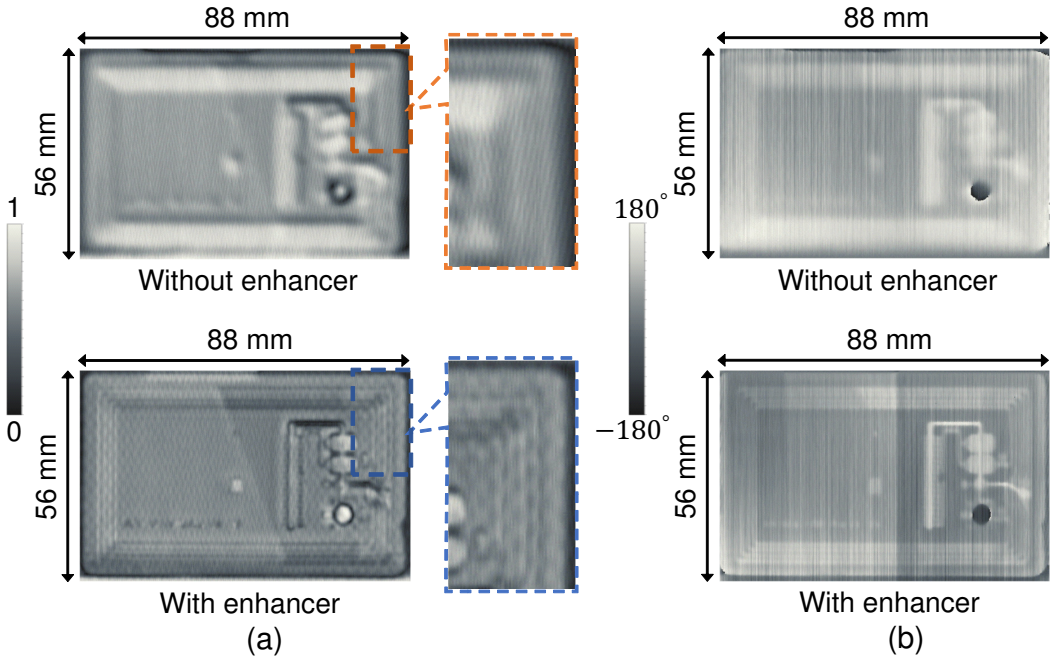

Figure 6.2.17: (a) Amplitude and (b) phase images of the IC card obtained with and without the enhancer.

clearly resolved with the enhancer, because the resolution obtained in this case was two times better than that obtained without the enhancer. In particular, with the enhancer, we could observe four vertical lines, corresponding to the four metal lines at the position indicated by the dashed-box. In contrast, without the enhancer, the image was blurred, and those metal lines could not be resolved. These results clearly indicate the impact of proposed resolution enhancement technique.

6.3 Conclusion

Two practical applications of Terajet were proposed and demonstrated. First, the THz E-field was concentrated into the EO probe to enhance the sensitivity by attaching the cube to the head of the EO probe. The enhancement of the detected THz intensity of 6 dB was obtained. The visualization of THz distributions from the F-band horn antenna was demonstrated. This indicated the negligible invasiveness of the proposed technique. The main lobes of the far-field patterns obtained from the measured near-field also agreed well with the simulated results. The degradation of the spatial resolution by this technique was found through this

study.

Second, the spatial resolution enhancement technique of the THz imaging system was proposed. For the first time, we demonstrated that a mesoscale dielectric cube can be used as a novel resolution enhancer by simply placing it at the focused imaging point of a CW-THz imaging system, regardless of the value of NA. This principle can be probably used both in reflection and transmission imaging systems. The characterization of beam profiles and the demonstration of the non-destructive imaging of the IC card indicated that the obtained resolution with the cube at 125 GHz was equivalent to the diffraction-limited resolution without the cube at 275 GHz, a frequency higher by a factor of 2.2. A broad bandwidth applicability of this technique was also confirmed by the simulation. This result has an impact on the practical THz imaging applications, because the utilization of a low THz frequency generally has advantages of high THz power and high transmission capability of many materials.

References

[6.1] R. C. Johnson, H. A. Ecker, and J. S. Hollis, *"Determination of far-field antenna patterns from near-field measurements,"* Proc. IEEE., **61**, pp. 1668-1694, 1973.

[6.2] Lord Rayleigh, *"Investigations in Optics, with special reference to the Spectroscope,"* Philos. Mag. 5th series, **8**, pp. 261-274, 1879.

[6.3] E. Abbe, *"Beitrage zur theorie des mikroskops und der mikroskopischen wahrnehmung,"* Arch. Mikrosk. Anat., **9**, pp. 413-468, 1873.

[6.4] M. Born and E. Wolf, *"Principles of optics,"* 6^{th} edition, Cambridge University Press, pp. 418-424, 1980.

[6.5] V. Pacheco-Pena, M. Beruete, I. V. Minin, and O. V. Minin, *"Terajets produced by dielectric cuboids,"* Appl. Phys. Lett., **105**, p. 084102, 2014.

[6.6] V. Pacheco-Pena, M. Beruete, I. V. Minin, and O. V. Minin, *"Multifrequency focusing and wide angular scanning of Terajets,"* Opt. Lett., **40**, pp. 245-248, 2015.

[6.7] I. V. Minin and O. V. Minin, *"Diffractive optics and nanophotonics: Resolution below the diffraction limit,"* Springer, 2016.

[6.8] C. Cremer and B. R. Masters, *"Resolution enhancement techniques in microscopy,"* Eur. Phys. J. H, **38**, pp. 281-345, 2013.

Chapter 7

Conclusions and future perspective

7.1 Conclusions of this dissertation

The motivation of this study is to extend the applicability of the EO near-field measurement to characterize THz devices above 100 GHz. Novel approaches to enhance the sensitivity and to reduce the invasiveness in the nonpolarimetric self-heterodyne EO detection system were proposed to achieve the objective of characterizing THz devices from 100 GHz to 500 GHz. The real impact of the EO measurement was shown by applying it to characterize several THz devices. The major results of this dissertation are as follows:

Chapter 2 described the principles of the optical-fiber-mounted EO detection techniques including homodyne, self-heterodyne, polarimetric, and nonpolarimetric techniques. The intrinsic sensitivity fluctuation issue of the polarimetric technique, which is caused by the fluctuation of the polarization state of the optical probe beam due to the ambient temperature changes or mechanical stress of the fibers, can be solved by the nonpolarimetric technique. The experimental setup of the nonpolarimetric self-heterodyne EO detection system was also described.

Chapter 3 described the experimental evaluation of the EO detection system based on the polarimetric and the nonpolarimetric techniques in the self-heterodyne configuration. The nonpolarimetric technique was superior to the polarimetric technique in terms of measurement stability, in which the standard deviation of measured amplitude was 2.6 times better.

Chapter 4 described the performance improvement techniques including the enhancement of the sensitivity and the reduction of the invasiveness and the interference with leaking noise. A DAST crystal, which exhibits a high EO coefficient, was employed as an EO probe to enhance the sensitivity or SNR. An improvement in the SNR of more than 10 dB in comparison with the ZnTe probe, which is one of the best inorganic EO probes, and the minimum detectable E-field of approximately 0.28 V/m at both the 100-GHz and 300-GHz bands were obtained. The 28-μW THz wave emitted from the J-band horn antenna was clearly visualized at 310 GHz by the DAST probe, whereas the ZnTe probe could not due to the lack of sensitivity. The SNR dependence on the optical components such as lasers and filters was experimentally evaluated. It was revealed that the excess laser noise influences the EO measurement in this system. A noise reduction schematic based on differential detection was proposed to reduce the excess laser noise. A reduction in the noise power of 3.6 dB was experimentally obtained.

For the invasiveness reduction, theoretical and experimental studies of the invasiveness of the head of the EO probe were described. It was found out that the conventional holder made from an acrylic dramatically affected the invasiveness compared to the one-cubic-millimeter EO probe itself at frequencies below 500 GHz. A styrofoam holder, which has a refractive index close to that of air, was employed to reduce the invasiveness by approximately 8 dB.

The issue of phase front distribution appearing in the amplitude image owing to the interference between the detected signal and noise in the electronics detection module was revealed. A signal processing method and a hardware improvement by reducing the ground group effect were proposed to solve this issue.

Chapter 5 described the impact of EO measurements by demonstrating the THz device characterization including the antenna, wavefront manipulating device, spherical-wave generation device, and Terajet. For the antenna characterization, the near-to-far-field transformation technique and the probe compensation technique were employed to characterize the radiation patterns of a standard horn antenna. The experimental results agreed well with the simulated results in the full F-band. These results indicated the effectiveness of this technique for the THz

antenna characterization. This technique has the advantages of compact and fast measurement compared to the conventional far-field measurement.

For the wavefront manipulating devices, the lens and the MHA were characterized at 125 GHz. The collimating phenomenon in the MHA was verified experimentally for the first time based on visualized results. The physical mechanism of this phenomenon was also explained by the experimental evaluation of radiation patterns. The collimating phenomenon of the MHA is probably due to its k-vector filtering effect, whereby the k-vector perpendicular to the MHA can pass through it but other k-vectors are filtered. The collimating phenomenon of the lens exhibited a gain-enhancement effect.

For the spherical-wave generation device, a Si-lens-mounted UTC-PD, which is used for THz spectroscopy applications, was characterized. It was the first THz device characterization up to 500 GHz by the EO probe. The visualized results from 30 GHz to 500 GHz showed the malfunction of this device at high frequency. This indicated the impact of the EO measurement for the diagnosis of malfunction of THz devices in a broad bandwidth.

The Terajet generating phenomenon from a dielectric cube was visualized for the first time. The experimental results agreed well with the simulated results. The Terajet generated under different incident angles were also experimentally characterized. The subwavelength beam waist was maintained for a wide incident angle of $\pm 45^{\circ}$. An interesting Gouy phase anomaly and its asymmetry under the oblique illumination were found and verified by the experiment and simulation.

Chapter 6 described the practical applications of one of characterized device, i.e., the Terajet, including the sensitivity enhancement of the EO probe and the high-resolution THz imaging. The THz radiation was concentrated into the EO probe by the cube to enhance the detected intensity. An enhancement in the detected intensity of approximately 6 dB was experimentally obtained at 125 GHz. The 2D visualization results also indicated the negligible invasiveness of this technique. The degradation of the spatial resolution owing to using a cube with wavelength-dimension was found and needed improvement.

A novel technique to obtain subwavelegnth resolution imaging by simply placing

the cube in the imaging point of the THz imaging system was demonstrated. The characterized results showed that the resolution below 0.6 λ can be obtained regardless of the size of the imaging point. The spatial resolution with the cube at 125 GHz was equivalent to the diffraction-limited resolution at 275 GHz, a higher frequency by a factor of 2.2. The high THz power and high transmitting capability are two benefits of employing low THz frequency but with the diffraction-limited resolution of a doubled frequency by this technique. Moreover, this technique can be applied in a broad bandwidth, e.g., 150 GHz bandwidth for the designed cube in this study. These results, together with the demonstrated imaging of the IC card, indicated the impact of the proposed technique in practical THz imaging applications.

7.2 Future perspective

Toward practical industrial applications of EO detection systems, there are two issues that should be considered. The first is a further enhancement of sensitivity and the spatial resolution. The second is a miniaturization or integration of the system.

Further enhancement of the sensitivity as well as the spatial resolution of the EO probe are necessary to characterize THz devices above 600 GHz (λ = 0.5 mm). The frequency band of 600 GHz has been attracting significant research interest owing to its possibility to be exploited for ultrafast wireless communication applications [7.1, 7.2], and nondestructive inspection applications [7.3–7.5]. The characterization of devices in this frequency band, such as an array structure of antennas and photomixers [7.7–7.9] is an upcoming demand. The phase matching between the generated THz E-field from each component of the array is a critical requirement of these devices to obtain a high output THz power and directivity [7.10].

Engineering and optimizing the EO crystal thickness is one of approaches to enhance the sensitivity [7.11] in the desired frequency band owing to the responsibility dependence on the thickness of the EO crystal [7.12]. The idea of gathering

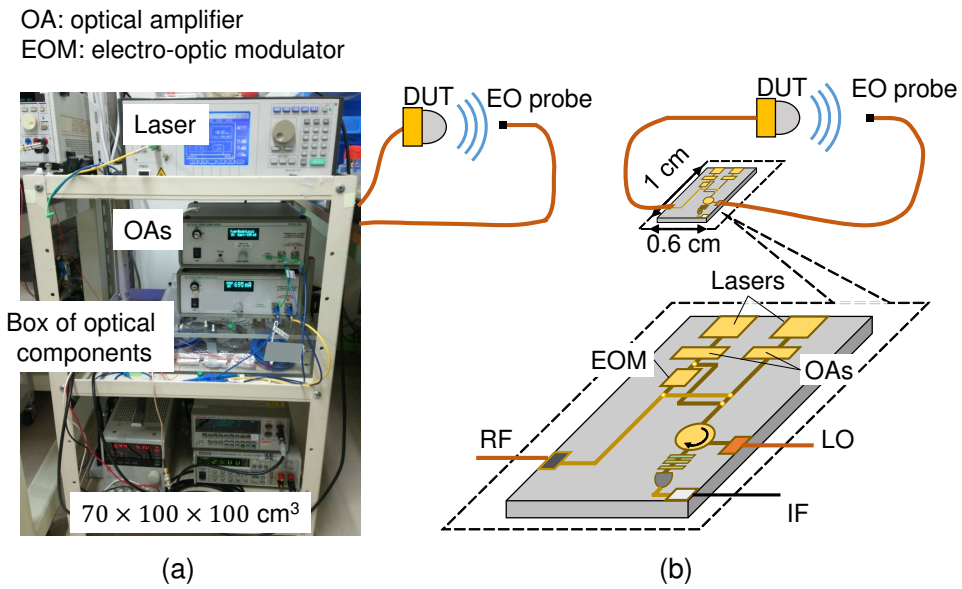

Figure 7.2.1: (a) Typical size of bulky EO detection system and (b) a compact integrated schematic.

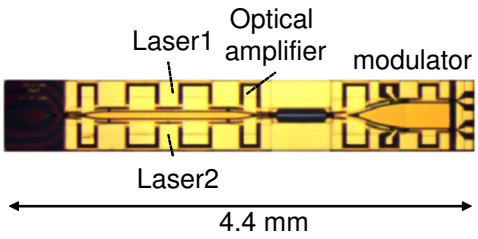

Figure 7.2.2: Example of photonic integrated chip for transmitter [7.15].

the THz E-field into the EO crystal based on the Terajet, of which we demonstrated a proof-of-concept in this study, can be considered for further study to enhance the sensitivity. The cube mounted on the head of the EO probe in this technique can be also engineered to function as a HR mirror and AR coating at the same time such that this technique can also minimize the E-field invasiveness of the EO probe.

We have exploited a one-cubic-millimeter EO crystal mounted on an optical fiber, which has the core diameter of 200 μm up till now. This spatial resolution is large to characterize THz E-field above 600 GHz. A smaller crystal and thinner optical fiber of approximately several tens of micrometers may need to be considered to improve the spatial resolution of the EO probe. The EO crystal can be mounted directly to a thin optical fiber, as reported elsewhere [7.13].

Second, Fig. 7.2.1(a) shows a typical EO detection system at the moment,

which is costly and bulky owing to using many independent optical components such as lasers, optical amplifiers, etc.. The integration or the miniaturization of the system is the next step to realize the practical industrial applications of EO measurements. Figure 7.2.1(b) depicts a schematic of a photonic integrated system. Recent development in photonic integration technology enables monolithic or hybrid integration of many optical components such as lasers, amplifiers, modulators, and photodiodes [7.14–7.16].

Figure 7.2.2 shows an example of an integrated on-chip device, which was demonstrated as a transmitter in a wireless communication application [7.15]. A compact integrated EO detection system of approximately several millimeters can be expected in the future. In addition to the benefits of compactness and cost reduction, the laser phase noise can also be reduced because the two optical sources and optical combiners are integrated on a single substrate such that all of them experience the same temperature fluctuations [7.16]. We remarked that the stability of the EO detection system can be influenced by ambient temperature change and that the excess laser noise should be reduced to improve the system performance.

Figure 7.2.3 depicts an alternative integration schematic based on all-optical-fiber —semiconductor fiber technology [7.17, 7.18]. The photonic-based generation DUT and the EO probe are connected to the RF and LO ports of a compact all-fiber box, as depicted in Fig. 7.2.3(a). The schematic inside the box is shown in Fig. 7.2.3(b). All of the optical components including lasers, optical amplifiers, frequency shifter, and optical filter fiber Bragg grating are inside the optical fiber.

Figures 7.2.4(a) and 7.2.4(b) show examples of fabricated silicon optical fiber with 15 µm silicon core inside 40 µm silica cladding [7.19] and the fiber with silicon p-i-n core [7.20]. Recent studies of inserting and manipulating semiconductors inside the optical fibers [7.21–7.23] open the possibility to realize all-optical-fiber integration in the future.

The semiconductor fiber technology has been attracting growing research interest since approximately a decade ago because it shows some advantages in comparison with the on-chip integration technology such as retaining robustness, flexibility of optical fibers [7.24], reducing complex couplings and losses between different ma-

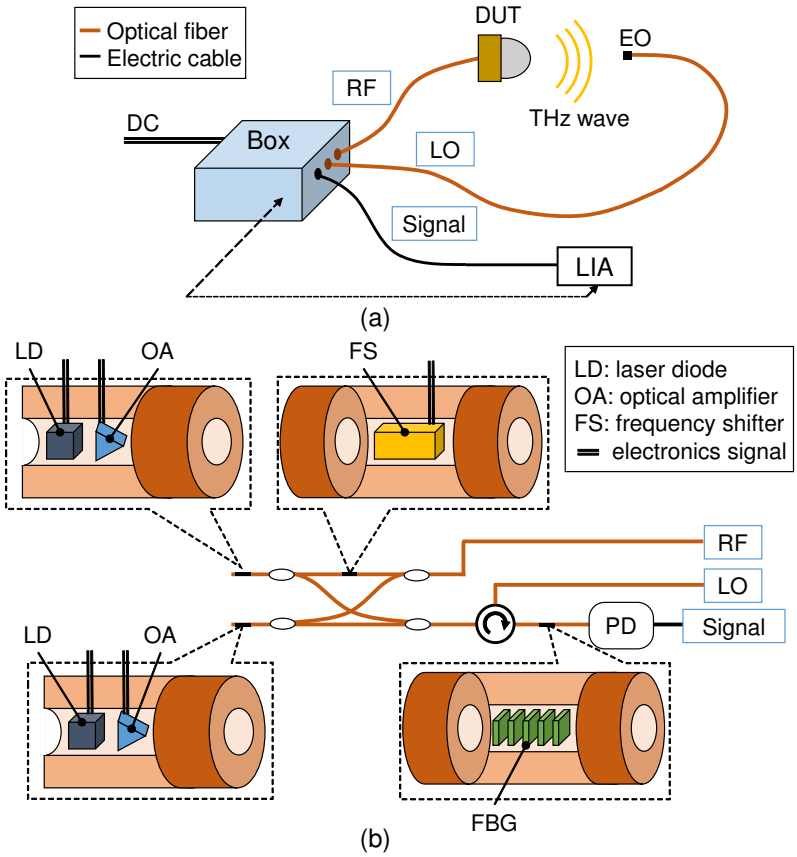

Figure 7.2.3: (a) Compact EO system in which (b) all optical components are integrated inside the fibers.

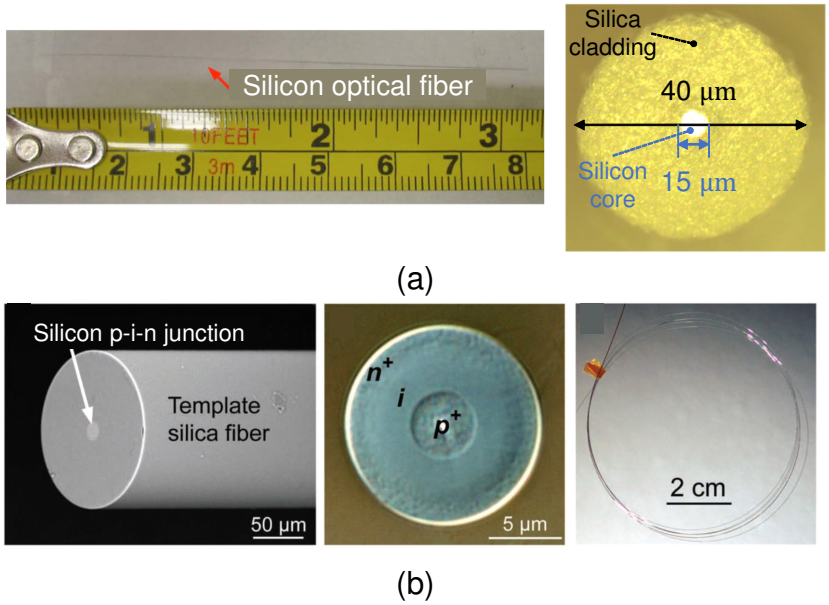

Figure 7.2.4: Examples of fabricated (a) silicon optical fiber [7.19] and (b) silicon p-i-n optical fiber [7.20].

terials in a hybrid integrated on-chip structure [7.25] as well as between the chip and the fiber of the EO probe. However, this technology still needs to overcome some hurdles, which includes fabricating long fibers and reducing attenuation losses inside the fibers [7.26]. Which integration technologies can allow the miniaturization of the EO system to adopt in the industrial market probably depends on their cost, performance, and usability.

References

[7.1] G. Ducournau, F. Pavanello, A. Beck, L. Tohme, S. Blin, P. Nouvel, E. Peytavit, M. Zaknoune, P. Szriftgiser, and J.F. Lampin, *"High-definition television transmission at 600 GHz combining THz photonics hotspot and high-sensitivity heterodyne receiver,"* Electron. Lett., **50**, pp. 413-415, 2014.

[7.2] T. Nagatsuma, G. Ducournau, and C. C. Renaud, *"Advances in terahertz communications accelerated by photonics,"* Electron. Lett., **50**, pp. 413-415, 2014.

[7.3] K. B. Cooper, R. J. Dengler, G. Chattopadhyay, E. Schlecht, J. Gill, A. Skalare, I. Mehdi, and P. H. Siegel, *"A high-resolution imaging radar at 580 GHz,"* IEEE Microw. Compon. Lett., **18**, pp. 64-66, 2008.

[7.4] K. B. Cooper, R. J. Dengler, N. Llombart, B. Thomas, G. Chattopadhyay, and P. H. Siegel, *"THz imaging radar for standoff personnel screening,"* IEEE Trans. THz Sci. Technol., **1**, pp. 169-182, 2011.

[7.5] D. T. Petkie, C. Casto, F. C. De Lucia, S. R. Murrill, B. Redman, R. L. Espinola, C. C. Frank, E. L. Jacobs, S. T. Griffin, C. E. Halford, J. Reynolds, S. O'Brien, and D. Tofsted, *"Active and passive imaging in the THz spectral region: phenomenology, dynamic range, modes, and illumination,"* J. Opt. Soc. Am. B, **25**, pp. 1523-1531, 2008.

[7.6] K. E. Peiponen, A. Zeitler, and M. K. Gonokami, *"Terahertz spectroscopy and imaging,"* Springer Series in Optical Sciences, **171**, pp. 513-515, 2013.

[7.7] I. F. Akyildiz, J. M. Jornet, and C. Han, *"Terahertz band: next frontier for wireless communications,"* Physical Commun. J., **12**, pp. 16-32, 2014.

[7.8] J. Haruki, K. Sakuma, and K. Kato, *"Synchronous THz wave combiner consisting of arrayed photomixers,"* 20th Microoptics Conference, 2015.

[7.9] K. Kato, *"Photonics technologies for high-power coherent THz generation,"* Progress in Electromagnetic Research Symposium (PIERS), 2016.

[7.10] K. Sakuma, J. Haruki, G. Sakano, K. Kato, S. Hisatake, and T. Nagatsuma, *"Coherent THz wave combiner composed of arrayed uni-traveling carrier photodiodes and planar lightwave circuit,"* Proc. of SPIE, **9747**, p. 974710, 2016.

[7.11] D. J. Lee, N. W. Kang, J. H. Choi, J. Kim, and J. F. Whitaker, *"Recent advances in the design of electro-optic sensors for minimally destructive microwave field probing,"* Sensors, **11**, pp. 806-824, 2011.

[7.12] Z. Zhao, A. Schwagmann, F. Ospald, D. C. Driscoll, H. Lu, A. C. Gossard, and J. H. Smet, *"Thickness dependence of the terahertz response in* ⟨110⟩ *–oriented GaAs crystals for electro-optic sampling at 1.55 μm,"* Opt. Express, **18**, pp. 15956-15963, 2010.

[7.13] D. J. Lee and J. F. Whitaker, *"An optical-fiber-scale electro-optic probe for minimally invasive high-frequency field sensing,"* Opt. Express, **16**, pp. 21587-21597, 2008.

[7.14] G. Carpintero, K. Balakier, Z. Yang, R. C. Guzman, A. Corradi, A. Jimenez, G. Kervella, M. J. Fice, M. Lamponi, M. Chitoui, F. V. Dijk, C. C. Renaud, A. Wonfor, E. A. J. M. Bente, R. V. Penty, I. H. White, and A. J. Seeds, *"Microwave photonic integrated circuits for millimeter-wave wireless communications,"* J. Lightwave Technol., **32**, pp. 3495-3501, 2014.

[7.15] F. V. Dijk, G. Kervella, M. Lamponi, M. Chtioui, F. Lelarge, E. Vinet, Y. Robert, M. J. Fice, C. C. Renaud, A. Jimenez, and G. Carpintero, *"Monolithically integrated InP heterodyne millimeter wave source for high data rate transmission,"* IEEE Photon. Technol. Lett., **26**, pp. 965-968, 2014.

[7.16] G. Carpintero, S. Hisatake, D. D. Felipe, R. Guzman, T. Nagatsuma, N. Keil, and T. Gobel, *"Photonics-based millimeter and terahertz wave generation using a hybrid integrated dual DBR polymer laser,"* IEEE MTT-S International Microwave Symposium (IMS), 2016.

[7.17] J. Ballato, T. Hawkins, P. Foy, B. Y. Kokuoz, C. McMillen, L. Burka, S. Morris, R. Stolen, and R. Rice, *"Advancements in semiconductor core optical fiber,"* Opt. Fiber Technol., **16**, pp. 399-408, 2010.

[7.18] U. Gibson, M. Fokine, N. Healy, S. Song, S. Svendson, U. Osterberg, A. C. Peacock, and J. Ballato, *"Semiconductor core fibers for optoelectronics,"* JSAP-OSA Joint Symposia, p. 6p-A410-1, 2017.

[7.19] B. Scott, K. Wang, V. Caluori, and G. Pickrell, *"Fabrication of silicon optical fiber,"* Opt. Eng., **48**, p. 100501, 2009.

[7.20] R. He, T. D. Day, M. Krishnamurthi, J. R. Sparks, P. J. Sazio, V. Gopalan, and J. V. Badding, *"Silicon p-i-n junction fibers,"* Adv. Mater., **25**, pp. 1461-1467, 2013.

[7.21] L. M. Xiao, N. Healy, U. Gibson, T. Hawkins, M. Jones, J. Ballato, and A. C. Peacock, *"Fusion splicing of silicon optical fibres,"* CLEO/Europe-EQEC, 2015.

[7.22] N. Healy, M. Fokine, Y. Franz, T. Hawkins, M. Jones, J. Ballato, A. C. Peacock, and U. J. Gibson, *"CO_2 laser-induced directional recrystallization*

to produce single crystal silicon-core optical fibers with low loss," Adv. Opt. Mater., **4**, pp. 1004-1008, 2016.

[7.23] E. F. Nordstrand, A. N. Dibbs, A. J. Eraker, and U. J. Gibson, *"Alkaline oxide interface modifiers for silicon fiber production,"* Opt. Mater. Express, **3**, pp. 651-657, 2013.

[7.24] A. C. Peacock, J. R. Sparks, and N. Healy, *"Semiconductor optical fibres: progress and opportunities,"* Laser Photon. Rev., **8**, pp. 53-72, 2014.

[7.25] D. Rand, B. C. Ellis, and P. R. Prucnal, *"Modal analysis of semiconductor cylinder fibers,"* IEEE Photon. Technol. Lett., **18**, pp. 31-33, 2006.

[7.26] A. C. Peacock, U. J. Gibson, and J. Ballato, *"Silicon optical fibres âĂŞ past, present, and future,"* Adv. Phys., **1**, pp. 114-127, 2016.

Acknowledgments

First and foremost, I would like to express my deepest appreciation and thanks to my enthusiastic supervisor, Professor Tadao Nagatsuma in the Graduate School of Engineering Science, Osaka University, for his valuable guidance, continued support, and cordial encouragement during my Master and Ph.D studies in Japan. I was truly honored to be accepted as the first international student in his laboratory. His enthusiasm for not only scientific researches but also practical social needs has been dramatically motivating and inspiring me. His patience, sympathy, and encouragement promoted my self-confidence to walk through a rough road to complete this dissertation.

I would like to express the sincerest gratitude to Professor Shintaro Hisatake, currently in Faculty of Engineering, Gifu University, for his supervision, unconditional support, and helpful discussions throughout my study. He not only supervised me technical knowledges but also supported me to obtain a scholarship for daily living. His exuberance motivated me a lot.

I would like to show my sincere appreciation to Professor Igor Vladilenovich Minin in National Research Tomsk Polytechnic University and Professor Oleg Vladilenovich Minin in National Research Tomsk State University, Russia, for their prompt advice and valuable discussions for my study. Their fruitful cooperation and encouragement helped me to understand the meaning and benefit of interdisciplinary research.

I would like to express my great gratitude to Professor Atsushi Sanada and Professor Masahiro Kitagawa in the Graduate School of Engineering Science, Osaka University, for their evaluation, valuable comments, and beneficial advice for the improvement of this dissertation.

I am really grateful to Professor Masayuki Fujita in the Graduate School of Engineering Science, Osaka University, for his constructive comments and advice during my study. His encouragement and support were greatly appreciated.

I would like to express my appreciation to Professor Kohei Hamaya, Professor Takashi Mukaiyama, and Professor Masayuki Abe in the Graduate School of

Engineering Science, Osaka University, for their valuable comments.

I would like to offer my special thank to Dr. Hirohisa Uchida in ARKRAY, Inc., Mr. Makoto Tojyo, Mr. Yoichi Oikawa, and Mr. Kunio Miyaji in Think-Lands Co., Ltd., for their valuable cooperation in my research. Their technical knowledges and professional working influenced and helped me a lot.

I would like to thank Dr. Sebastian Diebold and Mr. Kazuisao Tsuruda for their advice and encouragement in my research. I also learned a lot from their presentations and professional working.

I would like to thank all of my laboratory members during my study for their warm supports in both university and everyday life, especially, Mr. Yuuki Koda, Mr. Hikaru Nakajima, Mr. Koki Yamaguchi, Mr. Yusuke Isono, Mr. Naoyuki Fusao, and Mr. Daiki Kawakami in my research group for their discussions, hard working together, and sharing weal and woe. My grateful thanks are also extended to Mr. Yousuke Nishida, Mr. Ryoumei Yamada, Mr. Yusuke Kanai, Mr. Tsubasa Kurokawa, and Mr. Yusuke Kujime for their help in office equipments, Japanese translation, and interesting conversations everyday. Without their supports, my study would have been more difficult.

I would like to acknowledge Monbukagakusho (MEXT) Honors Scholarship, Japan Tobacco (JT) Asia Scholarship, and Japan Society for the Promotion of Science (JSPS) Research Fellowship for their financial supports of research and everyday life during my Master and Ph.D courses.

Finally, I am very much indebted to my family. Words are not enough to express how grateful I am to my parents and my girl friend, who have supported and taken care of me in every possible way to see the completion of this dissertation. Their expectation on me gave me tremendous power and patience to complete this dissertation.

List of publications

Academic articles with peer review

[1] **Hai Huy Nguyen Pham**, Shintaro Hisatake, and Tadao Nagatsuma, *"Characterization of an F-band horn antenna based on electro-optic near-field measurements,"* IEICE Transactions on Electronics, vol. E98-C, no. 8, pp. 866 – 872, August 2015.

[2] **Hai Huy Nguyen Pham**, Shintaro Hisatake, Oleg Vladilenovich Minin, Igor Vladilenovich Minin, and Tadao Nagatsuma, *"Three-dimensional direct observation of Gouy phase shift in a terajet produced by a dielectric cuboid,"* Applied Physics Letters, vol. 108, no. 19, pp. 191102-1 – 191102-4, May 2016.

[3] **Hai Huy Nguyen Pham**, Shintaro Hisatake, Oleg Vladilenovich Minin, Tadao Nagatsuma, and Igor Vladilenovich Minin, *"Asymmetric phase anomaly of terajet generated from dielectric cube under oblique illumination,"* Applied Physics Letters, vol. 110, no. 20, pp. 201105-1 – 201105-5, May 2017.

[4] **Hai Huy Nguyen Pham**, Shintaro Hisatake, Oleg Vladilenovich Minin, Tadao Nagatsuma, and Igor Vladilenovich Minin, *"Enhancement of spatial resolution of Terahertz imaging systems based on terajet generation by dielectric cube,"* APL Photonics, vol. 2, no. 5, pp. 056106-1 – 056106-9, May 2017.

[5] Shintaro Hisatake, **Hai Huy Nguyen Pham**, and Tadao Nagatsuma, *"Visualization of the spatial-temporal evolution of continuous electromagnetic waves in the Terahertz range based on photonics technology,"* Optica, vol. 1, no. 6, pp. 365 – 371, November 2014.

[6] Tadao Nagatsuma, Shintaro Hisatake, and **Hai Huy Nguyen Pham**, *"Photonics for millimeter-wave and Terahertz sensing and measurement,"* IEICE Transactions on Electronics, vol. E99-C, no. 2, pp. 173 – 180, February 2016.

[7] Tadao Nagatsuma, Shintaro Hisatake, Masayuki Fujita, **Hai Huy Nguyen Pham**, Kazuisao Tsuruda, Shigeru Kuwano, and Jun Terada, *"Millimeter-wave and Terahertz-wave applications enabled by photonics,"* IEEE Journal of Quantum Electronics, vol. 52, no. 1, 0600912, January 2016.

[8] Shintaro Hisatake, Hikaru Nakajima, **Hai Huy Nguyen Pham**, Hirohisa Uchida, Makoto Tojyo, Yoichi Oikawa, Kunio Miyaji, and Tadao Nagatsuma, *"Mapping of electromagnetic waves generated by free-running self-oscillating devices,"* Scientific Reports, vol. 7, 9203, August 2017.

Conference proceedings with peer review

[1] **Hai Huy Nguyen Pham**, Shintaro Hisatake, and Tadao Nagatsuma, *"Far-field antenna characterization in the sub-THz region based on electrooptic*

near-field measurements," Proceedings of International Topical Meeting on Microwave Photonics & 9th Asia-Pacific Microwave Photonics Conference (MWP/APMP2014), pp. 377-380, October 2014.

[2] **Hai Huy Nguyen Pham**, Hirohisa Uchida, Shintaro Hisatake, and Tadao Nagatsuma, *"Sensitivity comparison between DAST and ZnTe probes in the nonpolarimetric self-heterodyne electro-optic detection system,"* Proceedings of the 3rd International Symposium on Microwave/Terahertz Science and Applications & the 6th International Symposium on Terahertz Nanoscience (MTSA 2015/TeraNano 6), P1-5, July 2015.

[3] **Hai Huy Nguyen Pham**, Shintaro Hisatake, Hirohisa Uchida, and Tadao Nagatsuma, *"Evaluation of DAST crystals for nonpolarimetric self-heterodyne electro-optic detection of Terahertz waves,"* Proceedings of the 1st Photonics-applied Electromagnetic Measurement International Workshop (PEM), November 2015.

[4] **Hai Huy Nguyen Pham**, Shintaro Hisatake, Igor Vladilenovich Minin, Oleg Vladilenovich Minin, and Tadao Nagatsuma, *"Experimental characterization of terajet generated from dielectric cuboid under different illumination conditions,"* Proceedings of the 10th Global Symposium on Millimeter Waves (GSMM), pp. 120-122, May 2017.

[5] **Hai Huy Nguyen Pham**, Shintaro Hisatake, Igor Vladilenovich Minin, Oleg Vladilenovich Minin, and Tadao Nagatsuma, *"Subwavelength resolution of Terahertz imaging system enabled by a dielectric cuboid,"* Proceedings of the 24th Congress of the International Commission for Optics (ICO-24), August 2017.

[6] Shintaro Hisatake, **Hai Huy Nguyen Pham**, and Tadao Nagatsuma, *"Electric field visualization system for antenna characterization at Terahertz frequency based on a nonpolarimetric self-heterodyne EO technique,"* Proceedings of 2014 XXXIth General Assembly and Scientific Symposium (URSI GASS), pp. 1-4, August 2014.

[7] Shintaro Hisatake, **Hai Huy Nguyen Pham**, and Tadao Nagatsuma, *"Direct observation of Terahertz wavefront converted by a metal hole array,"* Proceedings of the 40th International Conference on Infrared, Millimeter, and Terahertz waves (IRMMW-THz 2015), pp. 1-2, August 2015.

[8] Koki Yamaguchi, Hikaru Nakajima, **Hai Huy Nguyen Pham**, Shintaro Hisatake, Tadao Nagatsuma, Hirohisa Uchida, Makoto Tojo, Yoichi Oikawa, and Kunio Miyaji, *"Electric-field visualization technique for evaluating radiation from automotive millimeter-wave radar,"* 2017 IEEE MTT-S International Conference on Microwaves for Intelligent Mobility (ICMIM), pp. 151-154, March 2017.

International conferences with peer review

[1] **Hai Huy Nguyen Pham**, Shintaro Hisatake, and Tadao Nagatsuma, *"Far-field antenna characterization in the sub-THz region based on electrooptic near-field measurements,"* International Topical Meeting on Microwave Photonics & 9th Asia-Pacific Microwave Photonics Conference (MWP/APMP2014), WC-7, Sapporo, Japan, October 2014.

[2] **Hai Huy Nguyen Pham**, Hirohisa Uchida, Shintaro Hisatake, and Tadao Nagatsuma, *"Sensitivity comparison between DAST and ZnTe probes in the nonpolarimetric self-heterodyne electro-optic detection system,"* the 3rd International Symposium on Microwave/Terahertz Science and Applications & the 6th International Symposium on Terahertz Nanoscience (MTSA 2015/TeraNano 6), P1-5, Okinawa, Japan, July 2015.

[3] **Hai Huy Nguyen Pham**, Shintaro Hisatake, Hirohisa Uchida, and Tadao Nagatsuma, *"Evaluation of DAST crystals for nonpolarimetric self-heterodyne electro-optic detection of Terahertz waves,"* the 1st Photonics-applied Electromagnetic Measurement International Workshop (PEM), FCA-1, Kyoto, Japan, November 2015.

[4] **Hai Huy Nguyen Pham**, Shintaro Hisatake, Igor Vladilenovich Minin, Oleg Vladilenovich Minin, and Tadao Nagatsuma, *"Experimental characterization of terajet generated from dielectric cuboid under different illumination conditions,"* the 10th Global Symposium on Millimeter Waves (GSMM), PS-10, Hong Kong, China, May 2017.

[5] **Hai Huy Nguyen Pham**, Shintaro Hisatake, Igor Vladilenovich Minin, Oleg Vladilenovich Minin, and Tadao Nagatsuma, *"Subwavelength resolution of Terahertz imaging system enabled by a dielectric cuboid,"* the 24th Congress of the International Commission for Optics (ICO-24), Tu1G-07, Tokyo, Japan, August 2017.

[6] Shintaro Hisatake, **Hai Huy Nguyen Pham**, and Tadao Nagatsuma, *"Electric field visualization system for antenna characterization at Terahertz frequency based on a nonpolarimetric self-heterodyne EO technique,"* 2014 XXXIth General Assembly and Scientific Symposium (URSI GASS), AB03.2, Beijing, China, August 2014.

[7] Shintaro Hisatake, **Hai Huy Nguyen Pham**, and Tadao Nagatsuma, *"Direct observation of Terahertz wavefront converted by a metal hole array,"* the 40th International Conference on Infrared, Millimeter, and Terahertz waves (IRMMW-THz 2015), W1A-4, Hong Kong, China, August 2015.

[8] Koki Yamaguchi, Hikaru Nakajima, **Hai Huy Nguyen Pham**, Shintaro Hisatake, Tadao Nagatsuma, Hirohisa Uchida, Makoto Tojo, Yoichi Oikawa,

and Kunio Miyaji, *"Electric-field visualization technique for evaluating radiation from automotive millimeter-wave radar,"* 2017 IEEE MTT-S International Conference on Microwaves for Intelligent Mobility (ICMIM), TU5-3, Nagoya, Japan, March 2017.

Domestic conferences

[1] **Hai Huy Nguyen Pham**, Shintaro Hisatake, and Tadao Nagatsuma, *"Continuous-wave Terahertz field visualization based on nonpolarimetric self-heterodyne EO technique,"* the 2014 IEICE General Conference (電子情報通信学会総合大会), C-14-11, Niigata, Japan, March 2014.

[2] **Hai Huy Nguyen Pham**, Shintaro Hisatake, and Tadao Nagatsuma, *"Characterization of a horn antenna at 125 GHz based on electro-optic near-field measurements,"* the 2015 IEICE General Conference (電子情報通信学会総合大会), C-14-3, Shiga, Japan, March 2015.

[3] **Hai Huy Nguyen Pham**, Shintaro Hisatake, and Tadao Nagatsuma, *"Experimental visualization of beam-collimating effect by metal hole array in THz region,"* the 76th Autumn Meeting Japan Society of Applied Physics (JSAP-OSA Joint Symposia 2015), 15a-2E-9, Nagoya, Japan, September 2015.

[4] **Hai Huy Nguyen Pham**, Shintaro Hisatake, Igor Vladilenovich Minin, Oleg Vladilenovich Minin, and Tadao Nagatsuma, *"Experimental evaluation of terajet produced by a dielectric cuboid in the THz region,"* the 63rd Spring Meeting Japan Society of Applied Physics (JSAP), 22a-H135-7, Tokyo, Japan, March 2016.

[5] **Hai Huy Nguyen Pham**, Shintaro Hisatake, Igor Vladilenovich Minin, Oleg Vladilenovich Minin, and Tadao Nagatsuma, *"Angular characteristic of terajet generated from dielectric cuboid in THz region,"* the 64th Spring Meeting Japan Society of Applied Physics (JSAP), 14a-211-7, Yokohama, Japan, March 2017.

[6] **Hai Huy Nguyen Pham**, Shintaro Hisatake, Igor Vladilenovich Minin, Oleg Vladilenovich Minin, and Tadao Nagatsuma, *"Exploit terajet generated from dielectric cuboid to enhance spatial resolution of THz imaging system,"* the 78th Autumn Meeting Japan Society of Applied Physics (JSAP-OSA Joint Symposia 2017), 7p-A409-4, Fukuoka, Japan, September 2017.

Technical reports/Research reports

[1] **Hai Huy Nguyen Pham**, Shintaro Hisatake, and Tadao Nagatsuma, *"F-band horn antenna characterization based on electro-optic near-field measurement,"* IEICE Technical Report on Microwave, Millimeter Waves and Photonics (MWP2015-4), vol. 115, no. 53, pp. 19-24, Tokyo, Japan, May 2015.

List of awards

[1] The Best Poster Award, *"Sensitivity comparison between DAST and ZnTe probes in the nonpolarimetric self-heterodyne electro-optic detection system,"* the 3rd International Symposium on Microwave/Terahertz Science and Applications & the 6th International Symposium on Terahertz Nanoscience (MTSA 2015/TeraNano 6), July 2015.

[2] The Best Poster Award, *"Evaluation of DAST crystals for nonpolarimetric self-heterodyne electro-optic detection of Terahertz waves,"* the 1st Photonics-applied Electromagnetic Measurement International Workshop (PEM), November 2015.